Modelling and Control of a Cable-Driven Parallel Robot
Methods for vibration reduction and motion quality improvement

Von der Fakultät Konstruktions-, Produktions- und Fahrzeugtechnik
der Universität Stuttgart
zur Erlangung der Würde eines Doktor-Ingenieurs (Dr.-Ing.)
genehmigte Abhandlung

Vorgelegt von
Christian Tobias Schenk
aus Nürtingen

Vorsitzender:	Prof. Dr.-Ing. Dr. h.c. Mathias Liewald
Hauptberichter:	PD Dr.-Ing. Andreas Pott
1. Mitberichter:	Prof. Dr. rer. nat. Heinrich H. Bülthoff
2. Mitberichter:	Univ.-Prof. Dr.-Ing. Dr. h.c. mult. Alexander Verl
Tag der mündlichen Prüfung:	03.06.2019

Institut für Steuerungstechnik der Werkzeugmaschinen und Fertigungseinrichtungen
(ISW)
der Universität Stuttgart

2019

Contents

List of Figures

List of Tables

List of Abbreviations

E_C	Elasticity module / Youngs' modulus
J_M	Inertia of a motor shaft
J_M	Inertia of the motor drum for rotations around the motor axis
L	Lagrangian energy function
L	Lipschitz constant
L_e	Ideal cable length
M_0	Standstill torque of a motor of type AX8033-0E21
M_i	Center of a panned pulley
S_C	Cross section
T	Kinetic energy
T_C	Kinetic energy of the Cables
T_M	Kinetic energy of the motor
T_P	Kinetic energy of the platform
T_e	Sampling time
T_{C_i}	Cable tension as combination of a dynamic component $T_{C_i,dyn}$ and a static component $T_{C_i,pre}$
T_{IMU}	Inertial Measurement Unit sampling time
T_{sim}	Simulation sampling time
U	Potential energy
V	Energy function as Lyapunov candidate
$V(x(t))$	Storage function

V_C	Potential energy of the cable
V_P	Potential energy of the platform
W_i	Weight for Unscented Kalman-Filter
$\boldsymbol{A}_i$	Offboard connection point at pulley i
$\boldsymbol{A}_{act,i}$	Activation matrix for cable i
$\boldsymbol{B}_\bullet$	System input matrix
$\boldsymbol{B}_i$	Onboard connection point for drivetrain i
$\boldsymbol{C}_\bullet$	System output matrix
$\boldsymbol{C}_i$	Contact point at which the cable leaves the pulley
$\boldsymbol{D}_\bullet$	System feed-through matrix
$\boldsymbol{D}_{C_i}$	Additional assigned damping for Port-Hamilton cable model
$\Delta\boldsymbol{\Phi}$	Change in parameter set for parameter calibration
$\Delta\bullet$	Uncertainty
$\boldsymbol{J}$	Jacobian matrix to map the platform pose to cable lengths and cable forces to platform wrenches
$\boldsymbol{K}_{1/2}$	Gain matrices for parameters estimation in Terminal Sliding-Mode Controller scheme
$\boldsymbol{K}_{i,el}$	Contribution of elasticity to the cable stiffness
$\boldsymbol{K}_{i,g}$	Contribution of geometry to the cable stiffness
Λ_i	Gain matrix for Sliding-Mode Controller
$\boldsymbol{M}$	Mass matrix
$\boldsymbol{P}_\bullet$	Covariance matrix for Kalman-Filter
Ψ_i	Matrix that transforms from generalised coordinates to modal coordinates for cable i
$\boldsymbol{R}_{\boldsymbol{\xi}}$	Measurement noise covariance matrix
$\boldsymbol{R}_{A_i}$	Rotation matrix to describe pulley panning
$\boldsymbol{T}$	Matrix with covariance eigenvectors for realistic measurement noise
$\boldsymbol{a}_i$	Vector pointing to the i offboard connection point

$\alpha_{UKF}, \lambda_{UKF}, \kappa_{UKF}$	Tuning parameters of the Unscented Kalman Filter
$\boldsymbol{b}_i$	Vector pointing to the i onboard connection point
$\boldsymbol{b}_{\ddot{\boldsymbol{x}}}$	Inertial Measurement Unit acceleration bias
$\bar{\bullet}$	Mean value or mean vector
$\bar{\boldsymbol{f}}$	Mean feasible force vector
$\bar{\boldsymbol{q}}_{C_i}$	Nominal distribution of mass elements of the Finite-Element Method based cable model
$\bar{\boldsymbol{q}}_{C_i}(0)$	Initial position of mass elements for Finite-Element Method based cable model, when the cable is completely unwound
β_i	Wrapping angle of pulley i
$\boldsymbol{\mu}$	Tuning parameter for Super-Twisting Sliding-Mode controller gain adaptation
$\boldsymbol{\mu}$	Tuning parameter for adaptive Super-Twisting Sliding-Mode Controller
$\boldsymbol{\nu}$	Orientation vector of the platform
$\boldsymbol{\omega}_i$	Vector of eigenfrequencies for cable i
$\boldsymbol{\sigma}$	Sliding variable
$\boldsymbol{\xi}$	Vector of lumped disturbances
$\boldsymbol{\xi}_R$	Measurement noise
$\boldsymbol{\zeta}$	External disturbance
$\boldsymbol{\zeta}_{C_i,D}$	Damping factor for cable i
$\boldsymbol{A}_\bullet$	System matrix
$\boldsymbol{D}_{C_i}$	Damping matrix of cable i
$\boldsymbol{G}$	Control input matrix
$\boldsymbol{I}$	Interconnection matrix for system in Port-Hamilton form
$\boldsymbol{J}_{FK}$	Jacobian matrix of $\boldsymbol{\Phi}_{FK}$ as a function of the platform pose $\boldsymbol{x}$ and measured cable lengths at iteration step k
$\boldsymbol{K}_{C_i}$	Stiffness matrix for cable i
$\boldsymbol{M}_{C_i}$	Inertia matrix of cable i

$\boldsymbol{Q}_{\zeta}$	Model covariance matrix for Kalman filter
$\boldsymbol{R}$	Damping matrix in systems in Port-Hamilton form
$\boldsymbol{\Lambda}_b$	Positive definite matrix to ensure boundary conditions
$\boldsymbol{\Lambda}_{1,m}$	Upper limit for Sliding-Mode Controller gain $\boldsymbol{\Lambda}_1$
$\boldsymbol{\Lambda}_{1/2}$	Positive definite gain matrix
$\boldsymbol{\Lambda}_{C_i}$	Design parameter for control of cable i
$\boldsymbol{\Lambda}_{SMC}$	Positive weight for sliding variable
$\boldsymbol{\Lambda}_{TSMC}$	Gain matrix of Terminal Sliding-Mode Controller
$\boldsymbol{\Omega}_{\boldsymbol{\Lambda}}$	Tuning parameter for Super-Twisting Sliding-Mode controller gain adaptation
$\boldsymbol{\Phi}$	Diffeomorphism, which allows to transform from angular velocities to Euler-rates
$\boldsymbol{\Phi}$	Set of n_p parameters
$\boldsymbol{\eta}$	Deflection of all elements from its equilibrium point
$\boldsymbol{\mathcal{Y}}$	Propagated Sigma points
$\boldsymbol{\xi}_k$	Measurement noise
$\boldsymbol{\xi}_q$	Non-conservative forces
$\boldsymbol{\zeta}_k$	Model noise
$\boldsymbol{\zeta}_{Q,k}$	Process noise accounted in the Kalman Filter
$\boldsymbol{c}$	Vector from $\mathcal{K}_P$ to $\mathcal{K}_{C_i}$
$\boldsymbol{f}$	Vector of cable forces
$\boldsymbol{f}_P$	Wrench that is applied at the platform
$\boldsymbol{f}_g$	Generalised forces
$\boldsymbol{f}_{i,j}$	Forces acting on cable i and element j
$\boldsymbol{l}_{i,j\|j+1}$	Vector going from the j^{th} element to the next element of cable i
$\boldsymbol{r}$	Position of the platform in $\mathcal{K}$
$\boldsymbol{w}_P$	Wrench acting on the platform
$\boldsymbol{x}_P$	Pose of the platform in $\mathcal{K}_W$

$\bullet_{des}$	Desired entity the system has to track
$\mathcal{K}_C$	Coordinate system fixed at the platform center of mass
$\mathcal{K}_P$	Platform coordinate system with axes $\S_P$,$\dagger_P$,$\ddagger_P$
$\delta_{i,FC}$	Contribution to the friction compensation
$\delta_{i,virt}$	Contribution of virtual control input for friction compensation
$\boldsymbol{e}$	Error vector
ϵ_{FK}	Damping factor for the forward kinematics to avoid singularities
ϵ_{STC}	Positive tuning parameter for Super-Twisting Sliding-Mode controller
$\boldsymbol{f}_n$	State function term of the nominal model
$\boldsymbol{f}_{null}$	Force vector assigned to the nullspace
γ_{C_i}	Panning angle of pulley i
$\boldsymbol{h}_n$	Output function term of the nominal model
$\hat{\bullet}$	Estimation of an entity $\bullet$
$\hat{k}_c(t)$	Estimated static friction coefficient
${}^P\boldsymbol{I}_P$	Platform inertia in platform frame
$\boldsymbol{I}_P$	Platform inertia in world frame
κ_{UKF}	Arbitrary scaling parameter, which is usually set to 0 [29]
$\boldsymbol{l}_{seg,i}$	Nominal distance from one mass-spring-damper element of cable i to the next mass-spring-damper element
$\lambda_{FC,1}, \lambda_{FC,2}$	Parameters for estimation of static friction coefficient
$\mathcal{K}_V$	Coordinate system fixed at the ground as Vicon reference
$\mathcal{K}_W$	World coordinate system with axes $\S_W$,$\dagger_W$,$\ddagger_W$
$\mathcal{K}_{C_i}$	Pulley attached coordinate system for cable i
$\mathcal{S}$	Sliding surface
$\mathcal{U}$	Set of feasible inputs
$\mathcal{V}$	Set of outputs
$\mathcal{X}$	Sigma-point vector

ω	Angular velocity of the platform
$\overline{\boldsymbol{a}}$	Upper limit for search region of offboard connection point
$\overline{\boldsymbol{b}}$	Upper limit for search region of onboard connection point
$\overline{\boldsymbol{u}}$	Upper limit for sliding mode control input
$\overline{t_i}$	Upper limit of feasible cable tension for cable i
$\boldsymbol{p}$	Generalised momentum
$\boldsymbol{q}$	Generalised coordinates
$\boldsymbol{q}_C$	Generalised coordinates assigned to the cables
$\boldsymbol{q}_M$	Generalised coordinates assigned to the motors
$\boldsymbol{q}_P$	Generalised coordinates of the platform
$\text{sign}^\star$	New signum function that accounts driving force in friction
$\tau_i^\star$	Torque value subscribed to motor i
τ_i	Applied torque of motor i
θ_{C_i}	Inclination angle of cable i
θ_{M_i}	Angle of motor i
$\boldsymbol{u}$	Control input
$\boldsymbol{u}_{FF}$	feed forward control input based on the nominal model of a system
$\boldsymbol{u}_{SMC}$	Sliding-Mode Control input
$\boldsymbol{u}_{\boldsymbol{\zeta},C_i}$	Vector of external disturbances
$\boldsymbol{u}_{b,C_i}$	Boundary forces
$\boldsymbol{u}_{b,k}$	Biased Inertial Measurement Unit measurement
$\boldsymbol{u}_{c,C_i}$	Control input for cable i
$\underline{\boldsymbol{a}}$	Lower limit for search region of offboard connection points
$\underline{\boldsymbol{b}}$	Lower limit for search region of onboard connection point
$\underline{\boldsymbol{u}}$	Lower limit for sliding mode control input
$\underline{t_i}$	Lower limit of feasible cable tension for cable i
$\boldsymbol{w}_P$	Wrench applied at the platform

$\boldsymbol{y}$	System output
$\boldsymbol{z}_{1,des}$	Desired trajectory in Euler-angles
$\boldsymbol{z}_{2,des}$	Desired velocities in Euler-rates
$\boldsymbol{z}_{eq}$	Equivalent control input
$\zeta_{i,j,\bullet}$	Damping factor for cable i, element j and direction $\bullet$
${}^{C_i}\bullet_{C_i}$	$\bullet$ stands here for $\boldsymbol{u}$,$\boldsymbol{v}$,$\boldsymbol{w}$ as the x,y,z components in frame of cable i
${}^{C_i}s$	Linear abscissa of cable i
${}^{C_i}x_{C_i}, {}^{C_i}y_{C_i}, {}^{C_i}z_{C_i}$	x, y, z components in frame of cable i
a_a	Amplitude of an arbitrary signal
$c_{C_i,\bullet}$	Damping coefficients for cable i
e_{PHS}	Effort variable
$f(\bullet)$	System function of arbitrary order
$f^{\star}_{lin}$	First resonance frequency of a linear system
$f^{\star}_{nonlin}$	First resonance frequency of a non-linear system
f_a	Frequency of an arbitrary signal
$f_{C_{i,dyn}}(t)$	Time varying tension signal
$f_{C_{i,pre}}$	Static tension signal
f_{PHS}	Flow variable
f_{m_i}	Mediate cable tension between minimum and maximum cable forces
f_{v_i}	Viscous friction
g	Gravity constant
$g(\bullet)$	Random nonlinear output function
i_{M_i}	Motor inertia
k_{M_i}	Motor elasticity
$k_{i,c}$	Static friction coefficient
l_i	Lenght of cable i
$l_{3,des,virt}$	Desired virtual cable length of motor three for friction compensation

l_{ext}	Cable length based on the kinematic model including winch panning
m	Number of cables
m_d	Nominal mass of one motor drum
$m_{C_i,j}$	Mass of element j of cable i
m_{C_i}	Mass of cable i
n_a	Dimension of an arbitrarily big system
n_p	Number of parameters to be identified
n_u	Number of elements of the control input
n_x	Number of states
n_y	Number of elements of the system output input
n_e	Number of mass elements on cable i
r_D	Nominal radius of all motor drums
r_C	Radius of one pulley
s_{LP}	Laplace variable
t_r	Convergence time
w	Supply rate of a system with Port-Hamilton structure
${}^{W}\boldsymbol{R}_P$	Orientation of the platform in $\mathcal{K} = \{\mathcal{O}, \mathcal{X}, \mathcal{Y}, \mathcal{Z}\}$
${}^{\boldsymbol{\nu}}\boldsymbol{E}_{\boldsymbol{\omega}}$	Matrix that transforms from angular velocities to Euler-rates
${}^{C_i}\boldsymbol{R}_W(\boldsymbol{q}_P)$	Rotationmatrix that transforms from $\mathcal{K}_W$ to $\mathcal{K}_{C_i}$
${}^{C_i}\boldsymbol{R}_{W_{x/z}}$	Rotation matrices to transform from world coordinate frame to cable coordinate frame
MiCaroSi	Mini Cable-Robot Simulator
TwinCAT	Windows Control and Automation Technology

Foreword

This part of my thesis is dedicated to all friends and colleagues, who contributed a lot to my personal development and the progress of this work. Sincerely, I want to thank Prof. Heinrich H. Bülthoff for financial and Carlo Masone for mental support. Furthermore, I want to thank PD Dr.-Ing. Andreas Pott for supervision, motivating talks and suggestions. He showed me a way out of difficult situations, every time I came to the ISW in Stuttgart with a head full of work related sorrows. Additionally, I want to mention my mentor Harald Teufel as well as Maria, Rainer, Mitch and the mechanical workshop for practical suggestions. Special thanks also to Philipp Tempel, Philipp Miermeister for inspiring talks and Univ.-Prof. Dr.-Ing. Dr. h.c. mult. Alexander Verl as well as Prof. Dr.-Ing. Dr. h.c. Mathias Liewald for completing my committee and corrections. My work, done here at MPI, speaks for the progress of my experience and acquired knowledge. The motivation and discipline to start this PhD was always present and my dedication to thrive never lowered. However, we should not forget, that our lives outside of work allows us to recreate and regain energy, which is essential. Thus, I want to dedicate this part also to those who motivated me, broadened my horizon and shaped my personality. The people I met over the last years, contributed a lot to my personal development. This includes especially all my colleagues Carlo Gerboni, Julia, Stefano, Mario, Marcin, Aamir, Sujit and Mikhail, but also Eduardo and Javiera, who I met in Chile. Thanks to Laura Fademrecht for strong coffee and inspiring discussions, to Mario who brought my passion for Salsa and Bachata to life and Tamara Schaffhauser for support and motivating talks. At the same time, I want to thank all salseros and salseras, especially Yvonne, Christin, Klara, Svenja for nice Salsa parties as well as Yasser, Lou and Jorge for a lot of patience and instructive lessons. Weekends and evenings full of work would not have been possible without those friends and colleges, dancing and sport as counterbalance. Thanks to Sylvia and Beatrice Barbazzeni, a very good friend and companion. Both of you contributed so much to my personal development. I am grateful for having met you Anja. You enrich my life every moment I am with you. Te quiero.

Abstract

Because of their parallel structure and the choice of drivetrain components, Cable-Driven Parallel Robots are able to exert high accelerations and exhibit large workspaces. Both properties make them perfect candidates for simulators. However, using Cable-Driven Parallel Robots as simulators raise new challenges. Those have to guarantee robustness and reliability, since simulators and human beings share the same workspace. Furthermore to assure precise tracking of a desired platform pose, velocity and acceleration, and a minimum of vibrations, sophisticated controllers and models have to be developed. Cables tend, because of their physical properties to vibrate, that are forwarded to the platform and degrade the simulation quality. Besides, static friction and aggressive control strategies can apply impulses and provoke vibrations in the drivetrain.

Sliding-Mode Controller are robust, but use a discontinuous signum function, which causes so-called chattering. Simulations showed, that an adaption of controller gains significantly reduce those controller induced vibrations. Experiments highlight especially the robustness of the proposed adaptive Super-Twisting Sliding-Mode Controller in presence of parameter uncertainties and external disturbances. External disturbances of up to 384% of the platform weight could not distract the platform position from its trajectory. The platform error always stayed in a desired area.

In simulation an adaptive friction compensation compensated almost completely time-varying static and viscous friction. It is worth to mention, that the proposed adaptive friction compensation does not require knowledge about the friction dynamics. Due to this, the the proposed algorithm is applicable for different types of time-varying friction. Experiments proved the efficiency of the proposed algorithm. The error made by viscous and static friction reduced to 0.5% and to 2.5% respectively of the error without friction compensation.

So far there exist no holistic approaches to reduces vibrations for a Cable-Driven Parallel Robot as a simulator. This thesis fills this gap and takes the platform and non-linear, coupled cable dynamics into account. Assuming taut cables, Finite-Element Method based models can predict precisely cable vibrations and are feasible for model-based controller synthesis. Port-Hamilton models facilitate the design of holistic model-based controller such as Interconnection Damping-Assignment Passivity-Based control. Those allow, to assign physical properties to the system, that differ from its original properties. Especially for

simulators this is an interesting feature, since simulators mimic the dynamics of various systems. Furthermore, Interconnection Damping-Assignment Passivity-Based Control allows to increase damping of a system, which is advantageous for vibration suppression Simulations with one cable, fixed at both ends, show that the energy, assigned to vibrations, can be reduced up to 63.82%.

Further experiments are necessary, in order to verify all control approaches. This requires the integration of additional sensors and fusion of all measurements. Thus, this work presents a dual Unscented Kalman-Filter for a Cable-Driven Parallel Robot, to facilitate further investigations on cable vibrations and their impact on the platform.

Zusammenfassung

Seilroboter können aufgrund ihrer parallel Struktur und dem Aufbau ihrer Antriebsstränge hohe Beschleunigungen erreichen und besitzen einen großen Arbeitsraum. Beide Eigenschaften ermöglichen den Einsatz als Simulatoren. Durch die Verwendung als Simulator ergeben sich jedoch neue Herausforderungen und Aufgabenstellungen. Zu diesen zählen Robustheit, präzises Folgeverhalten von Positionen, Geschwindigkeiten und Beschleunigungen und eine schwingungsarme Betriebsart. Seile neigen aufgrund ihrer physikalischen Eigenschaften zu Schwingungen, die an die Platform weitergegeben werden und dadurch die Simulationsqualität negativ beeinflussen. Desweiteren können statische Reibung und aggressive Regelungsstrategien Impulse applizieren, die Schwingungen am Antriebsstrang provizieren.

Sliding-Mode Controller sind robuste Regler, die auftgrund ihrer diskontinuierlichen Reglerstruktur schnell wechselnde Reglereingänge so genanntes "Chattering"/Zittern hervorrufen. Simulationen haben gezeigt, dass diese Effekte durch eine Adaptierung der Reglerparameter deutlich reduziert und regler-induzierte Vibrationen präveniert werden können. Experimentelle Untersuchungen heben vor allem die Robustheit bezüglich Parameterungenauigkeiten und der Einwirkung von Störgrößen hervor. Selbst bei einer Störgrößeneinwirkung von 384% der Gewichtskraft der Platform kann der Positionierungsfehler in vordefinierten Grenzen gehalten werden.

Eine adaptive Reibungskompensation erlaubt es in Simulation den Einfluss von variierender, statischer und viskoser Reibung beinahe vollständig zu kompensieren. Speziel sei hier erwähnt, dass die adaptive Reibungskompensation modellunabhängig ist. Dies hebt seine Anwendbarkeit auf unterschiedliche Formen von Reibung hervor. Experimente zeigen eine Verbesserung der Kompensation von viskoser Reibung um 2.5%. Anhand der ohnehin schon hohen Positioniergenauigkeit ist dies nochmals eine deutliche Verbesserung. Der Einfluss statischer Reibung konnte ebenfalls leicht reduziert werden.

Die Komplexität des Vorhabens Systemschwingungen ganzheitlich zu reduzieren, sollte nicht unterschätzt werden. Bisher gibt es keine Ansätze zur Schwingungsreduzierung von Seilrobotern als Simulatoren. Diese Thesis präsentiert ein ganzheitliches Model eines Seilroboters unter Berücksichtigung der Platform und Seildynamik als Port-Hamilton Model. Unter der Annahme gespannter Seile hat sich gezeigt, dass ein Finite-Elemente basiertes Seilmodel Seilschwingungen gut hervorsagen kann. Desweiteren eignet sich das Finite-

Elemente Model für die modellbasierte Reglersynthese. Port-Hamilton Modelle ermöglichen die Synthese modellbasierter Regler (Interconnection Damping-Assignment Passivity-Based Control), wodurch dem Roboter physikalische Eigenschaften (wie zusätzliche Dämpfung) aufgeprägt werden können. Simulationen zeigen, dass durch die Anpassung der Dämpfung die Schwingungsenergie eines Seils mit konstanter Seillänge um bis zu 63.82% reduziert werden kann.

Um alle noch ausstehenden Reglerstrukturen verifizieren zu können, sind weitere Experimente nötig. Dies erfordert außerdem die Integration weiterer Sensoren und die Fusion aller Messgrößen. Aus diesem Grund präsentiert diese Arbeit einen dualen Unscented Kalman-Filter für einen Seilroboter, um eine Grundlage für weitere Untersuchungen zur Seilschwingung und deren Einfluss auf Schwingungen an der Platform zu ermöglichen.

Chapter 1

Introduction

Cable-driven parallel robots belong to a class of robots that uses $m \in \mathbb{R}$ cables instead of rigid serial or parallel links in order to change the pose i.e. position and orientation of a platform in six dimensional space. To do so, ground placed motors wind/unwind the cables on/from a motor attached drum. One or more pulleys guide the cables to the platform connection points. Figure 1.1 shows the principle structure of a Cable-Driven Parallel Robot. Their parallel structure strengthen advantages, characterizing closed-chain architectures. Those are

- **Reduced mass and inertia:** Each joint of a serial manipulator carries one or more actuation units. Thus, the robot has to move its massive links as well as the actuation units to change the pose of the tip. Instead Cable-Driven Parallel Robots place the actuation units on the ground, reducing the moving mass significantly. Moreover, cables are a much lighter alternative (compared to massive links of a serial manipulator) to transmit forces.
- **Large payload to robot weight ratio:** Cable-Driven Parallel Robots have free capacities for additional payload, because of their reduced mass. Besides, their parallel structure benefits the distribution of stress (such as additional payload) on the system.
- **High dynamic performance:** Reduced mass and inertia, in addition to its parallel structure makes Cable-Driven Parallel Robots a perfect choice for fast and highly dynamic motions.
- **Large workspace:** Talking about workspace refers to the so called wrench-feasible workspace. The Wrench-Feasible Workspace consists of all reachable platform locations inside the systems space at which a set of forces and torques[1] can be applied on the platform without exceeding feasible cable tensions $\underline{t_i}$ and $\overline{t_i}$ [67].
- **Modularity and scalability:** Roughly speaking Cable-Driven Parallel Robots con-

[1] This set of forces and torques is also called wrench

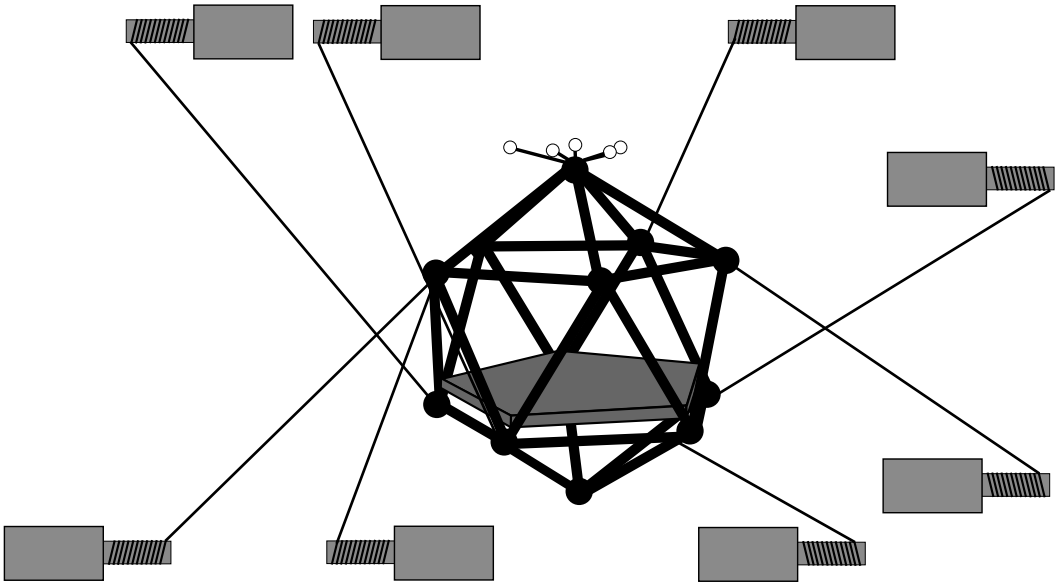

Figure 1.1: Sketch of a Cable-Driven Parallel Robot

sist of the platform (including additional equipment) and driving units (including the frame and additional sensors), connected in a modular structure, such that the number of actuation units, the system size and equipment is adaptable. Exploiting their modularity, as well as simple connections between these moduls, eases disassembling of the system. Especially mobile systems such as the String-Man [27] benefit from this feature. The combination of a light-weight structure and modularity makes Cable-Driven Parallel Robot scalable, leading to robots with small size like the IPAnema Mini [11], up to FAST [76], the largest robotic system ever build.

Their parallel structure also rises new challenges. Cables for instance, can only pull but not push. To avoid loss of controllability, the cables always have to stay under tension. Besides, their parallel structure hold the risk of collisions between cables and objects (for instance the platform) and between cables among themselves. Nevertheless, their advantages make Cable-Driven Parallel Robots suitable for diverse domains, i.e. pick and place tasks [31], entertainment industry [1], operations in large scales [76], rehabilitation [28] and also for simulation purposes [2, 68] (see Figure 4.18). Multiple research groups have influenced the landscape of parallel robotics with fully-constrained and under-constrained systems over the last decades. In [28] the authors present the String-Man (see Figure 1.3), a setup with parallel kinematics and cables for gait rehabilitation In [25] the authors investigate the musculoskeletal static workspace of a human shoulder as a cable-driven system. These two examples state, that Cable-Driven Parallel Robots also catch disciplines, different from pick and place tasks such as CoGiRo in [31], a ultra-high speed acting robot Falcon [79], the IPAnema family (see Figure 1.4a-1.4c) [11] and Segesta [62] whose construction allows to change configuration[2]. Other research projects exploit the advantage of a large workspace and scalability such as FAST (the largest Cable-Driven Parallel Robot ever built) which is a

[2]The way the cables are connected with the platform defines the configuration

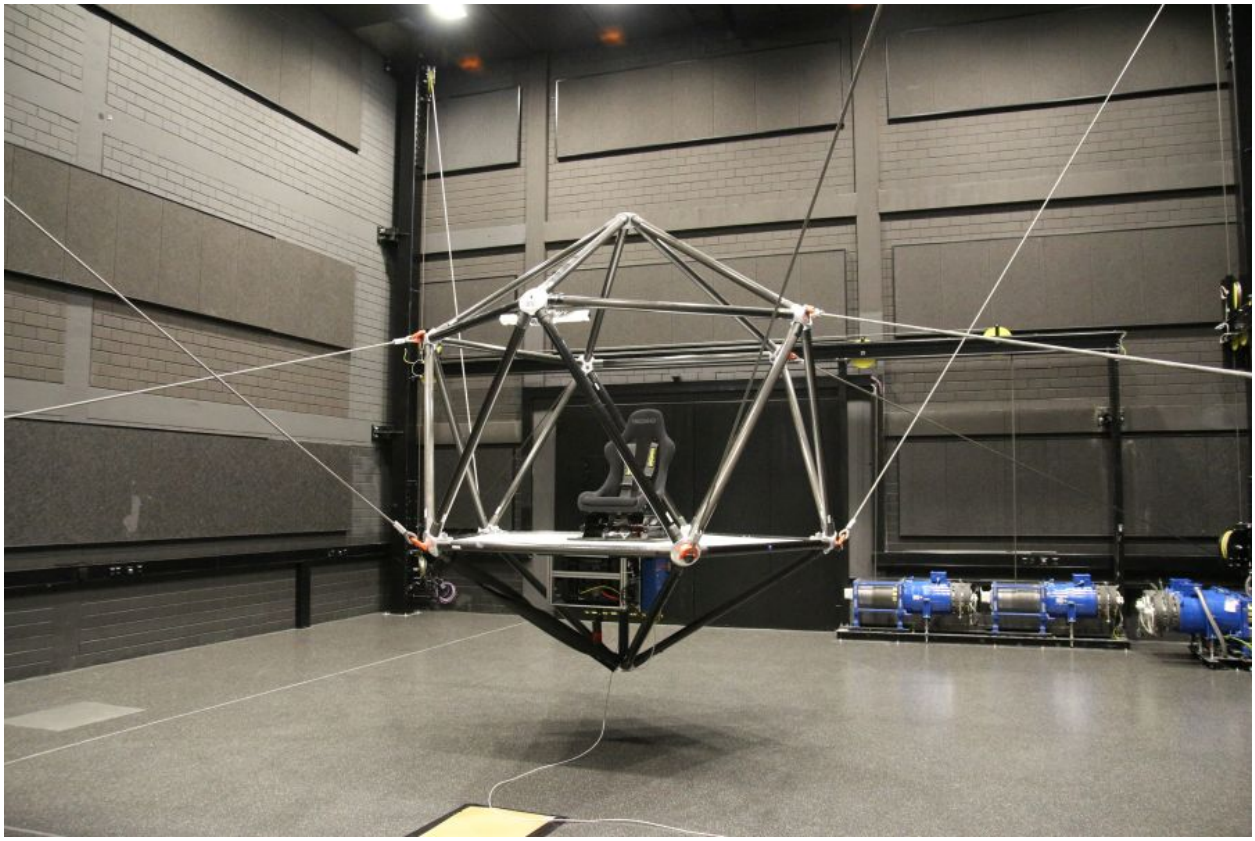

Figure 1.2: The Cablerobot Simulator at the Max-Planck Institute for Biological Cybernetics in Tübingen

radio telescope [76] and RoboCrane [73], designed for rough environments. The properties of parallel cable-driven system are even beneficial if the actuators are not placed on the ground. The authors in [17] fuse the ability of parallel wired systems for carrying heavy payloads, with the mobility of quadcopters for cooperative transportation tasks.

1.1 Motivation

At the Max-Planck Institute for Biological Cybernetics, researchers investigate human perception, cognition and action with different simulators such as the Cyber-Motion platform [32], the Cyber-Motion Simulator (CMS) [18] (a serial manipulator) and the Cable-Robot Simulator (CRS) [2]. The operators of these systems conduct experiments of different complexity. Some experiments consist of simple short linear and accelerations/decelerations tests without visual cues. Others include driving simulations with infinite simulation space, visual and perceptional cues.

The application of a Cable-Driven Parallel Robot as a simulator (with and without human-in-the-loop) raises new challenges regarding tracking accuracy and performance. Until now, researches mainly focus on precise position and velocity tracking. However, participants are

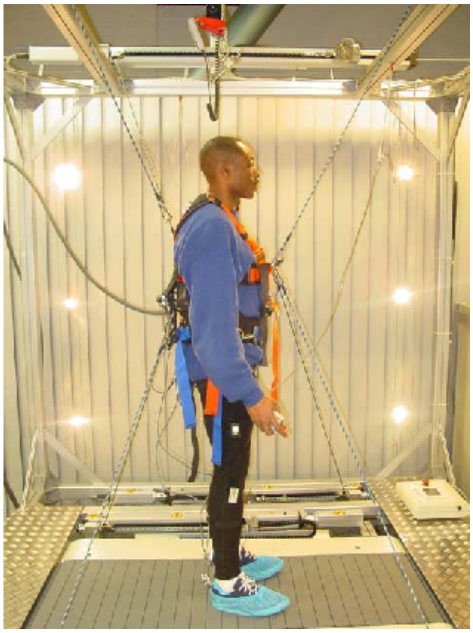

Figure 1.3: By courtesy to Dragoljub Surdilovic - String-Man

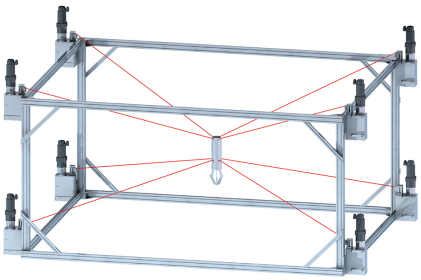

(a) By courtesy to Andreas Pott - IPAnema1

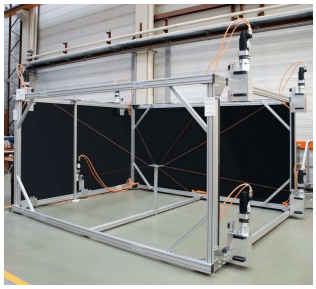

(b) By courtesy to Andreas Pott - IPAnema2

(c) By courtesy to Andreas Pott - IPAnema3

very sensitive to accelerations and vibrations[3]. An accurate tracking on acceleration level, including vibration attenuation, improves significantly the motion quality, which is crucial for simulators and guarantees reduction of physical stress on the system.

Efficient vibration suppression incorporates appropriate controller designs and models. Here, especially models for cables and friction are of interest, since both cables and bearings contribute to vibrations. However, commonly used friction models consider only constant viscous and static friction, but do not incorporate time dependencies of the friction characteristics and existing cable models for real-time applications do not account for all relevant effects. Moreover, cables are not observable and not completely controllable, which makes vibration suppression even more challenging.

Vibration suppression is only possible if the undergoing dynamics and characteristics are well understood and sophisticated models and control techniques are applied. Vibrations have multiple sources that are located in each drivetrain of a Cable-Driven Parallel Robot. Inappropriate control actions make motors one contributor to cable vibrations [22]. Second

[3]Humans sense already small changes in accelerations, higher than magnitudes of $0.04\frac{\mathrm{m}}{\mathrm{s}^2}$ in horizontal and higher than $0.08\frac{\mathrm{m}}{\mathrm{s}^2}$ in vertical direction [37]

contributor to vibrations is static friction [52] that exclusively appears in bearings. Last but not least, cables themselves forward cable vibrations to the attachment points on the platform (onboard connection points) and change the characteristics of vibrations because of their physical properties [21]. So far no holistic and generic attempts exist to suppress vibrations of a Cable-Driven Parallel Robot as a simulator, which defines the motivation of this thesis. This work identifies the main contributor for vibrations, analyses their characteristics and provides models and control techniques for vibration suppression and motion quality improvement.

1.1.1 Cable vibrations

Cables are components of the drivetrain with mass, elasticity and damping. Besides, non-linearities and cross-couplings make cable models complex, such that researchers often make one or multiple assumptions to ease the modelling process: i) massless springs [56, 97, 98, 22]; ii) linear behaviour [97, 5, 85, 41, 40]; iii) negligible damping [97, 38, 64]; iv) negligible lateral vibrations [97, 41, 64]; v) decoupled systems [97, 41, 64, 85]; vi) inextensible cables [44]. So far there exist no model, which incorporates all mentioned effects (including cable mass) and the winding process or changes in cable lengths. Every model includes system boundaries, at which energy can enter in, or expel from the system and has to guarantee energy preservation. Recently, researches have become more aware of this topic and focus also on the preservation of energy. In [35] the authors presented a model, that incorporates the winding process. However, still their model only considers longitudinal vibrations and does not incorporate cable bending and elongation because of their choice of basic functions [70]. The authors in [70] overcome this limitation with a suitable choice of basic functions and pave the way for more sophisticated cable models.

1.1.2 Drivetrain friction

Friction in drivetrains is also an important contributor to vibrations. Especially static friction (also denoted as stiction) ignites impulses to the corresponding cables which results in vibrations. Besides, friction is a complex non-linear [66] and time-varying phenomenon. Various models already exist and account for stiction, viscous friction, stick-slip and the Stribeck effect. Among those are the Armstrong, the Dahl, the Bristle and the Bliman & Slotine model. The Bristle model is not suitable for simulation because of its complexity; the Dahl model does not incorporate the Stribeck effect but comes with a minimal set of parameters; the Armstrong model requires tuning of eight parameters and a new initialisation when switching occurs and the model of Bliman & Slotine does not account for the Stribeck effect ([39] describes all those effects). All mentioned models focus on some specific friction effects, but do not adapt to changing friction characteristics or can not represent accurately

enough friction dynamics for zero velocity. To cope with changing friction characteristics, some authors use online parameter estimation [56, 14]. However, convergence of the parameter estimation for almost zero velocity is not guaranteed because of the signum function [53], used for static friction. In [93] the authors choose the Dahl model to compensate friction and reduce the platform position error by up to 70%. A set of force sensors provide data for parametrization of the Dahl model. However, additional force sensors might not always be available.

1.1.3 Control induced chattering

Changing payload [31], elastic system components [70] and external disturbances [55] demand robust control strategies. Sliding-mode controllers are (because of their robustness) attractive for control of Cable-Driven Parallel Robot. Classical Sliding-Mode Controller consist of a constant gain k and the discontinuous signum function, i.e. $k\text{sign}(\bullet)$, where,$\bullet$ includes an error variable and corresponding derivatives. The authors in [81, 31] present a robust Terminal Sliding-Mode controller with fixed gains. Often those gains are set to high values, such as in [31, 6] to achieve an efficient disturbance rejection and at the same time good tracking behaviour. However, high controller gains for Sliding-Mode Controller provoke chattering. Chattering describes controller induced vibrations with an amplitude that is proportional to the controller gains. This motivates to keep the controller gains as low as possible, to reduce chattering, noise amplification, energy consumption and sufficiently high to achieve an efficient perturbation rejection whenever it is possible. In [80] the authors tackle the problem of chattering by integrating the Sliding-Mode Control input. Integration of the discontinuous control input is known, to reduce chattering and is used in Super-Twisting Sliding-Mode Controllers, which are part of this work and will be analysed and evaluated later in Chapter 3. Literature provides multiple other approaches for vibration suppression and even compensation. Wave-based control [94] is proven to compensate vibrations, but only considers longitudinal vibrations. Input-shaping [87, 52] shapes the control input and inhibit upcoming vibrations, but requires full controllability. Cables can only pull, but neither push nor apply forces perpendicular to the cable direction, which makes - considering only one solely drivetrain - compensation of lateral vibrations impossible. Therefore, the assumptions made are invalid. This motivates to investigate more sophisticated control strategies.

1.2 Problem statement

This thesis tackles the problem of tracking accuracy for motion quality improvement and vibration suppression of a Cable-Driven Parallel Robot. The goal is, to move the platform of a Cable-Driven Parallel Robot in spatial space with reduced vibrations, given a minimal

set of measurement devices, e.g. Inertial Measurement Units, cable force and encoder measurements. Furthermore, the deficits of current models and control techniques motivate to investigate more sophisticated models and control strategies. This is not an easy task, due to three problems.

1. Cable-Driven Parallel Robot such as the Cablerobot Simulator [2] rely on a minimal set of different measurement devices, which provide data with high amount of information. The upcoming question is, how to process available sensor measurements to reconstruct the platform pose, velocity, acceleration and to provide information for suppression of vibration, induced by friction, improper control inputs and material properties of cables.

2. Cables are complex systems. A smart way to approach this topic is to subdivide the problem of modelling the entire system to the problem of modelling smaller subsystems, e.g. cables, platform and driving units in detail. Especially models that take consideration to the real nature of vibrations are still an open topic. Control is an even more difficult task, since cables are non-linear and unobservable systems, which inhibits model-based feed forward control for one cable.

3. All models and model-based controllers developed for this work must guarantee real-time capability, which is not granted per se. The task to design a model that represents all relevant effects and to design a feasible model-based controller, which offers a minimum of complexity, is challenging. Especially systems with stiff dynamic equations complicate a simulative evaluation such that a model-based controller might exist, but can not be evaluated easily in simulation.

Summarizing, many researches limit the efforts in developing sophisticated cable and friction models for the sake of simplicity. Such models have to incorporate cable mass, elasticity, damping, internal cross-couplings and changing cable lengths in spatial space, as well as static and dynamic friction and changes in friction characteristics. Moreover, chattering suppression, robustness and performance criteria put additional demands on the control, and limits the set of feasible control approaches.

1.3 Objective of this work

The goal of this work is to provide strategies for vibration reduction -caused by control actions, cable material properties and friction- as well as motion quality improvement in excess of the state of the art. To achieve this goal a good understanding of the system dynamics is crucial. Three conducted experiments revealed sources of vibrations and motivated to push on the development of more sophisticated cable and friction models, which are included in the model of a Cable-Driven Parallel Robot. Besides, a developed controller strategy relies

on the bare minimum of measurement inputs and reduces efficiently controller induced vibrations. This work is structured as follows: Chapter 2 focuses on the fundamentals, including the kinematics and dynamics of a redundant[4] Cable-Driven Parallel Robot with six degrees of freedom and eight cables as well as basics for a Super-Twisting Sliding-Mode Controller. Chapter 2 includes a derivation of the cable dynamics as a Finite-Element Method based model as well as an overview of Port-Hamilton modelling techniques. The chapter ends with the basics of the Unscented Kalman Filter for state and bias estimation. Chapter 3 is dedicated to the control of Cable-Driven Parallel Robots and applies the control techniques of the previous chapter. The problem of controller induced chattering motivates to modify the control structure. Simulations evaluate the proposed control strategy and show, that the controller meets the demands on robustness, chattering attenuation and tracking performance. Chapter 4 introduces the Mini Cable-Robot Simulator (MiCaRoSi) and the results of the calibration of kinematic and dynamic parameters parameters. Besides, Chapter 4 investigates the overall dynamics of the driving units and provides results for the modelling and analysis of cable dynamics with two common methods (Finite-Element Method and Dynamic Stiffness Matrix). The chapter ends with the experimental evaluation and validation of the proposed control strategies for High-Level Control (HLC) and friction suppression Concluding remarks and future perspectives complete this work.

1.3.1 Limitations of this work

Vibration compensation for a Cable-Driven Parallel Robot extends classical methods for vibration suppression, which limits the number of feasible control techniques, and motivates to develop of more sophisticated control strategies. The aim of this work is not to provide control strategies and models for perfect friction compensation, but rather to pioneer work with focus on vibration suppression of cable-driven mechanisms and motivation for future research in this direction.

[4]For redundant systems the number of actuator exhibits the degrees of freedom.

Chapter 2

Fundamentals

This chapter comprehends mathematical fundamentals for control, modelling (via Euler-Lagrange approach and Port-Hamilton approach) as well as state-estimation of Cable-Driven Parallel Robots. Under reasonable simplifications all required kinematic and dynamic equations for the platform and cables are derived. Furthermore, an Unscented-Kalman Filter (Unscented Kalman-Filter) for state and bias estimation for a Cable-Driven Parallel Robot is presented

Kinematic and dynamic models are the basis for controller synthesis [92]. Kinematic relations describe how system components move in a coordinate system, where the dynamics relate applied forces and moments on an object to its motion. Model-based controller synthesis, i.e. feedback and feed forward controllers, base on these equations. This underlines the importance of this chapter.

2.1 Kinematics

At the beginning, this section introduces to the simplified kinematic relations used for example in [92, 22, 20]. The notation 'simplified' relates to the fact, that pulley kinematics are neglected. The kinematic equations relate the platform pose, based on a set of kinematic parameters, to corresponding cable lengths l_i where $i = 1 \dots 8$ is the cable number. Those kinematic parameters are the offboard connection points $\boldsymbol{A}_i$ denoted with the vector $\boldsymbol{a}_i \in \mathbb{R}^{3\times1}$ and the onboard connection points at the platform $\boldsymbol{B}_i$, denoted with $\boldsymbol{b}_i \in \mathbb{R}^{3\times1}$ (see Figure 2.1). Note that $\boldsymbol{a}_i$ is the vector, pointing from world-frame $\mathcal{K}_W = \{\mathcal{O}_W, \mathcal{X}_W, \mathcal{Y}_W, \mathcal{Z}_W\}$ to pulley i, neglecting pulley panning (see Figure 2.2). A superscript which denotes the frame of reference will be omitted, if the corresponding vector is given in $\mathcal{K}_W$. For instance denotes $\boldsymbol{b}_i$ the vector pointing from $\mathcal{O}_P$ to B_i in $\mathcal{K}_W$ and ${}^P\boldsymbol{b}_i$ the vector pointing from $\mathcal{O}_P$ to B_i in $\mathcal{K}_P = \{\mathcal{O}_P, \mathcal{X}_P, \mathcal{Y}_P, \mathcal{Z}_P\}$. The coordinate system $\mathcal{K}_P$ is fixed at the geometrical center of the platform and the coordinate system $\mathcal{K}_W$ is fixed on the ground. The state vector

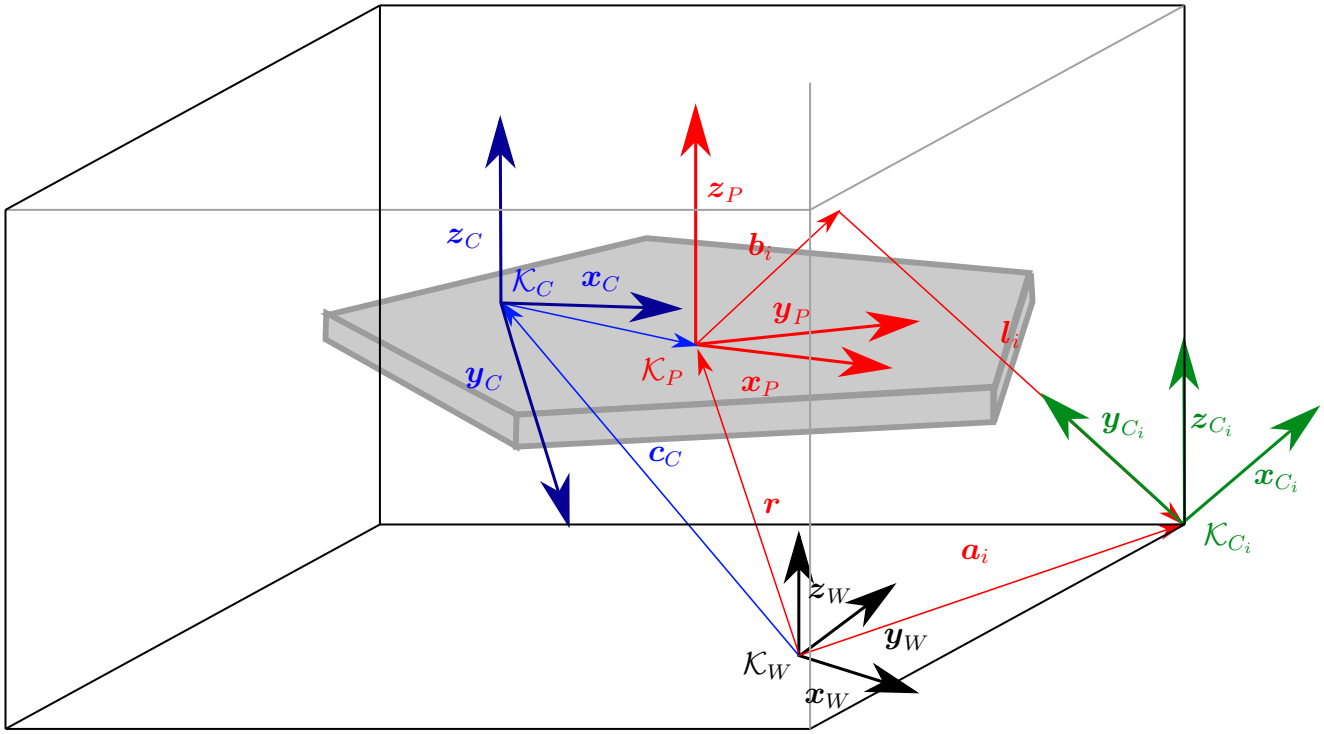

Figure 2.1: Coordinate systems and kinematic relations

$\boldsymbol{x}_P \in \mathbb{R}^{6\times1}$ expresses the platform position $\boldsymbol{r}$ and platform orientation $\boldsymbol{\nu} = [\phi\,\theta\,\psi]^{\mathrm{T}}$ in world frame $\mathcal{K}_W$. Alternatively, the orientation matrix ${}^W\boldsymbol{R}_P(\boldsymbol{\nu}) \in \mathbb{R}^{3\times3}$ which is a consecutive execution of rotations, describes the platform orientation of $\mathcal{K}_P$ with respect to $\mathcal{K}_W$ in $\mathcal{K}_W$, where are roll-pitch-yaw angles and $c_\bullet, s_\bullet$ is an abbreviation for $\cos(\bullet)$ and $\sin(\bullet)$ respectively The structure of ${}^W\boldsymbol{R}_P$ depends on the order of executed rotations. This work uses the convention of [22, 20, 92] which is:

$$
\begin{aligned}
{}^W\boldsymbol{R}_P(\boldsymbol{\nu}) &= {}^W\boldsymbol{R}_z(\psi)\,{}^W\boldsymbol{R}_y(\theta)\,{}^W\boldsymbol{R}_x(\phi) \\
&= \begin{bmatrix} c_\psi & -s_\psi & 0 \\ s_\psi & c_\psi & 0 \\ 0 & 0 & 1 \end{bmatrix} \begin{bmatrix} c_\theta & 0 & -s_\theta \\ 0 & 1 & 0 \\ s_\theta & 0 & c_\theta \end{bmatrix} \begin{bmatrix} 1 & 0 & 0 \\ 0 & c_\phi & -s_\phi \\ 0 & s_\phi & c_\phi \end{bmatrix} \\
&= \begin{bmatrix} c_\psi c_\theta & c_\psi s_\theta s_\phi - s_\psi c_\phi & c_\psi s_\theta c_\phi + s_\psi s_\phi \\ s_\psi c_\theta & s_\psi s_\theta s_\phi + c_\psi c_\phi & s_\psi s_\theta c_\phi - c_\psi s_\phi \\ -s_\theta & c_\theta s_\phi & c_\theta c_\phi \end{bmatrix}.
\end{aligned}
\tag{2.1}
$$

For the sake of brevity ${}^W\boldsymbol{R}_P$ will be used instead of ${}^W\boldsymbol{R}_P(\boldsymbol{\nu})$ in the sequel.

Often, the platform center of mass deviates from the geometrical platform center, because of additional equipment. To consider incoherence of the geometrical center of the platform and its center of mass, another coordinate system $\mathcal{K}_C$ -that is fixed at the platform center of mass- is introduced.

When we talk about the pose, velocity and acceleration of the platform we automatically refer to the pose $\boldsymbol{x}_P \in \mathbb{R}^{6\times1}$, velocity $\dot{\boldsymbol{x}}_P \in \mathbb{R}^{6\times1}$ and acceleration $\ddot{\boldsymbol{x}}_P \in \mathbb{R}^{6\times1}$ of $\mathcal{K}_P$ with

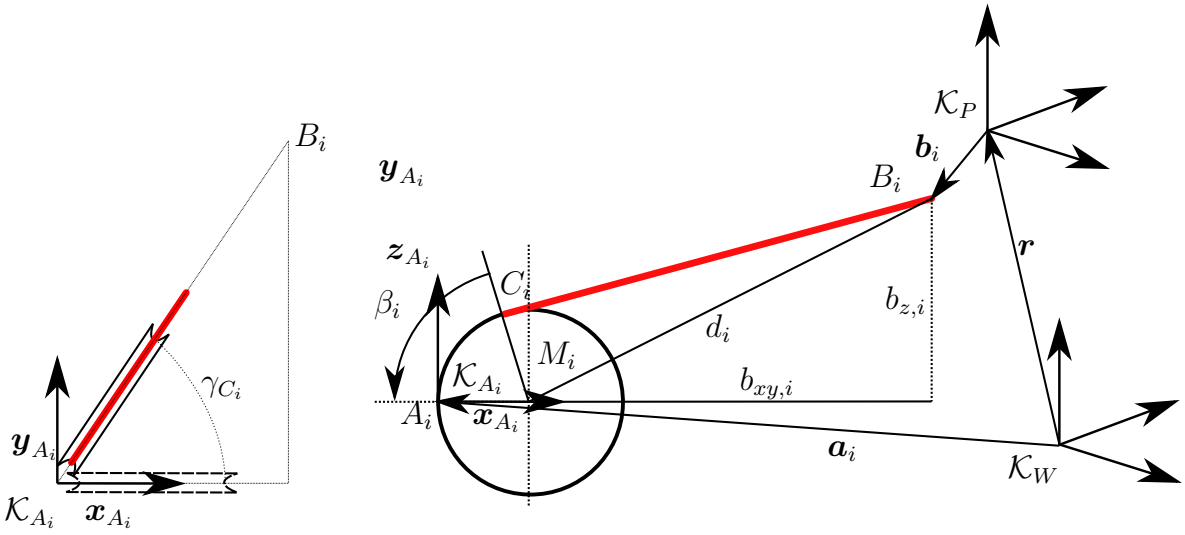

Figure 2.2: Sketch of panning pulley with the panning angle $\gamma_{i,R} \in \mathbb{R}$

respect to $\mathcal{K}_W$ in $\mathcal{K}_W$. A superscript $\dot{\bullet}$ is the common notation for the derivative of $\bullet$ with respect to time.

Note that the entity of interest is $\boldsymbol{x}_P$, $\dot{\boldsymbol{x}}_P$ and $\ddot{\boldsymbol{x}}_P$, but the system actuation works in joint-space with cable lengths with cable lengths $\boldsymbol{l} = \begin{bmatrix} l_1 & l_2 & l_3 & \dots & l_7 & l_8 \end{bmatrix}^{\mathrm{T}} \in \mathbb{R}^{8\times 1}$ and corresponding velocities $\dot{\boldsymbol{l}}$ and accelerations $\ddot{\boldsymbol{l}}$. The fundamental relation between the pose of the platform and the state of the robot, expressed by a vector of joint variables (e.g., actuators angles or cable lengths), is described by the forward kinematics and inverse kinematics respectively.

2.1.1 Inverse Kinematic

The inverse kinematics relates the platform pose to the cable lengths $\boldsymbol{l}$, based on the anchor points B_i on the movable platform (onboard connection points) and the anchor points at the pulley A_i (offboard connection points). The location of A_i in $\mathcal{K}_W$ is indicated by the vector $\boldsymbol{a}_i \in \mathbb{R}^3$ and the location of B_i in $\mathcal{K}_P$ is denoted by ${}^P\boldsymbol{b}_i \in \mathbb{R}^3$.

An extended model, that includes the kinematics of the pulleys was already presented in [9, 89, 59] such that this work will briefly summarize their results with the notations used in this work.

The offboard connection point vector $\boldsymbol{a}_i$ and a rotation matrix $\boldsymbol{R}_{A_i}$ describe the pulley location and orientation (see Figure 2.2). Additional, γ_{C_i} is the panning angle, C_i is the contact point at which the cable leaves the pulley, M_i is the center of the panned pulley, r_C is the radius of one pulley and β_i is the wrapping angle of cable i around pulley i. The

distance between M_i and B_i is:

$$\begin{aligned} d_i &= \sqrt{(b_{xy,i} - r_C)^2 + b_{z,i}^2} \\ b_{xy,i} &= \sqrt{b_{x,i}^2 + b_{y,i}^2}\,, \end{aligned} \tag{2.2}$$

where $\bullet_x, \bullet_y, \bullet_z$ is the component in x, y, z direction respectively of a three dimensional vector in $\mathcal{K}_W$. The free cable length, i.e. the length of a vector going from C_i to B_i is:

$$l_{f_i} = \sqrt{d_i^2 - r_C^2}\,, \tag{2.3}$$

and the wrapping angle is:

$$\beta = \arccos\left(\frac{l_{f_i}}{d_i}\right) + \arccos\left(\frac{b_{z,i}}{d_i}\right)\,, \tag{2.4}$$

such that the total cable length is

$$l_{ext} = l_{f_i} + \beta_i r_C\,. \tag{2.5}$$

Chapter 3 compares this model with the simplified kinematic model that disregard pulley panning and wrapping of a cable around the corresponding pulley, i.e. the case $\beta_i r_c = 0$ such that $\boldsymbol{l}_{ext} = \boldsymbol{l}_{f,i}$. Assuming fixed pulleys and $C_i = A_i$, simplifies the kinematics of the proximal anchor points and it presumes: i) no rotations of the pulley when the platform moves ii) no change in the contact point of the cable with the corresponding pulley (see Figure 2.1) iv) all the cables are in tension, v) all cable connections are ideal points, vi) there is no elongation of the cable, vii) the additional cable length that is unwinded by each turn of the drum in axial direction is negligible small.

Under these assumptions, the simplified total cable length is:

$$\boldsymbol{l}_i = l_i \boldsymbol{n}_i = \boldsymbol{a}_i - {}^W\boldsymbol{R}_P\, {}^P\boldsymbol{b}_i - \boldsymbol{r} = \boldsymbol{a}_i - \boldsymbol{b}_i - \boldsymbol{r}\,. \tag{2.6}$$

where $\boldsymbol{n}_i \in \mathbb{R}^{3\times 1}$ is a unit vector. The loop constraint (2.6) illustrated by Figure 2.1 reads:

$$\|\boldsymbol{l}_i\|_2 = l_i = \|\boldsymbol{a}_i - {}^W\boldsymbol{R}_P\, {}^P\boldsymbol{b}_i - \boldsymbol{r}\|_2\,. \tag{2.7}$$

Differentiating Equation (2.7) with respect to time, yields another important relation between $\dot{\boldsymbol{l}}$ and $\dot{\boldsymbol{x}} = [\dot{\boldsymbol{r}}^{\mathrm{T}}, {}^P\boldsymbol{\omega}^{\mathrm{T}}]^{\mathrm{T}}$, where ${}^P\boldsymbol{\omega} = [p\ q\ r]^{\mathrm{T}} \in \mathbb{R}^{3\times 1}$ is the angular velocity vector. Moreover, the angular velocity in the inertial frame $\mathcal{K}_W$ is simply $\boldsymbol{\omega} = {}^W\boldsymbol{R}_P\, {}^P\boldsymbol{\omega}$ and the relation between world/body frame angular velocity and roll-pitch-yaw rates $\dot{\boldsymbol{\nu}} = [\dot{\phi}, \dot{\theta}, \dot{\psi}]^{\mathrm{T}} \in$

$\mathbb{R}^{3\times1}$ is [63]

$$
\begin{aligned}
{}^{P}\boldsymbol{\omega} &= \begin{bmatrix} p \\ q \\ r \end{bmatrix} = \begin{bmatrix} 1 & 0 & -\sin\theta \\ 0 & \cos\phi & \sin\phi\cos\theta \\ 0 & -\sin\phi & \cos\phi\cos\theta \end{bmatrix} \begin{bmatrix} \dot{\phi} \\ \dot{\theta} \\ \dot{\psi} \end{bmatrix} = {}^{P}\boldsymbol{E}_{\boldsymbol{\nu}}(\boldsymbol{\nu})\dot{\boldsymbol{\nu}} \qquad (2.8) \\
\boldsymbol{\omega} &= \begin{bmatrix} \cos\theta\cos\psi & -\sin\psi & 0 \\ \cos\theta\sin\psi & \cos\psi & 0 \\ -\sin\theta & 0 & 1 \end{bmatrix} \begin{bmatrix} \dot{\phi} \\ \dot{\theta} \\ \dot{\psi} \end{bmatrix} = {}^{\boldsymbol{\omega}}\boldsymbol{E}(\boldsymbol{\nu})_{\boldsymbol{\nu}}\dot{\boldsymbol{\nu}} \qquad (2.9)
\end{aligned}
$$

Differentiating $\boldsymbol{b}_i$ with respect to time (and skipping some steps for conciseness), it follows

$$
\begin{aligned}
\dot{\boldsymbol{b}}_i &= \frac{\mathrm{d}\,{}^{W}\boldsymbol{R}_P{}^{P}\boldsymbol{b}_i}{\mathrm{d}t} = \frac{\partial {}^{W}\boldsymbol{R}_P{}^{P}\boldsymbol{b}_i}{\partial\phi}\dot{\phi} + \frac{\partial {}^{W}\boldsymbol{R}_P{}^{P}\boldsymbol{b}_i}{\partial\theta}\dot{\theta} + \frac{\partial {}^{W}\boldsymbol{R}_P{}^{P}\boldsymbol{b}_i}{\partial\psi}\dot{\psi} \\
&\overset{(2.1)}{=} {}^{W}\boldsymbol{R}_P S(\boldsymbol{\omega}_P){}^{P}\boldsymbol{b}_i = {}^{W}\boldsymbol{R}_P{}^{P}\boldsymbol{\omega}_P \times {}^{W}\boldsymbol{R}_P{}^{P}\boldsymbol{b}_i \\
&= \boldsymbol{\omega}_P \times \boldsymbol{b}_i = \boldsymbol{S}(\boldsymbol{\omega}_P)\,.
\end{aligned} \qquad (2.10)
$$

where $\boldsymbol{S}(\boldsymbol{\omega}_P)$ is the screw symmetric matrix

$$
\boldsymbol{S}(\boldsymbol{\omega}_P) = \begin{bmatrix} 0 & -\omega_z & \omega_y \\ \omega_z & 0 & -\omega_x \\ -\omega_y & \omega_x & 0 \end{bmatrix}. \qquad (2.11)
$$

With this setting, the relation between $\dot{l}_i$ and $[\dot{\boldsymbol{r}}^{\mathrm{T}}, \dot{\boldsymbol{\nu}}^{\mathrm{T}}]^{\mathrm{T}}$ by differentiating (2.7) is:

$$
\begin{aligned}
\dot{l}_i &= \frac{\mathrm{d}}{\mathrm{d}t}\sqrt{(\boldsymbol{a}_i - \boldsymbol{b}_i - \boldsymbol{r})^{\mathrm{T}}(\boldsymbol{a}_i - \boldsymbol{b}_i - \boldsymbol{r})} \\
&= -\frac{(\boldsymbol{a}_i - \boldsymbol{b}_i - \boldsymbol{r})^{\mathrm{T}}}{\sqrt{(\boldsymbol{a}_i - \boldsymbol{b}_i - \boldsymbol{r})^{\mathrm{T}}(\boldsymbol{a}_i - \boldsymbol{b}_i - \boldsymbol{r})}}\boldsymbol{I}_{3\times3}\dot{\boldsymbol{r}} - \frac{(\boldsymbol{a}_i - \boldsymbol{b}_i - \boldsymbol{r})^{\mathrm{T}}}{\sqrt{(\boldsymbol{a}_i - \boldsymbol{b}_i - \boldsymbol{r})^{\mathrm{T}}(\boldsymbol{a}_i - \boldsymbol{b}_i - \boldsymbol{r})}}\boldsymbol{I}_{3\times3}\dot{\boldsymbol{b}}_i \\
&= -\boldsymbol{n}_i^{\mathrm{T}}\dot{\boldsymbol{r}} - \boldsymbol{n}_i^{\mathrm{T}}(\boldsymbol{\omega} \times \boldsymbol{b}_i) \\
&= -\boldsymbol{n}_i^{\mathrm{T}}\dot{\boldsymbol{r}} - (\boldsymbol{b}_i \times \boldsymbol{n}_i)^{\mathrm{T}}\boldsymbol{\omega} \\
&= \boldsymbol{J}_{P,i}\dot{\boldsymbol{r}} + \boldsymbol{J}_{O,i}\boldsymbol{\omega} = \begin{bmatrix} \boldsymbol{J}_{P,i} & \boldsymbol{J}_{O,i} \end{bmatrix} \begin{bmatrix} \dot{\boldsymbol{r}} \\ \boldsymbol{\omega} \end{bmatrix}
\end{aligned} \qquad (2.12)
$$

where

$$
\boldsymbol{J} = \begin{bmatrix} -\boldsymbol{n}_1^{\mathrm{T}} & -(\boldsymbol{b}_1 \times \boldsymbol{n}_1)^{\mathrm{T}} \\ \vdots & \vdots \\ -\boldsymbol{n}_8^{\mathrm{T}} & -(\boldsymbol{b}_8 \times \boldsymbol{n}_8)^{\mathrm{T}} \end{bmatrix} = \begin{bmatrix} -\boldsymbol{n}_1^{\mathrm{T}} & -({}^{W}\boldsymbol{R}_P{}^{P}\boldsymbol{b}_1 \times \boldsymbol{n}_1)^{\mathrm{T}} \\ \vdots & \vdots \\ -\boldsymbol{n}_8^{\mathrm{T}} & -({}^{W}\boldsymbol{R}_P{}^{P}\boldsymbol{b}_8 \times \boldsymbol{n}_8)^{\mathrm{T}} \end{bmatrix}. \qquad (2.13)
$$

The Jacobian $\boldsymbol{J}$ does not only relate the platform velocity to the rate of cable lengths, but also the cable tensions $\boldsymbol{f} \in \mathbb{R}^{8\times1}$ to the wrench $\boldsymbol{f}_P \in \mathbb{R}^{6\times1}$ -that are all forces and torques acting at the platform due to $\boldsymbol{f}$. This relation will be relevant for deriving the dynamic equations of the platform.

2.1.2 Forward Kinematics

Forward kinematics, describes the mapping from cable lengths to the platform pose. In [65] the authors show, that for a parallel robot with 6 actuators there exist 40 possible solutions for the pose. Since a unique solution for a set of cable lengths does not exist, the platform pose can only be found iteratively. Commonly a Levenberg-Marquardt algorithm [8] suffice to solve the linear equation:

$$\boldsymbol{x}_{k+1} = \boldsymbol{x}_k + \boldsymbol{h}_{FK} \tag{2.14}$$

$$\left[\boldsymbol{J}_{FK}(\boldsymbol{x}_k)\boldsymbol{J}_{FK}^{\mathrm{T}}(\boldsymbol{x}_k) + \epsilon_{FK}\boldsymbol{I}\right]\boldsymbol{h}_{FK} = \boldsymbol{J}_{FK}^{\mathrm{T}}(\boldsymbol{x}_k)\boldsymbol{\Phi}_{FK}(\boldsymbol{x}_k)\,, \tag{2.15}$$

where $\Phi_{FK}(\boldsymbol{x}_k)$ is the error between the model based cable lengths $\boldsymbol{l}(\boldsymbol{x}_k)$ and the cable lengths provided by the motor encoders $\boldsymbol{l}$. Here, $\boldsymbol{J}_{FK}(\boldsymbol{x}_k)$ is the Jacobian matrix of $\boldsymbol{\Phi}_{FK}$ as a function of the platform pose and measured cable lengths at iteration step k when Equation (2.14) is solved for $\boldsymbol{h}_{FK}$ with $0 < \epsilon_{FK} << 1 \in \mathbb{R}$. The iteration process stops either after a fixed number of iteration steps or if a terminating condition is fulfilled. For instance, if $\boldsymbol{h}_{FK} < \boldsymbol{\eta}_{FK} \in \mathbb{R}^{8\times 1}$ for each element with $\boldsymbol{\eta}_{FK} \in \mathbb{R}^8$ as the minimum error to be achieved. In practise with a good initial guess, less then 15 iterations provide already a precise result. In [8] the author uses cable length measurements, provided by the motor encoders, to compute a box in which the platform has to be located. The geometrical center of this box represents the initial guess for the Levenberg-Marquardt algorithm:

$$\begin{aligned}
\boldsymbol{r}_i^{low} &= \boldsymbol{a}_i - (l_i + ||\boldsymbol{b}_i||_2)\begin{bmatrix}1 & 1 & 1\end{bmatrix}^{\mathrm{T}} \\
\boldsymbol{r}_i^{high} &= \boldsymbol{a}_i + (l_i + ||\boldsymbol{b}_i||_2)\begin{bmatrix}1 & 1 & 1\end{bmatrix}^{\mathrm{T}} \\
\boldsymbol{r}_i^{low} &= \max_i \boldsymbol{r}_i^{low} \\
\boldsymbol{r}_i^{high} &= \min_i \boldsymbol{r}_i^{high} \\
\boldsymbol{r}_o &= \frac{1}{2}\left(\boldsymbol{r}^{low} + \boldsymbol{r}^{high}\right)
\end{aligned} \quad . \tag{2.16}$$

Alternatively one could also use the previous pose as initial guess under the assumption that (2.14) converge to the actual pose.

2.2 Dynamics

This section deals with the dynamic equations for Cable-Driven Parallel Robot and maps positions, velocities and accelerations of the system to forces and torques, which is also known as inverse dynamic model [10]. Analog to the forward kinematics there exist a forward dynamic model which describes the mapping from forces and torques to positions, velocities and accelerations. The inverse dynamic model includes the generic dynamic equations for the

platform, based on the Newton-Euler or Euler-Lagrange approach under few assumptions: i) the geometrical structure of the platform is well known such that the inertia $\boldsymbol{I}_P \in \mathbb{R}^{3\times3}$ is known, ii) the platform is very stiff and iii) deviations of the geometrical center and the center of mass $\boldsymbol{c} \in \mathbb{R}^{3\times1}$ (see Figure 2.1) are either well known or negligible small. Cable-Driven Parallel Robots consists of multiple parts, i.e. rigid bodies (platform and driving units) and flexible components (cables). Deriving a model, that incorporates all components of a Cable-Driven Parallel Robot at once, is a burdensome task. Thus, a modelling approach that allows to split the system of interest in multiple subsystems and combine them - while preserving the fundamental rule of energy preservation - is beneficial. Port-Hamilton modelling picks up this idea and facilitates the modelling process significantly.

Next the platform and cable dynamics will be derived independently from each other. The Euler-Lagrange modelling approach bases on the Lagrangian energy function $L = T - U$, where T is the kinetic energy of the system and U is the potential energy. Disregarding holonomic and nonholonomic constraints, the Euler-Lagrangian equation of motion is

$$\frac{\mathrm{d}}{\mathrm{d}\,t}\left(\frac{\partial L}{\partial \dot{\boldsymbol{q}}}\right)^{\mathrm{T}} - \left(\frac{\partial L}{\partial \boldsymbol{q}}\right)^{\mathrm{T}} = \boldsymbol{\xi}_q \tag{2.17}$$

where $\boldsymbol{q} = [q_1\ q_2\ \ldots\ q_n]^{\mathrm{T}} \in \mathbb{R}^{n_a}$ is the vector of generalized coordinates and $\boldsymbol{\xi}_q \in \mathbb{R}^{n_a\times1}$ are the non-conservative forces, such as friction forces or external forces applied from the environment.

2.2.1 Platform dynamics

The basic dynamic equations for the platform are well understood and methods from classical mechanics [36] are applicable. Applying Equation (2.17) on the platform as a rigid body object with six degrees of freedom leads to a simple ordinary differential equation of second order. The following equations derive the platform dynamics based on the Euler-Lagrange approach. Therefore the kinetic energy of the platform is

$$T = \frac{1}{2} m_P \dot{\boldsymbol{r}}^{\mathrm{T}} \dot{\boldsymbol{r}} + \frac{1}{2} \boldsymbol{\omega}^{\mathrm{T}}\, {}^{P}\boldsymbol{I}_P\, \boldsymbol{\omega} \tag{2.18}$$

where $m_P \in \mathbb{R}$ is the mass of the moving platform and ${}^{P}\boldsymbol{I}_P \in \mathbb{R}^{6\times6}$ and $\boldsymbol{\omega}$ are the inertia tensor and angular velocity expressed with respect to the same frame of reference. In particular, the inertia tensor ${}^{P}\boldsymbol{I}_P$ in $\mathcal{K}_P$ is a constant matrix. Furthermore, if $\mathcal{K}_P$ is chosen as

the central frame of inertia then ${}^P\boldsymbol{I}$ is also diagonal. In $\mathcal{K}_W$, Equation (2.18) changes to

$$\begin{aligned} T &= \frac{1}{2}\begin{bmatrix}\dot{\boldsymbol{r}}\\ {}^P\boldsymbol{\omega}\end{bmatrix}^{\mathrm{T}} \underbrace{\begin{bmatrix} m\boldsymbol{I}_{3\times3} & \boldsymbol{0}_{3\times3}\\ \boldsymbol{0}_{3\times3} & {}^P\boldsymbol{I}_P\end{bmatrix}}_{{}^P\boldsymbol{M}} \begin{bmatrix}\dot{\boldsymbol{r}}\\ {}^P\boldsymbol{\omega}\end{bmatrix} \\ &= \frac{1}{2}\begin{bmatrix}\dot{\boldsymbol{r}}\\ \boldsymbol{\omega}\end{bmatrix}^{\mathrm{T}} \underbrace{\begin{bmatrix} m\boldsymbol{I}_{3\times3} & \boldsymbol{0}_{3\times3}\\ \boldsymbol{0}_{3\times3} & {}^W\boldsymbol{R}_P\,{}^P\boldsymbol{I}\,{}^P\boldsymbol{R}_W\end{bmatrix}}_{\boldsymbol{M}(\boldsymbol{\mu})} \begin{bmatrix}\dot{\boldsymbol{r}}\\ \boldsymbol{\omega}\end{bmatrix}. \end{aligned} \tag{2.19}$$

With Equation (2.18) and the potential energy

$$\mathcal{U} = m\begin{bmatrix}0 & 0 & g\end{bmatrix}^{\mathrm{T}}\boldsymbol{r} = \boldsymbol{g}^{\mathrm{T}}\boldsymbol{r}\,, \tag{2.20}$$

where g is the gravity constant. The Euler-Lagrange equation of motion (2.17) reads:

$$\frac{\mathrm{d}}{\mathrm{d}t}\left(\boldsymbol{M}(\boldsymbol{x})\dot{\boldsymbol{x}}\right) - \frac{1}{2}\left(\frac{\partial}{\partial\boldsymbol{x}}\dot{\boldsymbol{x}}^{\mathrm{T}}\boldsymbol{M}(\boldsymbol{x})\dot{\boldsymbol{x}}\right)^{\mathrm{T}} + \boldsymbol{g} = \boldsymbol{\xi}_q \tag{2.21}$$

such that the equation of motion results in:

$$\boldsymbol{M}(\boldsymbol{x})\ddot{\boldsymbol{x}} + \boldsymbol{C}(\boldsymbol{x},\dot{\boldsymbol{x}})\dot{\boldsymbol{x}} + \boldsymbol{n} = -\boldsymbol{J}^{\mathrm{T}}\boldsymbol{t} \tag{2.22}$$

$$\boldsymbol{M}(\boldsymbol{x}) = \begin{bmatrix} m\boldsymbol{I}_{3\times3} & \boldsymbol{0}_{3\times3}\\ \boldsymbol{0}_{3\times3} & \boldsymbol{I}_P\end{bmatrix} \tag{2.23}$$

$$\boldsymbol{C}(\boldsymbol{x},\dot{\boldsymbol{x}}) = \begin{bmatrix} \boldsymbol{0}_{3\times3} & \boldsymbol{0}_{3\times3}\\ \boldsymbol{0}_{3\times3} & \boldsymbol{S}(\boldsymbol{\omega})\,{}^P\boldsymbol{I}_P(\boldsymbol{\nu})\end{bmatrix} \tag{2.24}$$

$$\boldsymbol{S}(\bullet) = \begin{bmatrix} 0 & -\bullet_z & \bullet_y\\ \bullet_z & 0 & -\bullet_x\\ -\bullet_y & \bullet_x & 0\end{bmatrix} \tag{2.25}$$

$$\boldsymbol{n} = -\begin{bmatrix}0 & 0 & -mg & 0 & 0 & 0\end{bmatrix}^{\mathrm{T}} \tag{2.26}$$

$$\boldsymbol{I}_P(\boldsymbol{\nu}) = {}^W\boldsymbol{R}_P(\boldsymbol{\nu})\,{}^P\boldsymbol{I}_P\,{}^P\boldsymbol{R}_W(\boldsymbol{\nu}) \tag{2.27}$$

and for the case of incoherence of $\mathcal{K}_P$ and $\mathcal{K}_C$ [92]

$$\boldsymbol{M}(\boldsymbol{x})\ddot{\boldsymbol{x}} + \boldsymbol{C}(\boldsymbol{x},\dot{\boldsymbol{x}})\dot{\boldsymbol{x}} - {}^P\boldsymbol{f}_g = \boldsymbol{f}_u \tag{2.28}$$

$$\boldsymbol{M}(\boldsymbol{x}) = \begin{bmatrix} m_P\boldsymbol{I}_{3\times3} & m_P\boldsymbol{S}(\boldsymbol{c})^{\mathrm{T}}\\ m_P\boldsymbol{S}(\boldsymbol{c}) & \boldsymbol{H}\end{bmatrix} \tag{2.29}$$

$$\boldsymbol{C}(\boldsymbol{x},\dot{\boldsymbol{x}})\dot{\boldsymbol{x}} = \begin{bmatrix} m_P\boldsymbol{S}(\boldsymbol{\omega}_P)\boldsymbol{S}(\boldsymbol{\omega}_P)\times\boldsymbol{c}\\ \boldsymbol{S}(\boldsymbol{\omega}_P)\boldsymbol{H}\boldsymbol{\omega}_P\end{bmatrix} \tag{2.30}$$

$$\boldsymbol{H} = \boldsymbol{I} + m_P\boldsymbol{S}(\boldsymbol{c})\boldsymbol{S}(\boldsymbol{c})^{\mathrm{T}} \tag{2.31}$$

$${}^P\boldsymbol{f}_g = \begin{bmatrix}0 & 0 & -m_Pg & -m_P\boldsymbol{c}_yg & m_P\boldsymbol{c}_xg & 0\end{bmatrix} \tag{2.32}$$

Note that $\boldsymbol{M}(\boldsymbol{x})$ is symmetric. Furthermore, it is uniformly positive definite and thus invertible. This is a relevant property which is useful to express the non-linear platform dynamics as $\dot{\boldsymbol{x}} = f(\boldsymbol{x}) + g(\boldsymbol{x}, \boldsymbol{u})$ where $f(\boldsymbol{x})$ and $g(\boldsymbol{x}, \boldsymbol{u})$ are appropriate non-linear functions. Equation (2.28)-(2.32) finishes the derivation of the platform dynamics.

2.2.2 Cable dynamics

Literature provides different cable models amongst others Finite-Element Method based in [85, 5, 70, 45], Dynamic Stiffness Method based models in [41, 88], catenary equations in [57, 76], basic functions [71, 35] (Rayleigh-Ritz approach) and modal analysis [98]. Finite-Element Method and modal analysis based models are simple and reflect all relevant effects, e.g. internal cross-couplings, linear and non-linear elasticity and stiffness as well as damping. However, Finite-Element Method based models are sensitive for numerical problems and singularities. During the winding process an element of such a model might leave the system over the system borders which is in most cases a cube with the pulleys as the edges. In this particular case the systems energy is not preserved anymore. Models based on the Rayleigh-Ritz approach overcome this deficit. Dynamic Stiffness Matrix based models are more accurate than Finite-Element Method based models [21], but are not suitable for control design.

Elasticity, stiffness[1], damping, mass and couplings between eigenmodes [21] and non-linearities are unignorable effects that strongly affects performance and (in case of simulators) simulation quality. Creeping effects [47] are only relevant for applications with heavy payload. In literature those effects were partially not or even not at all taken into account for the sake of simplicity.

This section reviews two commonly used cable models, one based on the Finite-Element-Method and one based on partial differential equations. Later Chapter 4 will evaluate both models experimentaly and will give insights to the relevance of incorporating those effects.

Finite-Element Model

The authors in [70] use a fixed number of connected so-called rigid finite elements, to provide a realistic cable model with fixed end points and constant cable length. Linear springs and dampers connect two consecutive mass elements with each other and model linear elasticity and energy dissipation of the cable. In simulation two cables of fixed length hold a square object in an initial position. After a few seconds, an external force deflects the object briefly from its rest position and sets it free. Both cables and the object start to bounce in a realistic way.

[1] Here elasticity refers to elongation, whereat stiffness refers to bending of an object

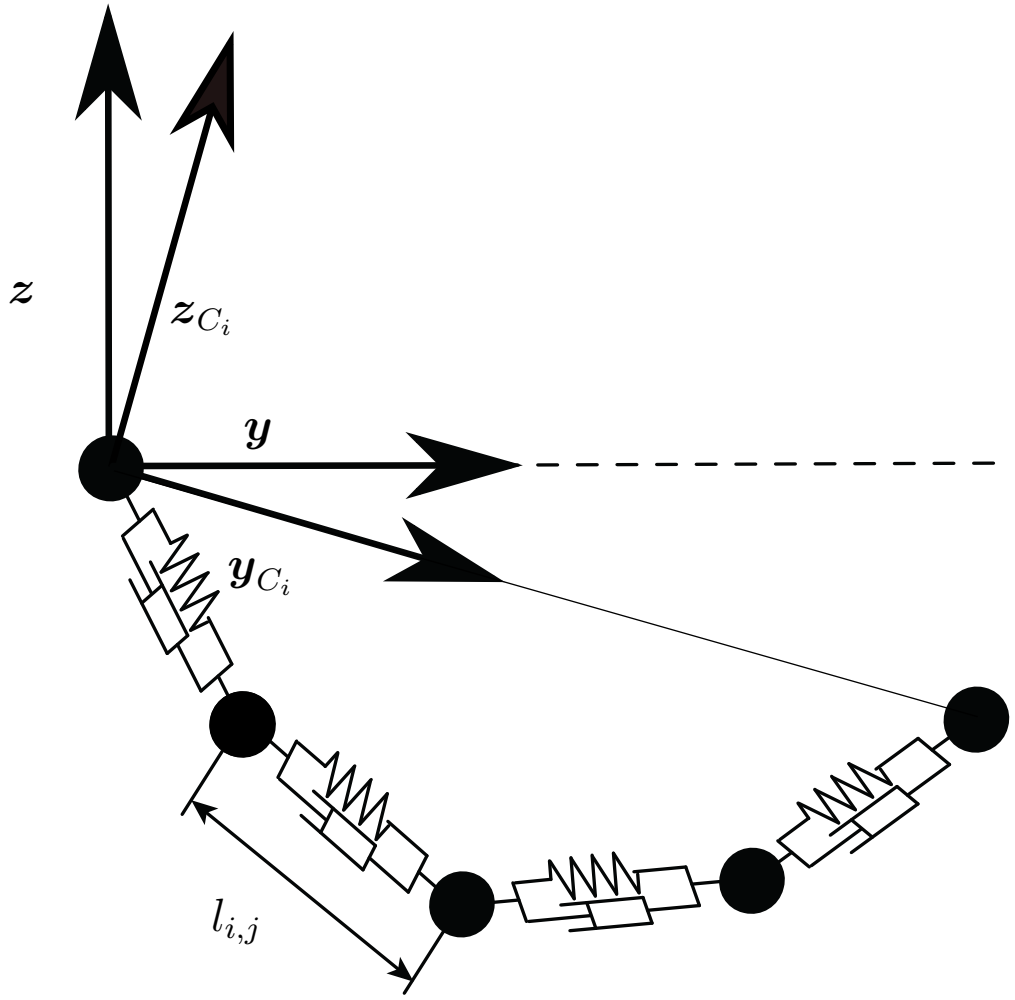

Figure 2.3: Finite-Element Method of one cable

This work picks up a similar model, based on the Finite-Element Method [85]. A finite number of mass elements is consecutively connected with springs and dampers, to model elasticity, damping (see Figure 2.3) and fixed at both ends. The second order ordinary differential equation

$$\begin{aligned}
\boldsymbol{f}_{i,j} &= \boldsymbol{M}_{C_i}\ddot{\boldsymbol{\eta}}_i + \boldsymbol{D}_{C_i}\dot{\boldsymbol{\eta}}_i + \boldsymbol{K}_{C_i}\boldsymbol{\eta}i && (2.33)\\
\boldsymbol{\eta}_i &= \begin{bmatrix}\boldsymbol{\eta}_1 & \dots & \boldsymbol{\eta}_{3n_{m_i}}\end{bmatrix} && (2.34)\\
\boldsymbol{M}_{C_i} &= \frac{1}{2}\mu \operatorname{diag}\left\{\|\boldsymbol{l}_{1,2}\|, \|\boldsymbol{l}_{1,2}+\boldsymbol{l}_{2,3}\|, \dots, \|\boldsymbol{l}_{n_e-1,n_e}\|\right\} \otimes \boldsymbol{I}_{3\times 3} &&\\
\boldsymbol{D}_{C_i} &= \operatorname{diag}\left\{\zeta_{i,1,x} \quad \zeta_{i,1,y} \quad \zeta_{i,1,z} \quad \dots \quad \zeta_{i,n_{m_i},x} \quad \zeta_{i,n_{m_i},y} \quad \zeta_{i,n_{m_i},z}\right\} && (2.35)\\
\boldsymbol{K}_{C_i} &= \boldsymbol{K}_{i,el} + \boldsymbol{K}_{i,g} && (2.36)
\end{aligned}$$

describes this concept and allow to write the dynamic equations in matrix form $\dot{\boldsymbol{x}} = \boldsymbol{A}(\boldsymbol{x}, \dot{\boldsymbol{x}}) + \boldsymbol{B}\boldsymbol{u}$, which is suitable for vibration analysis. Deflections $\boldsymbol{\eta}_i = \begin{bmatrix}\boldsymbol{\eta}_{i,1} & \dots & \boldsymbol{\eta}_{i,n_i}\end{bmatrix}$ $\in \mathbb{R}^{3n_i\times 1}$ of each element from their equilibrium point are the generalised coordinates and $\boldsymbol{f}_{i,j} \in \mathbb{R}^{3n_e\times 1}$ are forces, acting on the j^{th} element of cable i, where $j = 1 \dots n_e$. The

matrices $\boldsymbol{M}_{C_i} \in \mathbb{R}^{3n_e \times 3n_e}$, $\boldsymbol{K}_{C_i} \in \mathbb{R}^{3n_e \times 3n_e}$ and $\boldsymbol{D}_{C_i} \in \mathbb{R}^{3n_e \times 3n_e}$ denote the inertia matrix, stiffness matrix and damping matrix respectively of cable i. Elasticity compose of the elastic contribution

$$\boldsymbol{K}_{i,el} = \begin{bmatrix} \boldsymbol{K}_{i,el,1} & -\boldsymbol{K}_{i,el,1} & & & \\ -\boldsymbol{K}_{i,el,1} & \boldsymbol{K}_{i,el,1} + \boldsymbol{K}_{i,el,2} & -\boldsymbol{K}_{i,el,2} & & \\ & & \ddots & & \\ & & -\boldsymbol{K}_{i,el,n_e-1} & \boldsymbol{K}_{i,el,n_e-1} + \boldsymbol{K}_{i,el,n_e} & -\boldsymbol{K}_{i,el,n_e} \\ & & & -\boldsymbol{K}_{i,el,n_e} & \boldsymbol{K}_{i,el,n_e} \end{bmatrix}, \quad (2.37)$$

and the geometric contribution

$$\boldsymbol{K}_{i,g} = \begin{bmatrix} \boldsymbol{K}_{i,g,1} & -\boldsymbol{K}_{i,g,1} & & & \\ -\boldsymbol{K}_{i,g,1} & \boldsymbol{K}_{i,g,1} + \boldsymbol{K}_{i,g,2} & -\boldsymbol{K}_{i,g,2} & & \\ & & \ddots & & \\ & & -\boldsymbol{K}_{i,g,n_e-1} & \boldsymbol{K}_{i,g,n_e-1} + \boldsymbol{K}_{i,g,n_e} & -\boldsymbol{K}_{i,g,n_e} \\ & & & -\boldsymbol{K}_{i,g,n_e} & \boldsymbol{K}_{i,g,n_e} \end{bmatrix}. \quad (2.38)$$

The Kronecker product $\otimes$ allows to construct easily the mass matrix. Elasticity is usually referred to the longitudinal component, whereas for the lateral and vertical component stiffness is more precisely. Similar to this is the elongation referred to the longitudinal change of shape under stress and bending to the vertical and lateral change of shape.

Every entry of $\boldsymbol{K}_{i,el}$ and $\boldsymbol{K}_{i,g}$ is a 3×3 matrix and accounts for linear stiffness ${}^{T}/_{L_E}$ and linear elasticity ${}^{ES}/_{L_E}$ [64, 85, 5]:

$$\boldsymbol{K}_{i,g,j} = \frac{T}{L_e} \left(\boldsymbol{I}_{3\times 3} - \frac{\boldsymbol{l}_{i,j|j+1} \boldsymbol{l}_{i,j|j+1}^{\mathrm{T}}}{\|\boldsymbol{l}_{i,j|j+1}\|^2} \right) \quad (2.39)$$

$$\boldsymbol{K}_{i,el,j} = \frac{E_C S_C}{L_e} \frac{\boldsymbol{l}_{i,j|j+1} \boldsymbol{l}_{i,j|j+1}^{\mathrm{T}}}{\|\boldsymbol{l}_{i,j|j+1}\|^2} \quad (2.40)$$

Here, $\boldsymbol{l}_{i,j|j+1}$ denotes the vector going from the j^{th} element to the next element, i.e. $j+1$, E_C is the elasticity module[2], S_C is the cross section, T is the cable tension and L_e is the nominal cable length. Chapter 4 and Chapter 3 resume this model for an analysis of cable vibrations and for a Port-Hamilton model including cables, motors and the platform.

Partial-Derivative model

The second model goes back to 1974 when the author in [38] presented a linear cable model, that is suitable for free vibration and static analysis. The author presumed a cable sag to cable length ratio of 1 : 8 or less with one end point fixed at the origin of a coordinate system

[2]Sometimes the elasticity module is also called Youngs' modulus

$\mathcal{K}_{C_i}$ and one end-point fixed at the other end. This model was used in [50] to address the influence of sagging cables on the inverse kinematic. Further analysis with sagging cables was done by [41, 88]. Additionally, to the analysis of free vibrations, [46] investigated the influence of damping on the eigenfrequencies of an inclined cable with fixed ends.

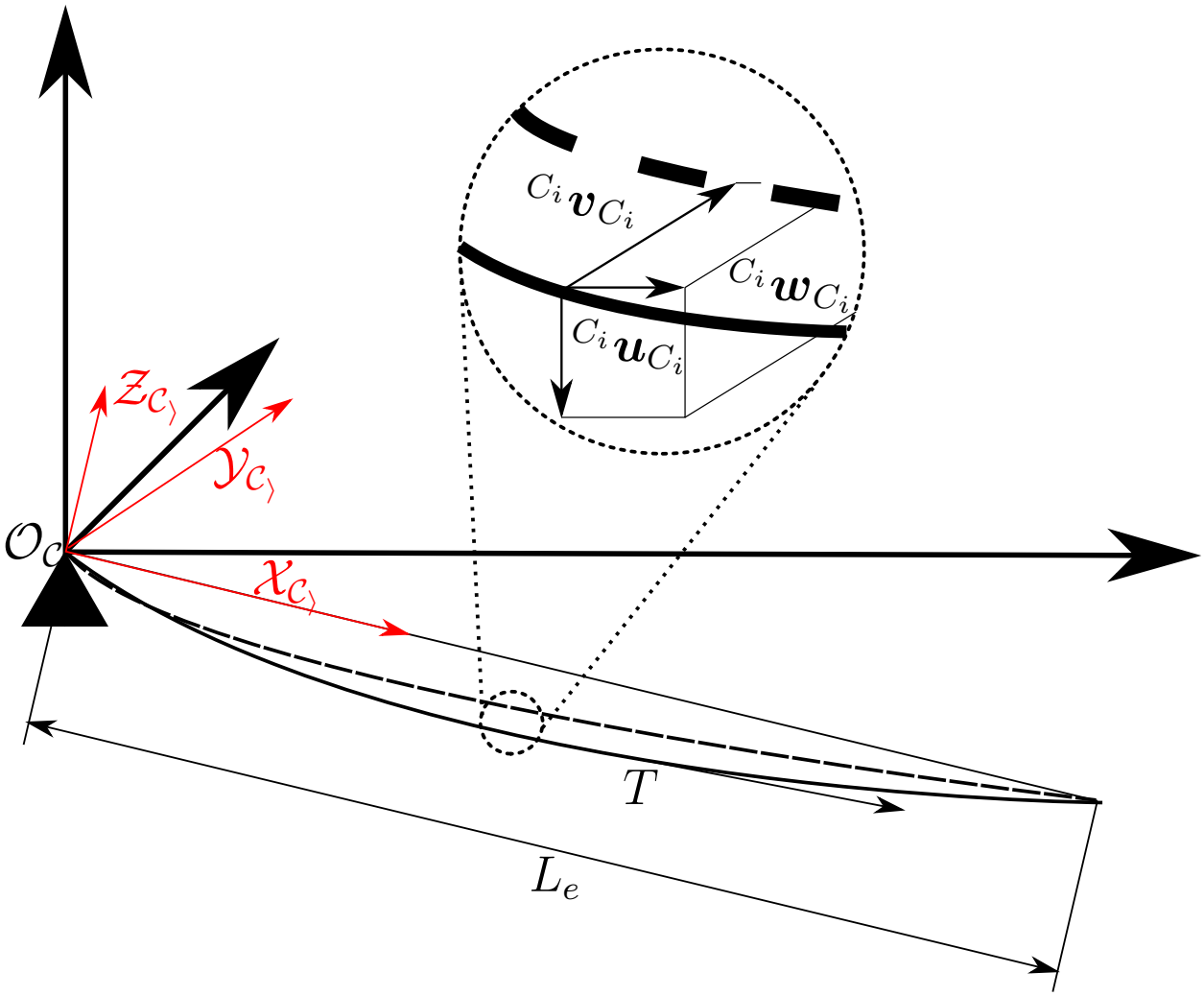

Figure 2.4: Sketch for Dynamic Stiffness Matrix based model

For this thesis the analysis of cable vibrations based on the Dynamic-Stiffness matrix is of interest, since the results are comparable to those of the Finite-Element Method based model in Section 2.2.2. The basic idea of the Dynamic Stiffness Matrix based approach, is to linearise a set of partial differential equations, derived by the Newton-Euler approach at one infinitesimal cable segment (see Figure 2.4) which according to [88, 41, 46] results in:

$$\begin{aligned}
\frac{\partial}{\partial {}^{C_i}x_{C_i}}\left\{T_{C_i}\left(\frac{\mathrm{d}^{C_i}x_{C_i}}{\mathrm{d}S_C}+\frac{\partial^{C_i}u_{C_i}}{\partial^{C_i}S_C}\right)\right\} &= m_{C_i}\frac{\partial^{2C_i}u_{C_i}}{\partial t^2}-m_{C_i}g\sin\theta_{C_i}+c_{x_i}\frac{\partial^{C_i}u_{C_i}}{\partial t}\\
\frac{\partial}{\partial {}^{C_i}x_{C_i}}\left\{T_{C_i}\left(\frac{\partial^{C_i}v_{C_i}}{\partial^{C_i}S_C}\right)\right\} &= m_{C_i}\frac{\partial^{2C_i}v_{C_i}}{\partial t^2}+c_{y_i}\frac{\partial^{C_i}v_C}{\partial t}\\
\frac{\partial}{\partial {}^{C_i}x_C}\left\{T_{C_i}\left(\frac{\mathrm{d}^{C_i}z_{C_i}}{\mathrm{d}S_C}+\frac{\partial^{C_i}w_{C_i}}{\partial^{C_i}S_C}\right)\right\} &= m_{C_i}\frac{\partial^{2C_i}w_{C_i}}{\partial t^2}-m_{C_i}g\cos\theta_{C_i}+c_{z_i}\frac{\partial^{C_i}w_{C_i}}{\partial t}\,,
\end{aligned} \tag{2.41}$$

with the comp ability equation:

$$\frac{h}{E_C S_C}\left(\frac{\mathrm{d}^{C_i}s}{\mathrm{d}^{C_i}x_{C_i}}\right)^3=\frac{\partial^{C_i}u_{C_i}}{\partial^{C_i}x_{C_i}}+\frac{\mathrm{d}^{C_i}y_{C_i}}{\mathrm{d}^{C_i}x_{C_i}}\frac{\partial^{C_i}v_{C_i}}{\partial^{C_i}x_{C_i}}\,, \tag{2.42}$$

where ${}^{C_i}x_{C_i}, {}^{C_i}y_{C_i}, {}^{C_i}z_{C_i}$ are the x, y, z coordinates of a mass element and ${}^{C_i}u_{C_i}, {}^{C_i}v_{C_i}, {}^{C_i}w_{C_i}$ are the corresponding deflections, ${}^{C_i}s$ is the linear abscissa and $T_{C_i} = T_{C_i,dyn} + T_{C_i,pre}$ is the cable tension, consisting of a dynamic component $T_{C_i,dyn}$ and a pre-tensing component $T_{C_i,pre}$. Besides, m_{C_i} is the cable mass, θ_{C_i} the inclination angle and $c_{C_i,\bullet}$ is the damping coefficients of the cable in $\bullet$ direction. In [88] the author assumes decoupled dynamics -which is valid when displacements are small and the cable is taut- and proposes a homogenous solution for Equation (2.41) as follows:

$${}^{C_i}w({}^{C_i}x_{C_i},t)=\tilde{w}({}^{C_i}x_{C_i})e^{i\omega_w t} \tag{2.43}$$

$${}^{C_i}v({}^{C_i}x_{C_i},t)=\tilde{v}({}^{C_i}x_{C_i})e^{i\omega_v t} \tag{2.44}$$

$${}^{C_i}h({}^{C_i}x_{C_i},t)=\tilde{h}({}^{C_i}x_{C_i})e^{i\omega_h t}\,, \tag{2.45}$$

with the amplitude $\hat{\bullet}$ and the frequencies $\omega_w \in \mathbb{R}, \omega_v \in \mathbb{R}, \omega_h \in \mathbb{R}$ in $[\mathrm{rad}/\mathrm{s}]$. Using the solutions (2.43-2.45) and assuming: i) small displacements; ii) a parabolic profile such that

$$\tau\frac{d^{C_i}x_{C_i}}{{}^{C_i}S_C}=h \qquad \text{and} \qquad T_{C_i}\frac{d^{C_i}x_{C_i}}{d^{C_i}S_C}=T_{C_i}\,;$$

iii) negligible small longitudinal displacements and iv) a fixed end; the Dynamic Stiffness Matrix of cable i reads [41]

$$\boldsymbol{K}(\omega)_{C_i}=\begin{bmatrix} {}^{C_i}K_{xx}(\omega_h)_{C_i} & 0 & {}^{C_i}K_{xz}(\omega_h)_i \\ 0 & {}^{C_i}K_{yy}(\omega_h)_{C_i} & 0 \\ {}^{C_i}K_{zx}(\omega_h)_{C_i} & 0 & {}^{C_i}K_{zz}(\omega_h)_i \end{bmatrix}. \tag{2.46}$$

The cable stiffness ${}^{C_i}\boldsymbol{K}(\omega)_i$ relates small displacements $\boldsymbol{\eta}_i$ from the equilibrium of one point on cable i to the corresponding cable force f_i. To finalize this subsection the stiffness elements

inside of Equation (2.46) reads:

$$K_{xx}(\omega_h)_{C_i} = \frac{E_C S_C}{L_e} \frac{1}{1 + \frac{\lambda_{C_i}^2}{\Omega_{C_i}^2}(\kappa_{C_i} - 1)} \tag{2.47}$$

$$K_{xz}(\omega_h)_{C_i} = K_{zx}(\omega_h)_{C_i} = \frac{E_C S_C}{L_e} \frac{\frac{1}{2}\epsilon_{C_i}(\kappa_{C_i} - 1)}{1 + \frac{\lambda_{C_i}^2}{\Omega_{C_i}^2(\kappa_{C_i} - 1)}} \tag{2.48}$$

$$K_{zz}(\omega_h)_{C_i} = \frac{E_C S_C \epsilon_{C_i}^2}{L_e \lambda_{C_i}^2 \kappa_{C_i}} - \frac{E_C S_C}{L_e} \frac{\frac{\epsilon_{C_i}^2}{4\lambda_{C_i}^2}\Omega_{C_i}^2 \left[\kappa_{C_i} + \frac{\lambda_{C_i}^2}{\Omega_{C_i}^2}(\kappa_{C_i} - 1)\right]}{1 + \frac{\lambda_{C_i}^2}{\Omega_{C_i}^2}(\kappa_{C_i} - 1)} \tag{2.49}$$

with

$$\begin{aligned}
\text{the damping ratio } \xi_{C_i} &= \frac{c_{C_i}}{2\mu_{C_i}\omega}\,, \\
\text{the natural frequency in } [^{rad}/_s] \ \omega_c &= \omega\sqrt{1 - 2\xi_{C_i} i}\,, \\
\text{the dimensionless natural frequency } \Omega_{C_i} &= \omega_{C_i} L_{C_i,0}\sqrt{\frac{\mu}{f_{C_i}}}\,, \\
\text{and two auxiliardy variables } \kappa_{C_i} &= \frac{\tan\left(\frac{\Omega_{C_i}}{2}\right)}{\frac{\Omega_{C_i}}{2}} \epsilon_{C_i} = \frac{8\delta_{C_i}}{L_0}\,.
\end{aligned}$$

The auxiliary variable ϵ_{C_i} relates the cable tension and the horizontal cable weight with the fundamental cable parameter

$$\lambda_{C_i}^2 = \left(\frac{\mu g L_{C_i,0}}{f_{C_i}}\right)^2 \frac{E_C S_C l}{f_{C_i} L_e} \cos(\theta_{C_i})^2\,,$$

and the cable length L_e. Since this model is based on simplifications and a linearisation of Equation (2.41) it is only valid if the limiting conditions [88]:

$$\begin{aligned}
\lambda_{C_i}^2 &\leq 24 \\
\text{and } \theta_{C_i} \leq 60°, \quad \epsilon_{C_i} &\leq 0.01 \left(\frac{\delta_{C_i}}{L_0} \leq \frac{1}{80}\right) \\
\text{or } \theta_{C_i} \leq 30°, \quad \epsilon_{C_i} &\leq 0.24 \left(\frac{\delta_{C_i}}{L_0} \leq \frac{1}{33}\right)\,,
\end{aligned} \tag{2.50}$$

are fulfilled. With the previous equation this section finishes. Chapter 4 will retrieve the fundamental Equations (2.33)-(2.47) for the analysis of cable vibrations.

A third promising method to derive a suitable cable model is the Rayleigh-Ritz approach. A set of basic functions -that have to fulfil the boundary conditions of the system- describe the shape of a cable. A simple structure makes this approach suitable for control design (in contrast to the approach based on partial differential equations) and provides a continuous solution (in contrast to the Finite-Element Method model).

When L_e approaches 0, the system stiffness (Equation (2.40)) approaches a singularity. The Rayleigh-Ritz[3] approach overcomes this conceptual missmatch, since no discretisation is necessary. Simulations in [71] and [35] show the numerical efficiency of the Rayleigh-Ritz approach.

2.3 Fundamentals in control

The Cablerobot Simulator as a simulator requires a high level of performance and tracking accuracy, but also robustness, reliability in spite of internal and external disturbances and safety, since human beings and machines share the same workspace. Internal disturbances include measurement noise, kinematic, dynamic parameter uncertainties, such as unprecisely known kinematic parameters and external disturbances including forces and torques, that are acting on the system components. Both, internal and external disturbances are combined to the lumped perturbations $\boldsymbol{\xi}$ This could be for instance an additional payload or a kickback[4]. Because of the simplified kinematic model, the kinematic parameters are not precisely known. Furthermore, the Cablerobot Simulator can carry additional equipment, that might change from experiment to experiment. Thus, dynamic parameters, i.e. the total mass, the mass distribution and the inertia might change.

Sliding-Mode Controllers are robust controllers, what makes them interesting for control of Cable-Driven Parallel Robots and fulfil predefined performance criteria in presence of such external and internal disturbances. Moreover, Sliding-Mode Controllers garuantee finite-time convergence under some mild assumptions and the ability for control with reduced-order compensator dynamics [99]. This thesis focus on Sliding-Mode Control as High-Level Controller and exploits their advantages.

2.3.1 Fundamentals of Sliding-Mode Controllers

Sliding-Mode Controllers are known for their robustness, what makes them a good candidate as High-Level Control of a Cable-Driven Parallel Robot. Furthermore Sliding-Mode Controllers achieve finite-time convergence of drive the so-called sliding variable $\boldsymbol{\sigma}$ in finite-time

[3]The Rayleigh-Ritz approach is also called Assumed-Mode approach.
[4]Kickbacks occur when the end-effector extrudes material like for example in [55] for sandblasting

to a sliding surface

$$\mathcal{S} = \{\boldsymbol{\sigma} \in \mathbb{R}^{n_a} : \boldsymbol{\sigma} = \mathbf{0}\} \,. \tag{2.51}$$

This sliding variable $\boldsymbol{\sigma}$ defines the composition of an error and its derivatives or integral respectivelly. Commonly $\boldsymbol{\sigma}$ is of the form:

$$\boldsymbol{\sigma} = \dot{\boldsymbol{e}} + \boldsymbol{\Lambda}_{SMC}\boldsymbol{e} \tag{2.52}$$

where $\boldsymbol{\Lambda}_{SMC} \in \mathbb{R}^{n_a \times n_a}$ is a positive definite matrix of proper size n_a, to weight the error $\boldsymbol{e} \in \mathbb{R}^{n_a \times 1}$. Equation (2.52) is a straight line denoted as sliding surface [99]. As soon as ideal sliding mode (2.51) is achieved, after a time t_r, an equivalent control input $\boldsymbol{z}_{eq} \in \mathbb{R}^{n_a \times 1}$ garuantuees, that $\boldsymbol{\sigma}$ stays on $\mathcal{S}$ for all time in presence of external and internal disturbances and $\boldsymbol{\zeta}$ respectivelly. This happens, when $\boldsymbol{e} = \dot{\boldsymbol{e}} = \mathbf{0}_{6\times 1}$ Furthermore Equation (2.51) is asymptotically stable if:

$$\dot{V} < 0 \quad , \text{ if } \boldsymbol{\sigma} \neq \mathbf{0} \tag{2.53}$$

$$\dot{V} \leq -\alpha V^{\frac{1}{2}} \tag{2.54}$$

$$\lim_{\|\boldsymbol{\sigma}\| \to \infty} V = \infty \tag{2.55}$$

Choosing $V = \frac{1}{2}\boldsymbol{\sigma}^{\mathrm{T}}\boldsymbol{\sigma}$ leads to the reachability condition:

$$\dot{V} = \boldsymbol{\sigma}\dot{\boldsymbol{\sigma}} \leq -\frac{\alpha}{\sqrt{2}}\,|\boldsymbol{\sigma}| = -\alpha V^{\frac{1}{2}} \tag{2.56}$$

and the convergence time

$$t_r \leq \frac{2V^{\frac{1}{2}}(0)}{\alpha} \tag{2.57}$$

and Equation (2.52) with $V = \boldsymbol{\sigma}^{\mathrm{T}}\boldsymbol{\sigma}$ provides suitable controller gains [99].The classical sliding mode controller $\boldsymbol{u} = f(\boldsymbol{x}_{des}, \dot{\boldsymbol{x}}_{des})^{-1} + \boldsymbol{\Lambda}\,\mathrm{sign}\,\boldsymbol{\sigma}$ achieves finite-time convergence to 1-sliding mode for a system $\dot{\boldsymbol{x}} = \boldsymbol{f}(x(t), \boldsymbol{u}(t)) + \boldsymbol{\zeta}(t)$, in presence of external disturbances $\boldsymbol{\zeta}$. However, motion platforms require two sliding-mode, i.e. $\boldsymbol{\sigma} = \dot{\boldsymbol{\sigma}} = \mathbf{0}_{6\times 1}$. Sliding-Mode controllers with the structure:

$$\boldsymbol{u} = \boldsymbol{\Lambda}_1\,\mathrm{sign}(\boldsymbol{\sigma}) + \boldsymbol{\Lambda}_2\,\mathrm{sign}(\dot{\boldsymbol{\sigma}}) \tag{2.58}$$

with two positive definite gain matrices $\boldsymbol{\Lambda}_1, \boldsymbol{\Lambda}_2$ of proper size track a trajectory up to acceleration level, but also cause chattering because of the discontinuous signum function. To reduce chattering, the discontinuous control input must be replaced with a continuous control input

$$\boldsymbol{u} = \boldsymbol{\Lambda}_1\,\|\boldsymbol{\sigma}\|^{\frac{1}{2}}\,\mathrm{sign}(\boldsymbol{\sigma})\,. \tag{2.59}$$

In abscence of lumped perturbations $\boldsymbol{\xi}$ Equation (2.59) drives the sliding variable to the sliding surface in

$$t_r = 2\boldsymbol{\Lambda}_1^{-1} \left\|\boldsymbol{\sigma}_0\right\|^{\frac{1}{2}} . \tag{2.60}$$

The Super-Twisting Sliding-Mode Controller

$$\begin{aligned} \boldsymbol{u}_{SMC} &= -\boldsymbol{\Lambda}_1 \left|\boldsymbol{\sigma}\right|^{\frac{1}{2}} \operatorname{sign}\left(\boldsymbol{\sigma}\right) + \boldsymbol{v} \\ \dot{\boldsymbol{v}} &= \begin{cases} -\boldsymbol{u}_{SMC} & \text{if } \left|\boldsymbol{u}_{SMC}\right| > \overline{\boldsymbol{u}} \\ -\boldsymbol{\Lambda}_2 \operatorname{sign}\left(\boldsymbol{\sigma}\right) & \text{if } \left|\boldsymbol{u}_{SMC}\right| \leq \overline{\boldsymbol{u}} \end{cases} . \end{aligned} \tag{2.61}$$

with the upper bound $\bar{\boldsymbol{u}}$ combines (2.58) and (2.59) and achieves finite-time convergence to 2-sliding mode [99, 7] in presence of $\boldsymbol{\xi}$ with reduced chattering due to its continuous component $|\boldsymbol{\sigma}|^{\frac{1}{2}} \operatorname{sign}(\boldsymbol{\sigma})$. Note, that $|\boldsymbol{\sigma}|^{\frac{1}{2}} \operatorname{sign}(\boldsymbol{\sigma})$ reduces chattering but can not completely eliminate chattering [101]. Chattering reduction motivate to exploid the properties of a Super-Twisting Sliding-Mode Controller in the control design for a Cable-Driven Parallel Robot. A further reduction of chattering effects is still possible. Besides the limits of robustness are extensible according to the real limits of the system. More precisely, the knowledge of an upper bound for $\boldsymbol{\xi}$ is not always available as presumed in [54, 72]. What follows, are conservatively high choosen gains to allow perturbation compensation at any time. However, high gains, combined with discontinuous control function, apply aggressive control actions and introduce chattering [56, 31]. Uncertainties do not constraint to parametric uncertainties, but also account for model uncertainties[5] and disturbances together. These limitations motivated to extend the Super-Twisting Sliding-Mode Controller with a gain adaptation that has the following properties:

- The gain adaptation incorporates compensation of model uncertainties, external disturbances and parametric uncertainties, summed up as lumped disturbances $\boldsymbol{\xi}$.

- The knowledge of an upper bound is obsolete. Thus, $\boldsymbol{\Lambda}_1$ and $\boldsymbol{\Lambda}_2$ increase whenever it is necessary and decrease whenever it is possible to compensate $\boldsymbol{\xi}$, fulfill predefined performance criteria and reduce control actions induced chattering and noise amplification

Remark 2.1: Modelling errors describe unknown dynamics whereas parameter uncertainties refer to unprecisely known parameters used to model known system dynamics.

[5] Model uncertainties include unmodelled effects

2.3.2 Realistic Measurement noise

Realistic measurement noise $\boldsymbol{\xi}_R \sim \mathcal{N}(\mathbf{0}, \boldsymbol{R}_{\boldsymbol{\xi}})$ is characterised by zero mean and a signal covariance matrix. Then $\boldsymbol{\xi}_{\boldsymbol{R}}$ can be constructed according to $\boldsymbol{\xi}_{\boldsymbol{R}} = \boldsymbol{T}\boldsymbol{v}_k$ with $\boldsymbol{v}_k = \sqrt{\lambda_i}\boldsymbol{r}_k$, $\boldsymbol{r}_k \sim \mathcal{N}(\mathbf{0}, \mathbf{1})$. Here λ_i is the i eigenvalue of the covariance matrix $\boldsymbol{R}_{\boldsymbol{\xi}}$ and $\boldsymbol{T}$ as the matrix of eigenvalues of $\boldsymbol{R}_{\boldsymbol{\xi}}$.

2.4 Port-Hamilton based modelling

Port-Hamilton modelling is an energy-based modelling technique that accounts for the fundamental law of energy preservation and provides a simple and unique model structure for all types of linear and nonlinear systems (thermal, electrical, mechanical and chemical) but also combinations amoung those. Storage, dissipation and exchange elements represent a system in Port-Hamilton form in a modular structure. Depending on the domain, energy is the product of force and velocity (for mechanical systems), current and voltage (electrical and magnetical systems), molar flow and chemical potential (chemical systems) or entropy flow and temperature (thermal systems). Table (2.1) reviews different combinations for all relevant domains. In [16] the authors present a network of heat exchangers in Port-Hamilton structure and prove passivity for one exchanger. The authors in [26] build a Port-Hamilton system for generic electro-chemical systems. An example for a mechanical system in Port-Hamilton structure is given by [15], where the authors reshape the physical properties of a quadrotor model in Port-Hamilton representation. Changing the physical properties of mechanical systems is an interesting feature for simulators such as the Cablerobot Simulator, since those mimic systems (such as planes, helicopters, cars) with different dynamics.

The attempt to model a Cable-Driven Parallel Robot as one system can be burdensome because of its high dimensionality and high complexity. A modular structure can split a complex multibody system into multiple smaller subsystems (platform, cables and driving units separately) and simplify the modelling process significantly. When all subsystems are available as Port-Hamilton system, the entire system can be assembled by so-called power-port. Those connect all subsystems and allow an exchange of energy as the product of flow f_{PHS} and effort variables e_{PHS} amoung each other [13]. The principle of power-ports leads to the definition of supply rates w, that is the amount of introduced and expelled energy to and from the system, i.e.:

$$w : \mathcal{U} \times \mathcal{V} \rightarrow \mathbb{R}\,, \tag{2.62}$$

with $\mathcal{U}$ as the set of feasible input and $\mathcal{V}$ as the set of outputs. The notation of a supply rate is relevant for the definition of dissipasion as a key feature for passivity. Passive systems are stable with respect to an output without any external input. Cables for example are output

Table 2.1: Power port combinations for Port-Hamilton models

Domain	flow variable $f_{PHS} \in \mathcal{F}$	effort variable $e_{PHS} \in \mathcal{E}$
electric	current	voltage
magnetic	voltage	current
potential translation	velocity	force
kinetic translation	force	velocity
potential rotation	angular velocity	torque
kinetic rotation	torque	angular velocity
chemical	molar flow	chemical potential
thermal	entropy flow	temperature

passive and stable systems. A fixed cable after applying a jerk, will start to oscillate around its equilibrium. Internal damping will immediately make those oscillations decay and bring the cable back to its stable equilibrium.

A system is called passive, if and only if the integral of w is limited by the difference of a positive definite storage function $V(x(t)) \in \mathcal{C}^1$ and its inital value $V(x_0)$ [13, 74]:

$$V(x(t)) - V(x_0) \leq \int_0^t w(\tau)\mathrm{d}\tau \,. \tag{2.63}$$

Moreover, a system is called lossless if $V(x(t)) - V(x_0)$ is exactly equal to the integral of the supply rate and is called strictly passive with respect to (2.62), if

$$V(x(t)) - V(x_0) < \int_0^t w(\tau)\mathrm{d}\tau \,.$$

If the storage function also fulfils $V(0) \geq 0$ and the system is strictly passive, then the equilibrium point is Lyapunov stable [23]. This is an important feature, since controllers based on energy shaping are able to drive the system to a desired state $x^\star$ such that $V(x^\star(t)) = V(0) \geq 0$ holds. In other words: once a controller drove the state of a system to the desired state $x^\star$, stability is established for a passive system. In the light of this knowledge, the Hamiltonian $H(x(t)) = T(x(t)) + V(x(t))$, that is the sum of the kinetic and potential energy of a system[6] is a reasonable candidate for a Lyapunov function.

Now given a set of generalised coordinates $\boldsymbol{q}$ with its velocities $\dot{\boldsymbol{q}}$ and the generalised mo-

[6]Here the word system is used in a very general sense and (in the context of this work) includes the entire Cable-Driven Parallel Robot. The principles presented in this section hold also for subsystems, e.g. cables, driving units and the platform anyway

mentum $\boldsymbol{p} = \boldsymbol{M}\dot{\boldsymbol{q}} \in \mathbb{R}^{6\times 1}$ the dynamic equation

$$\begin{aligned} \begin{bmatrix} \dot{\boldsymbol{q}} \\ \dot{\boldsymbol{p}} \end{bmatrix} &= (\boldsymbol{I} - \boldsymbol{R}) \begin{bmatrix} \frac{\partial H(\boldsymbol{p},\boldsymbol{p})}{\partial \boldsymbol{q}} \\ \frac{\partial H(\boldsymbol{p},\boldsymbol{p})}{\partial \boldsymbol{p}} \end{bmatrix} + \boldsymbol{G}(\boldsymbol{q},\boldsymbol{p})\boldsymbol{u} \\ \boldsymbol{y} &= \boldsymbol{G}^{\mathrm{T}}(\boldsymbol{q},\boldsymbol{p}) \begin{bmatrix} \frac{\partial H(\boldsymbol{q},\boldsymbol{p})}{\partial \boldsymbol{q}} \\ \frac{\partial H(\boldsymbol{q},\boldsymbol{p})}{\partial \boldsymbol{p}} \end{bmatrix} , \end{aligned} \tag{2.64}$$

represents a system with n_x dimensional state in Port-Hamilton form, with the output $\boldsymbol{y} \in \mathbb{R}^{n_y\times 1}$, the input $\boldsymbol{u} \in \mathbb{R}^{n_u\times 1}$, the screw-symmetric interconnection matrix $\boldsymbol{I} \in \mathbb{R}^{n_y\times n_y}$, the positive semi-definite diagonal damping matrix $\boldsymbol{R} \in \mathbb{R}^{n_x\times n_x}$ and the control input matrix $\boldsymbol{G}(\boldsymbol{q},\boldsymbol{p})$.:

$$\boldsymbol{G}(\boldsymbol{q},\boldsymbol{p}) = \frac{\partial}{\partial \boldsymbol{f}_j} \underbrace{\frac{\partial W}{\partial \boldsymbol{q}}}_{f_g} . \tag{2.65}$$

Equation (2.65) characterizes the relation between the control input matrix $\boldsymbol{G}$ and the work $W \in \mathbb{R}$ done at the controlled element. The generalised forces $\boldsymbol{f}_g$ result from the partial derivative of W with respect to the generalised coordinates $\boldsymbol{q}$. To derive $\boldsymbol{G}$, the generalised forces $\boldsymbol{f}_g$ are derivated with respect to the input force, which act on the controlled element j [36].

Defining $\boldsymbol{x} = \begin{bmatrix} \boldsymbol{q}^{\mathrm{T}} & \boldsymbol{p}^{\mathrm{T}} \end{bmatrix}^{\mathrm{T}}$ as the state vector and with Equation (2.64) the time derivative of $H(\boldsymbol{x})$ reads:

$$\dot{H}(\boldsymbol{x}) = \frac{\partial H(\boldsymbol{x})}{\partial \boldsymbol{x}} \frac{\partial \boldsymbol{x}}{\partial t} = - \underbrace{\frac{\partial^{\mathrm{T}} H(\boldsymbol{x})}{\partial \boldsymbol{x}} \boldsymbol{R} \frac{\partial H(\boldsymbol{x})}{\partial \boldsymbol{x}}}_{\tilde{\boldsymbol{R}}} + \boldsymbol{y}^{\mathrm{T}}\boldsymbol{u} \tag{2.66}$$

Assuming $w = \boldsymbol{y}^{\mathrm{T}}\boldsymbol{u} = 0$ the energy rate $\dot{H(\boldsymbol{x})}$ decreases by $-\tilde{\boldsymbol{R}}$ and the energy $H(\boldsymbol{x})$ dissipates, since $\boldsymbol{R}$ is a positive semi definite diagonal matrix. The quadratic term

$$\frac{\partial^{\mathrm{T}} H(\boldsymbol{x})}{\partial \boldsymbol{x}} \frac{\partial H(\boldsymbol{x})}{\partial \boldsymbol{x}} ,$$

induces

$$-\tilde{\boldsymbol{R}} < 0, \ \forall \frac{\partial H(\boldsymbol{x})}{\partial \boldsymbol{x}} .$$

Including $\boldsymbol{u}$ and $\boldsymbol{y}$, the total energy $H(\boldsymbol{x})$ decreases when

$$-\frac{\partial^{\mathrm{T}} H(\boldsymbol{x})}{\partial \boldsymbol{x}} \boldsymbol{R} \frac{\partial H(\boldsymbol{x})}{\partial \boldsymbol{x}} < 0 ,$$

and $\left\| \tilde{\boldsymbol{R}} \right\| > \boldsymbol{y}^{\mathrm{T}}\boldsymbol{u}$. Equation (2.66) shows, that $H(\boldsymbol{x})$ is a reasonable choice for a Lyapunov function.

Summarizing Port-Hamilton systems have some features which are beneficial for modelling and control Cable-Driven Parallel Robot. Their modular structure allows to split a complex system into smaller subsystem, which are easier to model. Power-ports combine those subsystems and describe the exchange of energy amoung them. Preservation of energy and passivity [13] are principle ideas and garuantee an easy proof for stability. Moreover, Passivity-Based Controller change the physical properties of mechanical systems in Port-Hamilton structure, which is an interesting feature for simulators such as the Cablerobot Simulator [2].

2.5 Unscented-Kalman Filter for state estimation

Section 2.1 already introduced the forward kinematics to derive the state $\boldsymbol{x}$ of a Cable-Driven Parallel Robot. As a matter of fact the forward kinematics can not account for cable elongation and cable slackness, i.e. influence of the cable dynamics on the platform. The error made by the forward kinematics, increases by the size of a Cable-Driven Parallel Robot. A direct measurement of the platform pose, velocity and acceleration is preferable. Unfortunately, the expenses of those measurement systems are disproportional to their advantages, especially since fusion of multiple cheap sensors can provide suitable results. Besides further sensors such as Inertia-Measurement Units for acceleration measurements might be already available. Then a Kalman Filter can incorporate additional information given by these measurement units and improve the estimation process. Besides, encoder measurements and acceleration measurements at the platform provide an insight to the cable dynamics, such that the Kalman-Filter is useful as an analysis tool for further investigations on cable dynamics.
Kalman Filters are broadly applied for this purpose and fuse one or more measurements from different types of sensors with different sampling times and noise characteristics to estimate the state $\hat{\boldsymbol{x}}_{k|k}$ of a system at each iteration step k:

$$\hat{\boldsymbol{x}}_{k+1} = \boldsymbol{A}_k\hat{\boldsymbol{x}}_k + \boldsymbol{B}_k\boldsymbol{u}_k + \boldsymbol{Q}_\zeta\boldsymbol{\zeta}_k \tag{2.67}$$

$$\boldsymbol{y}_k = \boldsymbol{C}_k\hat{\boldsymbol{x}}_k + \boldsymbol{D}_k\boldsymbol{u}_k + \boldsymbol{R}_\xi\boldsymbol{\xi}_k\,, \tag{2.68}$$

with the system state $\boldsymbol{x} \in \mathbb{R}^{n_x\times 1}$, the input $\boldsymbol{u} \in \mathbb{R}^{n_u\times 1}$, model noise $\boldsymbol{\zeta}_k \in \mathbb{R}^{n_x\times 1}$ with $\boldsymbol{\zeta} \sim (\boldsymbol{0}, \boldsymbol{Q}_\zeta)$, measurement noise $\boldsymbol{\xi}_k \in \mathbb{R}^{n_y\times 1}$ with $\boldsymbol{\xi} \sim (\boldsymbol{0}, \boldsymbol{R}_\xi)$, the system matrix $\boldsymbol{A}_k$ of the linear system, the input matrix $\boldsymbol{B}_k$, the output matrix $\boldsymbol{C}_k$ and the feedthrough matrix $\boldsymbol{D}_k$ of proper size. Here $n_u \in \mathbb{R}$ is the number of control inputs, $n_x \in \mathbb{R}$ is the number of states and $n_y \in \mathbb{R}$ is the number of outputs . Two or more steps build the structure of those filters: In the first step the Kalman Filter predicts a priory the next state estimate $\hat{\boldsymbol{x}}_{k|k+1}$, based on the previously corrected state estimate $\hat{\boldsymbol{x}}_{k-1|k-1}$ and the input $\boldsymbol{u}_k$ in presence of process noice $\boldsymbol{\zeta}_k$. Besides, an a priori covariance matrix $\boldsymbol{P}_{k|k-1}$ is computed, based on the system matrix $\boldsymbol{A}_k$ at timestep k, the positive definite model covariance matrix $\boldsymbol{Q}_\zeta$ with entries only on the

main diagonal and the measurement covariance matrix $\boldsymbol{R}_{\boldsymbol{\xi}}$. More precisely, the prediction step is:

$$\hat{\boldsymbol{x}}_{k|k+1} = \boldsymbol{A}_k \hat{\boldsymbol{x}}_{k-1|k-1} + \boldsymbol{B}_k \boldsymbol{x}_k \tag{2.69}$$

$$\boldsymbol{P}_{k|k-1} = \boldsymbol{A}_k \boldsymbol{P}_{k-1|k-1} \boldsymbol{A}_k^{\mathrm{T}} + \boldsymbol{Q}_{\zeta} \tag{2.70}$$

The second step incorporates sensor measurements $\boldsymbol{z}_k \in \mathbb{R}^{n_y}$ and accounts for measurement noise.

$$\tilde{\boldsymbol{y}}_k = \boldsymbol{z}_k - \boldsymbol{C}_k \hat{\boldsymbol{x}}_{k|k+1} \tag{2.71}$$

$$\boldsymbol{S}_k = \boldsymbol{R}_{\boldsymbol{\xi}} + \boldsymbol{C} \boldsymbol{P}_{k|k-1} \boldsymbol{C}^{\mathrm{T}} \tag{2.72}$$

$$\boldsymbol{K}_{KF,k} = \boldsymbol{P}_{k|k-1} \boldsymbol{C}^{\mathrm{T}} \boldsymbol{S}_k^{-1} \tag{2.73}$$

$$\hat{\boldsymbol{x}}_{k|k} = \hat{\boldsymbol{x}}_{k|k-1} + \boldsymbol{K}_{KF,k} \tilde{\boldsymbol{y}}_k \tag{2.74}$$

$$\boldsymbol{P}_{k|k} = (\boldsymbol{I}_{n_x \times n_x} - \boldsymbol{K}_k \boldsymbol{C}) \boldsymbol{P}_{k|k-1} \tag{2.75}$$

$$(\boldsymbol{I}_{n_x \times n_x} - \boldsymbol{K}_k \boldsymbol{C})^{\mathrm{T}} + \boldsymbol{K}_k \boldsymbol{R}_{\boldsymbol{\xi}} \boldsymbol{K}_k^{\mathrm{T}}, \tag{2.76}$$

when noise is present. Equation (2.69) - (2.76) are the well-known equations for a Kalman-Filter [96]. Note that multiple correction steps are possible if more than one sensor subscribes data to the filter. In addition, a posteriori measurements are possible, if the sampling time of a particular sensor exceeds the cycletime of the system. In general all measurements can have different sampling times and can be included in the estimation process. Equation (2.67)-(2.76) describe the two steps in the estimation process for linear systems. To cope with nonlinear systems of the following structure:

$$\boldsymbol{x}_{k+1} = f(\boldsymbol{x}_k, \boldsymbol{u}_k, \boldsymbol{\zeta}_k) \tag{2.77}$$

$$\boldsymbol{y}_k = g(\boldsymbol{x}_k, \boldsymbol{u}_k, \boldsymbol{\xi}_k) \tag{2.78}$$

the Extended Kalman-Filter linearises the system dynamics around the current working point $\hat{\boldsymbol{x}}_k$ The process noise is here denoted as $\boldsymbol{\zeta}_k$ and the matrices $\boldsymbol{A}_k$,$\boldsymbol{B}_k$,$\boldsymbol{C}_k$ and $\boldsymbol{D}_k$ are the linearised approximation of the nonlinear function $f(\boldsymbol{x}_k, \boldsymbol{u}_k, \boldsymbol{\zeta}_{Q,k})$

$$\boldsymbol{A}_k = \left.\frac{\partial f(\boldsymbol{x}, \boldsymbol{u}, \boldsymbol{\zeta}_k)}{\partial \boldsymbol{x}}\right|_{x_k} \boldsymbol{B}_k = \left.\frac{\partial f(\boldsymbol{x}, \boldsymbol{u}, \boldsymbol{\zeta}_k)}{\partial \boldsymbol{u}}\right|_{x_k} \tag{2.79}$$

$$\boldsymbol{C}_k = \left.\frac{\partial g(\boldsymbol{x}, \boldsymbol{u}, \boldsymbol{\xi}_k)}{\partial \boldsymbol{x}}\right|_{x_k} \boldsymbol{D}_k = \left.\frac{\partial g(\boldsymbol{x}, \boldsymbol{u}, \boldsymbol{\xi}_k)}{\partial \boldsymbol{u}}\right|_{x_k} \tag{2.80}$$

The index k denotes the sample of a discrete time system. But most common modelling techniques provide a continuous time model -denoted with an index c- such that a conversion

to a discrete time representation is required. The Laplace-Transformation:

$$A_k = \mathcal{L}^{-1}\left\{(s_{LP}I - A_c)^{-1}\right\}|_{t=h} = e^{At}|_{t=h} = e^{Ah} \tag{2.81}$$

$$B_k = \mathcal{L}^{-1}\left\{(s_{LP}I - A_c)^{-1}\frac{1}{s_{LP}}B_c\right\}|_{t=h} = \int_0^h e^{Ah}d\tau B_c \tag{2.82}$$

transforms the continuous system matrix and input matrix to its discrete compliment [34]. Here, h denotes the stepsize and s_{LP} the Laplace variable [24].

Both the Kalman Filter and the Extended Kalman Filter propagate the mean value of $\boldsymbol{x}_k$ through a linear function and obtain a new estimate $\boldsymbol{x}_{k+1}$. Both estimators disregard the covariance of the old estimate $\hat{\boldsymbol{x}}_k$ and do not account for model nonlinearities which results in a loss of information. Besides, linearising coupled and prefered against the Extended Kalman-Filter and the Kalman-Filter coupled systems can be very cumbersome. Chapter 3 and 4 will show, that cables are nonlinear and coupled systems. Due to this an estimation schem that preserves nonlinearities and couplings, as the Unscented Kalman-Filter does, is comfortable[7]. The Unscented Kalman filter takes a set of $2n_x + 1$ so-called sigma points $\boldsymbol{\mathcal{X}}$

$$\boldsymbol{\mathcal{X}}_0 = \bar{\boldsymbol{x}} \tag{2.83}$$

$$\boldsymbol{\mathcal{X}}_i = \bar{\boldsymbol{x}} + \left(\sqrt{(n_x + \lambda_{UKF})\boldsymbol{P}_x}\right)_i, i = 1, \ldots, n_x \tag{2.84}$$

$$\boldsymbol{\mathcal{X}}_i = \bar{\boldsymbol{x}} - \left(\sqrt{(n_x + \lambda_{UKF})\boldsymbol{P}_x}\right)_{i-n_x}, i = n_x + 1, \ldots, 2n_x \tag{2.85}$$

$$\lambda_{UKF} = \alpha_{UKF}^2(n_x + \kappa_{UKF}) - n_x\,, \tag{2.86}$$

around the mean value $\boldsymbol{x}_k$, propagates those points through the nonlinear function $f(\boldsymbol{x}_k, \boldsymbol{u}_k, \boldsymbol{\zeta}_{Q,k})$ and restores the estimate $\boldsymbol{x}_{k+1}$ (with the mean value $\bar{\boldsymbol{x}}$, covariance matrix $\boldsymbol{P}_x$ for $\boldsymbol{x}$, the dimension n_x of the state $\boldsymbol{x}$ and the tuning parameters of the Unscented Kalman Filter $\alpha_{UKF}, \lambda_{UKF}, \kappa_{UKF}$). This way the Unscented Kalman Filter considers the covariance before the estimate as well as the model nonlinearity. A closer look at the prediction and correction terms (see Equations (2.90) and (2.96)) reveals that the structure of the Unscented Kalman Filter is the same as for the Extended Kalman Filter. The first part includes the computation of the sigma points $\boldsymbol{\mathcal{X}}_{k-1}$

$$\boldsymbol{\mathcal{X}}_{k-1}^{-} = \begin{bmatrix} \mathbf{1}_{1\times n_x} \otimes \hat{\boldsymbol{x}}_{k-1} \\ \mathbf{1}_{1\times n_x} \otimes \hat{\boldsymbol{x}}_{k-1} + \gamma_{UKF}\sqrt{\boldsymbol{P}_{k-1}} \\ \mathbf{1}_{1\times n_x} \otimes \hat{\boldsymbol{x}}_{k-1} - \gamma_{UKF}\sqrt{\boldsymbol{P}_{k-1}} \end{bmatrix} \tag{2.87}$$

[7]The notation 'unscented' stems from the unscented transformation which applies a nonlinear function at a propability distribution and estimate its result.

and the prediction step:

$$\boldsymbol{\mathcal{X}}^{-}_{k|k-1} = f\left[\boldsymbol{\mathcal{X}}_{k-1}, \boldsymbol{u}_{k-1}\right] \tag{2.88}$$

$$\hat{\boldsymbol{x}}^{-}_{k} = \sum_{i=0}^{2n_x} W_i^{\boldsymbol{\mathcal{X}}} \boldsymbol{\mathcal{X}}_{k|k-1} \tag{2.89}$$

$$\boldsymbol{P}^{-}_{k} = \sum_{i=0}^{2n_x} W_i^{\boldsymbol{P}_x} \left[\boldsymbol{\mathcal{X}}_{i,k|k-1} - \hat{\boldsymbol{x}}^{-}_{k}\right] \left[\boldsymbol{\mathcal{X}}_{i,k|k-1} - \hat{\boldsymbol{x}}^{-}_{k}\right]^{\mathrm{T}} + \boldsymbol{Q}_{\boldsymbol{\zeta}} \tag{2.90}$$

Note that $\left[\boldsymbol{\mathcal{X}}_{i,k|k-1} - \hat{\boldsymbol{x}}^{-}_{k}\right]$ is a $n_x \times x_n$ matrix and $\otimes$ is the Kronecker product. All sigma points are propagated through the nonlinear function $f[\boldsymbol{\mathcal{X}}_{k-1}, \boldsymbol{u}_{k-1}]$. The second part corrects the predicted state $\hat{\boldsymbol{x}}^{-}_{k}$ with the measurement $\boldsymbol{y}$ and another set of sigma points.

$$\boldsymbol{\mathcal{X}}_{k-1} = \begin{bmatrix} \mathbf{1}_{n_x} \otimes \hat{\boldsymbol{x}}^{-}_{k} \\ \mathbf{1}_{n_x} \otimes \hat{\boldsymbol{x}}^{-}_{k} + \sqrt{(n_x + \gamma_{UKF})\boldsymbol{P}^{-}_{k}} \\ \mathbf{1}_{n_x} \otimes \hat{\boldsymbol{x}}_{k-1} - \sqrt{(n_x + \gamma_{UKF})\boldsymbol{P}^{-}_{k}} \end{bmatrix} \tag{2.91}$$

$$\boldsymbol{\mathcal{Y}}_{k-1} = g\left[\boldsymbol{\mathcal{X}}_{k-1}\right] \tag{2.92}$$

$$\hat{\boldsymbol{y}}^{-}_{k} = \sum_{i=0}^{2n_x} W_i^{\boldsymbol{\mathcal{X}}} \boldsymbol{\mathcal{Y}}_{i,k-1} \tag{2.93}$$

$$\boldsymbol{P}_{\hat{\boldsymbol{y}}_k \hat{\boldsymbol{y}}_k} = \sum_{i=0}^{2n_x} W_i^{\boldsymbol{P}_x} \left[\boldsymbol{\mathcal{Y}}_{i,k-1} - \hat{\boldsymbol{y}}^{-}_{k}\right] \left[\boldsymbol{\mathcal{Y}}_{i,k-1} - \hat{\boldsymbol{y}}^{-}_{k}\right]^{\mathrm{T}} + \boldsymbol{R}_{\boldsymbol{\xi}} \tag{2.94}$$

$$\boldsymbol{P}_{\hat{\boldsymbol{x}}_k \hat{\boldsymbol{y}}_k} = \sum_{i=0}^{2n_x} W_i^{\boldsymbol{P}_x} \left[\boldsymbol{\mathcal{X}}_{i,k-1} - \hat{\boldsymbol{x}}^{-}_{k}\right] \left[\boldsymbol{\mathcal{Y}}_{i,k-1} - \hat{\boldsymbol{y}}^{-}_{k}\right]^{\mathrm{T}} \tag{2.95}$$

$$\boldsymbol{K}_k = \boldsymbol{P}_{\hat{\boldsymbol{x}}_k \hat{\boldsymbol{y}}_k} \boldsymbol{P}^{-1}_{\hat{\boldsymbol{y}}_k \hat{\boldsymbol{y}}_k} \tag{2.96}$$

$$\hat{\boldsymbol{x}}_k = \hat{\boldsymbol{x}}^{-}_{k} + \boldsymbol{K}_k(\boldsymbol{y}_k - \hat{\boldsymbol{y}}^{-}_{k}) \tag{2.97}$$

$$\boldsymbol{P}_k = \boldsymbol{P}^{-}_{k} - \boldsymbol{K}_k \boldsymbol{P}_{\hat{\boldsymbol{y}}_k \hat{\boldsymbol{y}}_k} \boldsymbol{K}^{\mathrm{T}}_{k} \,. \tag{2.98}$$

Table 2.2: Unscented Kalman-Filter parameters

$\hat{\boldsymbol{x}}_{k-1}$	State estimate after correction at time instance k-1
$\boldsymbol{P}_{k-1}$	Covariance after correction at time instance k-1
$W_i^{\bullet}$	Weight of sigma point $i = 0 \dots 2n_x$ for mean value and covariance
$\boldsymbol{P}_k^-$	Covariance of prior sigma points
$\boldsymbol{P}_{\hat{\boldsymbol{y}}_k\hat{\boldsymbol{y}}_k}$	Covariance of posteriori sigma points
$\boldsymbol{P}_{\hat{\boldsymbol{x}}_k\hat{\boldsymbol{y}}_k}$	Cross-Covariance of posteriori sigma points
$\boldsymbol{P}_k^-$	Covariance of prior sigma points
$\boldsymbol{P}_k$	Covariance of posteriori sigma points
$\boldsymbol{R}_{\boldsymbol{\xi}}$	Noise covariance
$\boldsymbol{Q}_{\boldsymbol{\zeta}}$	Model covariance
$\mathcal{Y}_{k-1}$	Propagated sigma points
$\hat{\boldsymbol{y}}_k^-$	Mean value of propagated sigma points
$\boldsymbol{K}_k$	Unscented Kalman-Filter gain matrix for state correction at time instance k

In case of a linear function $g(\bullet)$ there is no need to compute another set of sigma points and one can directly use $\boldsymbol{g}[\hat{\boldsymbol{x}}_k^-]$. Table 2.2 shows all parameters of the Unscented Kalman-Filter Note that the Unscented Kalman-Filter assigns a weight according to [29]:

$$W_0^{\boldsymbol{\mathcal{X}}} = \frac{\gamma_{UKF}}{(n_x + \gamma_{UKF})} \tag{2.99}$$

$$W_0^{\boldsymbol{P}_x} = \frac{\gamma_{UKF}}{(n_x + \gamma_{UKF})} + (1 - \alpha_{UKF}^2 + \beta_{UKF}) \tag{2.100}$$

$$W_i^{\boldsymbol{\mathcal{X}}} = W_i^{\boldsymbol{P}_x} = \frac{1}{2(n_x + \gamma_{UKF})}, \qquad i = 1, \dots, 2n_x \tag{2.101}$$

to the corresponding sigma points, where $\gamma_{UKF} = \alpha^2(n_x + \kappa_{UKF}) - \gamma_{UKF}$. For a Gaussian distribution, $\beta = 2$ is optimal [29]. Besides, $\alpha_{UKF} \in (0, 1]$ and $\kappa_{UKF} \geq 0$ influence the spread of sigma point. For α_{UKF} close to one and high values for κ_{UKF}, the sigma points spread wider and vice versa for α_{UKF} and κ_{UKF} close to zero. For α_{UKF} close to 0, the Unscented Kalman-Filter put more weight on the mean and less weight on the covariance.

Using the Unscented Transform, the accuracy of the exactly known nonlinear function is preserved and the imprecisely-known probability distribution is estimated. Figure 2.5 depicts the idea of the Unscented Kalman filter and compares qualitatively the Unscented Kalman-Filter and the Extended Kalman-Filter [29]. In terms of computational effort the Unscented Kalman Filter is comparable to the Extended Kalman Filter [29, 30], although the Unscented Kalman-Filter requires to apply the nonlinear function on all sigma points. The Unscented Kalman-Filter does not require any linearisation and therefore no computation of a Jacobian matrix. The Extended Kalman-Filter approximates the nonlinear function $f(\boldsymbol{x}_k, \boldsymbol{u}_k, \boldsymbol{\zeta}_k)$ by the first element of the Taylor series, which results in an estimation error of order two [78] and accounts for reduced performance for highly nonlinear systems [77]. The Unscented Kalman-Filter instead reaches an estimation error of order three or four. This is beneficial for coupled and highly nonlinear systems such as cables.

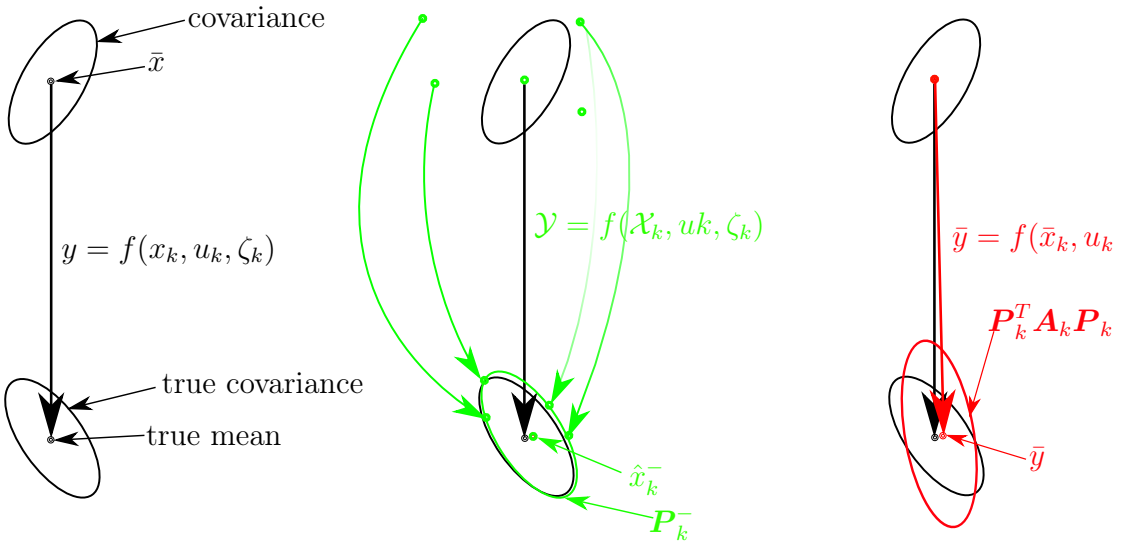

Figure 2.5: Comparison between Unscented Kalman-Filter and Extended Kalman-Filter

Summarizing, estimation for a Cable-Driven Parallel Robot via Unscented Kalman-Filter has the following advantages:

1. Fusion of multiple sensor input, includes information about cable dynamics and paves the way for further investigations on cable dynamics and vibration surpression
2. Cables are highly nonlinear and coupled systems, such that the Unscented Kalman-Filter is prefered against the Extended Kalman-Filter

Thus Kalman-Filters and especially the Unscented Kalman-Filter faciliate and allow state reconstruction and further investigations in excess of this work.

Chapter 3

Control

Content of this chapter is the overall control structure of a Cable-Driven Parallel Robot for vibration compensation and reduction. In the first part a friction compensation algorithm and tension distribution algorithm for motion control in introduced. The second part evaluates an adaptive Super-Twisting Sliding-Mode Controller in simulation. A Port-Hamilton based modelling and control strategy of one cable completes this chapter

This thesis focus on methods for vibration compensation and improvement of tracking accuracy of a Cable-Driven Parallel Robot. To attenuate chattering and vibrations one has to take actions on all levels of control and modelling. Vibrations describe a high frequency periodic swinging motion of an object around an equilibrium point, can damage system components, downgrade the systems performance and reduce tracking accuracy[1]. Figure 3.1 assigns contributors of vibrations to the corresponding components of a Cable-Driven Parallel Robot in a sketch. Those are controller induced vibrations, cable stiffness and static friction in bearings.

Friction is a complex, non-linear time varying tribologic phenomenon, that occurs foremost in bearings. Here, especially stiction is of interest. An applied driving force initiates a motion only if it expels static friction[2]. At this particular moment the system reacts with a jerk and introduces vibrations to the system. Additional, viscous friction applies a velocity-dependend force, that counteracts the systems motion and degrades tracking accuracy.

Friction characteristics may change, because abrasion in bearing worsen lubrication. Static inverted models do not account for changing friction characteristics and the classical sign function, used for static friction, does not capture the true nature of static friction [53]. Besides, the adaptive friction compensation algorithm [53], applied in this work, accounts for

[1] Accuracy is used here as an umbrella term for accuracy and precision. Accuracy is evaluated by the difference between the outcome of a process and the desired outcome. Precision describes the reliability of a process to provide the same output after every run [89]

[2] When the applied driving force compensates static friction it equals the break-away force [66]

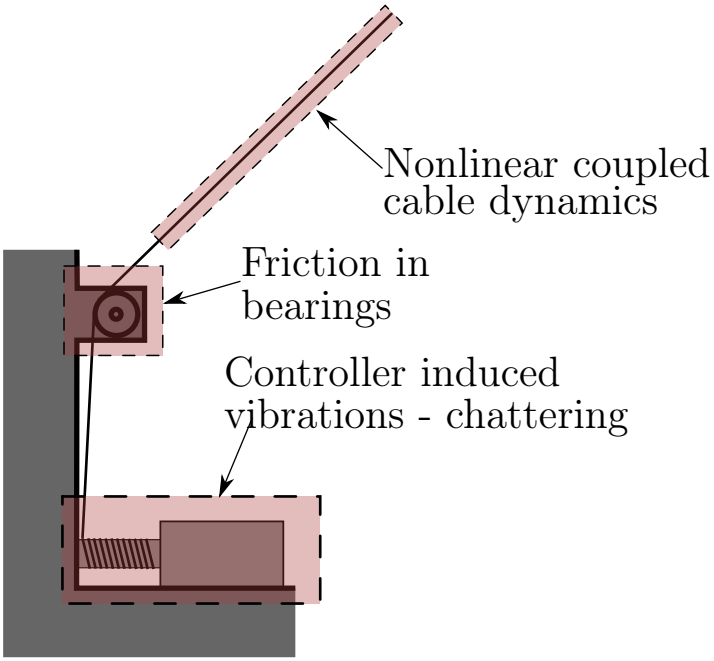

Figure 3.1: Mechanical components and contributors to vibrations

non-linearities, time-dependencies of lubrication, viscous and static friction with changing parameters. An alternative signum function accounts for a more realistic stiction model. In simulation the adaptive friction compensation is tasked to track a desired cable length under changing static and viscous friction and proves its efficiency. Many authors compensate vibrations by incorporating cable models in the dynamics of the entire system, using an inverted model to predict and counteract vibrations, or rely on appropriate control techniques. However, in some cases this strategy might not suffice due to uncertain parameters and time varying dynamics.

Robustness and high performance criteria on position, velocity and acceleration level put high demands on the control of a Cable-Driven Parallel Robot as a simulator. Sliding-Mode Control fulfil these requirements and thus, is chosen as High-Level Control.

Discontinuous function make classical Sliding-Mode Controllers robust, but also create chattering control inputs. The amplitude of chattering depends on the controller gains. High controller gains increase the amplitude of chattering and amplify noise, but also reduce errors and improve rejection of external disturbances (for high gain Sliding-Mode Controllers see for example [56, 31]). Low controller gains achieve the opposite. The adaptive Super-Twisting Sliding-Mode Controller, proposed in this work, adjusts the controller gains, to achieve both, reduced chattering and preservation of robustness and high tracking accuracy.

For evaluation in simulation the adaptive Super-Twisting Sliding-Mode Controller has to stear a redundant Cable-Driven Parallel Robot with six degrees of freedom and eight actuators along a predefined trajectory, while it is subject to perturbations A comparison between the proposed adaptive Super-Twisting Sliding-Mode Controller and a Terminal Sliding-Mode Controller, show the efficiency of the gain adaptation strategy. Cables are highly non-linear

and coupled systems and investigating sophisticated models, that account for all relevant effects, is of paramount importance. Port-Hamilton modelling provides a tool to derive such a model with a unified structure, that allows further analysis and model based controller synthesis. Thus, this chapter presents the Finite-Element Method based model of a Cable-Driven Parallel Robot in Port-Hamilton representation, which paves the way for Interconnection-Damping Assignment Passivity-Based Control design.

Additional sensors such as e.g. Inertial Measurement Units allow further investigations on cable dynamics and evaluation of the proposed controllers. Furthermore, fusion of multiple sensor input with a Dual Unscented Kalman-Filter improves the estimate of the platform pose, velocity and acceleration. At the same time, the dual Unscented Kalman-Filter compensates for Inertial Measurement Unit bias.

The following sections will give consideration to the problem of controller induced vibrations on all three layers of control and provide a sophisticated cable model.

3.1 First control layer - Low-Level Control

All developed controllers are implemented on the Mini Cablerobot Simulator, a redundant cable robot with six degrees of freedom and eight cables. Beckhoff Automation GmbH & Co. KG provides the drives and actuation units. Those come with a position/velocity torque joint-space cascade controller (see Figure 4.23). An external set-point generator computes a set of feasible cable positions, velocities and accelerations. Position control always implies active current and velocity control blocks whereas for velocity control only the current and velocity control block is active and the position control block is inactive. To improve the Low-Level Control performance TwinCAT allows tuning of the velocity controller via loop-shaping. TwinCAT is the motion control software, that allows operation of multiple Programmable Logic Controllers in real-time. For more details about the exact tuning procedure, check the online documentation of TwinCAT. The position and the torque controller does not require any further tuning. It is also worth to mention, that TwinCAT prioritizes running tasks in a priority list. To avoid high frequency vibrations the SAF and SVB[3] tasks must be set to higher priorities and have to run with higher sampling times, than all other tasks.

[3]SAF and SVB stands for 'Satz Ausführend' and SVB stands for 'Satz Vorbereitung'

3.2 Second control layer - Friction compensation and tension distribution

The second control layer compensates friction and adjusts the cable forces such that $\boldsymbol{f}$ stays in between a set of minimum and maximum cable forces, e.g. $\underline{\boldsymbol{f}}$ and $\overline{\boldsymbol{f}}$ or torques respectively. In position control, direct torque control is not possible. A mapping of desired cable forces to equivalent cable lengths in a virtual trajectory solves this problem and facilitates to track a desired trajectory $l_{i,des}$,$\dot{l}_{i,des}$ and $\ddot{l}_{i,des}$ using the virtual desired trajectory

$$l_{i,des,virt} = l_{i,des} + \delta_{i,TD} \tag{3.1}$$
$$\dot{l}_{i,des,virt} = \dot{l}_{i,des} + \dot{\delta}_{i,TD} \tag{3.2}$$
$$\ddot{l}_{i,des,virt} = \ddot{l}_{i,des} + \ddot{\delta}_{i,TD}\,. \tag{3.3}$$

A second virtual length $\delta_{i,FC}$ compensates for friction and extends the virtual desired cable lengths, velocities and accelerations to:

$$l_{i,des,virt} = l_{i,des} + \delta_{i,TD} + \delta_{i,FC} \tag{3.4}$$
$$\dot{l}_{i,des,virt} = \dot{l}_{i,des} + \dot{\delta}_{i,TD} + \dot{\delta}_{i,FC} \tag{3.5}$$
$$\ddot{l}_{i,des,virt} = \ddot{l}_{i,des} + \ddot{\delta}_{i,TD} + \ddot{\delta}_{i,FC}\,. \tag{3.6}$$

In [92] the author presents a PI controller-based tension adaptation with anti-wind-up, to adjust cable lengths according to the desired cable tensions provided by the tension distribution algorithm. The tension adaptation proposed there is simple, efficient and mature. Thus, this work focuses on the contribution of the proposed adaptive friction compensation algorithm and introduces briefly the closed-form solution from [12] for the tension distribution algorithm.

Friction in bearings, especially during start-stop phase of a motion, applies a jerk and ignites vibrations. Cables forward those vibrations to the platform. Participants perceive those as disturbances. Moreover, a sophisticated friction compensation and reduction improves systems performance and unburdens the High-Level Controller.

3.2.1 Friction and model based compensation

Friction itself occurs when two surfaces or layers in contact move relative to each other[4]. Many authors simplify friction to constant static and viscous friction, although friction is highly non-linear and complex [39]. Furthermore, abrasion in bearings lead to contamination of lubrication and changes the character of friction over time. In the light of this knowledge,

[4]Surfaces are related to solid materials, while layers are related to fluids

this thesis exploits the advantages of adaptive algorithms and a generic modelling approach, to handle all present effects of friction-based on encoder measurements only.At zero velocity the friction force oppose the driving force, which is applied to initiate motion. As soon as the driving force exceeds the break-away force[5], motion is induced. The standard signum function does not take the compensation of the driving force due to the friction force into account. Thus, the authors in [53] propose a new signum function. Equation (3.7) adopts the function structure of this new signum function with a physically more realistic form to provide a good tracking in slow motion or start-stop phases and uses the notation given for the drivetrain of a cablerobot:

$$\operatorname{sign}^{\star}(\bullet) = \begin{cases} 1 & \text{if } \dot{l} > 0 \text{ or } (\dot{l}(t) = 0 \text{ and } f_i(t) > k_{i,c}(t)) \\ -1 & \text{if } \dot{l} < 0 \text{ or } (\dot{l}(t) = 0 \text{ and } f_i(t) < k_{i,c}(t)) \\ \frac{f_{i,c}(t)}{k_{C_i}(t)} & \text{if } \dot{l} = 0 \text{ or } f_i(t) < k_{i,c}(t)) \end{cases} . \tag{3.7}$$

During start-stop phases Equation (3.7) represents better the characteristics of friction, than the standard signum function. Then the friction force reads
$f_{f_i}(\dot{l}_i(t), f_{c_i}(t), k_{c_i}(t)) = k_{c_i}(t) \operatorname{sign}^{\star}(\dot{l}(t), f_i(t), k_{c_i}(t))$, with a randomly time-varying parameter k_{c_i}.

This section evaluates the proposed algorithm in simulation based on the dynamic model

$$\ddot{l}(t) = f(\dot{l}(t), l(t), u(t)) = \frac{r_D}{i_{M_i}}(u_{C_i} - V_{f_i}(t)) - \frac{k_{M_i}}{i_{M_i}} l_i - \frac{f_{v_i}}{i_{M_i}} \dot{l}_i \tag{3.8}$$

$$\begin{bmatrix} \dot{l}_i \\ \ddot{l}_i \end{bmatrix} = \begin{bmatrix} 0 & 1 \\ -\frac{k_{M_i}}{i_{M_i}} & -\frac{f_{v_i}}{i_{M_i}} \end{bmatrix} \begin{bmatrix} l_i \\ \dot{l}_i \end{bmatrix} + \begin{bmatrix} 0 \\ \frac{r_D}{i_{M_i}} \end{bmatrix} (u_{c_i} - V_{f_i}(t)) \tag{3.9}$$

$$y = \begin{bmatrix} 1 & 0 \\ 0 & 1 \end{bmatrix} \begin{bmatrix} l_i \\ \dot{l}_i \end{bmatrix} , \tag{3.10}$$

which was also used in [64, 4, 91]. The control input $\boldsymbol{u}_{c,i}$ composes a pid control, feedforward inversion of the nominal model and the contribution of the friction compensation control according to

$$\begin{aligned} u_{c_i} &= f^{-1}(l_{des,i}(t), \dot{l}_{des,i}, \ddot{l}_{des,i}) + k_{p_i} e_i + k_{d_i} e_i \\ &+ k_i \int_0^t e_i \mathrm{d}t + \hat{k}_{c_i} \operatorname{sign}^{\star}(\dot{l}_i(t), f_i(t), k_{i,c}(t))_{c_i} , \end{aligned} \tag{3.11}$$

[5]The break-away force denotes a threshold force. A system start moving as soon as a driving force exceeds the break-away force

Table 3.1: Simulation parameters for friction compensation

$\lambda_{FC,1}$	$\lambda_{FC,2}$	k_{p_i}	k_{d_i}	k_{i_i}	$i_{m_i}\ [kgm^2]$	$f_{v_i}\ [Nm]$	ϵ_{FC}	$k_{M_i}N$
50	45	156.74	3.08	500	0.12	0.002	0.001	0.1

and changing static friction

$$V_{f_i}(t) = \begin{cases} 8\,\text{sign}^\star(\dot{l}_i(t), f_i(t), k_{c_i}(t)) & \text{if } t \leq 0.5s \\ 12\,\text{sign}^\star(\dot{l}_i(t), f_i(t), k_{c_i}(t)) & \text{if } 10.5s < t \leq 18s \\ 2\,\text{sign}^\star(\dot{l}_i(t), f_i(t), k_{c_i}(t)) & \text{if } t > 18s \end{cases}, \tag{3.12}$$

with viscous friction parameters $f_{v_i} \in \mathbb{R}$, motor inertia (see Table 3.1), $i_{M_i} \in \mathbb{R}$ and motor elasticity $k_{M_i} \in \mathbb{R}$. Goal is to follow a desired trajectory $l_{des,i}(t)$ and its derivative $\dot{l}_{des,i}(t)$ with unprecisely known system parameters $i_{M_i}, f_{Mv_i}, f_{Ms_i}, k_{M_i}$. The trajectory consists of two phases, e.g.: i) a phase with constant velocity and an abrupt changing point; ii) a sinusoidal trajectory with $1.5Hz$ and $0.8Hz$,i.e.:

$$l_{des,i} = \begin{cases} 0.25t & \text{if } t \leq 5s \\ -0.25(t - 10s) & \text{if } 5s < t \leq 0s \\ \sin(5(t - 10s)) & \text{if } 10s < t \leq 16.28s \\ \sin(10(t - 16.28s)) & \text{if } 16.28s < t \leq 25s\,, \end{cases} \tag{3.13}$$

with the inverted model $u(t) = f^{-1}(l_{des,i}(t), \dot{l}_{des,i}(t), \ddot{l}_{des,i}(t))$. The modified signum function and the gain adaptation law for one cable:

$$\text{sign}^\star = \begin{cases} 1 & \dot{l}_i > 0 \text{ or } (\dot{l}_i(t) = 0, f_i(t) > k_{i,c}(t)) \\ -1 & \dot{l}_i < 0 \text{ or } (\dot{l}_i(t) = 0, f_i(t) < k_{i,c}(t)) \\ 0 & \dot{l}_i = 0 \text{ or } f_i(t) = 0 \end{cases} \tag{3.14}$$

$$\dot{\hat{k}}_c(t) = \lambda_{FC,1}\,\text{sign}^\star(\bullet)\,[\dot{e}_{l_i}(t) + \lambda_{FC,2} e_{l_i}(t)]\,, \tag{3.15}$$

leads to an accurate tracking of the desired length $l_{des}(t)$ and its derivatives $\dot{l}_{des,i}(t)$, $\ddot{l}_{des,i}(t)$. The friction model based on the modified signum function (3.7) provides a realistic representation of the drivetrain dynamics. Static friction changes during the simulation, to model also changes due to abrasion in bearings and change of lubrication. Figure 3.2 shows the desired trajectory given by Equation (3.13) in blue and the current cable length with friction compensation including a PID-controller and feed forward control input in red. Disabling friction compensation spares PID-control and feed forward control, and results in the trend shown in green. Figures 3.3-3.6 zoom at the critical points during start-stop phases and sinusoidal trajectory. Analysing the reaction of the system with and without friction compensation reveal the following interesting insights:

- **Figure 3.3**: The friction compensation algorithm reacts immediately and compensates stiction and viscous friction, whereas, the uncompensated system starts moving with a delay since f_i did not oppose static friction and the PID-controller compensates slowly for the offset between the desired and the actual length. The system initiates motion, only when the driving force u_{c_i} excels the friction force $f_{s_i}\,\mathrm{sign}(l_i)$.

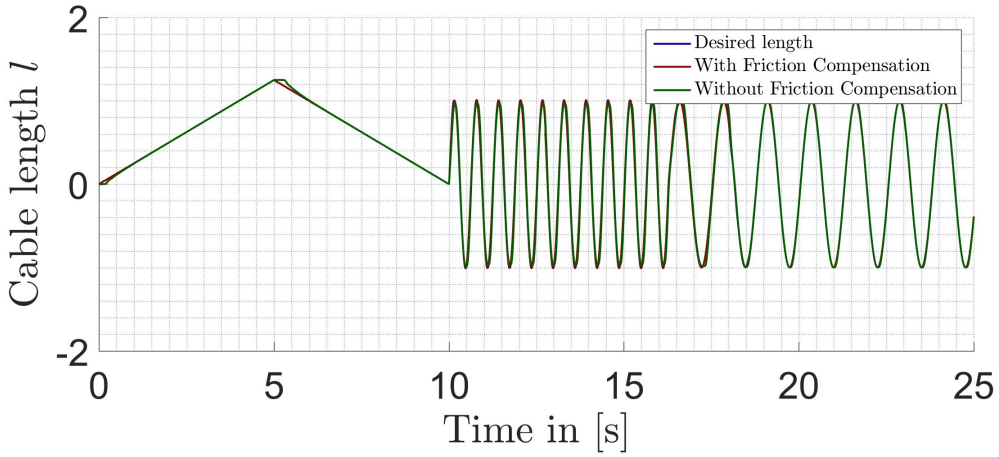

Figure 3.2: Entire simulation

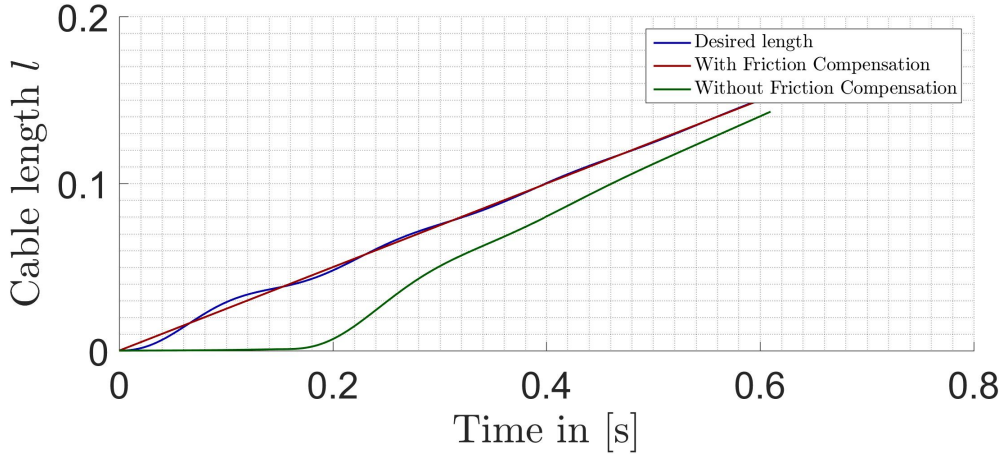

Figure 3.3: Start with transition

- **Figure 3.4**: At the turning point when $\dot{l}_i$ changes abruptly sign, the friction compensation algorithm shows the same behaviour as at the start of the simulation. Again the algorithm reacts immediately to the change of direction. On the contrary, without friction compensation the system reaches a plateau and stops moving when the velocity of the desired trajectory changes sign. As soon as the driving force excels the friction force, the system initiates again motion.

- **Figure 3.5 and 3.6**: The friction compensation algorithm slightly overshoots before the sinusoidal trajectory approaches a turning point. With friction compensation the absolute error is only 15% of the error without friction compensation (see Figure 3.7). And again the uncompensated system reaches a plateau since the friction force counteracts the driving force and inhibits motion. The compensated and the uncompensated

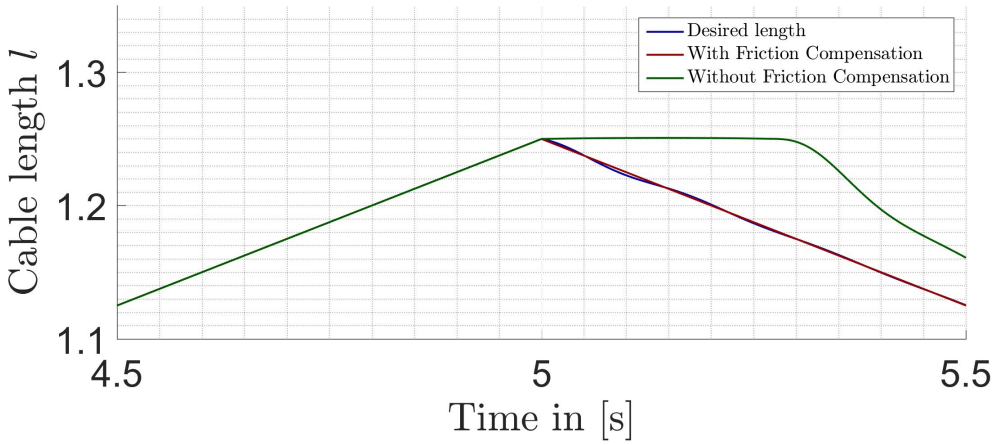

Figure 3.4: Turn point with abrupt velocity change

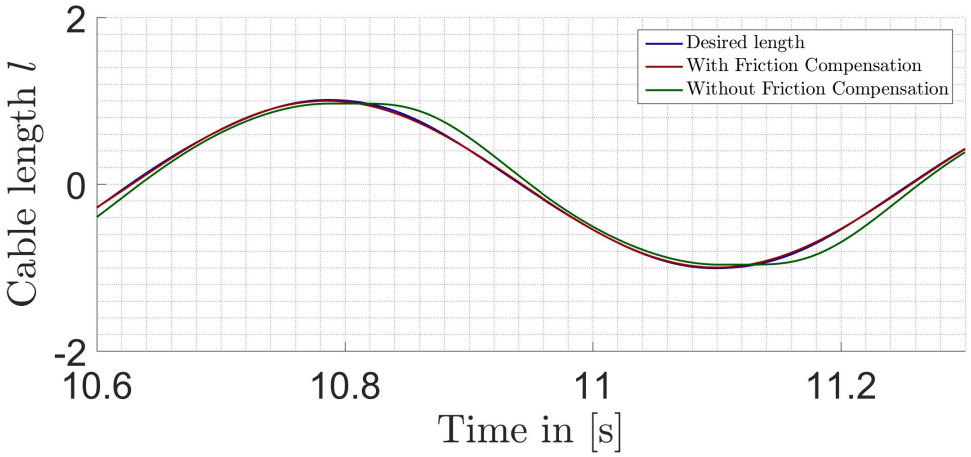

Figure 3.5: Sinusoidal trajectory with $1.5Hz$

system respond similar when the frequency of the desired sinusoidal trajectory decreases to 0.8Hz since viscous friction in Equation (3.12) also reduces from $12\,\mathrm{sign}^\star$ to $2\,\mathrm{sign}^\star$. Here, with friction compensation the error reduces to 20% of the error without friction compensation

The friction compensation algorithm proposed in the previous subsection is a composite controller that includes a PID-controller for position and velocity tracking, a feed forward component, based on an inverted nominal model of the drivetrain and an adaptive friction compensating component. In simulation the controller successfully tracks a desired trajectory in position and velocity in spite of changed model parameters and changing static friction, and thus reduces efficiently friction induced vibrations.

Tension distribution algorithm

Cables transmit forces from the actuators to the platform. Since cable can not push, but only pull, positive cable forces are mandatory over the entire trajectory of motion. Besides, the solutions have to be continuous [86]. Tension distribution algorithms finds a feasible

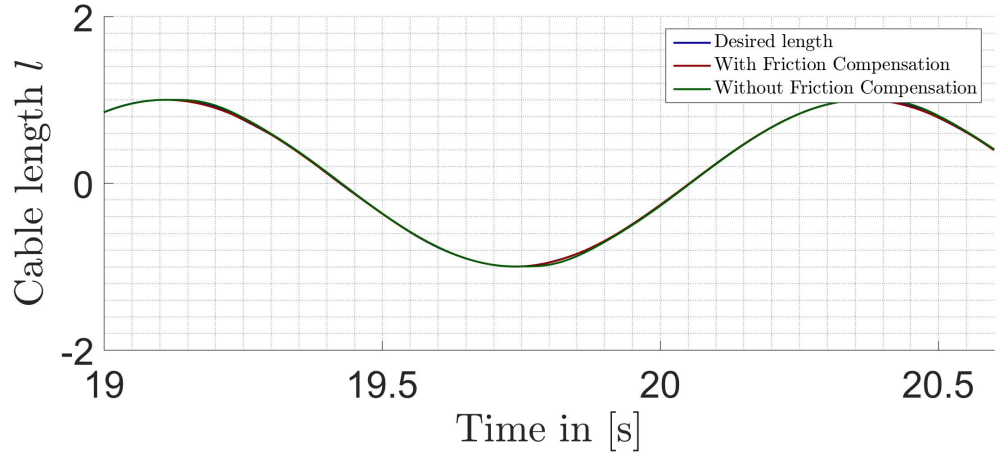

Figure 3.6: Sinusoidal trajectory with $0.8Hz$

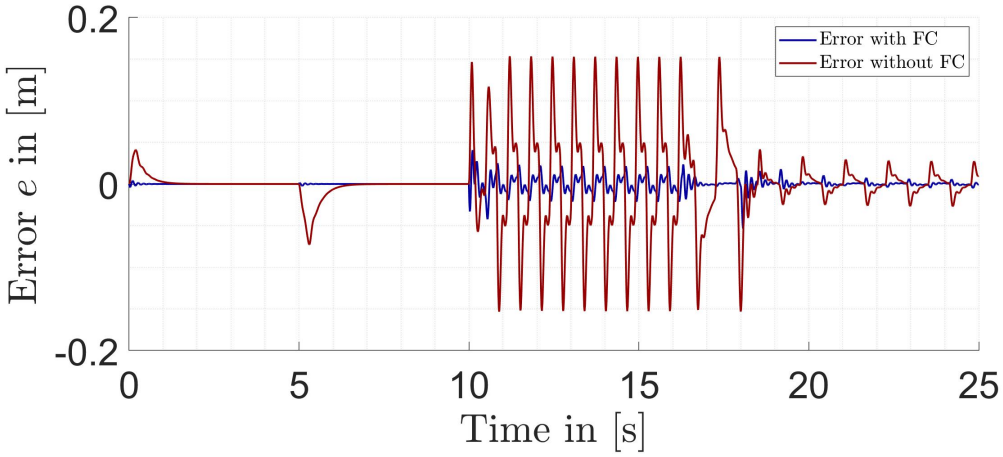

Figure 3.7: Error with and without adaptive friction compensation

set of cable forces, possibly satisfying some optimality criterion. A set of cable forces corresponding to a feasible wrench and a pose inside the Wrench-Feasible Workspace is feasible when all its components lay between minimal and maximal tension values $\underline{f}$ and $\overline{f}$ [3]. Besides, an implemented tension distribution algorithm needs to be real-time capable. Over time, researchers provided different solutions for the problem of finding a feasible set of cable forces based on: i) a closed-form solution [12]; ii) Interval analysis and iii) gradient based optimizers. The authors in [86] give an overview over those approaches. Additionaly there exist approaches based on linear programming [95], quadratic programming [3], Dykstras projection algorithm [61], puncture method, barycentric force distribution method and weighted sums of vertices. The book about Theory and Application of Cable-Driven Parallel Robots [10] gives a good overview over the computational efficiency and explains the principles of all mentioned force distributions algorithm.

Remark 3.1: The authors in [86, 12] adjust the cable forces such that they are close to the mediate value f_{m_i} of minimum and maximum cable forces f_{min_i} and f_{max_i} respectively In [12] the author proves the existence and uniqueness of the closed-form solution. Cable tension can also adapt to lower f_{low} or to higher f_{high}

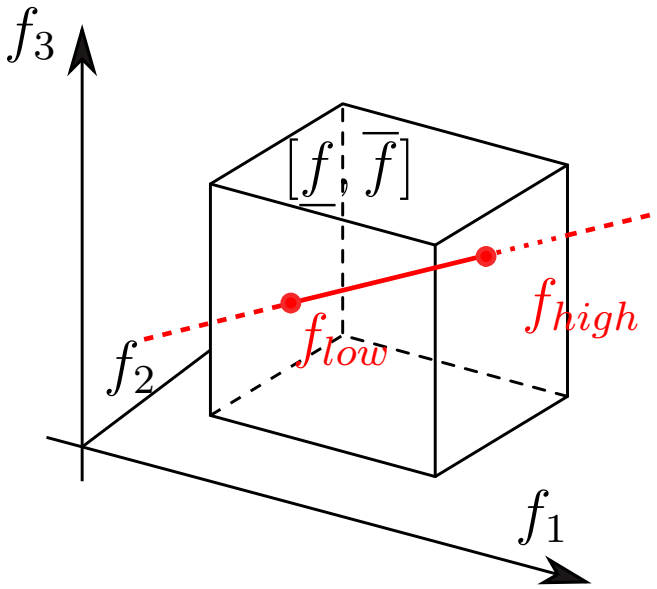

Figure 3.8: Shifting of cable tension reference point

values as long as they are inside this set of feasible cable forces $[\underline{f}, \overline{f}]$ (see for instance [75]). Lower cable forces reduce power consumption, higher values improve the systems stiffness. Mediate cable forces are beneficial for robustness against uncertain parameters and for safety [86]. Figure 3.8 illustrates this, based on a system with three cables.

In [12] the authors present a closed-form force distribution, that split the desired force vector $\boldsymbol{f}_{des}$ in the mean feasible force vector $\boldsymbol{f}_m$ and an additional force vector $\boldsymbol{f}_{null}$ and derive a solution of feasible cable forces:

$$\boldsymbol{f} = \boldsymbol{f}_m - \boldsymbol{J}(\boldsymbol{J}^{\mathrm{T}}\boldsymbol{J})^{-1}(\boldsymbol{w}_P + J^{\mathrm{T}}\boldsymbol{f}_m)\,. \tag{3.16}$$

The tension distribution algorithm will find a feasible set of cable forces, as long as a solution inside a m dimensional sphere -that is defined by the minimum and maximum cable forces- exist. The authors show that $\boldsymbol{f}$ is continues along a trajectory. The experiments, conducted for evaluation of the proposed High-Level Control used this closed-form solution, to compute feasible cable tensions. Besides Equation (3.16) provides an explicit solution for $\boldsymbol{f}$ and is real-time capable.

As a minimization problem the goal of finding a set of feasible cable forces is as follows:

$$\begin{aligned} \min \|\boldsymbol{f}\|_p &= \sqrt{\sum_{i=1}^{m} f_i^2} \\ \text{subject to } f_{min} &\leq f_i \leq f_{max} \\ w_j &= -\sum_{i=1}^{m} \boldsymbol{J}_{j,i}^{\mathrm{T}} f_i \end{aligned}$$

Matlab provides algorithms (for instance fmincon, lsqnonlin) to solve this classical constrained minimization problem. However, those algorithms find a solution iteratively and are not optimized for real-time capability.

Torque control offers the advantage of having direct access to the dimensions of interest, that are accelerations. This way we can command the desired forces, provided by the tension distribution algorithm directly to the drives, without taking the circumvent of additional computation for positions and velocities. On the other hand we can not exploit the properties of the cascade position and velocity control, which has already been tuned to full fill high requirements in precision and performance.

In position control, the external set-point generator in TwinCAT requires a desired position, velocity and acceleration. Thus, one must find an interpretation of desired torques as virtual cable lengths $\boldsymbol{\delta}_{virt,TD}$, cable velocities $\dot{\boldsymbol{\delta}}_{virt,TD}$ and cable accelerations $\ddot{\boldsymbol{\delta}}_{virt,TD}$. Concluding the task to find a set of feasible cable forces as virtual cable lengths, consists of three parts, e.g.: i) Map a wrench $\boldsymbol{w}_P$ to a set of feasible cable forces; ii) Adjust the cable lengths in such a way, that the current cable forces match the desired feasible cable forces and iii) Compute the corresponding cable velocities and accelerations by a differentiator.

3.3 Third control layer - High-level control, Adaptive Super-Twisting Sliding-Mode Control

The proposed tracking controller is an adaptive Super-Twisting Sliding-Mode controller with a feed forward control input i.e. the inverted nominal model of a Cable-Driven Parallel Robot. The model does only include the platform dynamics and does not consider cable dynamics. As Section 3.5 will show, the attempt to include cable dynamics in the dynamics of a Cable-Driven Parallel Robot is even under some simplifications a challenging task. Thus, this section abandons the cable dynamics and focus on position, velocity, acceleration tracking of the platform and disturbance compensation/rejection.

3.3.1 Model of a Cable-Driven Parallel Robot for an adaptive Super-Twisting Sliding-Mode Controller

Assuming massless and inelastic cables as well as a center of mass of the platform that differs from the geometrical center, denoted by $\boldsymbol{c}_P \in \mathbb{R}^{3\times 1}$, simplifies the model to

$$\boldsymbol{B}(\boldsymbol{x})\ddot{\boldsymbol{x}} + \boldsymbol{C}(\boldsymbol{x},\dot{\boldsymbol{x}})\dot{\boldsymbol{x}} - \boldsymbol{g}(\boldsymbol{x}) = \boldsymbol{u} = -\boldsymbol{J}^{\mathrm{T}}\boldsymbol{t}\ , \tag{3.17}$$

with the second state derivative $\ddot{\boldsymbol{x}} = [\ddot{\boldsymbol{r}}^{\mathrm{T}}\ \dot{\boldsymbol{\omega}}^{\mathrm{T}}]^{\mathrm{T}}$, the control input as a wrench $\boldsymbol{u} \in \mathbb{R}^{6\times 1}$ or cable forces $\boldsymbol{f} \in \mathbb{R}^{8\times 1}$. The remaining matrices $\boldsymbol{B}(\boldsymbol{x})$, $\boldsymbol{C}(\boldsymbol{x}, \dot{\boldsymbol{x}})$ and $\boldsymbol{g}(\boldsymbol{x})$ are given according to Equation (2.28-2.32). The inverted nominal model for feed forward control requires invertibility of $\boldsymbol{B}(\boldsymbol{x})$ at any time, which is given since the inertia matrix is positive definite, symmetric and thus invertible [84].

Note that $\frac{\mathrm{d}}{\mathrm{d}t}\boldsymbol{x} = [\boldsymbol{r}^{\mathrm{T}}\,\boldsymbol{\nu}^{\mathrm{T}}]^{\mathrm{T}} \neq [\dot{\boldsymbol{r}}^{\mathrm{T}}\,\boldsymbol{\omega}^{\mathrm{T}}]^{\mathrm{T}}$, because Euler-rates $\dot{\boldsymbol{\nu}}$ are not angular velocities $\boldsymbol{\omega}$ such that a change to regular form is necessary. The transformation matrix (2.9) changes from angular velocities to Euler-rates. With the new state $\bar{\boldsymbol{x}} = [\boldsymbol{x}_{\boldsymbol{\nu}}^{\mathrm{T}}\,\dot{\boldsymbol{x}}^{\mathrm{T}}]^{\mathrm{T}} = [\boldsymbol{r}^{\mathrm{T}}\,\boldsymbol{\nu}^{\mathrm{T}}\,\dot{\boldsymbol{r}}^{\mathrm{T}}\,\boldsymbol{\omega}^{\mathrm{T}}]^{\mathrm{T}}$ the system dynamics without lumped[6] perturbations $\boldsymbol{\xi}$ reads:

$$\dot{\bar{\boldsymbol{x}}} = \begin{bmatrix} \dot{\boldsymbol{r}} \\ {}^{\nu}\boldsymbol{E}_{\boldsymbol{\omega}}(\boldsymbol{\nu})\,\boldsymbol{\omega} \\ -\boldsymbol{B}(\boldsymbol{x}_{\boldsymbol{\nu}})^{-1}(\boldsymbol{C}(\boldsymbol{x}_{\boldsymbol{\nu}}, \dot{\boldsymbol{x}})\dot{\boldsymbol{x}} - \boldsymbol{g}(\boldsymbol{x}_{\boldsymbol{\nu}})) \end{bmatrix} + \begin{bmatrix} 0_{3\times n} \\ 0_{3\times n} \\ \boldsymbol{B}^{-1} \end{bmatrix} \boldsymbol{u} \tag{3.18}$$

$$\boldsymbol{y} = \begin{bmatrix} \boldsymbol{r} \\ \boldsymbol{\nu} \end{bmatrix}, \tag{3.19}$$

where $\boldsymbol{y}$ is the output vector and ${}^{\nu}\boldsymbol{E}_{\boldsymbol{\omega}}(\boldsymbol{\nu})$ is the transformation matrix. The relative degree for all entries of $\boldsymbol{x}$ equals 2 and the total relative degree equals 12. Thus an exact feedback linearisation of the system exists, using the diffeomorphism $\boldsymbol{\Phi}(\bar{\boldsymbol{x}})$ [43]. With the change of coordinates

$$\boldsymbol{z} = \begin{bmatrix} \boldsymbol{z}_1 \\ \boldsymbol{z}_2 \end{bmatrix} = \boldsymbol{\Phi}(\bar{\boldsymbol{x}}) = \begin{bmatrix} \boldsymbol{I}_{6\times 6} & \boldsymbol{0}_{6\times 6} \\ \boldsymbol{0}_{6\times 6} & \underbrace{\begin{bmatrix} \boldsymbol{I}_{3\times 3} & \boldsymbol{0}_{3\times 3} \\ \boldsymbol{0}_{3\times 3} & {}^{\nu}\boldsymbol{E}_{\boldsymbol{\omega}}(\boldsymbol{\nu}) \end{bmatrix}}_{\boldsymbol{A}(\boldsymbol{x}_{\boldsymbol{\nu}})} \end{bmatrix} \begin{bmatrix} \boldsymbol{x}_{\boldsymbol{\nu}} \\ \dot{\boldsymbol{x}} \end{bmatrix} \tag{3.20}$$

Equation (3.17) becomes:

$$\dot{\boldsymbol{z}}_1 = \boldsymbol{z}_2 \tag{3.21}$$

$$\dot{\boldsymbol{z}}_2 = \boldsymbol{f}(\bar{\boldsymbol{x}}) + \boldsymbol{h}(\bar{\boldsymbol{x}})\boldsymbol{u}\,, \tag{3.22}$$

with:

$$\boldsymbol{f}(\bar{\boldsymbol{x}}) = -\boldsymbol{A}(\boldsymbol{x}_{\boldsymbol{\nu}})\boldsymbol{B}^{-1}(\boldsymbol{x}_{\boldsymbol{\nu}})\left[\boldsymbol{C}(\boldsymbol{x}_{\boldsymbol{\nu}}, \dot{\boldsymbol{x}})\dot{\boldsymbol{x}} - \boldsymbol{g}(\boldsymbol{x}_{\boldsymbol{\nu}})\right] \tag{3.23}$$

$$+\dot{\boldsymbol{A}}(\boldsymbol{x}_{\boldsymbol{\nu}}, \dot{\boldsymbol{x}})\dot{\boldsymbol{x}} \tag{3.24}$$

$$\boldsymbol{h}(\bar{\boldsymbol{x}}) = \boldsymbol{A}(\boldsymbol{x}_{\boldsymbol{\nu}})\boldsymbol{B}^{-1}(\boldsymbol{x}_{\boldsymbol{\nu}})\,. \tag{3.25}$$

[6] The term lumped perturbations include unmodelled dynamics, parameter uncertainties, measurement noise and external disturbances

In practice the platform will never pitch more than $\pm 90°$ or in radians $\pm \pi/2$. Thus a valid assumption is to constraint θ_P to $\theta_P \in (-\pi/2, \pi/2)$. Constraining the pitch angle avoids singularities and assures that $\boldsymbol{h}(\bar{\boldsymbol{x}})$ is invertible.

Equation (3.23) assumes the absence of internal and external disturbances. In reality parameter uncertainties and external disturbances are present. Considering parameter uncertainties $\Delta \boldsymbol{f}$, measurement noise $\Delta \boldsymbol{h}$ and external disturbances $\boldsymbol{\zeta}$ extends the dynamic model (3.17) to:

$$\boldsymbol{B}(\boldsymbol{x}_{\boldsymbol{\nu}})\ddot{\boldsymbol{x}} + \boldsymbol{C}(\boldsymbol{x}_{\boldsymbol{\nu}}, \dot{\boldsymbol{x}})\dot{\boldsymbol{x}} - \boldsymbol{g}(\boldsymbol{x}_{\boldsymbol{\nu}}) = \boldsymbol{u} + \boldsymbol{\xi}\,, \tag{3.26}$$

with the vector of lumped perturbations $\boldsymbol{\xi} = \boldsymbol{h}_n\boldsymbol{\zeta} + \Delta \boldsymbol{f} + \Delta \boldsymbol{h}(\boldsymbol{u} + \boldsymbol{\zeta})$. Thus Equation (3.23) also has to change to:

$$\begin{aligned} \dot{\boldsymbol{z}}_1 &= \boldsymbol{z}_2 && (3.27)\\ \dot{\boldsymbol{z}}_2 &= \boldsymbol{f}_n + \Delta \boldsymbol{f} + \boldsymbol{h}_n\left(\boldsymbol{u} + \boldsymbol{\zeta}\right) + \Delta \boldsymbol{h}\left(\boldsymbol{u} + \boldsymbol{\zeta}\right) \\ &= \boldsymbol{f}_n + \boldsymbol{h}_n\boldsymbol{u} + \boldsymbol{\xi}\,, && (3.28) \end{aligned}$$

with the parametric uncertainties $\Delta \boldsymbol{f}$ and measurement noise $\Delta \boldsymbol{h}$. The kinematic parameters do not change significantly after their calibration, whereas the dynamic parameters, i.e.: mass, mass distribution and inertia might change from experiment to experiment due to the change of required equipment. The adaptive Super-Twisting Sliding-Mode Controller is the preferred choice to fulfil the task of letting the platform follow a desired trajectory in position and orientation $\boldsymbol{z}_{1,d} = [\boldsymbol{r}_d^{\mathrm{T}}\ \boldsymbol{\nu}_d^{\mathrm{T}}]^{\mathrm{T}} \in SE(3)$ as well as their time derivatives $\boldsymbol{z}_{2,d} = [\dot{\boldsymbol{r}}_d^{\mathrm{T}}\ \dot{\boldsymbol{\nu}}_d^{\mathrm{T}}]^{\mathrm{T}}$ and $\dot{\boldsymbol{z}}_{2,d} = [\ddot{\boldsymbol{r}}_d^{\mathrm{T}}\ \ddot{\boldsymbol{\nu}}_d^{\mathrm{T}}]^{\mathrm{T}}$ in Euler-rates in presence of lumped disturbances with unknown limit. In the sequel the full state $\boldsymbol{z}$ is available. This is true, since the forward kinematics reconstructs $\boldsymbol{z}$. The adaptive Super-Twisting Sliding-Mode Controller also requires $\boldsymbol{z}_2$ and $\dot{\boldsymbol{z}}_2$ which an arbitrary order sliding-mode differentiator provides.

3.3.2 Arbitrary order Sliding-Mode Differentiator

The arbitrary order Sliding-Mode Differentiator proposed in this work, estimates the platform pose, its derivatives, and exploits the properties of a Super-Twisting Sliding-Mode Controller, i.e.: Finite-time convergence of the estimated state $\hat{\boldsymbol{x}} \in \mathbb{R}^{6\times 1}$ to the actual state $\boldsymbol{x} \in \mathbb{R}^{6\times 1}$, robustness and asymptotic stability. Equation (3.29) has the typical structure of

a Super-Twisting Sliding-Mode Controller

$$\begin{cases} \dot{\hat{\boldsymbol{f}}}_0 = \boldsymbol{v}_0 & , \ \boldsymbol{v}_0 - \dot{\hat{\boldsymbol{f}}}_1 = -\lambda_{SMD,k} L^{k/k+1} \operatorname{sign}(\hat{\boldsymbol{f}}_0 - \boldsymbol{f}_0) + \hat{\boldsymbol{f}}_1 \\ \dot{\hat{\boldsymbol{f}}}_1 = \boldsymbol{v}_1 & , \ \boldsymbol{v}_1 - \dot{\hat{\boldsymbol{f}}}_2 = -\lambda_{SMD,k-1} L^{k-1/k} \operatorname{sign}(\hat{\boldsymbol{f}}_1 - \boldsymbol{v}_0) + \hat{\boldsymbol{f}}_2 \\ & \vdots \\ \dot{\hat{\boldsymbol{f}}}_{k-1} = \boldsymbol{v}_{k-1} & , \ \boldsymbol{v}_{k-1} - \dot{\hat{\boldsymbol{f}}}_{k-1} = -\lambda_{SMD,1} L^{1/2} \operatorname{sign}(\hat{\boldsymbol{f}}_{k-1} - \boldsymbol{v}_{k-2}) + \hat{\boldsymbol{f}}_k \\ \dot{\hat{\boldsymbol{f}}}_k = -\lambda_{SMD,k} & L \operatorname{sign}(\hat{\boldsymbol{f}}_k - \boldsymbol{v}_{k-1}) \end{cases} . \tag{3.29}$$

After adjusting the Lipschitz constant $L > 0$ for the last derivative to be estimated and the differentiator parameters $\lambda_{SMD,i}$ with $i = 1 \dots n_a$, the Sliding-Mode Differentiator guarantees exact tracking of $f_0(t)$ in absence of input noise. In presence of Lebesgue-measurable noise [99] the Sliding-Mode Differentiator guarantees good matching of the estimate $\hat{\boldsymbol{f}}_0$ and $\boldsymbol{f}_0$. The combination of an arbitrary-order robust exact Sliding-Mode Differentiator , forward kinematics and adaptive Super-Twisting Sliding-Mode Controller, guarantees convergence in finite-time of $\dot{\boldsymbol{\sigma}}$ and $\boldsymbol{\sigma}$ to the sliding surface, reduced chattering and vibrations, and relies on encoder measurements only as the bare minimum of measurement inputs.

3.3.3 Adaptive Super-Twisting Sliding-Mode Controller

The tracking controller is a composition of a feedforward control input $\boldsymbol{u}_{FF} \in \mathbb{R}^{6\times 1}$ based on the inversion of the nominal model (3.21-3.25) and a Sliding-Mode Controller input $\boldsymbol{u}_{SMC} \in \mathbb{R}^{6\times 1}$ i.e.:

$$\boldsymbol{u} = \boldsymbol{u}_{SMC} + \boldsymbol{u}_{FF} \, . \tag{3.30}$$

Using the simple relation $\boldsymbol{u} = -\boldsymbol{J}^{\mathrm{T}} \boldsymbol{f}$ and one of the tension distribution algorithms from above facilitates to compute the vector of desired cable forces $\boldsymbol{f}$. The goal of letting the platform follow a desired trajectory and its derivates equals to steer the tracking errors $\dot{\boldsymbol{e}} = \boldsymbol{z}_2 - \boldsymbol{z}_{2,d}$ and $\boldsymbol{e} = \boldsymbol{z}_1 - \boldsymbol{z}_{1,d}$ and the chosen sliding variable

$$\boldsymbol{\sigma} = \dot{\boldsymbol{e}} + \boldsymbol{\Lambda}_{SMC} \boldsymbol{e} \tag{3.31}$$

to zero. Again $\boldsymbol{\Lambda}_{SMC}$ is a positive definite diagonal matrix. The relative degree of $\boldsymbol{\sigma}$ is one since:

$$\boldsymbol{\sigma} = \dot{\boldsymbol{e}} + \boldsymbol{\Lambda} \boldsymbol{e} \tag{3.32}$$

$$\dot{\boldsymbol{\sigma}} = \boldsymbol{f}(\boldsymbol{z}) - \dot{\boldsymbol{z}}_{2,d} + \boldsymbol{\Lambda}(\boldsymbol{z}_2 - \boldsymbol{z}_{2,d}) + \boldsymbol{h}(\boldsymbol{z}) \boldsymbol{u} \tag{3.33}$$

This is an interesting feature of a Super-Twisting Sliding-Mode Controller. The Super-Twisting Sliding-Mode Controller drives the first time derivative of $\boldsymbol{\sigma}$ to zero and achieves tracking on acceleration level which is the second derivative of the desired trajectory, thus comes with reduced order dynamics

Adaptive Super-Twisting Sliding-Mode controller input $\boldsymbol{u}_{STC}$

The Super-Twisting Sliding-Mode Controller has the following two important properties: i) Due to the integration of the sign-function and the multiplication with $|\boldsymbol{\sigma}|^{1/2}$ the control input is continuous, thus reduces chattering ii) The adaptive Super-Twisting Sliding-Mode Controllers task is to compensate for lumped perturbations $\boldsymbol{\xi}$, that are not covered by the feedforward control input. The lumped perturbations $\boldsymbol{\xi}$ are bounded, but the upper bound is unknown. With constant controller gains, this leads to conservatively high controller gains, which are responsible for chattering, noise amplification and aggressive control actions. An upper bound ξ_{max} is often unknown, which makes controller gains adaptation useful. Thanks to the gain adaptation algorithm (3.34), the controller gains stay as low as possible and increase as much as necessary, to compensate $\boldsymbol{\xi}$ with unknown limits ξ_{max} and reduce chattering. The High-Level Control copes with lumped perturbations with unknown limits, i.e. $\|\boldsymbol{\xi}\|_2 \leq \xi_{max}$ and $\xi_{max} \geq 0$. Gain adaptation combines the advantages of high controller gains and low controller gains. Those are:

- **Low controller gains:** Reduced energy consumption, mechanical stress, noise amplification and chattering;

- **High controller gains:** High bandwidth, better compensation of perturbations

The gain adaptation law

$$\begin{aligned} \dot{\boldsymbol{\Lambda}}_1 &= \begin{cases} \boldsymbol{\Omega}_{\boldsymbol{\Lambda}} \operatorname{sign}\left(|\boldsymbol{\sigma}| - \boldsymbol{\mu}\right), & \text{if } \boldsymbol{\Lambda}_1 > \boldsymbol{\Lambda}_{1,m} \\ \boldsymbol{\eta}, & \text{if } \boldsymbol{\Lambda}_1 \leq \boldsymbol{\Lambda}_{1,m} \end{cases} \\ \boldsymbol{\Lambda}_2 &= 2\,\epsilon_{STC}\,\boldsymbol{\Lambda}_1 \\ \boldsymbol{\mu} &= 4\,\boldsymbol{\Lambda}_1\,T_e\,, \end{aligned} \tag{3.34}$$

originally stems from [101, 100]. Here $\boldsymbol{\Omega}_{\boldsymbol{\Lambda}} \in \mathbb{R}^{6\times6}$, $\boldsymbol{\Lambda}_{1,m} \in \mathbb{R}^{6\times6}$ and $\boldsymbol{\Lambda} \in \mathbb{R}^{6\times6}$ denote three positive definite diagonal matrices, $\epsilon_{SMC} \in \mathbb{R}^+$ is a positive tuning parameter and $T_e \in \mathbb{R}$ is the sampling time. The adaptive Super-Twisting Sliding-Mode Controller with gain adaptation (3.34) achieves $\|\boldsymbol{\sigma}\| \leq \boldsymbol{\mu}_1$ and $\|\dot{\boldsymbol{\sigma}}\| \leq \boldsymbol{\mu}_2$ with $\boldsymbol{\mu}_1 \geq \boldsymbol{\mu}$ and $\boldsymbol{\mu}_2 > \mathbf{0}$ in finite-time. Here $\boldsymbol{\mu}$ is a sensitivity factor. The higher $\boldsymbol{\mu}$, the more tolerant the controller is for errors.

Tuning $\boldsymbol{\mu}$ is not an easy task. Too high values reduce accuracy of the adaptive Super-Twisting Sliding-Mode Controller and inhibit to fulfil desired performance criteria, whereas too low values let $\boldsymbol{\Lambda}_1$ and $\boldsymbol{\Lambda}_2$ increase limitless and destabilize the system [33].

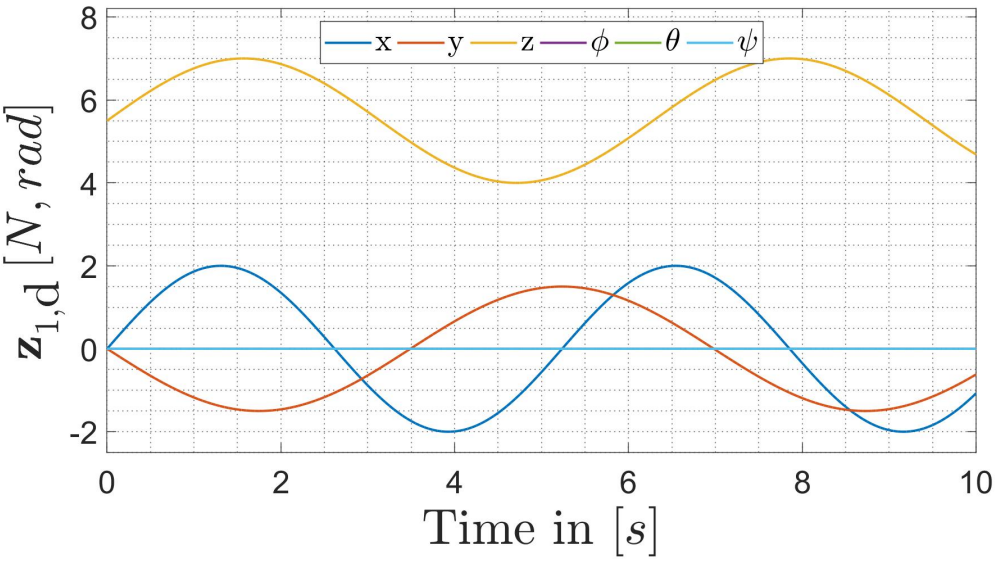

Figure 3.9: Desired trajectory for simulative evaluation of the adaptive Super-Twisting Sliding-Mode Controller

Feed forward control input $\boldsymbol{u}_{FF}$

The feedforward control input

$$\boldsymbol{u}_{FF} = \boldsymbol{b}_n^{-1} \left(\dot{\boldsymbol{z}}_{2,d} - \boldsymbol{a}_n \right) \ . \tag{3.35}$$

incorporates the nominal dynamic model of the system (3.21)-(3.22) and in theory should steer the platform along the desired trajectory in absence of uncertainties and disturbances.

Simulative evaluation of the adaptive Super-Twisting Sliding-Mode Controller

This section evaluates the adaptive Super-Twisting Sliding-Mode Controller in simulation. Task is, to let the end-effector follow a desired trajectory $\boldsymbol{z}_{1,d}$ (see Figure 3.9), its derivatives $\boldsymbol{z}_{2,d}$ and $\dot{\boldsymbol{z}}_{2,d}$ in presence of lumped perturbations $\boldsymbol{\xi}$ (see Figure 3.10). A comparison between the proposed adaptive Super-Twisting Sliding-Mode Controller with gain adaptation and a Terminal Sliding-Mode Controller [31] highlights the advantages of the proposed gain adaptation algorithm. A comparison of the adaptive Super-Twisting Sliding-Mode Controller and the Terminal Sliding-Mode Controller requires a common benchmark criteria. In this evaluation both controllers were tuned to achieve stability and to minimize $\boldsymbol{e}$ and $\dot{\boldsymbol{e}}$, disregarding chattering. Tuning the controllers result in the parameter set, shown in Table 3.3. Assuming deviations of the nominal model parameters $\boldsymbol{c}$,m_P and $\boldsymbol{I}_P$ from the actual values, gives consideration to the parameter uncertainties. Table 3.2 lists the nominal and actual dynamic and kinematic parameters of the simulated Cable-Driven Parallel Robot. Nominal values are denoted with an index n.

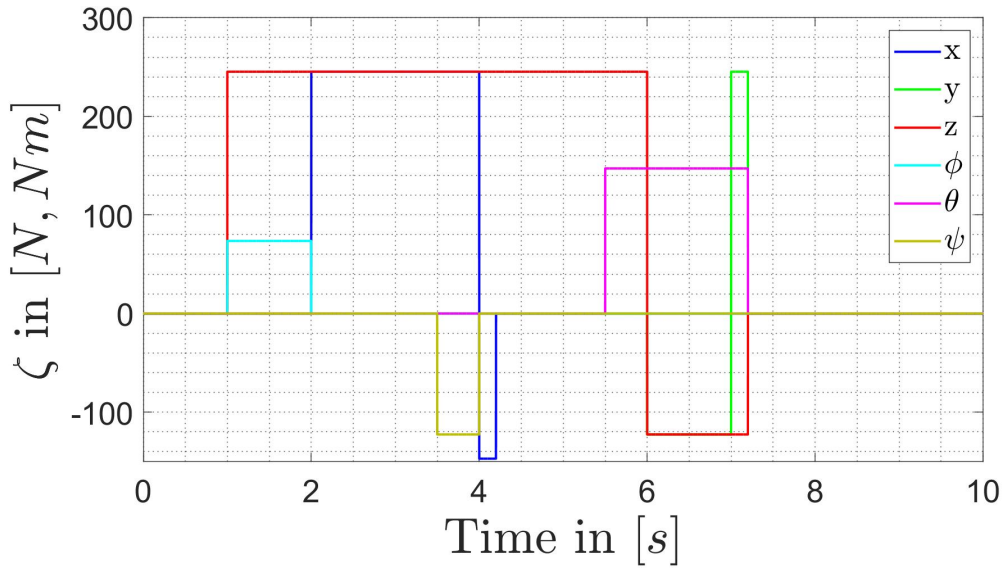

Figure 3.10: External disturbances for simulative evaluation of the adaptive Super-Twisting Sliding-Mode Controller

Table 3.2: Kinematic and dynamic parameters

Kinematic Parameters									**Dynamic Parameters**		
		x	y	z		x	y	z			
$\boldsymbol{a}_1$	$[m]$	5	5	10	$\boldsymbol{b}_1$ $[m]$	-0.5	0.4	0	m_n	$[kg]$	50
$\boldsymbol{a}_2$	$[m]$	5	5	1	$\boldsymbol{b}_2$ $[m]$	0	0.5	-0.4	$\boldsymbol{c}_n$	$[m]$	$\mathbf{0}$
$\boldsymbol{a}_3$	$[m]$	5	-5	10	$\boldsymbol{b}_3$ $[m]$	-0.5	-0.4	0	${}^P\boldsymbol{I}_{P,n}$	$[kgm^2]$	diag$\{[50, 50, 50]\}$
$\boldsymbol{a}_4$	$[m]$	5	-5	1	$\boldsymbol{b}_4$ $[m]$	0	-0.5	-0.4	m	$[kg]$	40
$\boldsymbol{a}_5$	$[m]$	-5	5	10	$\boldsymbol{b}_5$ $[m]$	0	0.5	0.4	$\boldsymbol{c}$	$[m]$	$\mathbf{0}$
$\boldsymbol{a}_6$	$[m]$	-5	5	1	$\boldsymbol{b}_6$ $[m]$	0.5	0.4	-0	${}^P\boldsymbol{I}_P$	$[kgm^2]$	diag$\{[40, 40, 40]\}$
$\boldsymbol{a}_7$	$[m]$	-5	-5	10	$\boldsymbol{b}_7$ $[m]$	0	-0.5	0.4			
$\boldsymbol{a}_8$	$[m]$	-5	-5	1	$\boldsymbol{b}_8$ $[m]$	0.5	-0.4	0			

Table 3.3: Adaptive Super-Twisting Sliding-Mode Controller parameters and limits - The notations for the Terminal Sliding-Mode Controller were taken from [31]

ASTSMC Parameters and Limits					
$\boldsymbol{\Omega_\lambda}$	$\boldsymbol{\Lambda}_{1,min}$	$\boldsymbol{\epsilon}$	$f_{i,min}$ $[N]$	$f_{i,max}$ $[N]$	
$1e^5$	$[10, 10, 10, 4, 4, 4]^{\mathrm{T}}$	0.75	10	10.000	
TSMC Parameters					
$\boldsymbol{K}_1$	$\boldsymbol{K}_2$	β	γ	ρ	$\boldsymbol{\Lambda}_{TSMC}$
$[3000, 2500, 3000, 150, 300, 500]$	$[1220, 700, 1000, 150, 300, 500]$	1	1.5	0.33	$[1000 \cdot \mathbf{1}^{6\times1}, 500 \cdot \mathbf{1}^{4\times1}]$

For more realistic encoder measurement zero mean Gaussian noise corrupts the signal. Over the entire simulation external torques and forces try to distract the platform from the desired trajectory (see Figure 3.10). Since $\boldsymbol{z}_1 = \boldsymbol{z}1, d$, $\boldsymbol{z}_2 = \boldsymbol{z}_{2,d}$ and $\dot{\boldsymbol{z}}_2 = \dot{\boldsymbol{z}}_{2,d}$, th error $\boldsymbol{e}$ and $\dot{\boldsymbol{e}}$ equals $\mathbf{0}$. After one second the external disturbances start to distort the platform by applying torques and forces in different directions, with partially more than half of the gravity force acting on the platform. In spite of these perturbations, Figures 3.11 and 3.13 depict an accurate tracking to the 2-sliding mode $\boldsymbol{\sigma} = \dot{\boldsymbol{\sigma}} = \mathbf{0}$. Spikes in Figure 3.11 occur whenever the external disturbances change abruptly and the controller (3.30) has to adjust to the new conditions. Those changes are unpredictable and a short deviation from 2-sliding mode is unavoidable. In practise the adaptive Super-Twisting Sliding-Mode Controller might require even more time to reduce this short deviation because of system communication delays that are disregarded in the simulation model[7]. Figures 3.11-3.16 compare the error $\boldsymbol{e}$, error in velocity $\dot{\boldsymbol{e}}$ and the cable forces $\boldsymbol{f}$ of the system using the adaptive Super-Twisting Sliding-Mode Controller or the Terminal Sliding-Mode Controller and reveal the following insights:

- **Figures 3.11-3.12:** Both controllers are able to compensate effectively the error $\boldsymbol{e}$. However the adaptive Super-Twisting Sliding-Mode Controller reduces the error significantly faster than the Terminal Sliding-Mode Controller and limits the maximal error to less than $0.005m$. In comparison, the Terminal Sliding-Mode Controller reaches a maximum error of almost $0.02m$ which is 4 times higher. A reason for the slower error dynamics of the Terminal Sliding-Mode Controller might be, because the Terminal Sliding-Mode Controller adapts its model parameters to compensate external disturbances [22].

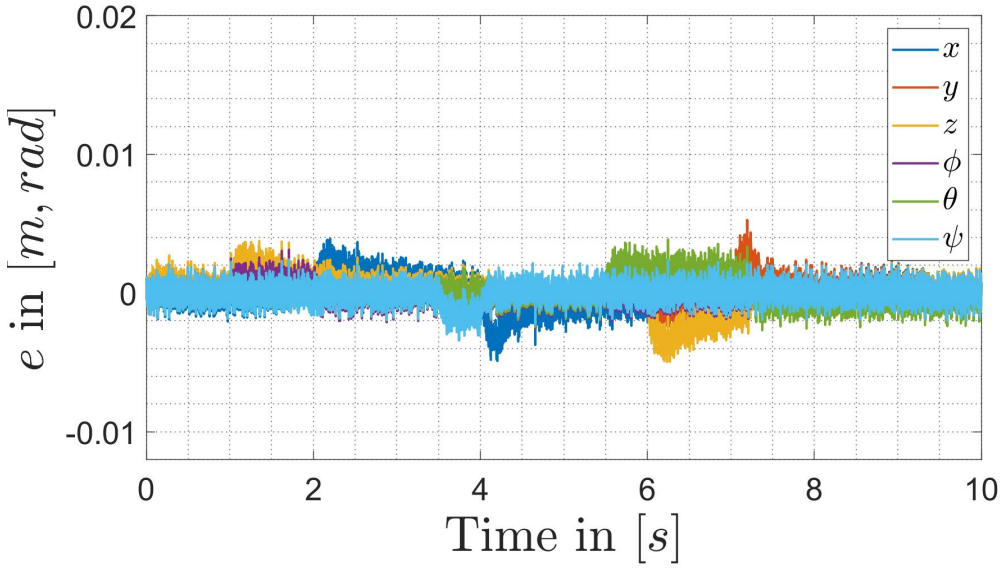

Figure 3.11: Evaluation of the adaptive Super-Twisting Sliding-Mode Controller in simulation and comparison with a Terminal Sliding-Mode Controller with constant controller gains - Error $\boldsymbol{e}$ of the adaptive Super-Twisting Sliding-Mode Controller

[7]Those communication delays are the composition of the real-time environment cycle-time, the mechanical system response, communication of Programmable Logical Controllers and drives

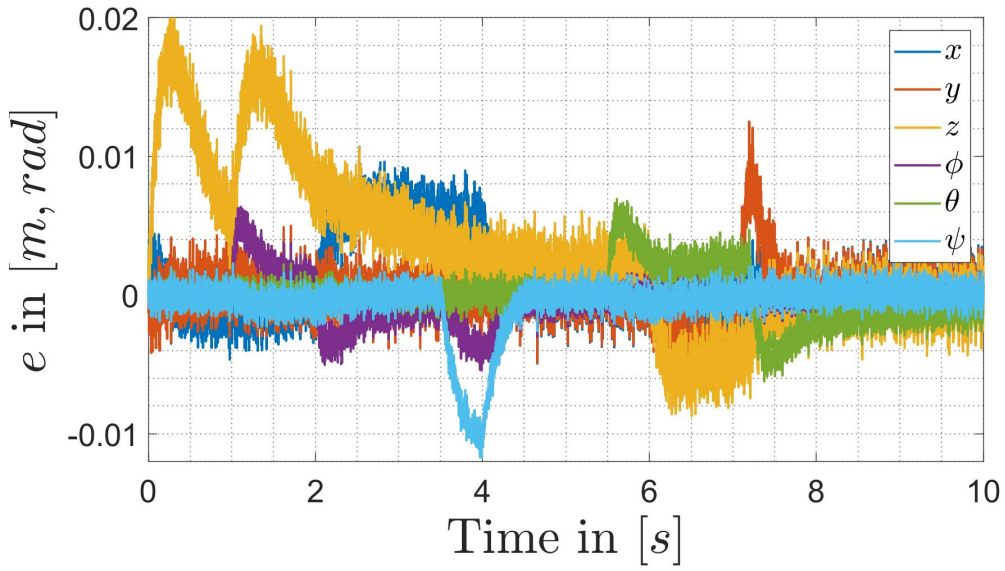

Figure 3.12: Evaluation of the adaptive Super-Twisting Sliding-Mode Controller in simulation and comparison with a Terminal Sliding-Mode Controller with constant controller gains - Error $\boldsymbol{e}$ of the Terminal Sliding-Mode Controller

- **Figures 3.13-3.14:** Evaluating $\dot{\boldsymbol{e}}$ reveals the same insight as in Figures 3.11-3.12. Furthermore, the gain adaptation algorithm rebound to the adaptive Super-Twisting Sliding-Mode Controller advantage. Amplification of chattering due to high controller gains are distinct in Figure 3.14, whereas the gain adaptation algorithm inhibits this effect.

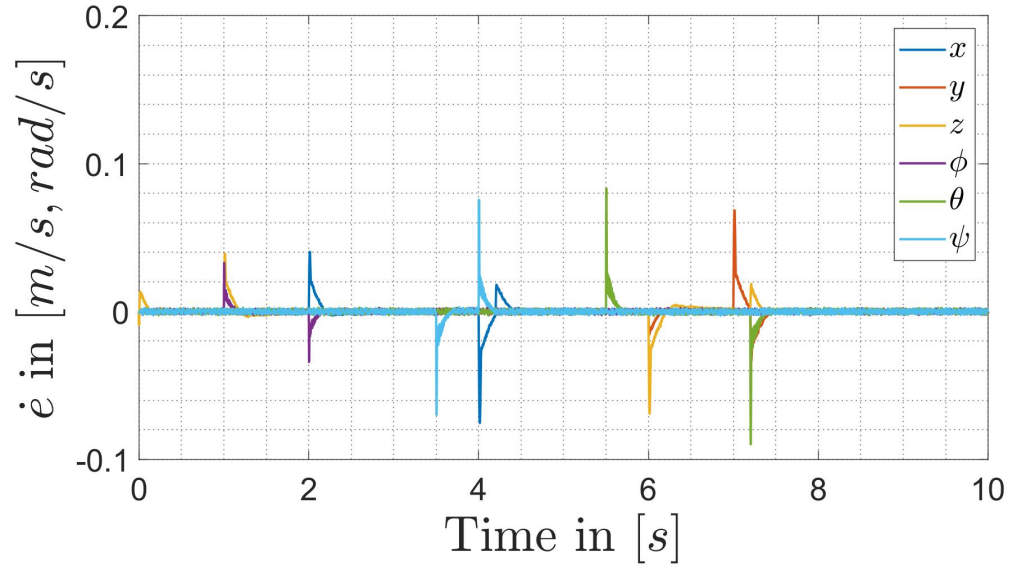

Figure 3.13: Evaluation of the adaptive Super-Twisting Sliding-Mode Controller in simulation and comparison with a Terminal Sliding-Mode Controller with constant controller gains - Error in velocities $\dot{\boldsymbol{e}}$ of the adaptive Super-Twisting Sliding-Mode Controller

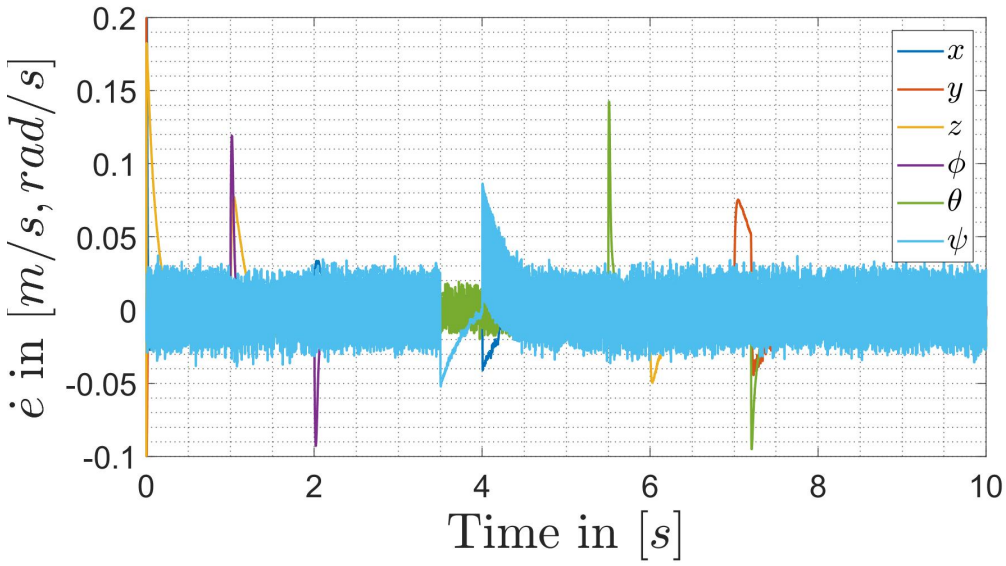

Figure 3.14: Evaluation of the adaptive Super-Twisting Sliding-Mode Controller in simulation and comparison with a Terminal Sliding-Mode Controller with constant controller gains - Error in velocity $\dot{\boldsymbol{e}}$ of the Terminal Sliding-Mode Controller

- **Figures 3.15-3.16:** Comparing the cable forces demonstrates again the advantages of gain adaptation. The Terminal Sliding-Mode Controller exhibits over the entire simulation distinctly stronger vibrations due to its high controller gains. Those vibrations are a composition of noise amplification and controller induced chattering due to the discontinuous signum function.

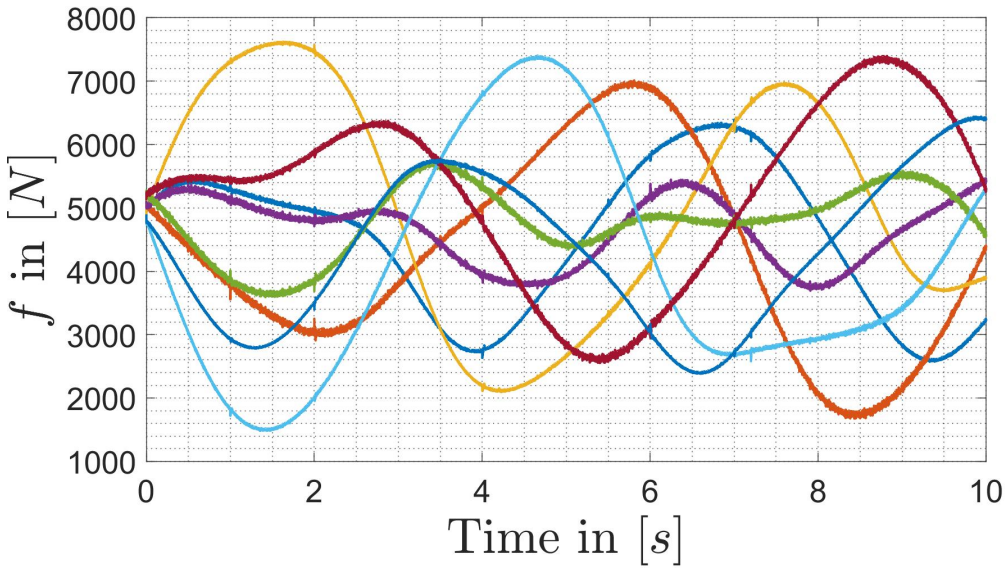

Figure 3.15: Evaluation of the adaptive Super-Twisting Sliding-Mode Controller in simulation and comparison with a Terminal Sliding-Mode Controller with constant controller gains - Cable forces $\boldsymbol{f}$ of the adaptive Super-Twisting Sliding-Mode Controller

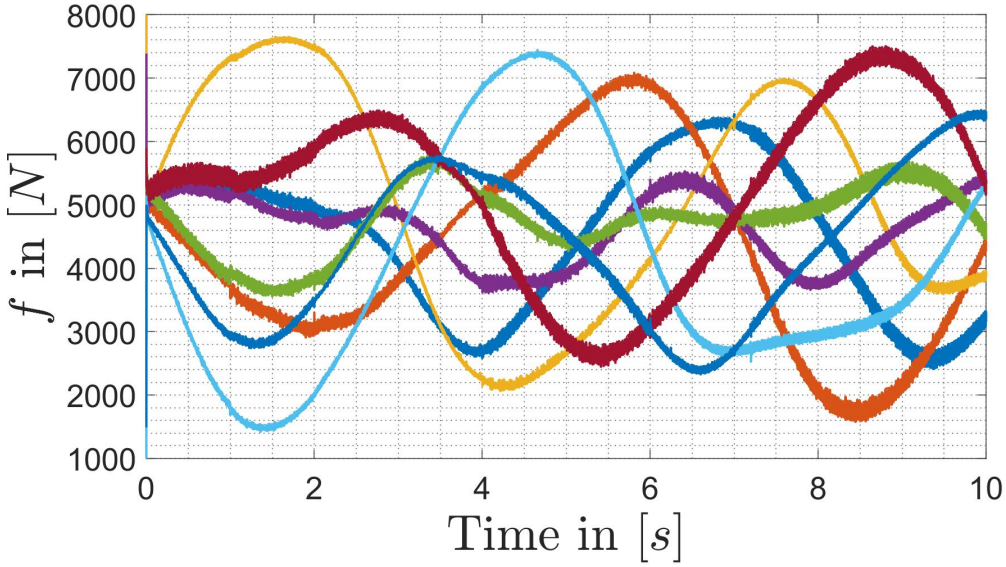

Figure 3.16: Evaluation of the adaptive Super-Twisting Sliding-Mode Controller in simulation and comparison with a Terminal Sliding-Mode Controller with constant controller gains - Cable tensions $\boldsymbol{f}$ of the Terminal Sliding-Mode Controller

Chattering effects decrease when the Terminal Sliding-Mode Controller controller gains are low. However, reducing chattering this way happens to the expense of less tracking accuracy which was benchmark for this simulation.

3.3.4 Adaptive Super-Twisting Sliding-Mode Disturbance Observer

Assuming a precisely known system model, $\boldsymbol{u}_{FF}$ should track a desired trajectory and unburden the controller. Unmodelled dynamics and varying dynamic parameters put more load on the High-Level Controller. This happens for instance during pick and place tasks with unknown heavy load or because of changing system equipment.

A model based disturbance compensation is still a promising approach to reject disturbances. In the previous sections, Sliding-Mode Controller theory proved to be suitable for High-Level Control and state differentiation. Moreover, Sliding-Mode Controller theory enables disturbance estimation.

The typical structure of an observer is the composition of the known dynamic model (see Equation (3.23)) and a correction term, depending on the domain of control theory. The Sliding-Mode Disturbance Observer introduced here, exploits the advantages of a Super-Twisting Sliding-Mode Controller, adapts its parameters according to the gain adaptation algorithm (3.34) and bases on the nominal model (3.23) such that the observer dynamics result in.:

$$\dot{\hat{\boldsymbol{z}}}_1 = \hat{\boldsymbol{z}}_2 + \boldsymbol{\Lambda}_{1,SMO}\sqrt{\|\boldsymbol{z}_1 - \hat{\boldsymbol{z}}_1\|}\,\mathrm{sign}(\boldsymbol{z}_1 - \hat{\boldsymbol{z}_1}) \tag{3.36}$$

$$\dot{\hat{\boldsymbol{z}}}_2 = \boldsymbol{a}_n + \boldsymbol{b}_n\boldsymbol{u} + \boldsymbol{\Lambda}_{2,SMO}\,\mathrm{sign}(\boldsymbol{z}_1 - \hat{\boldsymbol{z}_1})\,, \tag{3.37}$$

with

$$\boldsymbol{\mu} = 0.04\ \boldsymbol{\Lambda}_{1,SMO} T_{sim} \tag{3.38}$$

$$\boldsymbol{a}_n = \boldsymbol{A}\boldsymbol{B}^{-1}(C(\hat{\boldsymbol{z}}_1\hat{\boldsymbol{z}}_2) - \boldsymbol{g}) + \dot{\boldsymbol{A}} \begin{bmatrix} \dot{\hat{\boldsymbol{x}}}_1 \\ \dot{\hat{\boldsymbol{x}}}_2 \end{bmatrix} \tag{3.39}$$

$$\boldsymbol{b}_n = \boldsymbol{A}\boldsymbol{B}^{-1} \tag{3.40}$$

and gain adaptation for the Sliding-Mode Observer:

$$\dot{\boldsymbol{\Lambda}}_1 = \begin{cases} \boldsymbol{\Omega}_{\boldsymbol{\Lambda}} \operatorname{sign}\left(|\boldsymbol{z}_1 - \hat{\boldsymbol{z}}_1| - \boldsymbol{\mu}\right), & \text{if } \boldsymbol{\Lambda}_1 > \boldsymbol{\Lambda}_{1,m} \\ \boldsymbol{\eta}, & \text{if } \boldsymbol{\Lambda}_1 \leq \boldsymbol{\Lambda}_{1,m} \end{cases} \tag{3.41}$$

$$\boldsymbol{\Lambda}_2 = 2\,\epsilon\,\boldsymbol{\Lambda}_1 \tag{3.42}$$

$$\boldsymbol{\mu} = 4\,\boldsymbol{\Lambda}_1\,T_e\,, \tag{3.43}$$

with the simulation sampling time T_{sim}. In simulation, a series of external forces act on the platform with the dynamics of Equation (3.21) and (3.22) Figure 3.17 depicts an accurate prediction of $\boldsymbol{\zeta}$ (dashed lines) and converges in $0.1s$ to $\boldsymbol{\zeta}$ with reduced chattering, thanks to the gain adaptation algorithm (3.41).

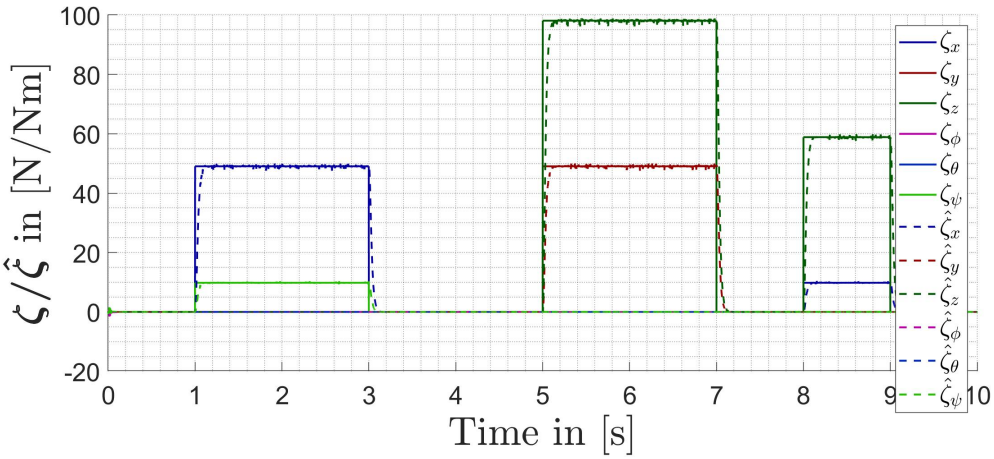

Figure 3.17: Disturbance observation with adaptive Super-Twisting Sliding-Mode Disturbance Observer

3.4 State estimation via Unscented Kalman Filter for a Cable-Driven Parallel Robot

A Cable-Driven Parallel Robot as simulator requires not only an accurate positioning of the platform, but also an accurate platform acceleration measurement, to incorporate the influence of cable dynamics on the platform. A platform-mounted Inertial Measurement Unit measures directly the platform acceleration. However, Inertial Measurement Unit measurements are biased. The motivation for this section is to estimate the real platform pose,

velocity and acceleration as precise as possible by an estimation scheme, that fuses encoder, force and Inertial Measurement Unit measurements. It is a well known fact, measurements from different sources -independent of the measurement quality- provides better estimation results than measurements of one single sensor with high quality. Additionally, this estimation scheme has to account for measurement noise, various sampling times, discrete time signals and Inertial Measurement Unit bias. This way, one avoids using expensive hardware tracking systems and paves the way for further investigations on cable dynamics and their influence on the platform. Placed at the onboard connection points, Inertial Measurement Units detect vibrations and therefore could allow, to evaluate future controllers for vibration suppression in joint space. The Unscented Kalman-Filter is a promising estimation algorithm, that incorporates noisy measurements and improves state estimation by sensor fusion for highly non-linear system dynamics. Depending on the number of sensors, there can be more than one prediction or correction step in one estimation algorithm. The estimation strategy proposed here, consists of two parts. The first part is a standard linear Kalman-Filter and estimates the platform pose, its velocity as well as the Inertial Measurement Unit bias, in one prediction step by a simple kinematic model. The subsequent correction step corrects the predicted state based on encoder measurements. In this first correction step the forward kinematics reconstruct the platform pose. The second part consists of an Unscented Kalman-Filter with one prediction step, based on the nominal model (3.21) and (3.22) motor torque measurements. The subsequent correction step incorporates the unbiased Inertial Measurement Unit measurement from the previous bias estimation.

3.4.1 Prediction and Correction via biased Inertial Measurement Unit and encoder measurement:

Note that the first prediction and correction step requires only a kinematic model

$$\hat{\boldsymbol{x}}_{k|k+1,1} = \boldsymbol{A}_d \hat{\boldsymbol{x}}_{k-1|k-1,12} + \boldsymbol{B}_d \boldsymbol{u}_k \tag{3.44}$$

$$\boldsymbol{y}_k = \boldsymbol{C}_k \hat{\boldsymbol{x}}_{k|k+1,1}\,, \tag{3.45}$$

with the system and control input matrix[8]

$$\boldsymbol{A}_d = \begin{bmatrix} \boldsymbol{I}_{3\times3} & \boldsymbol{I}_{3\times3}T_{IMU} & \boldsymbol{0}_{3\times3} \\ \boldsymbol{0}_{3\times3} & \boldsymbol{I}_{3\times3} & -\boldsymbol{I}_{3\times3}T_{IMU} \\ \boldsymbol{0}_{3\times3} & \boldsymbol{0}_{3\times3} & \boldsymbol{I}_{3\times3} \end{bmatrix} \tag{3.46}$$

$$\boldsymbol{B}_d = \begin{bmatrix} \boldsymbol{0}_{3\times3} \\ \boldsymbol{I}_{3\times3}T_{IMU} \\ \boldsymbol{0}_{3\times3} \end{bmatrix} \tag{3.47}$$

$$\tag{3.48}$$

, the Inertial Measurement Unit sampling time T_{IMU} and the biased Inertial Measurement Unit measurement $\boldsymbol{u}_{b,k}$ at time step k. The state vector consist of the platform pose, velocity and Inertial Measurement Unit acceleration bias i.e.

$$\hat{\boldsymbol{x}}_{k|k+1,1} = [x,\, y,\, z,\, \phi,\, \theta,\, \psi,\, \dot{x},\, \dot{y},\, \dot{z},\, \dot{\phi},\, \dot{\theta},\, \dot{\psi},\, b_{\ddot{x}},\, b_{\ddot{y}},\, b_{\ddot{z}},\, b_{\ddot{\phi}},\, b_{\ddot{\theta}},\, b_{\ddot{\psi}}] \mid_{k|k+1} , \tag{3.49}$$

An a priori error covariance matrix is:

$$\boldsymbol{P}_{k|k-1,1} = \boldsymbol{A}_k \boldsymbol{P}_{k-1|k-1,1} \boldsymbol{A}_k^{\mathrm{T}} + \boldsymbol{Q}_{k,1} . \tag{3.50}$$

The second subscript denotes the first part of the estimation algorithm. Since the estimation scheme consists of two parts which are connected with each other, $\hat{\boldsymbol{x}}_{k-1|k-1,12}$ consists of the previous estimated platform pose, platform velocity $\hat{\boldsymbol{x}}_{k-1|k-1,2}$ and the previous bias estimation from $\hat{\boldsymbol{x}}_{k-1|k,1}$. Afterwards Equation (3.51) computes the:

$$\tilde{\boldsymbol{y}}_k = \boldsymbol{z}_k - \boldsymbol{C}_k \hat{\boldsymbol{x}}_{k|k+1,1} \tag{3.51}$$

$$\boldsymbol{S}_{k,1} = \boldsymbol{R}_{\boldsymbol{\xi},1} + \boldsymbol{C}_1 \boldsymbol{P}_{k|k-1,1} \boldsymbol{C}_1^{\mathrm{T}} \tag{3.52}$$

$$\boldsymbol{K}_{k,1} = \boldsymbol{P}_{k|k-1,1} \boldsymbol{C}_1^{\mathrm{T}} \boldsymbol{S}_{k,1}^{-1} \tag{3.53}$$

$$\hat{\boldsymbol{x}}_{k|k,1} = \hat{\boldsymbol{x}}_{k|k-1,1} + \boldsymbol{K}_{k,1} \tilde{\boldsymbol{y}}_k \tag{3.54}$$

, where $\tilde{\boldsymbol{y}}$ is the estimation error, $\Sigma_{k,1}$ is the measurment covariance matrix, $\boldsymbol{K}_{k,1}$ is the correction gain and $\hat{\boldsymbol{x}}_{k|k,1}$ is the corrected state and the a posteriori error covariance matrix

$$\boldsymbol{P}_{k|k,1} = (\boldsymbol{I} - \boldsymbol{K}_{k,1}\boldsymbol{C}_1)\boldsymbol{P}_{k|k-1,1}(\boldsymbol{I} - \boldsymbol{K}_{k,1}\boldsymbol{C}_1)^{\mathrm{T}} + \boldsymbol{K}_{k,1}\boldsymbol{R}_{\boldsymbol{\xi},1}\boldsymbol{K}_{k,1}^{\mathrm{T}} \tag{3.55}$$

and corrects the predicted vector $\hat{\boldsymbol{x}}_{k|k+1,1}$ according to $\hat{\boldsymbol{x}}_{k,1} = \hat{\boldsymbol{x}}_{k,1}^{-} + \boldsymbol{K}_{k,1}(\boldsymbol{x}_{k,1} - \hat{\boldsymbol{y}}_{k,1})$, where $\boldsymbol{K}_{k,1}$ is the gain matrix (3.53).

[8]The second row in Equation (3.46) incorporates the estimated bias and includes it in the estimation process.

3.4.2 Prediction and Correction via cable force and unbiased Inertial Measurement Unit measurement

Part two incorporates the nominal dynamic model of the platform as in Equation (3.23) and (3.25) with $\boldsymbol{c} = \boldsymbol{0}_3$. The procedure for the prediction and the correction step via cable force and unbiased Inertial Measurement Unit measurement is analogue to the previous procedure for prediction and correction via encoder and bias Inertial Measurement Unit measurements. However, now the Unscented Kalman-Filter is preferred against the linear Kalman-Filter, because of the non-linear dynamic model. Then with the dynamics given in Equation (2.28) and Equation (2.69) the dynamic model for the Unscented Kalman-Filter reads:

$$\begin{bmatrix} \dot{\boldsymbol{\mathcal{X}}}_i^- \\ \ddot{\boldsymbol{\mathcal{X}}}_i^- \end{bmatrix}_{k+1,2}^- = \boldsymbol{A}_d(\boldsymbol{\mathcal{X}}_i^-, \dot{\boldsymbol{\mathcal{X}}}_i^-) \begin{bmatrix} \dot{\boldsymbol{\mathcal{X}}}_i^- \\ \ddot{\boldsymbol{\mathcal{X}}}_i^- \end{bmatrix}_{k,2}^- + \boldsymbol{B}_d \boldsymbol{u}_k + \boldsymbol{Q}_{\boldsymbol{\zeta},2} \boldsymbol{\zeta}_k \tag{3.56}$$

$$\boldsymbol{\mathcal{Y}}_k = \boldsymbol{C}_d \begin{bmatrix} \dot{\boldsymbol{\mathcal{X}}}_i^- \\ \ddot{\boldsymbol{\mathcal{X}}}_i^- \end{bmatrix}_{k,2}^- + \boldsymbol{D}_d \boldsymbol{u}_k + \boldsymbol{R}_{\boldsymbol{\xi},2} \boldsymbol{\xi}_k \,, \tag{3.57}$$

where $\boldsymbol{Q}_{\boldsymbol{\zeta},2}$ is the model covariance matrix and $\boldsymbol{R}_{\boldsymbol{\xi},2}$ is the measurement covariance matrix. The state vector $\boldsymbol{\mathcal{X}}$ in calligraphic letters denotes a set of $2n_x + 1$ so-called sigma points. Those sigma points consist of the mean state and $2n_x$ vectors, distributed in geometric meaningful way. Those are chosen as in Equation (2.83-2.85)

The Unscented Kalman-Filter with unscented transform accounts this way for the mean and the covariance. The correction step then corrects the predicted state $\hat{\boldsymbol{x}}_{k+1}$ with the predicted state $\hat{\boldsymbol{x}}_k^-$, i.e.:

$$\hat{\boldsymbol{x}}_{k+1,2} = \hat{\boldsymbol{x}}_{k+1,2}^- + \boldsymbol{K}_{k,2}(\hat{\boldsymbol{x}}_{k,1}^- - \boldsymbol{y}_k) \tag{3.58}$$

and provides the new estimate for the platform pose and velocity. Note that $\boldsymbol{A}_d$ is the discrete representation of $\boldsymbol{A}_c$ in Equation (3.61). Applying the Laplace-Transformation (2.81) on the system dynamic equation (3.61) is time consuming and the resulting matrices are complex. A numerical approximation [34] of $\boldsymbol{A}_d$ and $\boldsymbol{B}_d$ up to order four:

$$\boldsymbol{A}_d = \boldsymbol{I} + \boldsymbol{A}_c + \frac{\boldsymbol{A}_c^2 h^2}{2!} + \frac{\boldsymbol{A}_c^3 h^3}{3!} + \ldots + \frac{\boldsymbol{A}_c^{n_a} h^{n_a}}{n_a!} \tag{3.59}$$

$$\boldsymbol{B}_d = \left(\boldsymbol{I} h + \frac{\boldsymbol{A}_c h^2}{2!} + \frac{\boldsymbol{A}_c^2 h^3}{3!} + \ldots + \frac{\boldsymbol{A}_c^{n_a - 1} h^{n_a}}{n_a!} \right) \boldsymbol{B}_c \tag{3.60}$$

$$\boldsymbol{A}_c = \begin{bmatrix} \boldsymbol{0}_{n \times n} & \boldsymbol{I}_{n \times n} \\ \boldsymbol{0}_{n \times n} & -\boldsymbol{M}(\boldsymbol{x})^{-1} \boldsymbol{C}(\dot{\boldsymbol{x}}, \boldsymbol{x}) \end{bmatrix} \tag{3.61}$$

$$\boldsymbol{B}_c = \begin{bmatrix} \boldsymbol{0}_{n \times n} & \boldsymbol{0}_{n \times n} \\ \boldsymbol{0}_{n \times n} & -\boldsymbol{M}(\boldsymbol{x})^{-1} \end{bmatrix} , \tag{3.62}$$

yields accurate results and limits the computational complexity. The Unscented Kalman-

Filter has some important features: i) It is robust against data loss and corruption, since it includes measurements from different sources, i.e.: an Inertia Measurement Unit, encoder measurements and cable force sensor. ii) Based on a simple kinematic model, the estimation scheme estimates Inertial Measurement Unit bias and corrects incoming biased Inertial Measurement Unit measurements. iii) The Unscented Kalman-Filter executes a new correction step, whenever a new sensor measurement is available, even if every sensor comes with a different sampling time.

> **Remark 3.2:** Data from Inertial Measurement Unit measurements provide information about the drivetrain dynamics and their instant impact on the platform. This thesis does not incorporate further investigations on this topic in terms of a more accurate model but wants to motivate for further investigations in this direction.

This section focus on state estimation of a Cable-Driven Parallel Robot itself and evaluates the Unscented Kalman-Filter in simulation. A feedforward control input alone with an exactly known dynamic model drives the system of a redundant Cable-Driven Parallel Robot with eight cables along a desired trajectory in absence of disturbances and uncertainties. Goal is, to reconstruct the platform pose given encoder, Inertial Measurement Unit and cable force measurements by the Unscented Kalman-Filter under the following assumptions:

- Encoder measurements from the motors, Inertial Measurement Unit and cable force measurements are available and corrupted with realistic zero mean Gaussian noise (see Section 2.3.2).
- Sole integration of Inertial Measurement Unit measurements drifts due to constant Inertial Measurement Unit bias $\boldsymbol{b}_{\ddot{\boldsymbol{x}}}$. To obtain feasible Inertial Measurement Unit measurements the linear Kalman-Filter (see Equation (3.44)-(3.55)) estimates the Inertial Measurement Unit bias (see Figure 3.18). Figure 3.18 depicts the real Inertial Measurement Unit bias $\boldsymbol{b}_{\ddot{\boldsymbol{x}}} = \begin{bmatrix} 0.5 & -0.5 & 1 & 0 & 0 & 0 \end{bmatrix}^{\mathrm{T}}$ and the corresponding estimate $\hat{\boldsymbol{b}}_{\ddot{\boldsymbol{x}}}$. The linear Kalman-Filter estimates precisely after $5s$ the Inertial Measurement Unit bias.
- Sensor measurements are discrete, corrupted with noise (see Figure 3.19) and provided with different sampling times. The system cycle-time is set to $100Hz$ whereas the motors, e.g. torque measurements and encoder measurements provide data with $20Hz$ and the Inertial Measurement Unit provides data with $10Hz$.

The data quality of the encoders, the force sensor and the Inertial Measurement Unit is poor and due to this, underlines the robustness of the Dual Unscented Kalman-Filter. Figure 3.20 shows the desired trajectory in solid lines, the reconstructed pose via Unscented Kalman-Filter in dashed lines and reveals a very precise state estimation in spite of corrupted

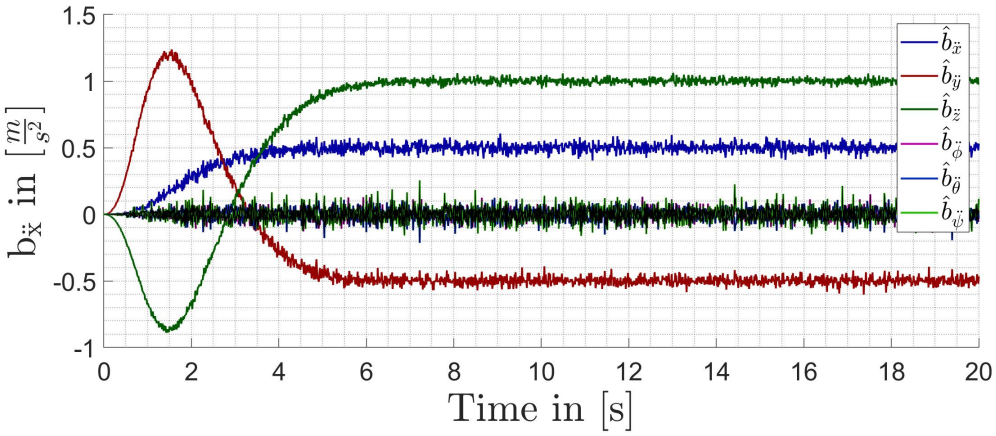

Figure 3.18: Inertial Measurement Unit bias estimation

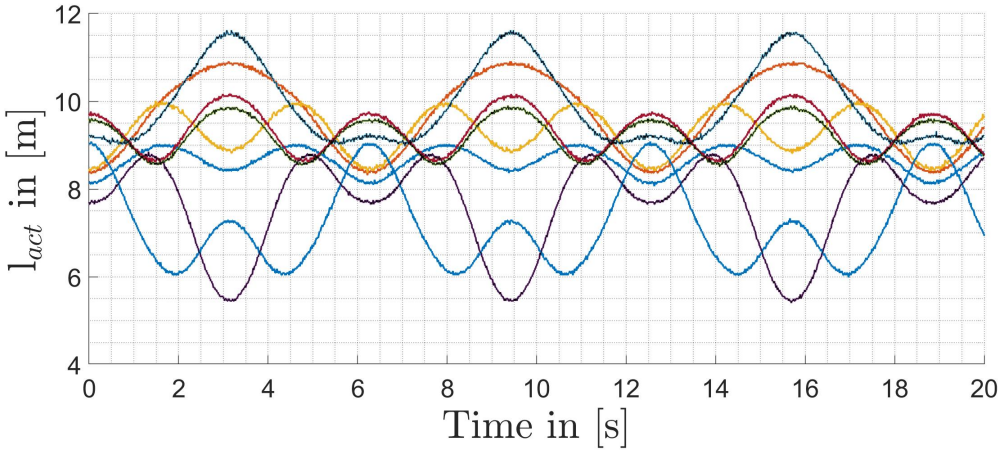

Figure 3.19: Encoder measurement signal subscripted to the Dual Unscented Kalman-Filter

measurements with varying sampling times.

The proposed Dual Unscented Kalman-Filter for a Cable-Driven Parallel Robot provides an Inertial Measurement Unit bias estimation, is robust against measurement noise and fuses data from different sensors with different sample times. The Dual Unscented Kalman-Filter provides similar results as the forward kinematic, but furthermore incorporate the drivetrain dynamics, in particular cable elasticity. Thus the Unscented Kalman-Filter provides a tool for evaluation of future vibrations suppressing control strategies.

3.5 Port-Hamilton based modelling of a Cable-Driven Parallel Robot including cable dynamics

Every model includes system boundaries at which energy can enter in or expel from the system and has to guarantee energy preservation. Assuming a system that includes only one cable, the boundaries of this particular system are the onboard connection point at the platform and the winch. As soon as the cable length increases, mass and energy will

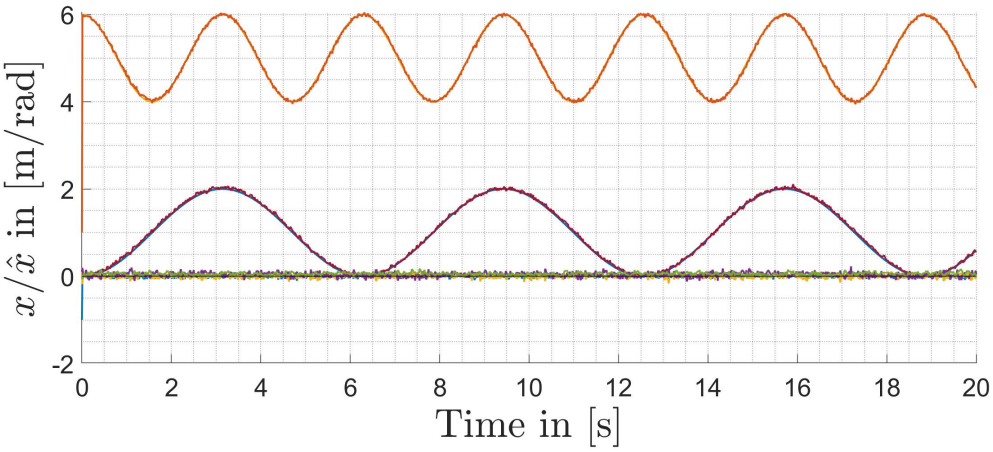

Figure 3.20: Estimation result of Unscented Kalman-Filter

enter the system over the boundary at the winch. If not the same amount of energy leaves the system at the same time, this violates the law of energy preservation. Section 3.5.1 presents a Finite-Element Method based cable model that incorporates all relevant effects and extends the model of a Cable-Driven Parallel Robot by the cable dynamics in Port-Hamilton representation. Finite-Element Method based models are simple and accurate for taut cables as Chapter 4 will show. Afterwards, Section 3.5.2 extends this model to the model of a Cable-Driven Parallel Robot. Then given the model in Port-Hamilton representation will pave the way for an Interconnection-Damping-Assignment Passivity-Based Controller [74, 13]. Interconnection Damping-Assignment Passivity-Based Control is capable of shaping the physical properties of a system. For simulators this is an attractive feature, since simulators mimic the motion of systems, e.g.: cars, planes or helicopters with physical properties that differ from those of a Cable-Driven Parallel Robot [19].

3.5.1 Port-Hamilton based modelling and simulation of a cable with fixed length and fixed end-points

This section presents the Finite-Element Method based model of one cable in Port-Hamilton representation (see Equation (2.64)). This model incorporates inertia, internal cross-couplings, elasticity, damping and holonomic constraints, i.e.: fixed end-points and thus zero velocity at the end-points. The elasticity matrix $\boldsymbol{K}_{C_i}$ is the composition of an elastic contribution $\boldsymbol{K}_{el,i}$ and a geometric contribution $\boldsymbol{K}_{g,i}$ and represents elasticity that is a key feature of cables.

> **Remark 3.3:** DSM based models are also a good choice to model a cable, but are not suitable for controller design.

The model of a cable in Port-Hamilton representation requires knowledge about the kinetic and potential energies as a function of a set of generalised coordinates $\boldsymbol{q} \in \mathbb{R}^{n_a \times 1}$ and

generalised momentum $\boldsymbol{p} \in \mathbb{R}^{n_a \times 1}$, with $\boldsymbol{q} = [\boldsymbol{q}_1^{\mathrm{T}}, \boldsymbol{q}_2^{\mathrm{T}}, \ldots, \boldsymbol{q}_{n_e}^{\mathrm{T}}]^{\mathrm{T}}$, $\boldsymbol{p} = [\boldsymbol{p}_1^{\mathrm{T}}, \boldsymbol{p}_2^{\mathrm{T}}, \ldots, \boldsymbol{p}_{n_e}^{\mathrm{T}}]^{\mathrm{T}}$ and the position $\boldsymbol{q}_i$ and momentum $\boldsymbol{p}_i$ of element i. The cables of such a Finite-Element Method based model consists of n_e consecutively connected mass-spring-damper elements and is fixed at both ends. This correlates to a cable with fixed length, attached at the ith onboard connection point $\boldsymbol{B}_i$ at one end and at the offboard connection point A_i at the other end. The distance between two consecutive elements is $\boldsymbol{l}_{seg,i}$ and shall not change, even when the cable changes its length due to elongation in reality $l_{seg,i}$ differs among all elements due to cable elasticity. However, this variation is irrelevant for the platform kinematics. Furthermore, stiffness and elasticity does not change significantly. This distance between to elements refers to the distance of two consecutive elements in an initial rest position vector:

$$\bar{\boldsymbol{q}}_{C_i}(0) = \begin{bmatrix} \boldsymbol{a}_i \\ \boldsymbol{a}_i - \frac{1}{n_i - 1}({}^{W}\boldsymbol{a}_i - \boldsymbol{a}_i\boldsymbol{\prime}) \\ \vdots \\ \boldsymbol{a}_i\boldsymbol{\prime} \end{bmatrix} \in \mathbb{R}^{3n_i}, \tag{3.63}$$

for cable i with $\bar{\boldsymbol{q}}_{C_i}(0) = \begin{bmatrix} \bar{\boldsymbol{q}}_{C,i,1}(0)^{\mathrm{T}} & \ldots & \bar{\boldsymbol{q}}_{C,i,n_i}(0) \end{bmatrix}$ and $\boldsymbol{a}_i\boldsymbol{\prime} = \max(||a_k - a_i||), k = 1 \ldots m, k \neq i$. Every cable with mass (which is subject to gravity) will bend, depending on the cable material and on the cable pretension. Higher pretension reduces bending, while lower pretension and higher cable mass increases bending [21]. Again $\boldsymbol{a}_i \in \mathbb{R}^{3\times 1}$ is the vector of one offboard connection point for cable i. Then the distance between two consecutive elements k and $k+1$ is:

$$l_{seg,i,j} = \left|\left|\bar{\boldsymbol{q}}_{C,i,j}(0) - \bar{\boldsymbol{q}}_{C,i,j+1}(0)\right|\right| = l_{seg,i} \tag{3.64}$$

Again, the superscript describing the world frame, are skipped for the sake of brevity. Transforming the generalised coordinates of element j (denoted by the subindex) from $\mathcal{K}_W$ to $\mathcal{K}_{C_i}$ (correspondingly denoted by the superscript) is possible by ${}^{C_i}\boldsymbol{q}_{C_i} = {}^{C_i}\boldsymbol{R}_W(\boldsymbol{q}_P)\boldsymbol{q}_{C_i}$. For the sake of consistency ${}^{C_i}\boldsymbol{R}_W(\boldsymbol{q}_P)$ is here a function of the platform pose. The platform pose is not part of the generalised coordinates and is constant if both cable ends are fixed. Given the vector close loop of Equation (2.6) and (3.64) the nominal positions of all elements distribute uniformly along the cable according to:

$$\bar{\boldsymbol{q}}_{C_i} = \begin{bmatrix} \boldsymbol{q}_{Pt} + \boldsymbol{R}_P{}^{P}\boldsymbol{b}_i + (n_i - 1)l_{seg,i}\boldsymbol{d} \\ \boldsymbol{q}_{Pt} + \boldsymbol{R}_P{}^{P}\boldsymbol{b}_i + (n_i - 2)l_{seg,i}\boldsymbol{d} \\ \vdots \\ \boldsymbol{q}_{Pt} + \boldsymbol{R}_P{}^{P}\boldsymbol{b}_i + l_{seg,i}\boldsymbol{d} \\ \boldsymbol{q}_{Pt} + \boldsymbol{R}_P{}^{P}\boldsymbol{b}_i \end{bmatrix} \tag{3.65}$$

$$\boldsymbol{d} = \frac{\boldsymbol{a}_i - \boldsymbol{q}_{Pt} - \boldsymbol{R}_P{}^{P}\boldsymbol{b}_i}{|\boldsymbol{a}_i - \boldsymbol{q}_{Pt} - \boldsymbol{R}_P{}^{P}\boldsymbol{b}_i|}. \tag{3.66}$$

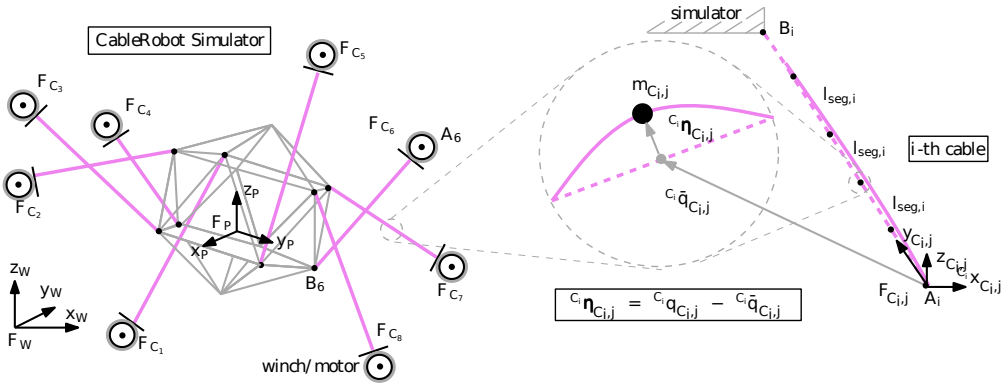

Figure 3.21: Redundant Cable-Driven Parallel Robot with 8 cables and detailed sketch of a taut individual cable

> **Remark 3.4:** Equation (3.63) and Equation (3.65) describe both the position of all mass elements, assuming rigid cables. Note that $\bar{\boldsymbol{q}}_{C_i}(0)$ describe the element positions when cable i goes from winch i to the winch on the opposite side of the system, whereas $\bar{\boldsymbol{q}}_{C_i}$ describes the element position when cable i goes from winch i to the corresponding onboard connection point.

The left side in Figure 3.21 shows the cables, the platform with all onboard and offboard connection points, corresponding platform coordinate frame and the world frame. Note, that all cables are depicted as straight lines without bending. Bending of one cable is shown on the right hand side of Figure 3.21. A coordinate system $\mathcal{K}_{C_i}$ is placed at the offboard connection point A_i[9]. In [19, 21] the $\boldsymbol{y}_{C_i}$-axis of $\mathcal{K}_{C_i}$ points along the cable to the platform and the $\boldsymbol{x}_{C_i}$ and $\boldsymbol{z}_{C_i}$ axis are perpendicular to the $\boldsymbol{y}_{C_i}$ axis. A reasonable way to set $\boldsymbol{x}_{C_i}$ and $\boldsymbol{z}_{C_i}$ is along the principle axes of eigenmodes. Exciting the eigenmodes of the cable, leads to vibrations in direction of the main axes because of cross-couplings. One can assign a covariance matrix to positions of maximum amplitude at the cable over time. Two axes, that are the eigenvectors to this corresponding covariance matrix, describe the shape of these circles (see Figure 3.22) and are reasonable candidates for $\boldsymbol{z}_{C_i}$ and $\boldsymbol{x}_{C_i}$ This information locks $\boldsymbol{x}_{C_i}$ and $\boldsymbol{z}_{C_i}$

The right side of Figure 3.21 shows the i-th cable, with deflection of one element

$$ {}^{C_i}\boldsymbol{\mu}_{C_i,j} = {}^{C_i}\boldsymbol{q}_{C_i} - {}^{C_i}\bar{\boldsymbol{q}}_{C_i}\,, \tag{3.67} $$

from its nominal position in $\mathcal{K}_{C_i}$. So far, the general platform coordinates are given in $\mathcal{K}_W$, where as the generalised cable coordinates are still given in $\mathcal{K}_{C_i}$. Control of the platform and the cables will take place with respect to $\mathcal{K}_W$. To achieve a unified representation, the cable coordinates in $\mathcal{K}_{C_i}$ must be transformed in $\mathcal{K}_W$.

The next step is to find the transformation from $\mathcal{K}_{C_i}$ to $\mathcal{K}_W$ and vice versa. A rotation matrix ${}^{C_i}\boldsymbol{R}_W$ describes this transformation and consists of the product of two rotation matrices

[9]Note that the order of coordinate systems $\mathcal{K}_{C_i}$ in Figure 3.21 is random

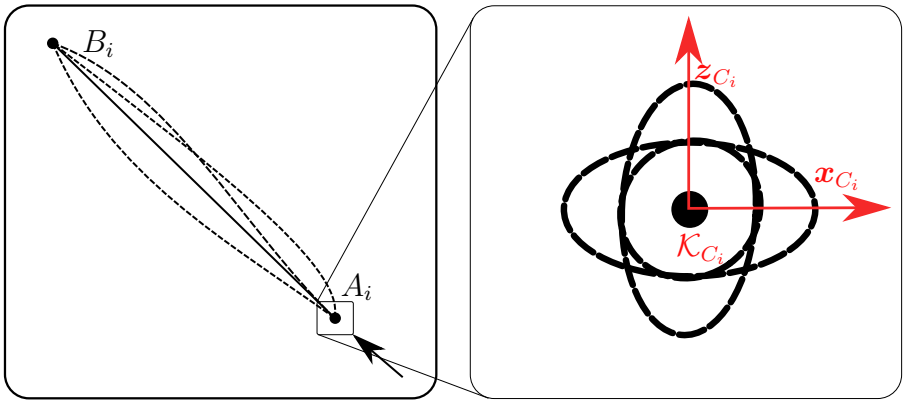

Figure 3.22: Reasonable choice of axes for each cable coordinate system $\mathcal{K}_{C_i}$. The left figure shows snapshots of a cable fixed at the onboard and offboard connection points with deflections during excitation in dashed lines and the cable vector $\boldsymbol{l}_i$ according to Equation (2.6) in a solid line. The right picture shows maximal cable deflections at A_i along the cable (solid line) and the principle axes of the attached coordinate system $\mathcal{K}_{C_i}$.

${}^{C_i}\boldsymbol{R}_{W_x}$ and ${}^{C_i}\boldsymbol{R}_{W_z}$

$$ {}^{C_i}\boldsymbol{R}_W(\theta_z, \theta_x) = {}^{C_i}\boldsymbol{R}_{W,x}(\theta_x)\,{}^{C_i}\boldsymbol{R}_{W,z}(\theta_z), \tag{3.68} $$

where

$$ \begin{aligned} {}^{C_i}\boldsymbol{R}_{W,x} &= \begin{bmatrix} 1 & 0 & 0 \\ 0 & c_x & s_x \\ 0 & -s_x & c_x \end{bmatrix}, \boldsymbol{F}_{xy} = \begin{bmatrix} 1 & 0 & 0 \\ 0 & 1 & 0 \\ 0 & 0 & 0 \end{bmatrix} \\ {}^{C_i}\boldsymbol{R}_{W,z} &= \begin{bmatrix} c_z & s_z & 0 \\ -s_z & c_z & 0 \\ 0 & 0 & 1 \end{bmatrix}, \boldsymbol{F}_{yz} = \begin{bmatrix} 0 & 0 & 0 \\ 0 & 1 & 0 \\ 0 & 0 & 1 \end{bmatrix} \end{aligned} \tag{3.69} $$

$$ \begin{aligned} \theta_x &= \boldsymbol{c}_{1,x}(i)\pi + \boldsymbol{c}_{2,x}(i) cos^{-1}\left(\frac{\sqrt{(\boldsymbol{F}_{xy}\,{}^{C_i}\boldsymbol{R}_{W,z}\boldsymbol{l}_i)^{\mathrm{T}}(\boldsymbol{F}_{xy}\,{}^{C_i}\boldsymbol{R}_{W,z}\boldsymbol{l}_i)}}{\sqrt{({}^{C_i}\boldsymbol{R}_{W,z}\boldsymbol{l}_i)^{\mathrm{T}}({}^{C_i}\boldsymbol{R}_{W,z}\boldsymbol{l}_i)}}\right) \\ \theta_z &= \boldsymbol{c}_{1,z}(i)\pi + \boldsymbol{c}_{2,z}(i) cos^{-1}\left(\frac{\sqrt{(\boldsymbol{F}_{xy}\boldsymbol{F}_{yz}\boldsymbol{l}_i)^{\mathrm{T}}(\boldsymbol{F}_{xy}\boldsymbol{F}_{yz}\boldsymbol{l}_i)}}{\sqrt{(\boldsymbol{F}_{xy}\boldsymbol{l}_i)^{\mathrm{T}}(\boldsymbol{F}_{xy}\boldsymbol{l}_i)}}\right), \end{aligned} \tag{3.70} $$

Depending on the system configuration $\boldsymbol{c}_\bullet(i) \in \mathbb{R}^{8\times 1}$ changes. The cable length vector $\boldsymbol{l}_i$ for cable i is given by Equation (2.6). Under the assumption of fixed cable lengths, the kinetic energy for one cable reads:

$$ T_{C_i} = \frac{1}{2}\,{}^{C_i}\dot{\boldsymbol{q}}_{C_i}^{\mathrm{T}}\boldsymbol{M}_{C_i}(\boldsymbol{q}_P)\,{}^{C_i}\dot{\boldsymbol{q}}_{C_i}\,, \tag{3.71} $$

$$ T_{C_i} = \frac{1}{2}\dot{\boldsymbol{q}}_{C_i}^{\mathrm{T}}\,{}^{C_i}\boldsymbol{R}_W(\boldsymbol{q}_P)^{\mathrm{T}}\boldsymbol{M}_{C_i}(\boldsymbol{q}_P)\,{}^{C_i}\boldsymbol{R}_W(\boldsymbol{q}_P)\dot{\boldsymbol{q}}_{C_i}\,, \tag{3.72} $$

with the mass matrix

$$ \boldsymbol{M}_{C_i}(\boldsymbol{q}_P) = \frac{1}{2}\mu\ \mathrm{diag}\left\{l_{seg,i}, 2l_{seg,i}, \cdots, 2l_{seg,i}, l_{seg,i},\right\} \otimes \boldsymbol{I}_{3\times 3}\,, \tag{3.73} $$

where $(\bullet_1 \otimes \bullet_2)$ denotes the Kronecker product of $\bullet_1$ and $\bullet_2$. For now ${}^{C_i}\boldsymbol{R}_W(\boldsymbol{q}_P)$ is constant

since the platform pose is fixed and thus $\frac{\mathrm{d}}{\mathrm{d}t}{}^{C_i}\boldsymbol{R}_W(\boldsymbol{q}_P) = \boldsymbol{0}^{3n_i}$. The potential energy of one cable is the composition of the gravitational potential energy $V_{C_i,g}$ and the contribution of the cable elasticity $V_{C_i,el}$, i.e.:

$$
\begin{aligned}
V_{C_i} &= V_{C_i,g} + V_{C_i,el} && (3.74)\\
V_{C_i,el} &= \frac{1}{2}\boldsymbol{\mu}(\boldsymbol{q}_P)^{\mathrm{T}\,C_i}\boldsymbol{R}_W(\boldsymbol{q}_P)^{\mathrm{T}}\boldsymbol{K}_{C_i}{}^{C_i}\boldsymbol{R}_W(\boldsymbol{q}_P)\boldsymbol{\mu}(\boldsymbol{q}_P) && (3.75)\\
V_{C_i,g} &= \sum_{j=1}^{n_i} m_{C_i,j} g\ \boldsymbol{q}_{C_i,j}^{\mathrm{T}}\boldsymbol{e}_3, && (3.76)
\end{aligned}
$$

where g is the gravitational constant, $\boldsymbol{e}_3 = \begin{bmatrix}0 & 0 & 1\end{bmatrix}^{\mathrm{T}}$ and $\boldsymbol{K}_{C_i}$ the stiffness matrix according to Equation (2.36). Then the Hamiltonian energy function for one cable is the sum of Equation (3.72)-(3.76):

$$
\begin{aligned}
H = T_{C_i} + V_{C_i} = &\frac{1}{2}{}^{C_i}\dot{\boldsymbol{q}}_{C_i}^{\mathrm{T}}\boldsymbol{M}_{C_i}(\boldsymbol{q}_P){}^{C_i}\dot{\boldsymbol{q}}_{C_i}\\
&+\frac{1}{2}\boldsymbol{\mu}(\boldsymbol{q}_P)^{\mathrm{T}\,C_i}\boldsymbol{R}_W(\boldsymbol{q}_P)\boldsymbol{K}_{C_i}{}^{C_i}\boldsymbol{R}_W(\boldsymbol{q}_P)\boldsymbol{\mu}(\boldsymbol{q}_P)\\
&+\sum_{j=1}^{n_i} m_{C_i,j} g\ \boldsymbol{q}_{C_i,j}^{\mathrm{T}}\boldsymbol{e}_3\,.
\end{aligned}
\qquad (3.77)
$$

Equation (2.64) shows a system in Port-Hamilton representation based on flow and effort variables

$$
\begin{bmatrix}\dot{\boldsymbol{q}}_{C_i}^{\mathrm{T}} & \dot{\boldsymbol{p}}_{C_i}^{\mathrm{T}}\end{bmatrix}^{\mathrm{T}} \qquad \textbf{and} \qquad \begin{bmatrix}\frac{\partial H(\boldsymbol{p}_{C_i},\boldsymbol{q}_{C_i})}{\partial \boldsymbol{q}_{C_i}}^{\mathrm{T}} & \frac{\partial H(\boldsymbol{p}_{C_i},\boldsymbol{q}_{C_i})}{\partial \boldsymbol{p}_{C_i}}^{\mathrm{T}}\end{bmatrix}^{\mathrm{T}}
$$

Given (3.77), those are:

$$
\begin{aligned}
\frac{\partial H(\boldsymbol{q}_{C_i},\boldsymbol{p}_{C_i})}{\partial \boldsymbol{q}_{C_i}} &= {}^{C_i}\boldsymbol{R}_W^{\mathrm{T}}\boldsymbol{K}_{C_i}{}^{C_i}\boldsymbol{R}_W\boldsymbol{\mu}(\boldsymbol{q}_P) && (3.78)\\
&\quad +\boldsymbol{M}_{C_i}(\boldsymbol{q}_P)\boldsymbol{1}_{n_i\times 1}\otimes\begin{bmatrix}0 & 0 & g\end{bmatrix}^{\mathrm{T}} && (3.79)\\
\frac{\partial H(\boldsymbol{q}_{C_i},\boldsymbol{p}_{C_i})}{\partial \boldsymbol{p}_{C_i}} &= {}^{C_i}\boldsymbol{R}_W^{\mathrm{T}}\boldsymbol{M}_{C_i}(\boldsymbol{q}_P){}^{C_i}\boldsymbol{R}_W\boldsymbol{p}_{C_i}\,. && (3.80)
\end{aligned}
$$

Including the control input $\boldsymbol{u}_{c,C_i}$ boundary forces $\boldsymbol{u}_{b,C_i}$ and external disturbances $\boldsymbol{u}_{\zeta,C_i}$, the Port-Hamilton representation for cable i then is:

$$\begin{bmatrix}\dot{\boldsymbol{q}}\\ \dot{\boldsymbol{p}}\end{bmatrix} = \left(\underbrace{\begin{bmatrix}\boldsymbol{0}_{3n_i} & \boldsymbol{I}_{3n_i}\\ -\boldsymbol{I}_{3n_i} & \boldsymbol{0}_{3n_i}\end{bmatrix}}_{\boldsymbol{I}_C} - \underbrace{\begin{bmatrix}\boldsymbol{0}_{3n_i} & \boldsymbol{0}_{3n_i}\\ \boldsymbol{0}_{3n_i} & \boldsymbol{D}\end{bmatrix}}_{\boldsymbol{R}}\right) \tag{3.81}$$

$$\begin{bmatrix}\frac{\partial H(\boldsymbol{p},\boldsymbol{q})}{\partial \boldsymbol{q}}\\ \frac{\partial H(\boldsymbol{p},\boldsymbol{q})}{\partial \boldsymbol{p}}\end{bmatrix} + \boldsymbol{G}\boldsymbol{u}_{c,C_i} + \boldsymbol{u}_{b,C_i} + \boldsymbol{u}_{\zeta,C_i} \tag{3.82}$$

$$\boldsymbol{y} = \boldsymbol{G}^{\mathrm{T}}(\boldsymbol{q},\boldsymbol{p})\begin{bmatrix}\frac{\partial H(\boldsymbol{p},\boldsymbol{q})}{\partial \boldsymbol{q}}\\ \frac{\partial H(\boldsymbol{p},\boldsymbol{q})}{\partial \boldsymbol{p}}\end{bmatrix}. \tag{3.83}$$

The boundary force $\boldsymbol{u}_{b,C_i}$ accommodates for the boundary conditions, i.e.

$$\boldsymbol{p}_{C_i,1} = \boldsymbol{a}_i \tag{3.84}$$

$$\boldsymbol{p}_{C_i,n_i} = \boldsymbol{r} + {}^{W}\boldsymbol{R}_P{}^{P}\boldsymbol{b}_i \tag{3.85}$$

and is chosen as:

$$\boldsymbol{u}_{b,C_i} = \begin{bmatrix}\boldsymbol{0}_{3n_i\times 1}\\ \boldsymbol{\Lambda}_b\begin{bmatrix}\left(\boldsymbol{q}_{C,1} - A\right)\\ \boldsymbol{0}_{3(n_i-2)\times 1}\\ \left(\boldsymbol{q}_{C,n_i} - \boldsymbol{q}_P - {}^{W}R_P(\boldsymbol{q}_P)^{P}\boldsymbol{b}_i\right)\end{bmatrix}\end{bmatrix}, \tag{3.86}$$

with a positive definite matrix $\boldsymbol{\Lambda}_b$, which has entries only on the main diagonal. This boundary force are equivalent to the Lagrangian multiplier for systems in Euler-Lagrange representation. Indeed, substituting Equation (3.78) and (3.80) in (3.81) and using $\boldsymbol{p}_{C_i} = \boldsymbol{M}_{C_i}\dot{\boldsymbol{q}}_{C_i}$, one obtains an ordinary differential equation of second order which is the Euler-Lagrange representation with boundary constraints and external disturbances.

3.5.2 Control of one cable in Port-Hamilton structure

Based on Equation (2.65) the control input matrix for one cable simply reads:

$$\boldsymbol{G} = \begin{bmatrix}\boldsymbol{0}_{3\times 3n_i} & \tilde{\boldsymbol{G}}^{\mathrm{T}}\end{bmatrix}^{\mathrm{T}} = \begin{bmatrix}\boldsymbol{0}_{3\times 3n_i} & \boldsymbol{I}_{3\times 3} & \boldsymbol{0}_{3\times 3(n_i-1)}\end{bmatrix}. \tag{3.87}$$

The boundary conditions inhibit motion of the first element. Thus for simulation the control input is acting at the second element. Assuming full state measurement of $\boldsymbol{q}_{C_i}$, the following controller improves significantly cable vibrations. Choosing

$$\begin{aligned}\boldsymbol{u}_{c,C_i} &= -\tilde{\boldsymbol{G}}^{\mathrm{T}}\left(\tilde{\boldsymbol{G}}\tilde{\boldsymbol{G}}^{\mathrm{T}} - \epsilon\boldsymbol{I}_{3n_i}\right)^{-1}\boldsymbol{D}_{C_i}^{\mathrm{T}}\boldsymbol{M}_{C_i}^{-1}\boldsymbol{p}_{C_i}\\ &= -\tilde{\boldsymbol{G}}^{\dagger}\boldsymbol{D}_{C_i}^{\mathrm{T}}\boldsymbol{M}_{C_i}^{-1}\boldsymbol{p}_{C_i}\end{aligned} \tag{3.88}$$

with $\epsilon \in \mathbb{R}^+$ sufficiently small[10], the additional positive definite diagonal damping matrix $\boldsymbol{D}_{C_i}$ and the positive definite diagonal matrix $\boldsymbol{\Lambda}_{C_i} \in \mathbb{R}^{3n_i}$ as design parameters, achieves an increase of $\boldsymbol{R}$ in Equation (3.81). The following proof will show that $\boldsymbol{u}_{c,C_i}$ according to Equation (3.88) increases $\boldsymbol{R}$ and stabilizes the system (3.81).

Proof. First we substitute

$$\boldsymbol{M}_{C_i}^{-1}\boldsymbol{p}_{C_i} = \frac{\partial \boldsymbol{H}(\boldsymbol{q}_{C_i}, \boldsymbol{p}_{C_i})}{\partial \boldsymbol{p}_{C_i}} \tag{3.89}$$

Now including (3.89) in (3.88) and later in (3.81) leads to:

$$\begin{aligned}\begin{bmatrix}\dot{\boldsymbol{q}}_{C_i}\\ \dot{\boldsymbol{p}}_{C_i}\end{bmatrix} = &\left(\underbrace{\begin{bmatrix}\boldsymbol{0}_{3n_i} & \boldsymbol{I}_{3n_i}\\ -\boldsymbol{I}_{3n_i} & \boldsymbol{0}_{3n_i}\end{bmatrix}}_{\boldsymbol{I}_{C_i}} - \underbrace{\begin{bmatrix}\boldsymbol{0}_{3n_i} & \boldsymbol{0}_{3n_i}\\ \boldsymbol{0}_{3n_i} & \boldsymbol{D}_{Friction}\end{bmatrix}}_{\boldsymbol{R}_{C_i}}\right)\begin{bmatrix}\frac{\partial \boldsymbol{H}(\boldsymbol{q}_{C_i},\boldsymbol{p}_{C_i})}{\partial \boldsymbol{q}_{C_i}}\\ \frac{\partial \boldsymbol{H}(\boldsymbol{q}_{C_i},\boldsymbol{p}_{C_i})}{\partial \boldsymbol{p}_{C_i}}\end{bmatrix} + \boldsymbol{u}_b\\ &- \underbrace{\begin{bmatrix}\boldsymbol{0}_{3n_i\times 3}\\ \tilde{\boldsymbol{G}}\end{bmatrix}\tilde{\boldsymbol{G}}^{\mathrm{T}}\left(\tilde{\boldsymbol{G}}\tilde{\boldsymbol{G}}^{\mathrm{T}} - \epsilon \boldsymbol{I}_{3n_i}\right)^{-1}}_{\approx \begin{bmatrix}\boldsymbol{0}_{3n_i\times 3n_i}\\ \boldsymbol{I}_{3n_i}\end{bmatrix}} \boldsymbol{D}_{C_i}\frac{\partial \boldsymbol{H}(\boldsymbol{q}_{C_i}, \boldsymbol{p}_{C_i})}{\partial \boldsymbol{p}_{C_i}},\end{aligned} \tag{3.90}$$

and

$$\begin{bmatrix}\dot{\boldsymbol{q}}_{C_i}\\ \dot{\boldsymbol{p}}_{C_i}\end{bmatrix} = \left(\underbrace{\begin{bmatrix}\boldsymbol{0}_{3n_i} & \boldsymbol{I}_{3n_i}\\ -\boldsymbol{I}_{3n_i} & \boldsymbol{0}_{3n_i}\end{bmatrix}}_{\boldsymbol{J}_{C_i}} - \underbrace{\begin{bmatrix}\boldsymbol{0}_{3n_i} & \boldsymbol{0}_{3n_i}\\ \boldsymbol{0}_{3n_i} & \boldsymbol{D}_{Friction} + \boldsymbol{D}_{C_i}\end{bmatrix}}_{\bar{\boldsymbol{R}}}\right)\begin{bmatrix}\frac{\partial \boldsymbol{H}(\boldsymbol{q}_{C_i},\boldsymbol{p}_{C_i})}{\partial \boldsymbol{q}_{C_i}}\\ \frac{\partial \boldsymbol{H}(\boldsymbol{q}_{C_i},\boldsymbol{p}_{C_i})}{\partial \boldsymbol{p}_{C_i}}\end{bmatrix} + \boldsymbol{u}_{b,C_i}, \tag{3.91}$$

with $\bar{\boldsymbol{R}} > \boldsymbol{R}$ since $\boldsymbol{D}_{C_i} > 0$

Passivity and stability proofs of (3.91) in Port-Hamilton representation are very comfortable. Taking the Hamiltonian H of a system (2.64) as Lyapunov function candidate V provides:

- Positive Lyapunov function: $V(\boldsymbol{x}) = H(\boldsymbol{x}) \geq 0$ and,

[10] Introducing ϵ is necessary to ensure that the pseudo inverse of $\boldsymbol{G}$ exists

- Negative time derivative of the Lyapunov function:

$$\begin{aligned}\dot{V}(\boldsymbol{x}) &= \frac{\partial H(\boldsymbol{x})}{\partial \boldsymbol{x}}^{\mathrm{T}} \dot{\boldsymbol{x}} = -\frac{\partial H(\boldsymbol{x})}{\partial \boldsymbol{x}}^{\mathrm{T}} \boldsymbol{R} \frac{\partial H(\boldsymbol{x})}{\partial \boldsymbol{x}} + \frac{\partial H(\boldsymbol{x})}{\partial \boldsymbol{x}}^{\mathrm{T}} \boldsymbol{G} \boldsymbol{u}_{c,C_i} \\ &= -\frac{\partial H(\boldsymbol{x})}{\partial \boldsymbol{x}} \boldsymbol{R} \frac{\partial H(\boldsymbol{x})}{\partial \boldsymbol{x}} - \frac{\partial H(\boldsymbol{x})}{\partial \boldsymbol{x}}^{\mathrm{T}} \boldsymbol{G} \tilde{\boldsymbol{G}}^{\dagger} \boldsymbol{D}_{C_i} \boldsymbol{M}_{C_i}^{-1} \boldsymbol{p}_{C_i} \\ &= -\frac{\partial H(\boldsymbol{x})}{\partial \boldsymbol{x}} \boldsymbol{R} \frac{\partial H(\boldsymbol{x})}{\partial \boldsymbol{x}} - \underbrace{\frac{\partial H(\boldsymbol{x})}{\partial \boldsymbol{p}_{C_i}}^{\mathrm{T}} \boldsymbol{D}_{C_i} \frac{\partial H(\boldsymbol{x})}{\partial \boldsymbol{p}_{C_i}}}_{\leq 0} \leq 0 \end{aligned} \tag{3.92}$$

□

In general every system

$$\begin{bmatrix} \dot{\boldsymbol{q}} \\ \dot{\boldsymbol{p}} \end{bmatrix} = (\boldsymbol{I} - \boldsymbol{R}) \begin{bmatrix} \frac{\partial \boldsymbol{H}(\boldsymbol{q}_{C_i}, \boldsymbol{p}_{C_i})}{\partial \boldsymbol{q}_{C_i}} \\ \frac{\partial \boldsymbol{H}(\boldsymbol{q}_{C_i}, \boldsymbol{p}_{C_i})}{\partial \boldsymbol{p}_{C_i}} \end{bmatrix} \tag{3.93}$$

in Port-Hamilton form with a positive definite damping matrix $\boldsymbol{R}$ and no external control input is strictly passive. A control input which increases $\boldsymbol{R}$, makes the Hamiltonian H dissipate faster.

Note that $\boldsymbol{u}_{C_i} \in \mathbb{R}^{3\times 1}$ requires application of a 3 dimensional force, although cables can exert forces in only one dimension, i.e. they can only pull. In this case Equation (3.87) changes to

$$\boldsymbol{G} = \begin{bmatrix} \boldsymbol{0}_{3\times 3n_i} & \tilde{\boldsymbol{G}}^{\mathrm{T}} \end{bmatrix}^{\mathrm{T}} = \begin{bmatrix} \boldsymbol{0}_{3\times 3n_i} & \mathrm{diag}\{[0\,,1\,,0]\} & \boldsymbol{0}_{3\times 3(n_i-1)} \end{bmatrix} . \tag{3.94}$$

When $\boldsymbol{u}_{C_i} = u_{C_i} \in \mathbb{R}$ the previous proof does not hold only under the assumption of decoupled dynamics. Thus it is still an open task to proof stability and passivity for the particular case of a scalar control input with coupled dynamics. As mentioned before, full state measurement is not available and one has to lower one's sights regarding the controller performance. However, assuming measurement of the second last element and the second element still provides information to guess the power of vibrations. This corresponds to Inertial Measurement Unit measurements at the onboard connection point at at the pulley. Already the controller proposed by Equation (3.95) let vibrations decay and vibrations reduce faster as the following simulation results state.

In this simulation one cable with 10 elements and dynamics in Port-Hamilton structure is subject to external forces that act as step force function from $0.4s$ to $2.9s$, from $5.15s$ to $6.15s$ and from $10.3s$ to $11.3s$ on the 5^{th} cable. After the cable is released again, the controller in Equation (3.95) adjusts the cable tensions to drive $\boldsymbol{p}_{C_i}$ to zero. This simulation distinguishes between three cases:

C1) Observation of all elements and control of the element proximal to the pulley by a wrench

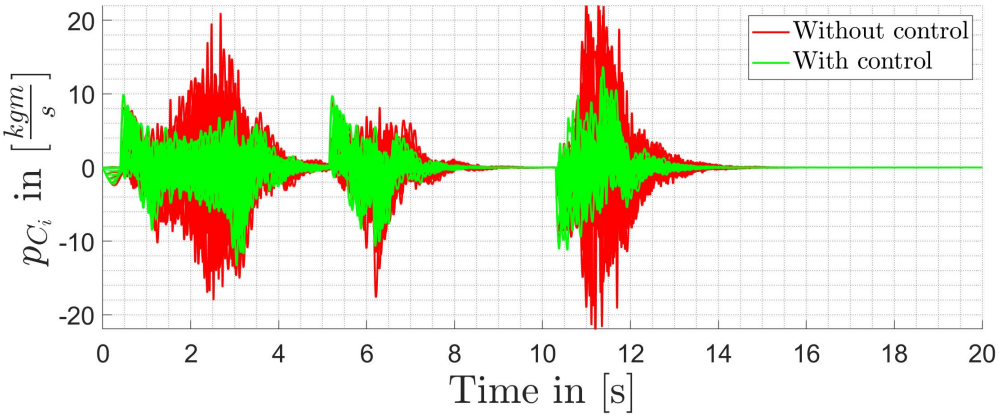

Figure 3.23: Generalised momentum for one cable - Condition C1)

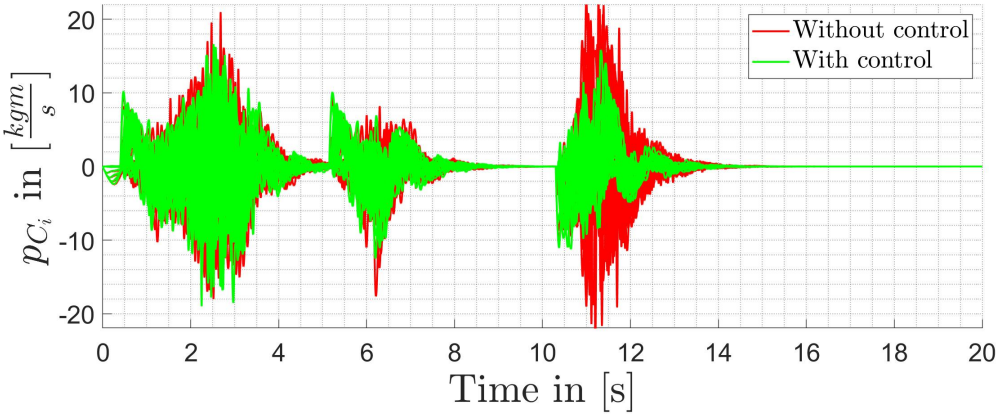

Figure 3.24: Generalised momentum for one cable - Condition C2)

C2) Observation of pulley panning and motion of the element proximal to the platform with control of the element proximal to the pulley in cable direction only

C3) Ideal case of full observation and full control of every element

Figure 3.23 shows the generalised momentum of all markers under condition C1). Red lines illustrate the generalised momentum for the uncontrolled cable and green lines denote the generalised momentum for the controlled cable. Although, there is no possibility to control the markers between the winch and the platform, the control input (3.88) suppresses efficiently cable vibrations in the scope of its abilities. Figure 3.26 shows the sum of kinetic energies over all elements for the uncontrolled and the controlled system with full state measurement and control of the element proximal to the pulley. The kinetic energy is more intuitive for rating the controller performance. Over the entire simulation the controller reduces the energy assigned to vibration. The sum of kinetic energies for the controlled system under condition C1) reduces by maximal 92.53% at 11.28s with respect to the uncontrolled

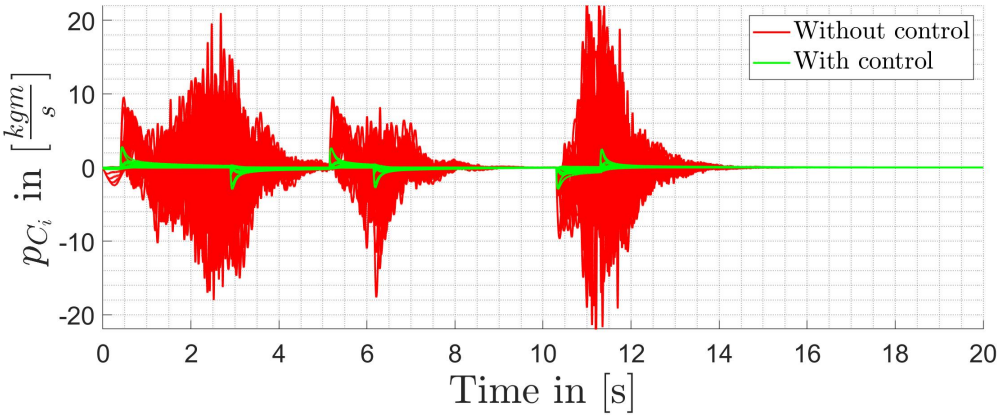

Figure 3.25: Generalised momentum for one cable - Condition C3) $\tilde{G} = I_{3n_e \times 3n_e}$

system. Now, assuming condition C2), the ideal control input (3.88) changes to:

$$\boldsymbol{u}_{c,C_i} = -\boldsymbol{G}^{\mathrm{T}} \left(\boldsymbol{G}\boldsymbol{G}^{\mathrm{T}} - \epsilon \boldsymbol{I}_{3n_i}\right)^{-1} \boldsymbol{\Lambda}_{C_i} \boldsymbol{A}_o \boldsymbol{M}_{C_i}^{-1} \boldsymbol{p}_{C_i} \tag{3.95}$$

$$\boldsymbol{A}_o = \mathrm{diag}\{\left[\boldsymbol{0}_{1\times 3}, \boldsymbol{1}_{1\times 3}, \boldsymbol{0}_{1\times 3(n_i-4)+1}, [0,1,0], \boldsymbol{0}_{1\times 3}\right]\}. \tag{3.96}$$

With (3.95), vibrations are suppressed slightly worse (see Figure 3.24). The maximal sum of kinetic energies for the controlled system now reduces to 63.82% at 11.36s with respect to the uncontrolled system (see Figure 3.27). However, this degradation is marginal. Comparing Figure 3.24 and Figure 3.25 under condition C2) (see Figure 3.27 and Figure 3.28) with the idealistic case C3), one concludes, that the limitation in control are more relevant for vibration suppression, than full state measurement. Full control here means $\tilde{G} = I_{3n_e \times 3n_e}$.

Remark 3.5: So far the control input limits to control of one cable. Applying the proposed controller, two problems must be solved:

1. Distinguish desired accelerations, i.e. $\ddot{\boldsymbol{x}}_{des}$, and undesired accelerations, i.e. vibrations.

2. Distribute the computed wrench among all cables.

A simple high-pass filter filters desired and undesired accelerations to solve problem 1. Problem 2 refers to the tension distribution.

To draw a conclusion, the simple control input (3.88) and (3.95) suppress vibrations in the light of its possibilities. Since only bare control and measurement possibilities are given, one has to lower ones expectations regarding vibration suppression. However the proposed controller has, once incorporated in a holistic framework (including all cables), the potential to further improve.

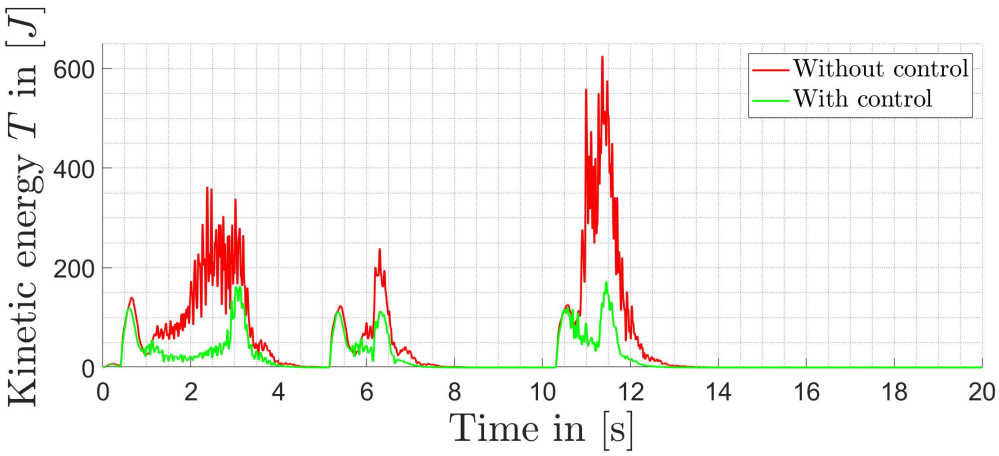

Figure 3.26: Sum of kinetic energies for one cable - Condition C1)

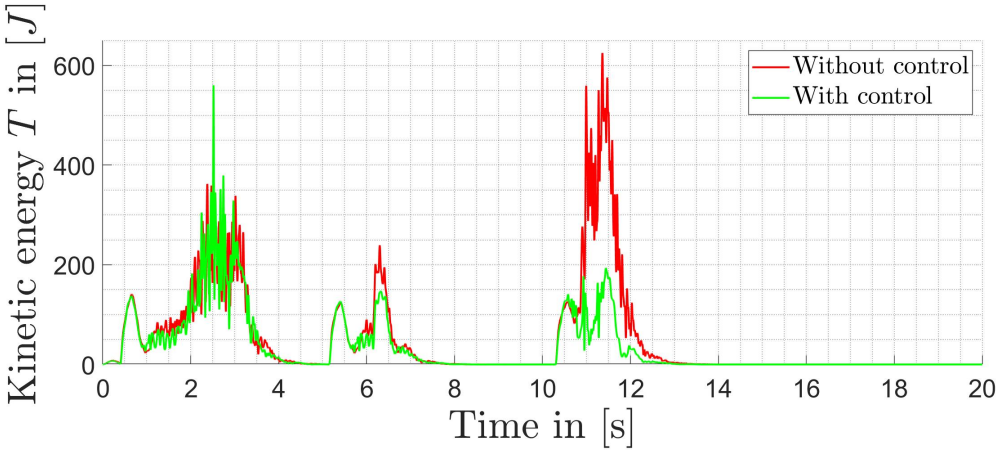

Figure 3.27: Sum of kinetic energies for one cable - Condition C2)

3.5.3 Port-Hamilton based modelling of the entire system

Section 3.5.1 provided all necessary kinematic and dynamic equations for a cable in Port-Hamilton representation. Those generic equations are valid for all cables and will be incorporated in the entire model. Note that the state vector of generalised coordinates and momentum then extends to $\boldsymbol{q} = [\boldsymbol{q}_P^{\mathrm{T}}\, \boldsymbol{q}_C^{\mathrm{T}}\, \boldsymbol{q}_M^{\mathrm{T}}]^{\mathrm{T}}$ where $\boldsymbol{q}_P \in \mathbb{R}^{3\times 1}$ are the generalised coordinates assigned to the platform, $\boldsymbol{q}_C = [\boldsymbol{q}_{C_1}^{\mathrm{T}}\, \boldsymbol{q}_{C_2}^{\mathrm{T}}\, \dots\, \boldsymbol{q}_{C_{n_i-1}}^{\mathrm{T}}\, \boldsymbol{q}_{C_{n_i}}^{\mathrm{T}}]^{\mathrm{T}} \in \mathbb{R}^{3n_i\times 1}$ and $\boldsymbol{q}_M \in \mathbb{R}^{8\times 1}$ are the generalised coordinates assigned to the motors. According to the size of $\boldsymbol{q}$ the rotation matrices for all cables, ${}^{C_i}\boldsymbol{R}_W(\boldsymbol{q}_P)$ extend to and for all cables

$$
\begin{aligned}
{}^{C}\bar{\boldsymbol{R}}_W(\boldsymbol{q}_P) &= \operatorname{diag}\left\{{}^{C,1}\hat{\boldsymbol{R}}_W(\boldsymbol{q}_P), \dots, {}^{C,8}\hat{\boldsymbol{R}}_W(\boldsymbol{q}_P)\right\} && (3.97)\\
{}^{C_i}\hat{\boldsymbol{R}}_W(\boldsymbol{q}_P) &= \operatorname{diag}\left\{{}^{C_i}\boldsymbol{R}_W(\boldsymbol{q}_P), \dots, {}^{C_i}\boldsymbol{R}_W(\boldsymbol{q}_P)\right\}\,. && (3.98)
\end{aligned}
$$

This assumptions implies a negligible influence of vibrations on the orientation of each element. For kinematics, this assumption is valid [19]. Then with the rotation matrix for all

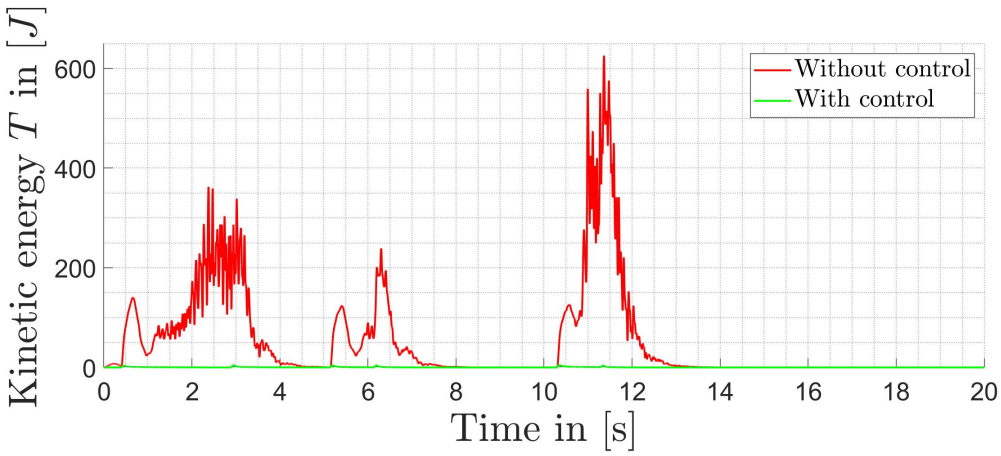

Figure 3.28: Sum of kinetic energies for one cable - Condition C3) $\tilde{G} = I_{3n_e \times 3n_e}$

cables and elements, the transformation of ${}^{C}\boldsymbol{q}_C = \begin{bmatrix} {}^{C_1}\boldsymbol{q}_{C_1} & \dots & {}^{C_m}\boldsymbol{q}_{C_m} \end{bmatrix}$ to $\boldsymbol{q}_C$ is:

$$\boldsymbol{q}_C = {}^{W}\bar{\boldsymbol{R}}_C(\boldsymbol{q}_P)\,{}^{C}\boldsymbol{q}_C\,,\; {}^{C}\boldsymbol{q}_C = {}^{C}\bar{\boldsymbol{R}}_W(\boldsymbol{q}_P)\boldsymbol{q}_C\,. \tag{3.99}$$

This transformation describes the position of all elements and the platform in the same frame $\mathcal{K}_W$.

The kinetic energy of each cable in Equation (3.77) depends on ${}^{C_i}\dot{\boldsymbol{q}}_{C_i}$ such that the time derivative of Equation (3.99):

$${}^{C}\dot{\boldsymbol{q}}_C = {}^{C}\dot{\bar{\boldsymbol{R}}}_W(\boldsymbol{q}_P)\,{}^{W}\boldsymbol{q}_C + {}^{C}\bar{\boldsymbol{R}}_W(\boldsymbol{q}_P)\,{}^{W}\dot{\boldsymbol{q}}_C\,, \tag{3.100}$$

with ${}^{C}\dot{\bar{\boldsymbol{R}}}_W$ is required. Note that ${}^{C}\dot{\bar{\boldsymbol{R}}}_W$ consists of submatrices ${}^{C_i}\dot{\bar{\boldsymbol{R}}}_W$ and each submatrix is a 3×3 matrix:

$${}^{C_i}\dot{\bar{\boldsymbol{R}}}_W(\boldsymbol{q}_P) = \begin{bmatrix} {}^{C_i}\dot{\boldsymbol{R}}_{W,11}(\boldsymbol{q}_P) & {}^{C_i}\dot{\boldsymbol{R}}_{W,12}(\boldsymbol{q}_P) & {}^{C_i}\dot{\boldsymbol{R}}_{W,13}(\boldsymbol{q}_P) \\ {}^{C_i}\dot{\boldsymbol{R}}_{W,21}(\boldsymbol{q}_P) & {}^{C_i}\dot{\boldsymbol{R}}_{W,22}(\boldsymbol{q}_P) & {}^{C_i}\dot{\boldsymbol{R}}_{W,23}(\boldsymbol{q}_P) \\ {}^{C_i}\dot{\boldsymbol{R}}_{W,31}(\boldsymbol{q}_P) & {}^{C_i}\dot{\boldsymbol{R}}_{W,32}(\boldsymbol{q}_P) & {}^{C_i}\dot{\boldsymbol{R}}_{W,33}(\boldsymbol{q}_P) \end{bmatrix}. \tag{3.101}$$

Each entry of (3.101) is:

$$\begin{aligned} {}^{C_i}\dot{\boldsymbol{R}}_{W,kl}(\boldsymbol{q}_p) &= \left(\frac{\partial {}^{C_i}\boldsymbol{R}_{W,kl}(\boldsymbol{q}_P)}{\partial \boldsymbol{q}_P}\right)^{\mathrm{T}} \dot{\boldsymbol{q}}_P \\ &= \underbrace{\nabla {}^{C_i}\boldsymbol{R}_{W,kl}(\boldsymbol{q}_P)}_{\in \mathbb{R}^{1\times 6}}\,\underbrace{\dot{\boldsymbol{q}}_P}_{\in \mathbb{R}^{6\times 1}} \end{aligned}$$

with $\nabla = \left[\frac{\partial}{\partial \boldsymbol{q}_{Pt}}\;\frac{\partial}{\partial \boldsymbol{q}_{Pr}}\right] = \left[\frac{\partial}{\partial x_p}\;\frac{\partial}{\partial y_p}\;\frac{\partial}{\partial z_p}\;\frac{\partial}{\partial \phi}\;\frac{\partial}{\partial \theta}\;\frac{\partial}{\partial \psi}\right]$. In compact form Equation (3.101) reads:

$${}^{C_i}\dot{\boldsymbol{R}}_W(\boldsymbol{q}_P) = \boldsymbol{D}_{C_i}(\boldsymbol{q}_P)\boldsymbol{S}_{C_i}(\dot{\boldsymbol{q}}_P) \in \mathbb{R}^{3\times 3}, \tag{3.102}$$

where

$$D_{C_i}(\boldsymbol{q}_p) = \begin{bmatrix} \nabla^{C_i}\boldsymbol{R}_{W,11}(\boldsymbol{q}_P) & \nabla^{C_i}\boldsymbol{R}_{W,12}(\boldsymbol{q}_P) & \nabla^{C_i}\boldsymbol{R}_{W,13}(\boldsymbol{q}_P) \\ \nabla^{C_i}\boldsymbol{R}_{W,21}(\boldsymbol{q}_P) & \nabla^{C_i}\boldsymbol{R}_{W,22}(\boldsymbol{q}_P) & \nabla^{C_i}\boldsymbol{R}_{W,23}(\boldsymbol{q}_P) \\ \nabla^{C_i}\boldsymbol{R}_{W,31}(\boldsymbol{q}_P) & \nabla^{C_i}\boldsymbol{R}_{W,32}(\boldsymbol{q}_P) & \nabla^{C_i}\boldsymbol{R}_{W,33}(\boldsymbol{q}_P) \end{bmatrix} \in \mathbb{R}^{3\times 18}$$

$$\boldsymbol{S}_{C_i}(\dot{\boldsymbol{q}}_p) = \begin{bmatrix} \dot{\boldsymbol{q}}_P & \boldsymbol{0}_{6\times 1} & \boldsymbol{0}_{6\times 1} \\ \boldsymbol{0}_{6\times 1} & \dot{\boldsymbol{q}}_P & \boldsymbol{0}_{6\times 1} \\ \boldsymbol{0}_{6\times 1} & \boldsymbol{0}_{6\times 1} & \dot{\boldsymbol{q}}_P \end{bmatrix} \in \mathbb{R}^{18\times 3}.$$

Reformulating the product $\boldsymbol{S}_{C_i}(\dot{\boldsymbol{q}}_P)\ \boldsymbol{q}_{C,i,j}$ leads to the comfortable formulation:

$$\boldsymbol{S}_{C_i}(\dot{\boldsymbol{q}}_P)\ \boldsymbol{q}_{C_i,j} = \underbrace{\begin{bmatrix} \dot{\boldsymbol{q}}_P\ \boldsymbol{q}_{C_i,j,x} \\ \dot{\boldsymbol{q}}_P\ \boldsymbol{q}_{C_i,j,y} \\ \dot{\boldsymbol{q}}_P\ \boldsymbol{q}_{C_i,j,z} \end{bmatrix}}_{\in\mathbb{R}^{18\times 1}} = \underbrace{\begin{bmatrix} \boldsymbol{I}_{6\times 6}\ \boldsymbol{q}_{C_i,j,x} \\ \boldsymbol{I}_{6\times 6}\ \boldsymbol{q}_{C_i,j,y} \\ \boldsymbol{I}_{6\times 6}\ \boldsymbol{q}_{C_i,j,z} \end{bmatrix}}_{\boldsymbol{\Lambda}_i(\boldsymbol{q}_{C_i})\in\mathbb{R}^{18\times 6}} \dot{\boldsymbol{q}}_P, \tag{3.103}$$

Finally, inserting Equations (3.101)-(3.103) in Equation (3.100) leads to:

$${}^{C}\dot{\boldsymbol{q}}_C = \bar{\boldsymbol{D}}_C(\boldsymbol{q}_P)\bar{\boldsymbol{\Lambda}}_C(\boldsymbol{q}_C)\dot{\boldsymbol{q}}_P + \bar{\boldsymbol{R}}(\boldsymbol{q}_P)\dot{\boldsymbol{q}}_C \tag{3.104}$$

$${}^{C}\dot{\boldsymbol{q}}_C = \bar{\boldsymbol{\Gamma}}_C(\boldsymbol{q}_P,\boldsymbol{q}_C)\dot{\boldsymbol{q}}_P + \bar{\boldsymbol{\Omega}}_C(\boldsymbol{q}_P)\dot{\boldsymbol{q}}_C\,. \tag{3.105}$$

Given the kinematic equation for all cables and the platform from Chapter 2 all relations are available to continue with the dynamics of the entire system. The kinetic energy of the system includes the kinetic energy T_P of the platform, of the cables T_C and of the motors T_M, such that the total kinetic energy becomes:

$$\begin{aligned} T &= T_P + T_C + T_M \\ T_P &= \frac{1}{2}\ \dot{\boldsymbol{q}}_P^{\mathrm{T}}\ \boldsymbol{M}_P(\boldsymbol{q}_P)\ \dot{\boldsymbol{q}}_P \\ T_C &= \frac{1}{2}\sum_{i=1}^{m}\left({}^{C_i}\dot{\boldsymbol{q}}_{C_i}^{\mathrm{T}}\boldsymbol{M}_{C_i}(\boldsymbol{q}_P){}^{C_i}\dot{\boldsymbol{q}}_{C_i}\right) \end{aligned}, \tag{3.106}$$

with:

$$\boldsymbol{M}_P(\boldsymbol{q}_P) = \begin{bmatrix} m_P\boldsymbol{I}_{3\times 3} & \boldsymbol{0}_{3\times 3} \\ \boldsymbol{0}_{3\times 3} & {}^{\mu}\boldsymbol{E}_{\boldsymbol{\omega}}^{\mathrm{T}}(\boldsymbol{q}_{Pr}){}^{W}\boldsymbol{R}_P^{\mathrm{T}}{}^{P}\boldsymbol{I}_P{}^{W}\boldsymbol{R}_P{}^{\boldsymbol{\omega}}\boldsymbol{E}_{\boldsymbol{\mu}}(\boldsymbol{q}_{Pr}) \end{bmatrix}. \tag{3.107}$$

Equation (3.104) inserted in Equation (3.106), the kinetic energy of all cables changes to:

$$\begin{aligned} T_C = &\frac{1}{2}\sum_{i=1}^{m}\Big[\dot{\boldsymbol{q}}_{C_i}^{\mathrm{T}}\Big(\boldsymbol{\Omega}_i^{\mathrm{T}}(\boldsymbol{q})\boldsymbol{M}_{C_i}(\boldsymbol{q}_P)\boldsymbol{\Omega}_i(\boldsymbol{q})\Big)\dot{\boldsymbol{q}}_{C_i} \\ &+ \dot{\boldsymbol{q}}_P^{\mathrm{T}}\Big(\boldsymbol{\Gamma}_i^{\mathrm{T}}(\boldsymbol{q})\boldsymbol{M}_{C_i}(\boldsymbol{q}_P)\boldsymbol{\Gamma}_i(\boldsymbol{q})\Big)\dot{\boldsymbol{q}}_P \\ &+ 2\ \dot{\boldsymbol{q}}_{C_i}^{\mathrm{T}}\boldsymbol{\Omega}_i^{\mathrm{T}}(\boldsymbol{q})\boldsymbol{M}_{C_i}(\boldsymbol{q}_P)\boldsymbol{\Gamma}_i(\boldsymbol{q})\dot{\boldsymbol{q}}_P\Big]. \end{aligned} \tag{3.108}$$

For the sake of simplicity, a rotation cylinder with inertia $\boldsymbol{I}_M = {}^1\!/_2\, m_d r_d^2$ represents one motor with the kinetic energy

$$T_M = \frac{1}{2}\sum_{i=1}^{m} \dot{\theta}_{M_i}^2 m_d r_d^2 \tag{3.109}$$

where $\dot{\theta}_{M_i}$ is the motor angle of motor i, $m_d \in \mathbb{R}^+$ is the nominal mass and $r_d \in \mathbb{R}^+$ is the nominal radius of one motor drum. There is no contribution of the motors to the potential energy, since those are placed on the ground. The potential energies include only the contribution of the platform and the cables. Thus the total potential energy of the system is:

$$\begin{aligned} V(\boldsymbol{q}) &= V_P(\boldsymbol{q}) + V_C(\boldsymbol{q}) && (3.110)\\ V_P(\boldsymbol{q}) &= m_P g\ \boldsymbol{q}_P^{\mathrm{T}}\ [0\ 0\ 1\ 0\ 0\ 0] && (3.111)\\ V_C(\boldsymbol{q}) &= V_{Cg} + V_{Ce} && (3.112) \end{aligned}$$

and

$$\begin{aligned} V_{Cg}(\boldsymbol{q}) &= \sum_{i=1}^{m}\sum_{j=1}^{n_i} m_{C_i,j} g\ \boldsymbol{q}_{C_i,j}^{\mathrm{T}} \boldsymbol{e}_3^{\mathrm{T}} \\ V_{Ce} &= \sum_{i=1}^{m} V_{Ce,1} \\ V_{Ce,i} &= \frac{1}{2}({}^{C_i}\boldsymbol{q}_{C_i} - {}^{C_i}\bar{\boldsymbol{q}}_{C_i}(\boldsymbol{q}_P))^{\mathrm{T}} \boldsymbol{K}_{C_i}(\boldsymbol{q}_P)({}^{C_i}\boldsymbol{q}_{C_i} - {}^{C_i}\bar{\boldsymbol{q}}_{C_i}(\boldsymbol{q}_P)) \\ &= \frac{1}{2}(\boldsymbol{q}_{C_i} - \bar{\boldsymbol{q}}_{C_i}(\boldsymbol{q}_P))^{\mathrm{T}} \bar{\boldsymbol{K}}_{C_i}(\boldsymbol{q}_P)(\boldsymbol{q}_{C_i} - \bar{\boldsymbol{q}}_{C_i}(\boldsymbol{q}_P))\,. \end{aligned} \tag{3.113}$$

where $\boldsymbol{K}_{C_i}$ is the stiffness matrix based on Equation (2.37)-(2.40) for cable i and

$$\bar{\boldsymbol{K}}_{C_i}(\boldsymbol{q}_P) = {}^{C_i}\boldsymbol{R}_W^{\mathrm{T}}(\boldsymbol{q}_P)\boldsymbol{K}_{\boldsymbol{\eta}}\,{}^{C_i}\boldsymbol{R}_W(\boldsymbol{q}_P)\,, \tag{3.114}$$

considers the change from individual cable frame to world frame. So far the cable lengths are constant and there is no winding/unwinding of the cables. When the cable lengths change, mass and energy transfers from the corresponding cable to the motor during the winding process and from the corresponding motor to the cable during the unwinding process. During the winding process the distance between an element proximal to the winch and the winch shrinks and the elasticity (2.40) of a cable segment approaches singularity. This is a conceptual flaw of the Finite-Element Method model. The right side of Figure 3.29 sketches the winding process in three steps. In the upper plot, the position of the first element equals the winch position of cable i, i.e. $\boldsymbol{q}_{C_i,1} = \boldsymbol{a}_i$ The middle and lower sketch illustrate the situation when the first or the first three elements are part of the motor. To circumvent this problem, $l_{seg,i}$ is assumed as constant, although the distance between the element proximal to the winch and the winch itself decreases. Detecting the pass of one element from a cable to the corresponding motor is easy. The projection of a vector pointing from the mass element

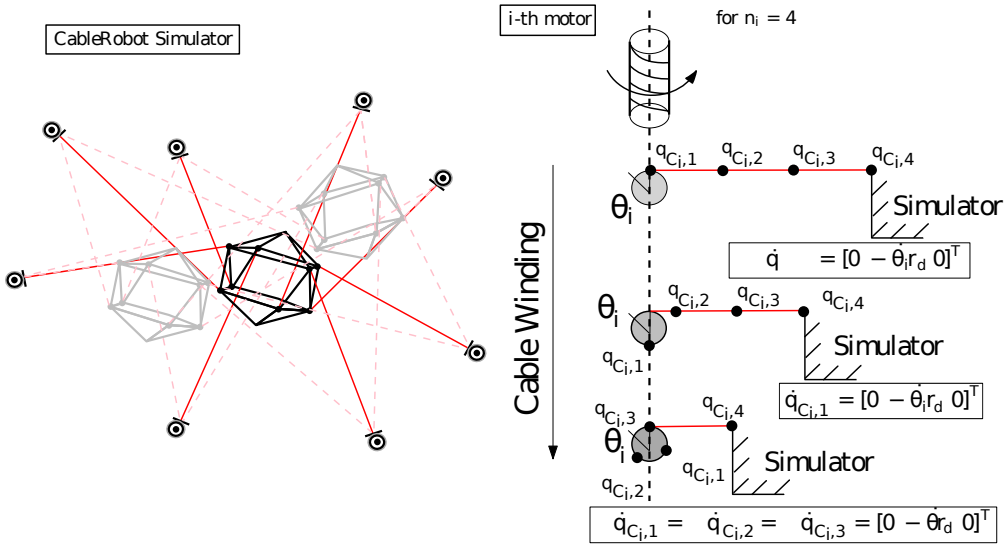

Figure 3.29: CDPR is in motion. The left sketch shows the Cable-Driven Parallel Robot in different poses and different cable length. To change the platform pose the cable lengths must change and cables wind on/unwind from the motor drum. The right sketch illustrates the winding process of motor i with $n_i = 4$ elements. The shorter the cable gets, the more mass elements transfer from cable side to motor side and attach rigidly on the drum. In this particular moment the wound elements do not contribute to the cable energy anymore.

of interest to the winch on the cable vector indicates the moment of transition by a change of the sign. Figure 3.30 illustrates this principle and shows how to compute the elements of an activation matrix $\boldsymbol{A}_{act,i}$ for cable i. This activation matrix consists of 1 or 0 on the main diagonal, depending whether an element is still free to move or part of the drum. In case of a free element $A_{j,j} = 1$ for $j = 1 \dots n_i$ and in case of a wound element $A_{j,j} = 0$. For each cable i, $\boldsymbol{A}_{act,i} \in \mathbb{R}^{3n_i}$ is:

$$\boldsymbol{A}_{act,i} = \operatorname{diag} \begin{bmatrix} \mathbf{1}_{3\times 1} \frac{1}{2} \left(1 + \operatorname{sign}\left((\boldsymbol{l}_{i,a|1} - \boldsymbol{a}_i)^{\mathrm{T}} \boldsymbol{l}_i\right)\right) \\ \mathbf{1}_{3\times 1} \frac{1}{2} \left(1 + \operatorname{sign}\left((\boldsymbol{l}_{i,a|2} - \boldsymbol{a}_i)^{\mathrm{T}} \boldsymbol{l}_i\right)\right) \\ \vdots \\ \mathbf{1}_{3\times 1} \frac{1}{2} \left(1 + \operatorname{sign}\left((\boldsymbol{l}_{i,a|n_i} - \boldsymbol{a}_i)^{\mathrm{T}} \boldsymbol{l}_i\right)\right) \end{bmatrix} \tag{3.115}$$

The product $\boldsymbol{A}_{act,i}\dot{\boldsymbol{q}}_{C_i}$ set the velocities of the wound elements to zero and keeps the velocities of the free elements. Now replacing $\dot{\boldsymbol{q}}_{C_i}$ with $\boldsymbol{A}_{act,i}\dot{\boldsymbol{q}}_{C_i}$ changes the kinetic energy of all cables to:

$$\begin{aligned} T_C = & \frac{1}{2} \sum_{i=1}^{m} \Big[\dot{\boldsymbol{q}}_{C_i}^{\mathrm{T}} \boldsymbol{A}_{act,i}^{\mathrm{T}} \bar{\boldsymbol{M}}_{C_i}(\boldsymbol{q}) \boldsymbol{A}_{act,i} \dot{\boldsymbol{q}}_{C_i} \\ & + \dot{\boldsymbol{q}}_P^{\mathrm{T}} \Big(\boldsymbol{A}_{act,i}^{\mathrm{T}} \boldsymbol{\Gamma}_{C_i}^{\mathrm{T}}(\boldsymbol{q}) \boldsymbol{M}_{C_i}(\boldsymbol{q}_P) \boldsymbol{\Gamma}_{C_i}(\boldsymbol{q}) \boldsymbol{A}_{act,i} \Big) \dot{\boldsymbol{q}}_P \\ & + 2 \, \dot{\boldsymbol{q}}_{C_i}^{\mathrm{T}} \boldsymbol{A}_{act,i}^{\mathrm{T}} \bar{\boldsymbol{M}}_{PC_i}(\boldsymbol{q}) \dot{\boldsymbol{q}}_P \Big] , \end{aligned} \tag{3.116}$$

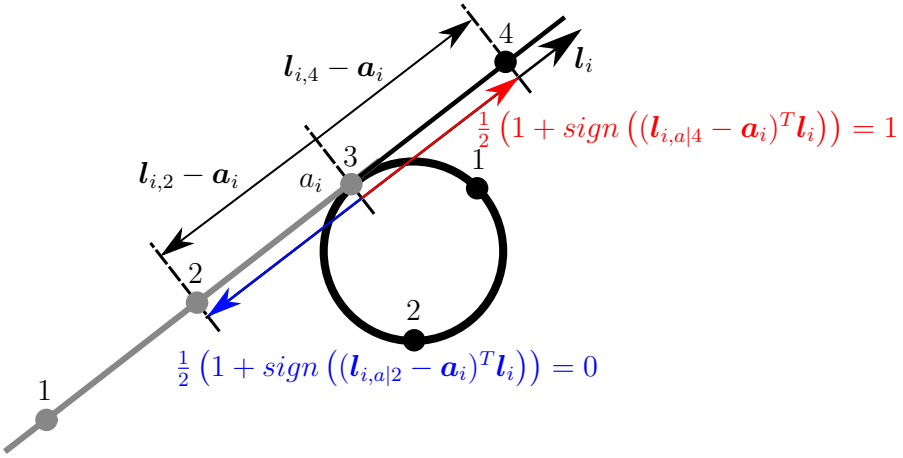

Figure 3.30: Transition of one motor from cable i to motor i and detection. The left side of the sketch illustrate all winded markers if the cable is not wound on the winch but continues in direction of the cable vector $\boldsymbol{l}_i$. The blue arrow illustrates the projection of $\boldsymbol{l}_{i,2} - \boldsymbol{a}_i$ on the cable vector $\boldsymbol{l}_i$. The scalar product of $\boldsymbol{l}_{i,a|2} - \boldsymbol{a}_i$ on $\boldsymbol{l}_i$ is negative and indicates that the element is wound. Here $\boldsymbol{l}_{i,a|j}$ is the vector pointing from the offboard connection point A_i to the corresponding element j. The red arrow illustrates the projection of $\boldsymbol{l}_{i,a|4} - \boldsymbol{a}_i$ on the cable vector $\boldsymbol{l}_i$. The scalar product of $\boldsymbol{l}_{i,4} - \boldsymbol{a}_i$ on $\boldsymbol{l}_i$ is positive and indicates that the element not part of the drum.

with:

$$\begin{aligned}
\mathbb{R}^{3n\times 3n} \ni \bar{\boldsymbol{M}}_C(\boldsymbol{q}) &= \text{blkdiag}\{\bar{\boldsymbol{M}}_{C,1}(\boldsymbol{q}), \cdots, \bar{\boldsymbol{M}}_{C,m}(\boldsymbol{q})\} \\
\mathbb{R}^{3n_i\times 3n_i} \ni \bar{\boldsymbol{M}}_{C_i}(\boldsymbol{q}) &= \boldsymbol{\Omega}_i^T(\boldsymbol{q})^{C_i}\boldsymbol{M}_{C_i}(\boldsymbol{p}_P)\boldsymbol{\Omega}_{C_i}(\boldsymbol{q}) \\
\mathbb{R}^{3n\times 6} \ni \bar{\boldsymbol{M}}_{PC}(\boldsymbol{q}) &= [\bar{\boldsymbol{M}}_{PC_i}^T(\boldsymbol{q}) \ \cdots \ \bar{\boldsymbol{M}}_{PC_i}^T(\boldsymbol{q})]^T \\
\mathbb{R}^{3n_i\times 6} \ni \bar{\boldsymbol{M}}_{PC_i}(\boldsymbol{q}) &= \boldsymbol{\Omega}_{C_i}^T(\boldsymbol{q})^{C_i}\boldsymbol{M}_{C_i}(\boldsymbol{p}_P)\boldsymbol{\Gamma}_{C_i}(\boldsymbol{q}),
\end{aligned}$$

the motor kinetic energy to:

$$T_M = \frac{1}{2}\sum_{i=1}^{m}\dot{\theta}_{M_i}^2(m_d + \underbrace{\sum_{j=1}^{n_i-\text{tr}(\boldsymbol{A}_{act,i})} m_{i,j}}_{:=0,\ \text{if}\ \text{tr}(\boldsymbol{A}_{act,i})=n_i})r_d^2, \tag{3.117}$$

and the potential cable energies to:

$$\begin{aligned}
V_C(\boldsymbol{q}) &= V_{Cg}(\boldsymbol{q}) + \sum_{i=1}^{m} V_{Ce,i} \\
V_{Cg}(\boldsymbol{q}) &= \sum_{i=1}^{m}\sum_{j=1}^{n_i} m_{C_i,j}g\ \boldsymbol{A}_{act,i}\boldsymbol{q}_{C_i,j}.\boldsymbol{e}_3 \\
V_{Ce_i}(\boldsymbol{q}) &= \frac{1}{2}\boldsymbol{\eta}_{C_i}^{\mathrm{T}}\boldsymbol{A}_{act,i}^{\mathrm{T}}\bar{\boldsymbol{K}}_{\boldsymbol{\eta}}\boldsymbol{A}_{act,i}\boldsymbol{\eta}_{C_i},
\end{aligned} \tag{3.118}$$

The winding process makes a Finite-Element Method based model a switching system. There exist approaches to proof dissipativity for these kind of systems [48, 49].

3.5.4 Summary of Chapter 3

Chapter 3 presents the model of a Cable-Driven Parallel Robot as well as proper control strategies, tackling the problem of vibration reduction on multiple levels. Chapter 3 also identifies most relevant sources for vibrations in three components. Literature research and experimental investigations revealed multiple sources for vibrations. Those with the most impact are:

- **Controller induced vibrations:** Actuation units such as motors induce motion to a system. Discontinuous or aggressive control strategies provoke chattering and induce vibrations to the drivetrain. A sophisticated control strategy is important to avoid or at least reduce controller induced vibrations.
- **Friction in mechanical components:** Most common types of friction are viscous, Coulomb and static friction. Viscous friction occurs, when two surfaces are in contact with each other and move with different velocities. During standstill the driving force applied by the motors oppose static friction force. As soon as the driving force expels the maximal stiction force, i.e. the break-away force, a jerk is induced to the cables. This jerk induces to the system vibrations.
- **Cable properties:** One step closer to the platform, cable elasticity and rigidity propagates and initiates vibrations due to elasticity and stiffness

To reduce vibrations on a control level the proposed control strategy splits up in three parts, i.e.:

- **Low-Level Controller tuning:** A control cascade including position, velocity and torque control provides more accurate results in terms of position and velocity tracking than direct torque control. On the other hand, including position and velocity control also requires additional controller tuning. The Beckhoff TwinCAT documentation provides a guide to tune the velocity controller by loop shaping and facilitates low-level controller tuning for this system. Proper cycletimes, prioritisation of tasks and well tuned controller parameters make the Low-Level Control track the desired trajectories smoothly.
- **Second control layer for compensation of friction in bearing:** Friction in bearings is one of the main contributor to vibrations. Especially stiction is of interest, since as soon as the driving force exceeds the break-away force, an impulse induces cable vibrations. This chapter proposes an adaptive friction compensation to incorporate time varying friction characteristics and stiction.
- **High-Level Control:** To achieve 2-sliding mode, i.e. position, velocity and acceleration tracking, Chapter 3 proposes an adaptive Super-Twisting Sliding-Mode Controller, that reduces chattering effects and preserves the advantages of Sliding-Mode

Controllers. A gain adaptation algorithm significantly reduces chattering and assures efficient perturbation compensation and good tracking performance. The combination of an adaptive Super-Twisting Sliding-Mode Controller, an arbitrary order Sliding-Mode Differentiator, an adaptive Super-Twisting Sliding-Mode Disturbance Observer and the Forwards Kinematics guarantee finite-time convergence, efficient perturbation rejection and robustness against lumped perturbations with a minimal set of measurements devices.

Second to last Chapter 3 presents a Dual Unscented Kalman-Filter for state and Inertial Measurement Unit bias estimation. Forward Kinematics suffices reconstruction of the platform pose, but does not incorporate platform acceleration and the impact of drivetrain dynamics on the platform. Besides more advanced control techniques for a Cable-Driven Parallel Robot rely on measurements of platform accelerations to incorporate cable dynamics in the control strategy. Thus Inertial Measurement Unit measurements can also be part of the platform state estimation. Finally this chapter presents the model of a single cable based on a Finite-Element Method model, fixed at both ends and subject to external disturbances and gravity. A simple stabilising control input reduces cable vibrations significantly and is proven to increase the systems dissipation rate. Simulations underline the efficiency. The model of one single cable then extends to the model of a Cable-Driven Parallel Robot including all cable dynamics and the platform in Port-Hamilton representation. This model also accounts for the winding process. Figure 3.31 illustrates the entire proposed control strategy for a Cable-Driven Parallel Robot, used in this work.

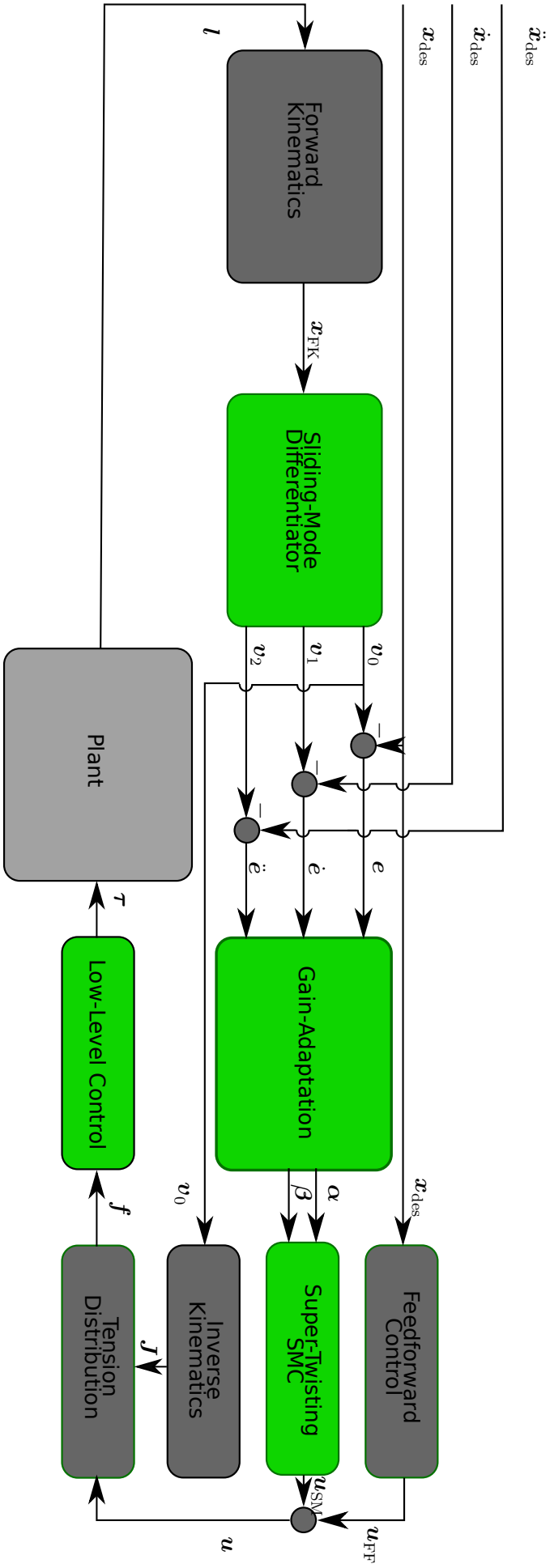

Figure 3.31: Control structure implemented in [20] and [22]. Blocks with green background depict contributions of this work. Those are the Sliding-Mode Differentiator, the gain adaptation algorithm, the Super-Twisting Sliding-Mode Controller and the investigation on a suitable Low-Level Control choice.

Chapter 4

Experimental evaluation

This chapter briefly introduces the Cablerobot Simulator [2] and the Mini Cablerobot Simulator. The calibration procedure of dynamic/kinematic parameters, and an analysis of the drivetrain characteristics are presented. Analysis of cable vibrations provide important insight into the cable dynamics and underlines the controller choice and cable model in Chapter 3. Finally, this chapter experimentally evaluates the adaptive Super-Twisting Sliding-Mode Controller and the adaptive friction compensation proposed in Chapter 3. Experiments prove the efficiency of the proposed control strategies

Chapter 1 introduces the principles of Cable-Driven Parallel Robots, their advantages and new challenges for Cable-Driven Parallel Robot as simulators. Chapter 3 provides solutions for vibration suppression, friction compensation, and also states, that cables are complex and non-linear systems with internal cross-couplings. The first section of this chapter underlines these statements with two experiments, which were conducted at the Cablerobot Simulator and answer three important questions:

Q1) To which extend hold the assumptions made in literature?

Q2) Can the models (Finite Element Method and Partial Differential Equations) presented in Chapter 2 cover all relevant effects?

Q3) What concludes for the design and choice of suitable controllers and models?

4.1 Cablerobot Simulator - Modelling and analysis of cable vibrations

Cables are components of the drivetrain with mass, elasticity and damping. Besides, nonlinearities and cross-couplings make cable models complex systems such that researchers

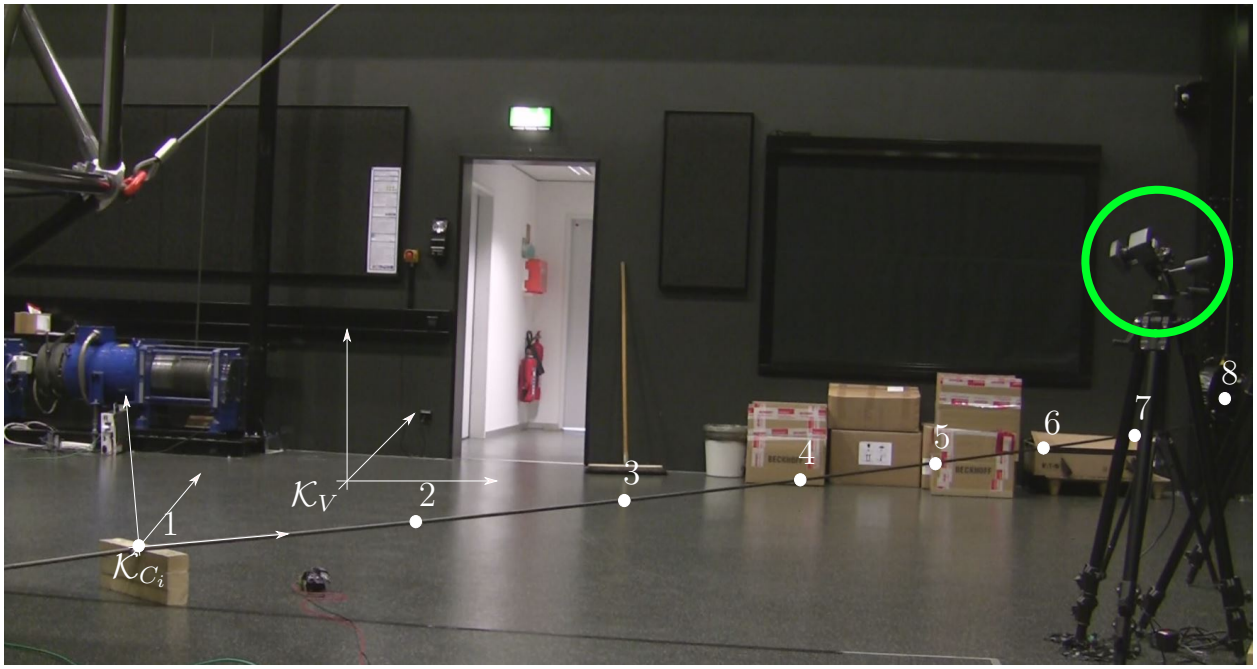

Figure 4.1: Experimental setup for evaluation of the two presented cable models (Finite-Element Method and Dynamic Stiffness Matrix based)

often assume i) massless springs; ii) linear behaviour; iii) negligible damping; iv) negligible lateral vibrations; v) decoupled systems; to simplify the modelling process.

A deeper understanding of the undergoing cable dynamics motivates to conduct the experiments presented in this chapter. The findings of these experiments provide information to answer Q2) and highlight the importance of robust controllers and sophisticated friction and cable models.

The experimental setup consists of a motion tracking system from VICON, one cable with a diameter of $14mm$ that is attached at one end to the ground and connected at the other end to its corresponding motor[1]. To track the motion of this cable, seven reflecting markers with a diameter of $25mm$ were uniformly distributed along the cable and one additional marker at the corresponding pulley of the Cablerobot Simulator (see Figure 4.1). A tracking system with four near infrared cameras cover the space with $7m \times 3m \times 3m$ and locates the marker with a sampling rate of $250Hz$. This setup corresponds to a cable model with two fixed ends. Each motor is able to exert torques up to $12.16kNm$, which results in a cable tension of up to $14000N$. To provoke cable vibrations, the motor applies a tension signal $f_{C_i}(t) = f_{C_{i,dyn}}(t) + f_{C_{i,pre}}$ with a time varying component $f_{C_{i,dyn}}(t)$ and a static component $f_{C_{i,pre}}$. The four near infrared cameras track the marker positions ${}^V\boldsymbol{p}_{C_i,j} = \begin{bmatrix} {}^V\boldsymbol{p}_{C_i,j,x} & {}^V\boldsymbol{p}_{C_i,j,y} & {}^V\boldsymbol{\mu}_{C_i,j,z} \end{bmatrix}$ of each marker $j = 1 \dots 8$ with an accuracy of $0.5mm$ in a new ground-placed frame $\mathcal{K}_V$ (see Figure 4.1).

[1]The cables of the Cablerobot Simulator were designed to move an end-effector with $m_P = 500kg$

Remark 4.1: The tracking system requires to set a ground placed coordinate system $\mathcal{K}_V$ as a reference for the marker positions. Thus the deflections of all markers are given in the VICON frame as ${}^{V}\boldsymbol{\mu}_{C_{i,j}}$ for cable i and marker j. Moreover, one can choose $\mathcal{K}_V = \mathcal{K}_W$.

The rotation matrix describing the orientation of $\mathcal{K}_V$ in $\mathcal{K}_{C_i}$ is

$$ {}^{C_i}\boldsymbol{R}_W(\theta_z, \theta_x) = {}^{C_i}\boldsymbol{R}_{V,x}(\theta_x)\,{}^{C_i}\boldsymbol{R}_{V,z}(\theta_z), \tag{4.1} $$

where ${}^{C_i}\boldsymbol{R}_{V,x}(\theta_z)$,${}^{C_i}\boldsymbol{R}_{V,x}(\theta_z)$,$\theta_x$ and θ_z are given according to Equation (3.68-3.70).

Experiment one investigates the inner damping of a cable with the experimental setup described above. Damping describes the decay of oscillations in a system after excitation and is subdivided into external and internal damping. External damping denotes the decay of oscillations due to friction between a solid material and a fluid whereas inner damping denotes the decay of oscillations due to friction between molecules. The latter one depends on the material structure and intermolecular forces.

With a pretension of $f_{C_{i,pre}} = 4500\text{N}$ the cable is taut. An evaluation of both linear models provides reasonable results, only when the cable is taut, since then non-linearities are less evident. After a time t_{step} a step increment $f_{C_{i,dyn}} = 1000\text{N}$ initiates a deflection of the cable length from its initial static equilibrium and causes vibrations to the cable which decays exponentially. The decay time depends on the damping factors $\boldsymbol{\zeta}_{C_i,D} = \begin{bmatrix}\zeta_{C_i,x} & \zeta_{C_i,y} & \zeta_{C_i,z}\end{bmatrix}$ and is incorporated in Equation (2.33) by the diagonal damping matrix $\boldsymbol{D}_{C_i} = \text{diag}(-2\zeta_{C_i,x}\omega\ -2\zeta_{C_i,y}\omega\ -2\zeta_{C_i,z}\omega)$. The structure of $\boldsymbol{D}_{C_i}$ is given by the solution of the well known ordinary differential equation of harmonic oscillations [42]. More precise, the damping factor for marker j and cable i is:

$$ \zeta_{C_i,j,x} = \frac{1}{\sqrt{1+\left(\frac{2\pi}{\nu_{C_i,j,x}}\right)^2}}, \tag{4.2} $$

$$ \zeta_{C_i,j,y} = \frac{1}{\sqrt{1+\left(\frac{2\pi}{\nu_{C_i,j,y}}\right)^2}}, \tag{4.3} $$

$$ \zeta_{C_i,j,z} = \frac{1}{\sqrt{1+\left(\frac{2\pi}{\nu_{C_i,j,z}}\right)^2}} \tag{4.4} $$

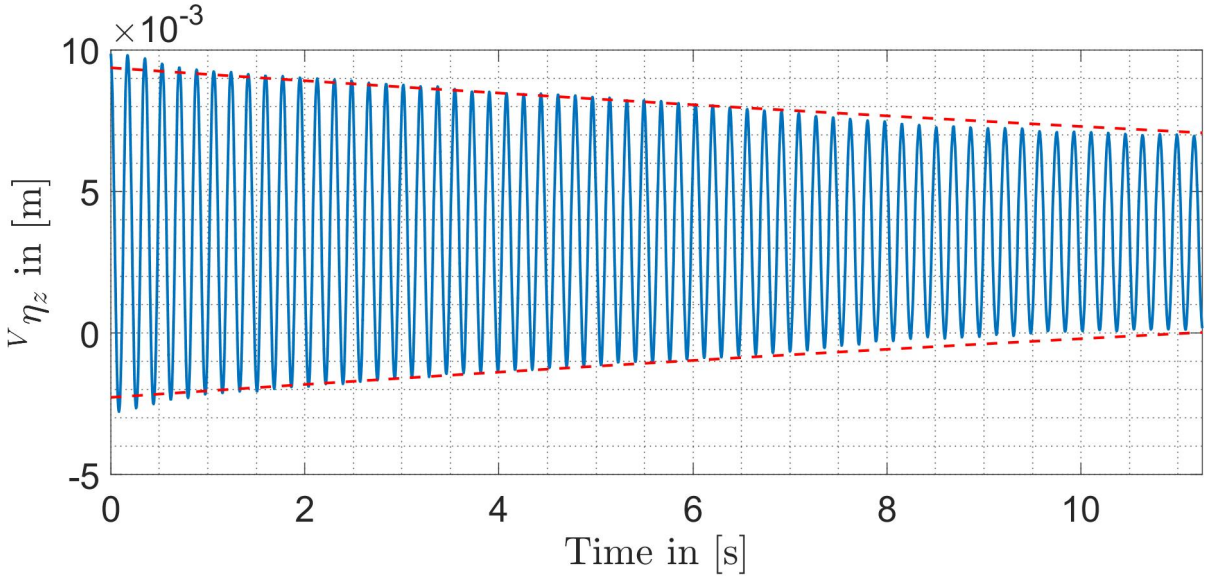

Figure 4.2: Decay of in-plane cable vibrations for marker five in first experiment

$$\nu_{C_i,j,x} = \ln\left(\frac{\overline{\eta}_{C_i,j,x}(k)}{\overline{\eta}_{C_i,j,x}(k+1)}\right), \tag{4.5}$$

$$\nu_{C_i,j,y} = \ln\left(\frac{\overline{\eta}_{C_i,j,y}(k)}{\overline{\eta}_{C_i,j,y}(k+1)}\right), \tag{4.6}$$

$$\nu_{C_i,j,z} = \ln\left(\frac{\overline{\eta}_{C_i,j,z}(k)}{\overline{\eta}_{C_i,j,z}(k+1)}\right), \tag{4.7}$$

where $\overline{\eta}_{C_i,j,z}(k)$ denotes an arbitrary peak and $\overline{\boldsymbol{\eta}}_{C_i,j,z}(k+1)$ the subsequent peak. Figure 4.2 shows in blue the deflection in ${}^{C_i}\boldsymbol{z}_{C_i}$ of marker five over time and the damping curve $e^{-2\zeta_{C_i,5,z}\omega t}$ in red. There is no significant difference among all markers which is why marker five can be seen as a representative. The cable begins to oscillate with an amplitude of 6.25mm and in $20s$ the oscillations decay to 60% and implies a low damping factor.

Given Equation (4.2) and (4.7) and Figure 4.2, the damping ratios for marker five are $\zeta_{C_i,5,x} = 0.0095$, $\zeta_{C_i,5,y} = 0.0044$ and $\zeta_{C_i,5,z} = 0.0028$[2]. In conclusion, the system damping is insignificant and Equation (2.33) reduces to

$$\boldsymbol{f}_i = \boldsymbol{M}_{C_i}\ddot{\boldsymbol{\eta}}_i + \boldsymbol{K}_{C_i}\boldsymbol{\eta}_i\,. \tag{4.8}$$

This is an important finding, since neglecting the damping matrix $\boldsymbol{D}_{C_i}$ simplifies modal analysis. The solution of the eigenvalue problem (see Equations (4.10)-(4.13) spares imaginary solutions. The second experiment answers the question how precise the Finite-Element Method and the Dynamic Stiffness Matrix based models can predict real resonance frequencies. Resonance is only possible if one out of at least two connected systems drives another one to oscillate. Thus, the motor exerts a sinusoidal tension signal $f_{C_i}(t) = f_{C_i,pre} + f_{C_i,dyn}(t)$

[2]Evaluating data in ${}^{C_i}\boldsymbol{x}_{C_i}$ and ${}^{C_i}\boldsymbol{y}_{C_i}$ direction for all other markers does not provide more information.

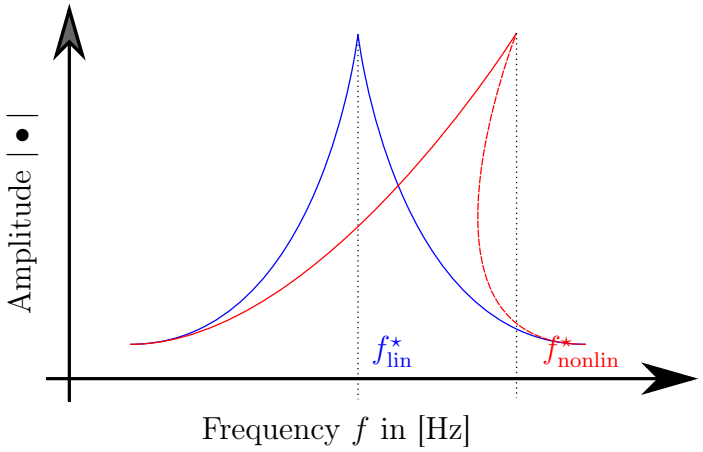

Figure 4.3: Backbone curve and resonance frequency for an equivalent linear system

with

$$f_{C_{i,dyn}}(t) = a\cos(2\pi f t) = J_M \frac{d^2\theta}{\mathrm{d}t^2}$$

on the cable. The motor can only excite resonance frequencies $f^{\star}$ if $f = f^{\star}$. Thus the frequency increases over one run from 0Hz to 22Hz with an incremental step of 0.5Hz every 5^{th} period. Additionally, the operation conditions, defined by the pretension level and the amplitude, change after each run, to incorporate dependency of the resonance frequencies on the pretension level. The operation conditions are:

C1 $T_{pre} = 2600$N and $A = 560$N (*lightly sagging cable*);

C2 $T_{pre} = 4500$N and $A = 480$N (*taut cable*);

C3 $T_{pre} = 7700$N and $A = 950$N (*very taut cable*).

Note, that the amplitude in condition C3 is higher than in conditions C2 and C1 because no pronounced vibrations were visible at lower amplitudes.

> **Remark 4.2:** The amplitude of deflections is irrelevant for the resonance frequencies of linear systems. However, more sophisticated analysis techniques reveal the influence of amplitudes on eigenfrequencies for non-linear systems. The resonance frequencies in non-linear systems is a function of the systems energy [82] which results in so called backbone curves[3]. The Fast-Fourier-Transformation of a vibrating beam depicts a shift of the actual resonance frequency to higher frequencies when the amplitude increases. Figure 4.3 illustrates this effect in a sketch. The first resonance frequency $f^{\star}_{nonlin}$ at which the corresponding non-linear system has its maximum amplitude differs from the first resonance frequency $f^{\star}_{lin}$. A non-linear analysis of cable vibrations is out of the scope of this thesis and, in spite of this

[3]For a vibrating string the energy is proportional to the amplitude of oscillations

knowledge, will not further be pursuited.

The experiment conducted in this section also provides information about internal cross-couplings. This way vibrations can occur in in-plane direction although a cable force can only be applied in out-of-plane direction (for an illustration of the terms 'in-plane' and 'out-of-plane' see Figure 4.4). Note, that cables can only pull and exert forces in out-of-plane

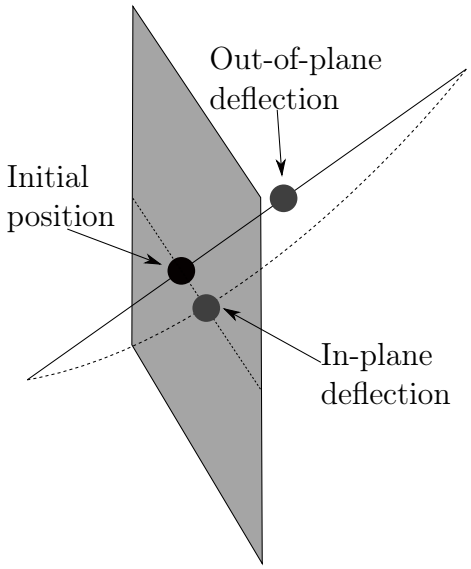

Figure 4.4: Sketch for in-plane motion and out-of-plane direction motion

motion such that the cable is subject to the force applied by the motor and the gravitational force. Figures 4.5-4.10 show phase-plots in $x_{C_i}, y_{C_i}, z_{C_i}-$direction for all conditions of marker five in $\mathcal{K}_{C_i}$. and provide the following results:

- **Figures 4.8-4.10** show the phase-plots related to the $\boldsymbol{z}_{C_i}$-direction. The amplitudes in those plots are distinctly higher than in Figure 4.5-4.7. The contribution of gravity to the potential energy is probably the reason for higher amplitudes in $\boldsymbol{z}_{C_i}$-direction. Deflections decrease when the pretension $f_{i,pre}$ increases from $2600N$ to $4500N$. A further decrease in the amplitude from $4500N$ to $7700N$ is not visible. According to Equation (2.38), the geometrical contribution to the cable stiffness is a function of the cable tension. Increasing the cable stiffness results in higher restoring forces which counteract deflections. Thus, higher cable tensions also reduce the amplitude of vibrations. Out-of-plane vibrations start after the in-plane vibrations.

- **Figures 4.5-4.10** give an insight of the characteristics of cable dynamics by mapping time t and deflection ${}^{V}\boldsymbol{\mu}_{C_i}$ to the corresponding deflection rate ${}^{V}\dot{\boldsymbol{\mu}}_{C_i}$. However, this illustration is inappropriate to visualize resonance frequencies. A Power-Spectral-Density is a suitable way to depict resonance frequencies, by mapping the power of a signal over its frequency spectrum.

- **Figures 4.11-4.13** show the Power-Spectral Density estimation of marker five for all conditions and provide more information:

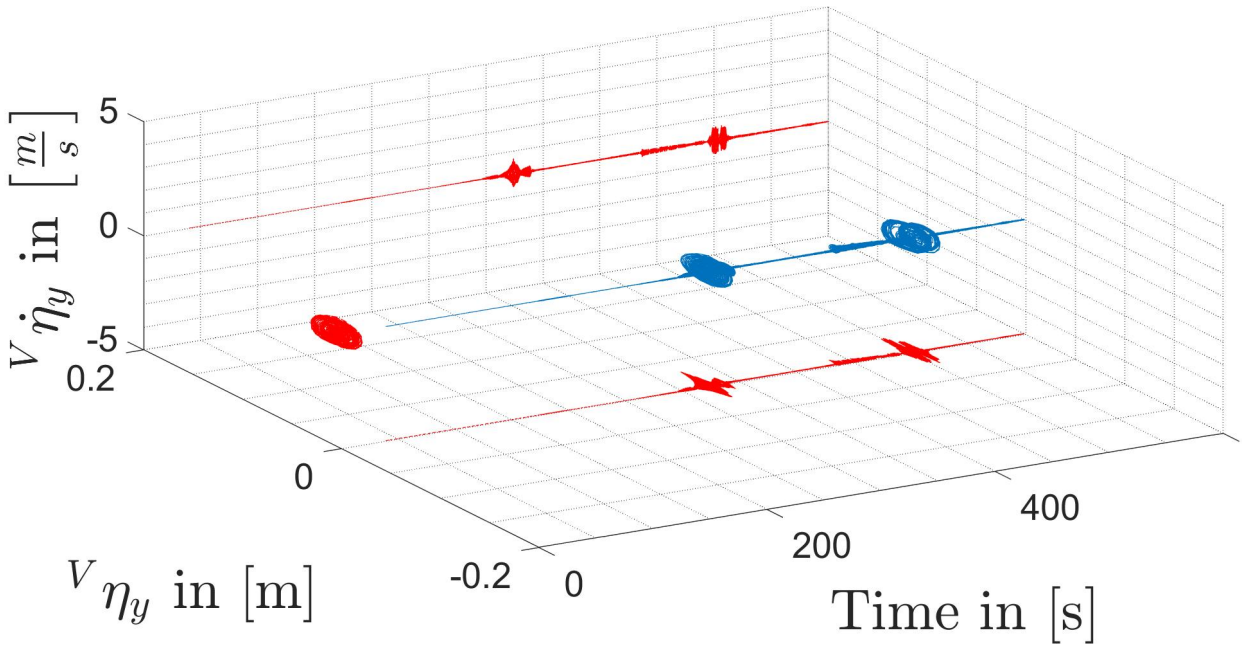

Figure 4.5: Phase-plot under condition C1 in y-direction

1. Every visible distinct peak (marked with squares) represents the signal power under the corresponding eigenfrequency. Over the entire frequency spectrum several ripples occur. These are visible, under condition C1 and reveal a chaotic behaviour when the pretension decreases.

2. Longitudinal vibrations are more evident under condition C1 and become less evident with increasing cable tension in condition C2 and C3.

3. In between these peaks some indistinct peaks occur, that probably belong to the eigenfrequencies of other system components, such as the pulley itself or the frame. During the experiment, these components started to vibrate audibly.

4. Close to resonance in-plane oscillations are higher than in out-of-plane oscillations. This might be, due to the potential energy stored in the cable.

5. Peaks in $\boldsymbol{z}_{C_i}$-direction often go hand in hand with peaks in $\boldsymbol{x}_{C_i}$ and $\boldsymbol{y}_{C_i}$-direction with lower amplitude. Out-of-plane oscillations and lateral oscillation as well as circular in-plane motions[4] occur after in-plane oscillations. Cross-couplings describe the ability of a non-linear system to transfer energy between different modes.

Experimental results presented so far gave important information about the cable characteristics and define benchmark criteria for both cable models of Section 2.2.2.

Here, this benchmark is the ability to reproduce the resonance frequencies in Figure 4.11-4.13. To obtain the eigenfrequencies $\omega^\star$ in $^{rad}/_s$ based on the Dynamic Stiffness Matrix approach,

[4]Circular in-plane motion describes motions of a marker along a circle in ${}^{C_i}\boldsymbol{z}_{C_i} - {}^{C_i}\boldsymbol{x}_{C_i}$ plane of a cable.

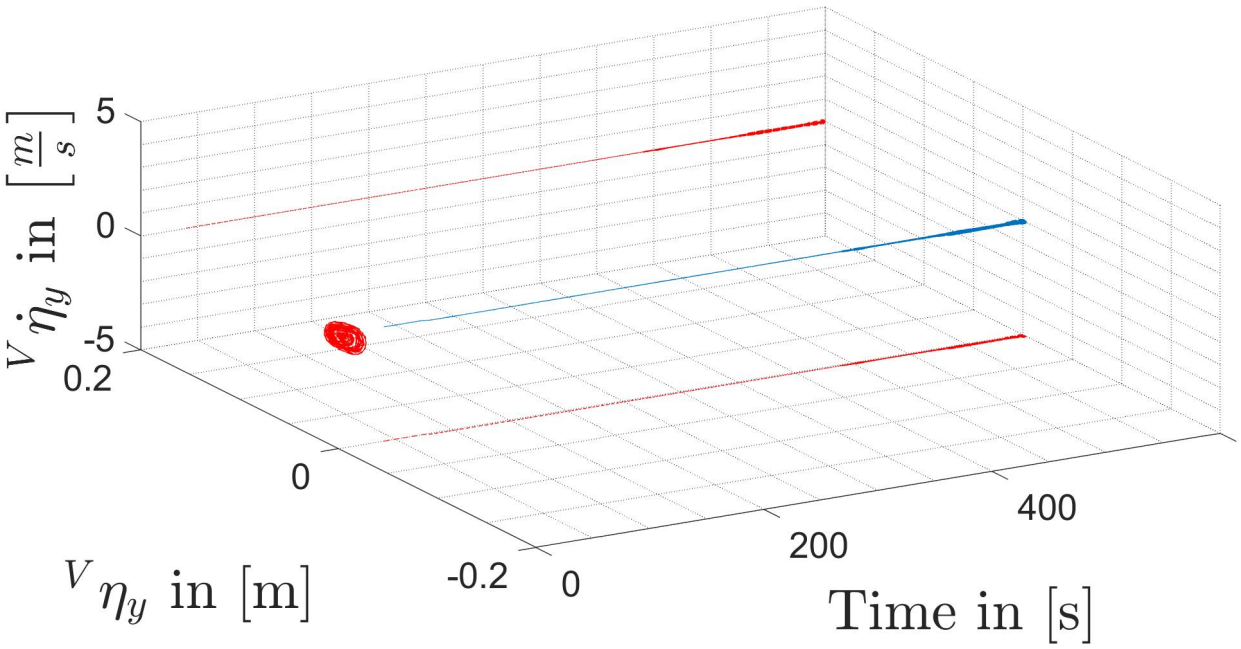

Figure 4.6: Phase-plot under condition C2 in y-direction

one has to compute the trace of the dynamic stiffness matrix in Equation (2.46), which is a function of the frequency ω. Note, that computing the trace of Equation 2.46 does not incorporate the cross couplings but only the decoupled linear components K_{xx}, K_{yy} and K_{zz}. Since Equation 2.46 was derived under the assumption of linear dynamics, it is valid to neglect the cross-coupling components K_{xz} and K_{zx}. Figures 4.14-4.16 show $\|K_{zz}\|$ over ω for all conditions C1-C3. Every peak denotes an eigenfrequency at which the stiffness increases and the resonance occurs. Comparison of the figures reveals a shift in these eigenfrequencies for different cable tension levels, i.e. an increase of resonance frequency follows an increase of static cable tensions. This effect matches the observation from the experiments conducted in this chapter. Table 4.1 shows the resonance frequencies computed with the Dynamic Stiffness Matrix, the results from the Power-Spectral Density estimation analysis and the modal analysis of the Finite-Element Method model. Values in brackets are the relative error of the corresponding method (Dynamic Stiffness Matrix or Finite-Element Method) with respect to the results of the Power-Spectral Density estimation. Under condition C1 the Dynamic Stiffness Matrix based model comes up with an error of -26.03%. This is because the true value of resonance frequencies were extracted manually from Figures 4.11-4.13. Already a resonance frequency of 4.1Hz instead of 3.49Hz for the first mode of condition C1 leads to an error of -7.3% for the Dynamic Stiffness Matrix based model and 10.24% for the Finite-Element Method model which seems to be more realistic than 26.03% for the Dynamic Stiffness Matrix based model. The resonance frequencies based on the Dynamic Stiffness Matrix are close to the resonance frequencies provided by the Power-Spectral Density estimation when the cable is taut, i.e. under condition C2 and C3. Under low cable tensions (condition C1 the Dynamic Stiffness Matrix based model is less accurate. This is reasonable since non-linearities and cross-couplings are more evident for loose cables and the Dynamic Stiffness Matrix based model does not incorporate these effects. Thus the dif-

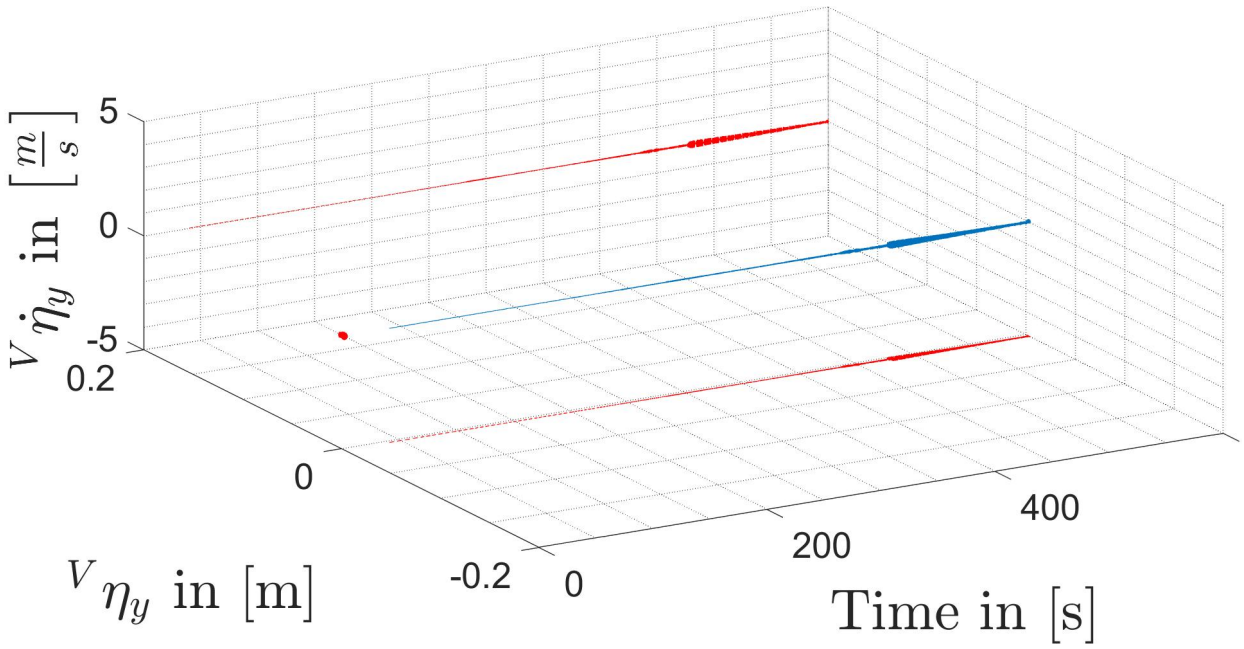

Figure 4.7: Phase-plot under condition C3 in y-direction

ference between the Power-Spectral Density estimation and the results from the Dynamic Stiffness Matrix are higher under condition C1 than under condition C2 and C3.

The Finite-Element Method based model follows the same trend. For taut cables the matching between the Power-Spectral Density estimation and the Finite-Element Method based model is better and decreases when the tension level is low.

In both experiments, the motor applied two different input force signals in the cable direction to provoke oscillations. In the first experiment the input force signal was a step function. The oscillations decayed with a low damping ratio (see Equation (4.2)-4.7). It turned out that the cable is only weakly damped and damping is apparently negligible in the modelling process. With $\boldsymbol{D}_i = \mathbf{0}_{3n_e \times 3n_e}$, the solution of Equation (4.9) spares imaginary solutions and simplifies the analysis of vibrations based on the Finite-Element Method.

Presuming free vibrations and no damping, i.e. $\boldsymbol{f} = \mathbf{0}$ and $\boldsymbol{D}_i$, such that Equation (2.33) turns to (4.8) and with $\boldsymbol{f}_i = \mathbf{0}$ to:

$$\boldsymbol{M}_{C_i}\ddot{\boldsymbol{\eta}} + \boldsymbol{K}_{C_i}\boldsymbol{\eta} = \mathbf{0}\,. \tag{4.9}$$

Previous experimental results substantiate negligible damping. To consider fixed end points $\boldsymbol{\mu}_{i,1} = \boldsymbol{\mu}_{i,n_e} = \mathbf{0}_{n_r \times 1}$, the first and the last n_r columns and rows of $\boldsymbol{M}_{C_i}$ and $\boldsymbol{K}_{C_i}$ as well as $\boldsymbol{\mu}_{i,1}$ and $\boldsymbol{\mu}_{i,n_e}$ have to be removed. This cancels the end-point dynamics and accounts for holonomic constraints. Moreover, it is necessary to normalise Equation (4.9) with a suitable coordinate transformation

$$\boldsymbol{\eta}_i = \boldsymbol{\Psi}_i\tilde{\boldsymbol{\eta}}_i \tag{4.10}$$

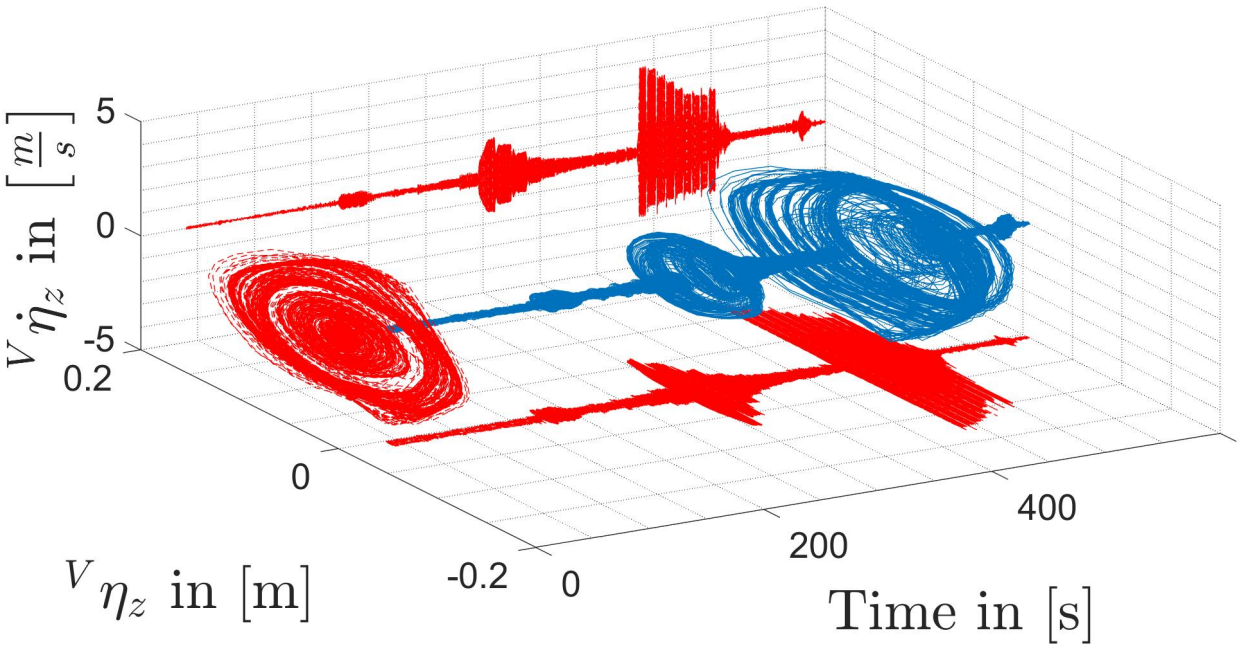

Figure 4.8: Phase-plot under condition C1 in z-direction

such that

$$\tilde{\ddot{\boldsymbol{\eta}}}_i + \Lambda_i \tilde{\boldsymbol{\eta}}_i = \mathbf{0}_{n_r n_i} \tag{4.11}$$

is a normalised representation of Equation (4.9) where

$$\boldsymbol{\Psi}^{-1}\boldsymbol{M}_i\boldsymbol{\Psi} = \boldsymbol{I}_{3n_i\times 3n_i} \tag{4.12}$$

$$\boldsymbol{\Psi}^{-1}\boldsymbol{K}_i\boldsymbol{\Psi} = \underbrace{\operatorname{diag}\left(\omega_{i,1}^2, \omega_{i,2}^2, \ldots, \omega_{i,n_i}^2\right)}_{\boldsymbol{\Lambda}} \tag{4.13}$$

M_i has entries only on its main diagonal and thus,

$$\boldsymbol{\Psi} = \operatorname{diag}\{\frac{1}{\sqrt{m_{C_i,1}}}, \frac{1}{\sqrt{m_{C_i,2}}}, \ldots, \frac{1}{\sqrt{m_{C_i,n_e}}}\} \tag{4.14}$$

$$k = 1 \ldots n_e\,, \tag{4.15}$$

$$\begin{aligned} m_{C_i,1} &= \frac{1}{2}\sqrt{\mu\,\|l_{1,2}\|}, \quad m_{C_i,2} = \frac{1}{2}\sqrt{\mu\,\|\boldsymbol{l}_{1,2} + \boldsymbol{l}_{2,3}\|}\,, \\ m_{C_i,n_e-1} &= \frac{1}{2}\sqrt{\mu\,\|\boldsymbol{l}_{n_e-2,n_e-1} + \boldsymbol{l}_{n_e-1,n_e}\|} \\ m_{C_i,n_e} &= \frac{1}{2}\sqrt{\mu\,\|\boldsymbol{l}_{n_e-1,n_e}\|} \end{aligned} \tag{4.16}$$

The second experiment consisted of three parts. In each part the pretension and the amplitude of a sinusoidal input function with incrementally increasing frequency changed. The system goes into resonance, every time the frequency of the input force signal is close to one of the resonance frequencies assigned to lateral and longitudinal eigenmodes. Four near-infrared cameras from VICON tracked the motion of eight reflecting markers. Those markers were uniformly distributed along the cable. The second experiment reveals the following findings:

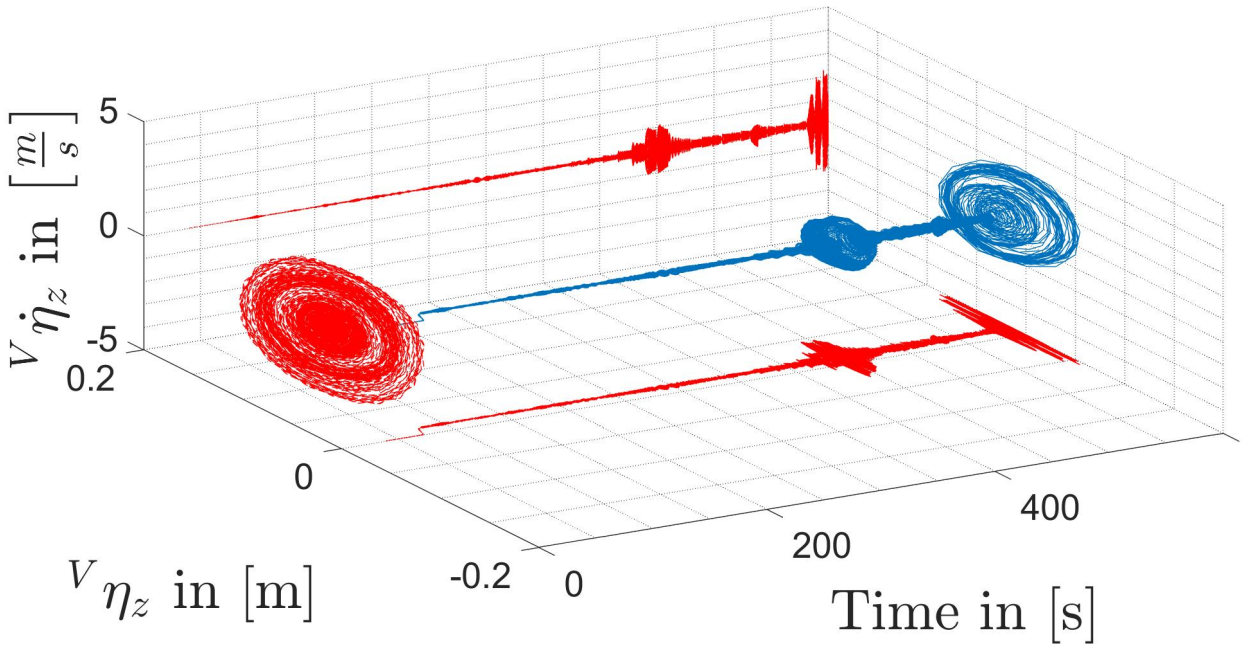

Figure 4.9: Phase-plot under condition C2 in z-direction

4.1.1 Concluding remarks for controller design and further investigations

The experiments conducted at the Cablerobot Simulator exhibits that active vibration suppression is an important aspect and highlights the importance of proper control strategies. Controllers with low controller gains avoid aggressive control actions and chattering. An adaptive Super-Twisting Sliding-Mode Controller as presented in Chapter 3 and the adaptive Friction Compensation algorithm account for this aspect. Sections 4.2.5 to 4.2.6 confirm the efficiency of both controllers. Although both controllers cope efficiently with stiction and controller induced vibrations, they are only able to suppress longitudinal, but not lateral vibrations. A model based holistic approach such as Interconnection Damping-Assignment Passivity-Based Control incorporates cable dynamics and therefore also accounts for lateral vibrations. This reasons for the development of a holistic model in Port-Hamilton representation for the design of an Interconnection Damping-Assignment Passivity-Based Controller.

4.2 Mini Cablerobot Simulator - Drivetrain characteristics, modelling and experimental evaluation

The Mini Cablerobot Simulator (MiCaRoSi) (Figure 4.18) is a Cable-Driven Parallel Robot with eight actuators of type AM8033-0E21 from Beckhoff, three translative and three rotative degrees of freedom. Its platform is a smaller replica of the Cablerobot Simulator platform.

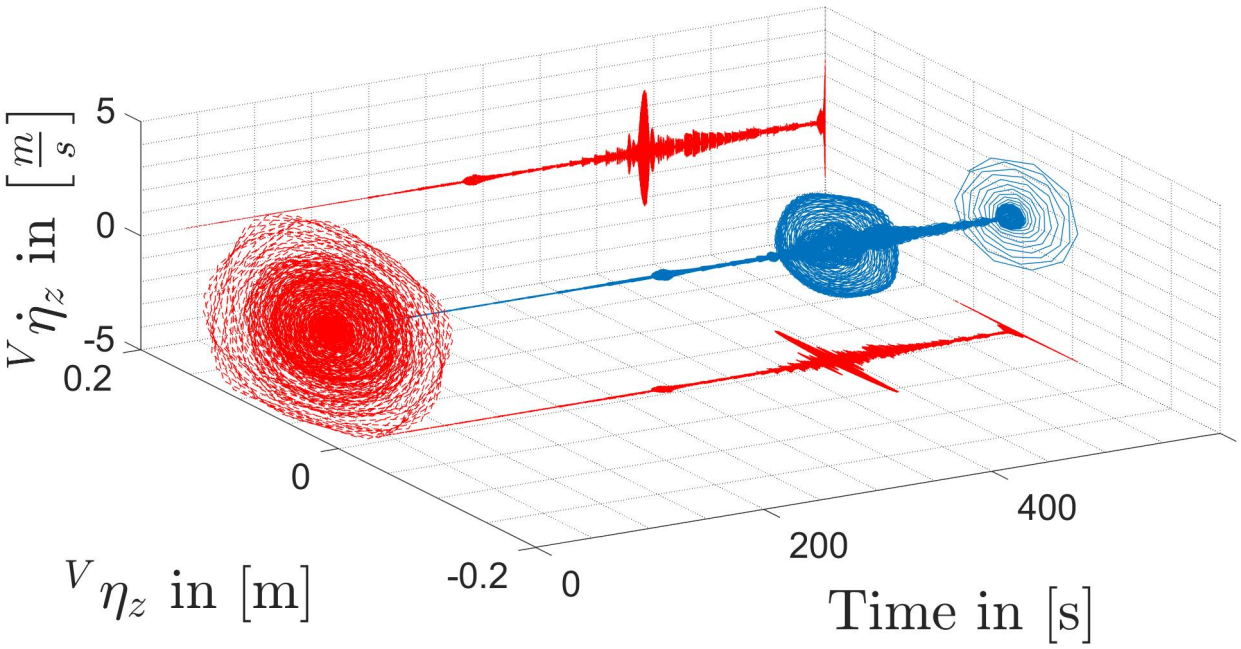

Figure 4.10: Phase-plot under condition C3 in z-direction

Four[5] near-infrared cameras from Vicon track five markers mounted on top of the platform (see Figure 4.20b and 4.18) with a sampling frequency of up to $250Hz$ and an accuracy up to $0.5mm$. Those cameras and the motors subscribe data to the drives which forward the incoming data to TwinCAT (Windows Control and Automation Technology) . TwinCAT is an off-the-shelves software provided by Beckhoff that enable to run multiple Programmable Logic Controller simultaneously in real-time. Furthermore, TwinCAT comes with a run-time environment, a programming environment for NC-axis control and code development. Originally, the MiCaRoSi was build as a test bench for controllers and estimators. After evaluation, those controllers and estimator shall be implemented on the Cablerobot Simulator. Thus, all algorithms implemented at the MiCaRoSi must fulfil the requirements given for the Cablerobot Simulator. For instance, the Cablerobot Simulator does not rely on external tracking devices. Thus, the VICON tracking system of the MiCaRoSi is only allowed for calibration of kinematic parameters and experimental evaluation, but not to provide state feedback via the infra-red tracking system VICON.

Four $940W$ compact dual servo drives power the system and enable to wind and unwind $1mm$ thick steel cables on a drum of $39.15mm$ diameter (4.19a). Three to four pulleys and winches for each drivetrain guide cables to the platform connection points. The power provided by the motors is high enough to move the platform with a weight of $m_P = 2.6kg$ and an inertia tensor of ${}^P I_P = diag\left\{[0.04613, 0.04613,\ 0.04873]\right\} kgm^2$ given with respect to the principle platform axes. Eight rotational joints (Figure 4.20a) connect the cables with the platform and facilitates a fast release. Given a desired cable length or alternatively a desired torque, TwinCAT allows position, velocity or direct torque control. Figure 4.23 shows the

[5]In theory only three cameras are necessary to capture all markers. But in case of occlusion a reconstruction of the platform pose is impossible with only three cameras

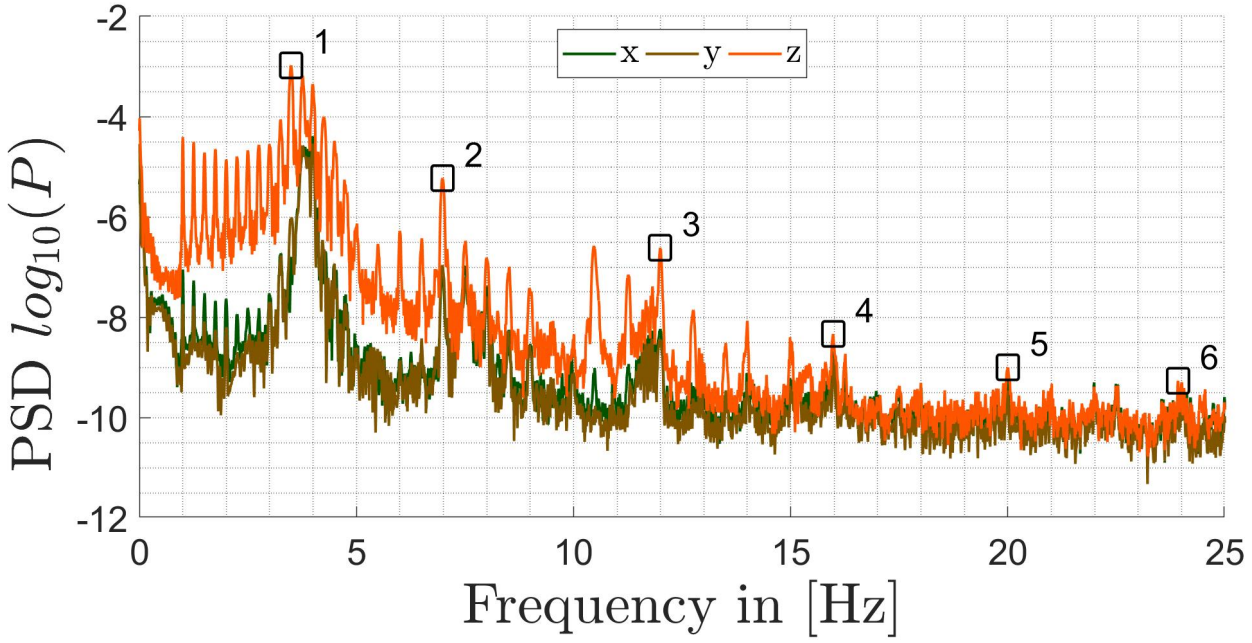

Figure 4.11: Power-Spectral-Density analysis for marker 5 under condition C1. The signal power spectrum is plotted over the range of relevant frequencies. Squares mark distinct eigenfrequencies.

control architecture of the MiCaRoSi. Going from left to right a position, velocity and torque controller is implemented in cascade structure. The operator can change the operation mode from position control (position, velocity and torque control blocks are enabled), to velocity control (velocity and torque control blocks are enabled), to direct torque control only. Direct torque control is a challenging task, since a precise tracking of torques does not imply a good tracking of positions, velocities and accelerations. Direct torque control without improving extensions means to disable velocity and position control and to suspend velocity and position tracking.

The following experiment tackles the accuracy of direct torque control and velocity tracking. In an experiment, one motor is detached from its cable and run in direct torque control. The implemented Low-Level Control has to follow the desired torque trajectory

$$\tau_{i,des} = a_a \cos(2\pi f_a t) = J_M \frac{d^2\theta_a}{dt^2} \tag{4.17}$$

with stepwise increasing frequency f_a from 0 to $33Hz$ and fixed amplitude a_a. Figure 4.21 depicts in experiment an exact tracking of the desired torque while Figure 4.22 states a decrease in velocity when the frequency of the driving force increases. This statement opens a discussion about the anticipated accuracy of direct torque control. A simple mechanical relation explains this behaviour. The motors inertia leads to a slow response and to the previously mentioned drop in velocity. Assuming perfect tracking, i.e. $\tau_i = \tau_{i,des} \in \mathbb{R}$ and

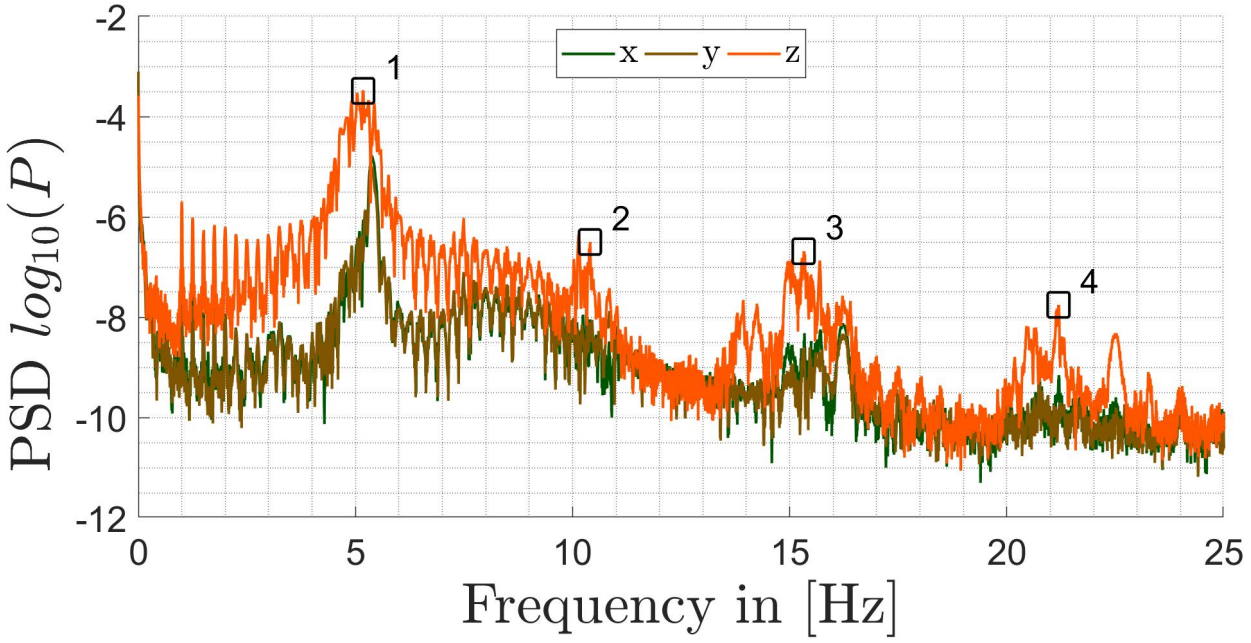

Figure 4.12: Power-Spectral-Density analysis for marker 5 under condition C2. The signal power spectrum is plotted over the range of relevant frequencies. Squares mark distinct eigenfrequencies.

an inertia $J_M \in \mathbb{R}$ around the motor shaft axis it is:

$$\tau_{i,des} = a_a \cos(2\pi f_a t) \quad = \quad J_M \frac{d^2\theta_a}{dt^2} = J_M \frac{d}{dt}\dot{\theta}_a \tag{4.18}$$

$$\int_0^t \frac{a_a}{J_M} \cos(2\pi f_a t)\mathrm{d}t \quad = \quad \dot{\theta}_a \tag{4.19}$$

$$\frac{a_a}{J_M 2\pi f_a} \sin(2\pi f_a t) \quad = \quad \hat{\dot{\theta}}_a \sin(2\pi f_a t) = \dot{\theta}_a \tag{4.20}$$

Hence, the amplitude $\hat{\dot{\theta}}_a$ is inversely proportional to the frequency f_a. This explains the decreasing amplitude of the velocity although a good torque tracking is achieved. To draw a conclusion, direct torque control facilitates to control cable tensions directly and is not sensitive to kinematic uncertainties. On the other hand a good tracking of desired torques in direct torque control does not imply a precise tracking of position and velocity. As a consequence position and velocity control is preferred against direct torque control [6]. Position control to achieve tracking of a desired platform pose presumes accurate kinematic parameters. Thus calibration of kinematic parameters is an important part of the modelling process and strongly affect the controller accuracy.

4.2.1 Calibration of kinematic parameter

The kinematic parameters are involved in the Jacobian matrix, that maps desired cable forces to wrenches and cable lengths to the platform pose. They affect both, feedback and

[6] Here, position control denotes control of cable lengths.

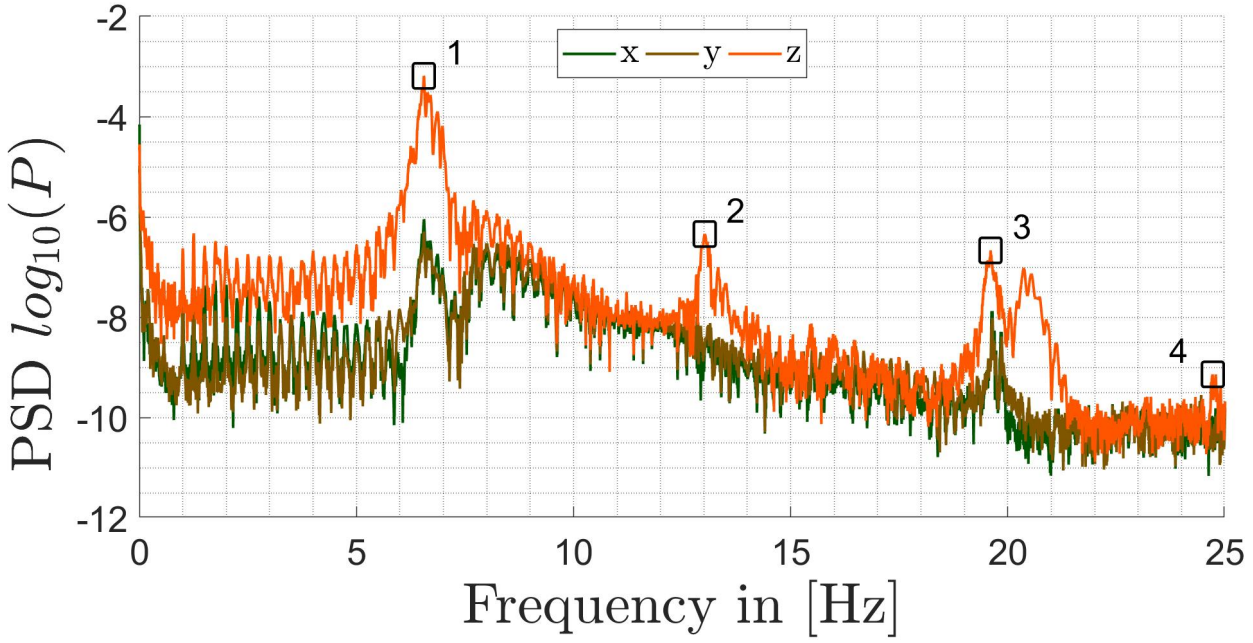

Figure 4.13: Power-Spectral-Density analysis for marker 5 under condition C3. The signal power spectrum is plotted over the range of relevant frequencies. Squares mark distinct eigenfrequencies.

force distribution, which underlines the importance of the calibration process. The following two approaches are simple and effective for a offline calibration of kinematic and dynamic parameters. In [83] the authors use a regression approach to solve for the parameters of interest. Given a function

$$\boldsymbol{y} = \boldsymbol{f}(\boldsymbol{x}, \Phi) \tag{4.21}$$

$$\Phi = \boldsymbol{f}(\boldsymbol{x}, \boldsymbol{y})^{-1} \tag{4.22}$$

linear in its n_p parameters $\boldsymbol{\Phi} \in \mathbb{R}^{n_p \times 1}$, there exist a least-squared solution of Equation (4.22) called regression. Given the iterative equation $\boldsymbol{\Phi}^{k+1} = \boldsymbol{\Phi}^k + \Delta\boldsymbol{\Phi}$ we are now looking for $\Delta\boldsymbol{\Phi}$. Approximating Equation (4.21) with a Taylor series and neglecting terms higher than order one yields:

$$\boldsymbol{y} = \boldsymbol{f}(\Phi) + \underbrace{\frac{\partial f(\Phi)}{\partial \Phi}|_{\Phi=\Phi_k} \Delta\Phi}_{\Delta \boldsymbol{y}} \tag{4.23}$$

$$\Delta y = \underbrace{\frac{\partial f(\Phi)}{\partial \Phi}|_{\Phi=\Phi_k}}_{\Xi_k} \Delta\Phi \tag{4.24}$$

Assuming a nonsingular pseudo-inverse matrix $(\Xi_k \mathrm{d}\Xi_k)^{-1} \Xi_k^{\mathrm{T}}$ reads[7]:

$$\Delta\Phi = \left(\Xi_k^{\mathrm{T}} \Xi_k\right)^{-1} \Xi_k^{\mathrm{T}} \Delta y \tag{4.25}$$

[7]If the smallest singular value of a singular value decomposition tends to zero, the matrix is approaching a singularity. If $\left(\Xi_k^{\mathrm{T}} \Xi_k^{-1}\right) \Xi_k^{\mathrm{T}}$ is singular a damping factor $\epsilon \in \mathbb{R}^+$ changes the pseudo-inverse to $\left(\Xi_k^{\mathrm{T}} \Xi_k\right)^{-1} \Xi_k^{\mathrm{T}} + \epsilon \boldsymbol{I}^{n_p \times n_p}$. With $0 < \epsilon$ and $\epsilon << 1$, the result is more inaccurate but still leads to an accurate solution

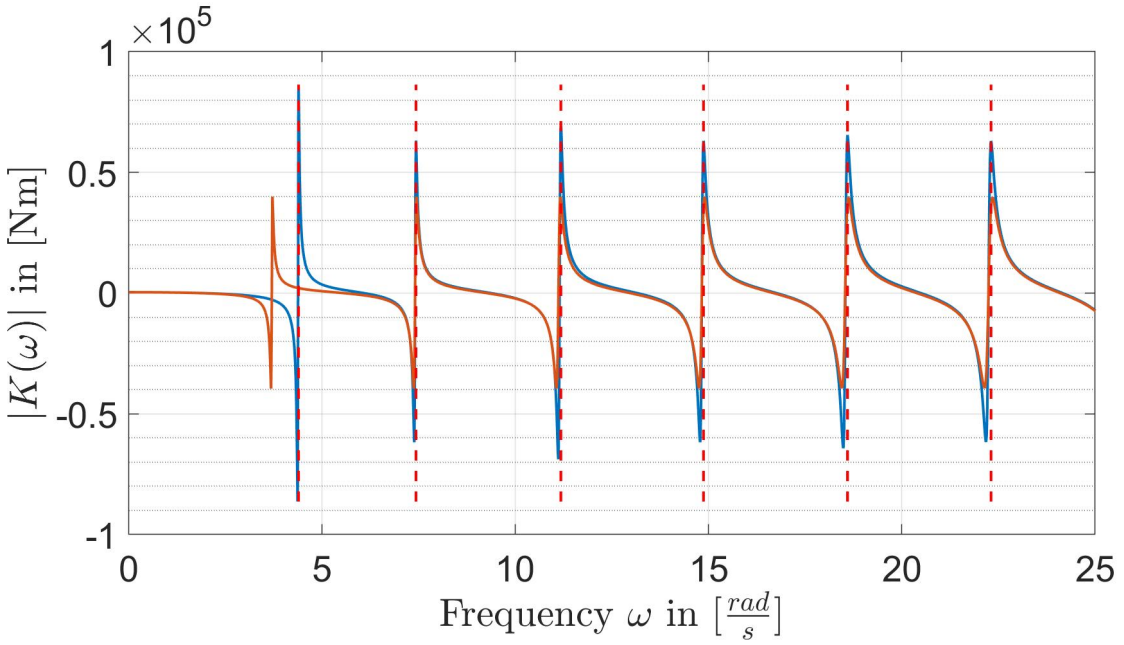

Figure 4.14: Change in stiffness due to resonance - Condition C1

Applied on Equation (2.7) it is:

$$\Xi_k = \begin{bmatrix} \frac{\partial l_1}{\partial a_{1,x}} & \frac{\partial l_1}{\partial a_{1,y}} & \cdots & \frac{\partial l_1}{\partial b_{1,y}} & \frac{\partial l_1}{\partial b_{1,z}} \\ \frac{\partial l_2}{\partial a_{1,x}} & \ddots & \ddots & \ddots & \vdots \\ \vdots & \ddots & \ddots & \ddots & \frac{\partial p_{n-1}}{\partial r_n} \\ \frac{\partial l_m}{\partial a_{1,x}} & \cdots & \cdots & \frac{\partial l_1}{\partial b_{1,y}} & \frac{\partial l_1}{\partial b_{1,z}} \end{bmatrix} \tag{4.26}$$

with the parameter vector

$$\Phi_k = \begin{bmatrix} a_{1,x} & a_{1,y} & a_{1,z} & \dots & b_{m,x} & b_{m,y} & b_{m,z} \end{bmatrix} \mathrm{d} \in \mathbb{R}^{24\times 1} \tag{4.27}$$

and the block diagonal matrices blkdiag{•}. After 10 iterations Equation (4.23)-(4.27) already provides a precise result.

Alternatively, one may describe the problem of finding a feasible set of parameters as the following quadratic minimization problem over all measurement samples: A set of onboard and offboard connection points $\boldsymbol{B}$ and $\boldsymbol{A}$ respectively has to fulfil:

$$\begin{bmatrix} \boldsymbol{a}_i^\star \\ \boldsymbol{b}_i^\star \end{bmatrix} = \min_{a_i, b_i} \left\{ \sum_{j=1}^{N} \rho_{i,j} - \| \boldsymbol{a}_i - \boldsymbol{r} - {}^W R_P \, {}^P \boldsymbol{b}_i \|^2 \right\} \tag{4.28}$$

$$\text{s.t.} \quad \boldsymbol{a}_i \in [\underline{\boldsymbol{a}}, \overline{\boldsymbol{a}}], \ \boldsymbol{b}_i \in [\underline{\boldsymbol{b}}, \overline{\boldsymbol{b}}] \tag{4.29}$$

where $\underline{\boldsymbol{a}}$, $\overline{\boldsymbol{a}}$ and $\underline{\boldsymbol{b}}$, $\overline{\boldsymbol{b}}$ are the boundaries of the search region. Table 4.2 lists the resulting parameters of the calibration process, based on Equation (4.21) and (4.22)

So far the simplified kinematic model is assumed to be accurate enough to describe the

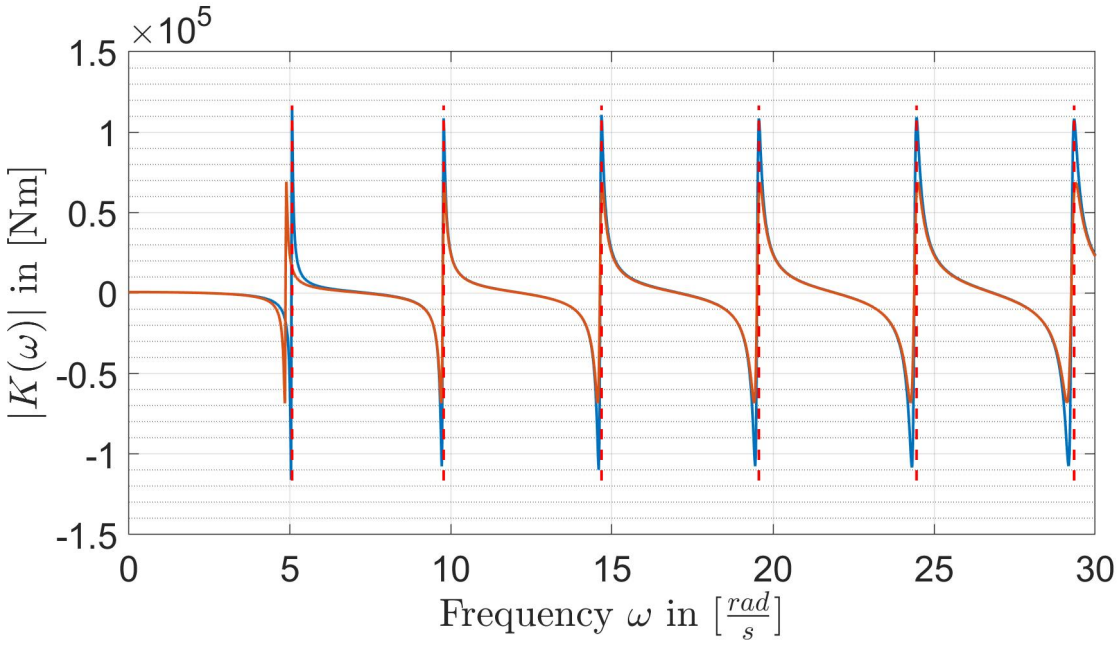

Figure 4.15: Change in stiffness due to resonance - Condition C2

platform motion in $\mathcal{K}_W$. However, still a verification of this statement is missing. Thus, the next section will answer the question, how accurate the simplified model is.

4.2.2 Kinematic accuracy of the Mini Cablerobot Simulator

This subsection compares (as a proof of validity) the simplified model with fixed anchor points A_i and the extended model [90] based on nominal kinematic parameters $\boldsymbol{A}$, $\boldsymbol{B}$ from the CAD model. The extended model incorporates pulley rotations, the change of the contact point C in Figure 2.2 during platform motion and is a benchmark for the simplified model.

Now, for a set of points $P_{kin} = [\boldsymbol{p}_1, \boldsymbol{p}_2, \ldots, \boldsymbol{p}_{N_{kin}}]$ with $\boldsymbol{p}_k = [p_{k,1}, p_{k,2}, p_{k,3}]^{\mathrm{T}}$, $l_{P,k,j} \leq p_{k,j} \leq u_{P,k,j}$, $k = 1 \ldots N_{kin}, j = 1 \ldots 3$ in Cartesian space, the difference between the extended and the simplified model in terms of cable lengths is $\boldsymbol{d}_{kin} = \boldsymbol{l} - \boldsymbol{l}_{ext}$ where $\boldsymbol{d}_{kin} \in \mathbb{R}^{8\times 1}$. Here $u_{P,k,j}$ and $l_{P,k,j}$ denotes the upper and lower bounds in Cartesian space. Figure 4.24-4.28 marks all points P_{kin} for which $\max\{\boldsymbol{d}_{kin,k}(\boldsymbol{p}_k)\}$ is less than $1.463mm$ as blue dots with the parameters given in Table 4.3 and illustrates the Wrench-Feasible Workspace [8] as a red convex volume in Figure 4.28. A point $\boldsymbol{p}_k$ of P_{kin} is valid if $d_{kin,k}(\boldsymbol{p}_k) < d_{kin,max}$ where $d_{kin,max}$ in Figure 4.24-4.27 is $1.287mm$,$1.346mm$, $1.404mm$ and $1.463mm$ respectively. In this particular case, the Wrench-Feasible Workspace covers only a small volume of the working space. In general, the Wrench-Feasible Workspace does not only depend on the geometry of the cablerobot, but also on the set of desired wrenches and feasible cable tensions [58]. Furthermore, the choice of approaches to compute the Wrench-Feasible Workspace affects its size and shape. Green planes illustrate boundaries of a cube inside the Wrench-Feasible Workspace in which the

[8] The wrench-feasible workspace was computed with the shifting hyper-plane method from [60]

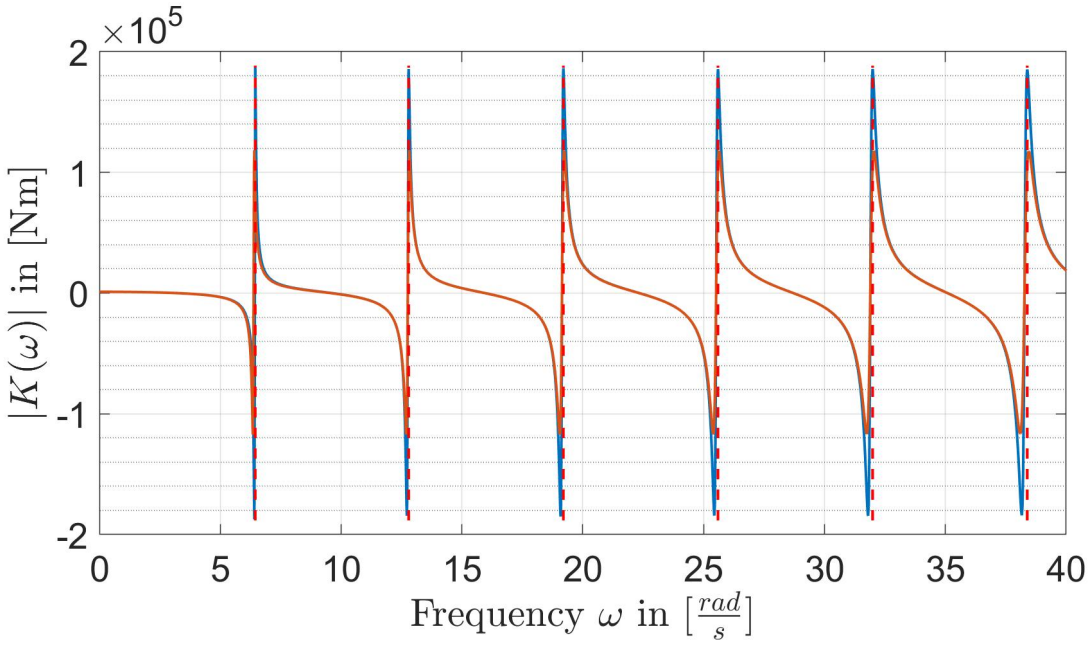

Figure 4.16: Change in stiffness due to resonance - Condition C3

system can operate while each element of $\boldsymbol{l} - \boldsymbol{l}_{ext}$ does not exceed a limit of 1.463mm inside the Wrench-Feasible Workspace .

4.2.3 Calibration of dynamic parameters

Mass and the inertia with respect to the principle axes are the two dynamic parameters of the platform. Both are known precisely enough. Thus only the dynamic parameters of the drivetrain remain open. Equation (4.30) is a well known representation of the drivetrain dynamics and includes constant static and viscous friction as well as inertia and stiffness of the motor [64, 91, 4]. The calibration process applied at the dynamic relation:

$$-r_D f_i = i_{m,i}\ddot{\theta}_M + f_{v,i}\dot{\theta}_M + f_{s,i}\,\mathrm{sign}(\dot{\theta}_M) + k_{M,i}\theta_M - \tau_i \tag{4.30}$$

should provide the desired parameters, i.e. constant inertia $i_{m,i}$, viscous and static friction $f_{v,i}$,$f_{s,i}$ and motor stiffness k_i for drivetrain i. The applied torque is denoted by τ_i and the radius of the drum is r_D. It turned out, that Equation (4.30) does not consider present effects i.e. non-linear friction and time varying friction characteristics since no feasible parameter set could be found. Thus Equation 4.30 is not suitable as model for the drivetrain and for the design of a friction compensation. However, Chapter 3 presents a solution to this problem and Section 4.2.5 will evaluate the proposed solution experimentally.

Table 4.1: Summary of resonance frequencies for three different operating conditions.

mode	condition C1		
	Power-Spectral Density estimation	Dynamic Stiffness Matrix	Finite-Element Method
1	3.49	4.40 (-26.03%))	3.68 (-5.32%)
2	6.98	7.43 (-6.48%)	9.43 (-9.34%)
3	11.99	11.17 (6.78%)	10.30 (14.10%)
4	15.98	14.86 (6.98%)	12.95 (18.93%)
	condition C2		
1	5.18	5.06 (2.02%)	4.84 (6.65%)
2	7.17	10.4 (-6.58%)	9.78 (-5.98%)
3	15.32	14.67 (4.22%)	13.55 (11.55%)
4	21.19	19.55 (7.72%)	17.04 (19.57%)
	condition C3		
1	6.55	6.44 (1.61%)	6.33 (3.43%)
2	13.02	12.79 (1.77%)	12 33 (5.28%)
3	19.6	19.19 (2.11%)	17.72 (9.57%)
4	24.72	25.58 (-3.48%)	22.29 (9.82%)

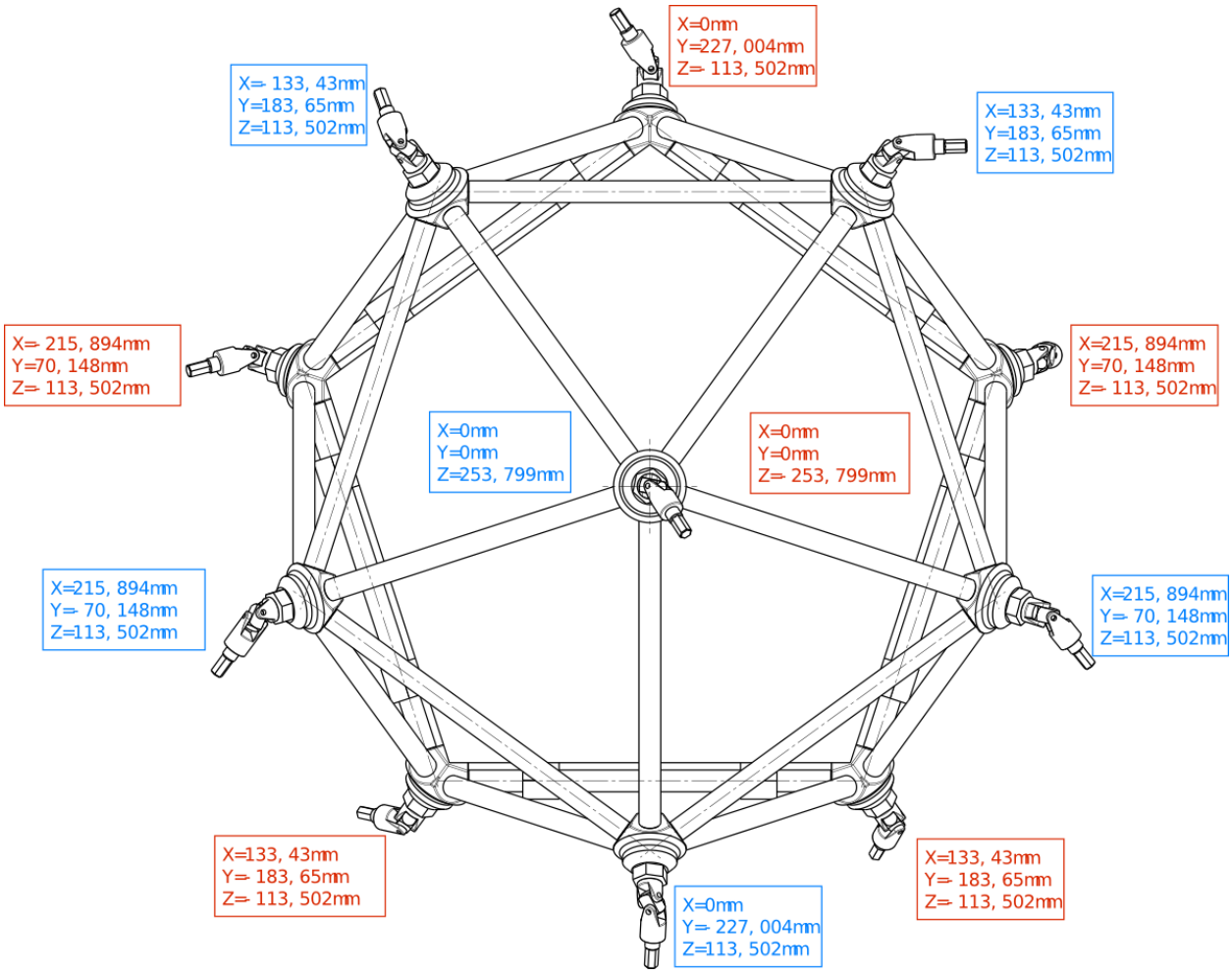

Figure 4.17: CAD drawing of the platform with onboard connection points ${}^{P}B_i$, $i = 1 \dots 12$

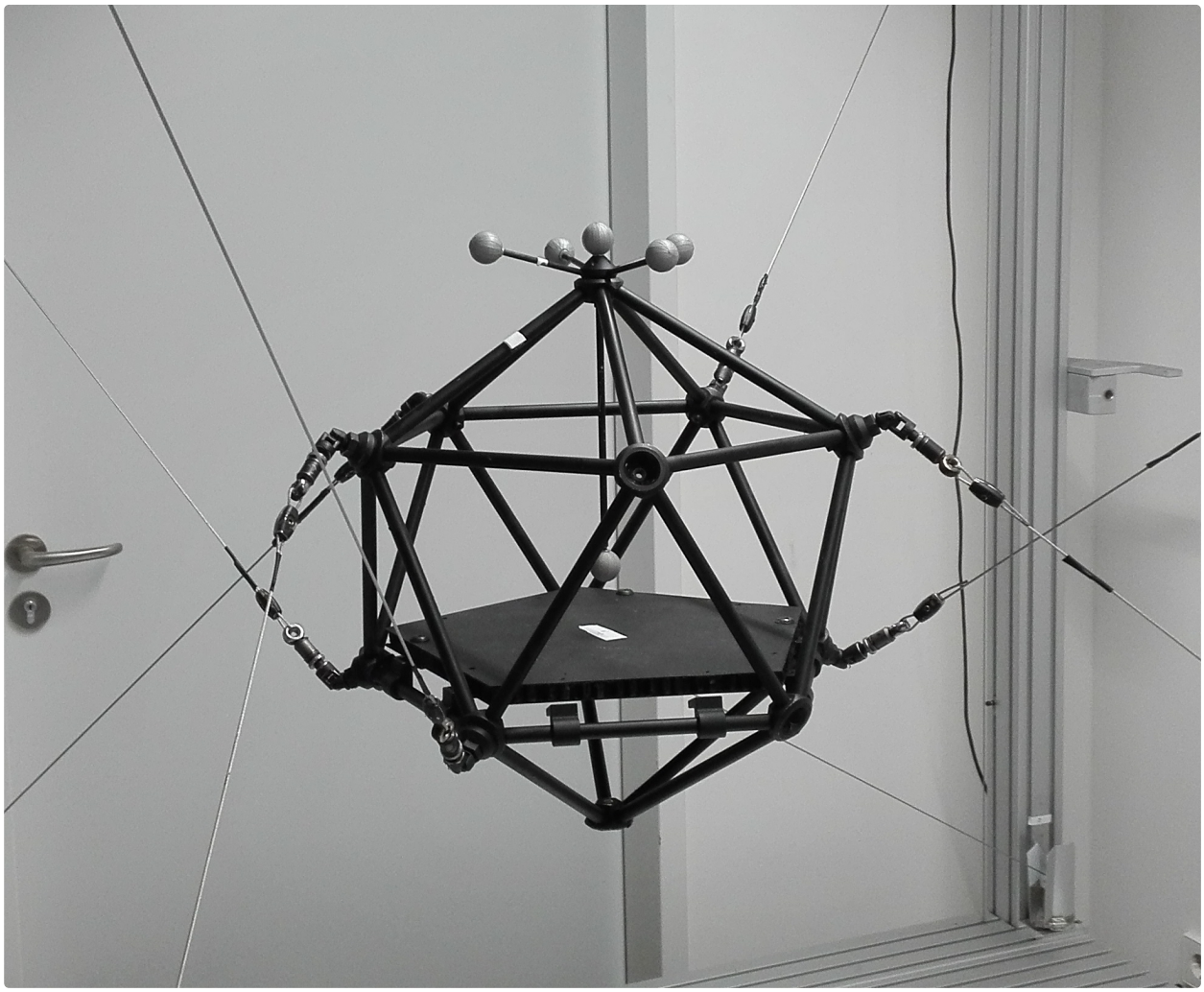

Figure 4.18: Mini Cablerobot Simulator

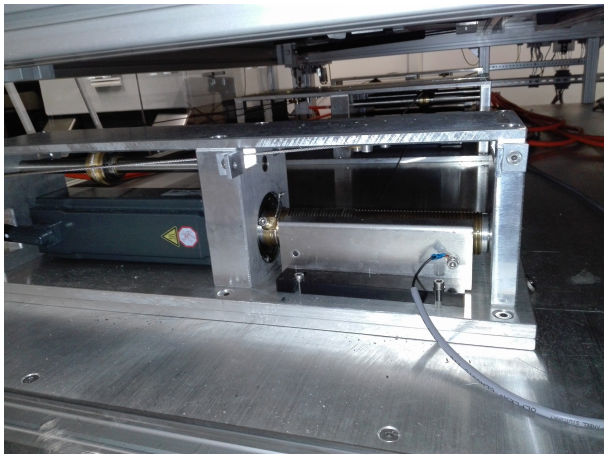

(a) Driving units of the Mini Cablerobot Simulator

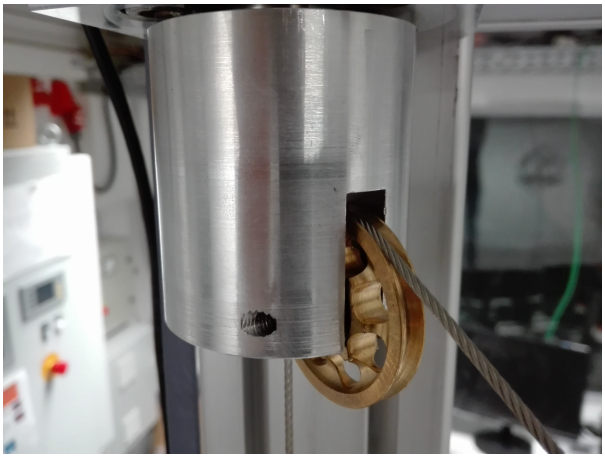

(b) Last pulley in drivetrain. One bearing allows rotations around the vertical axis and another bearing allows rotations of the wheel to unwind the corresponding cable

Figure 4.19: Driving units of the Mini Cablerobot Simulator

(a) Onboard connection points - rotational joints

(b) Vicon camera

Figure 4.20: Near-infrared camera and onboard connecting element

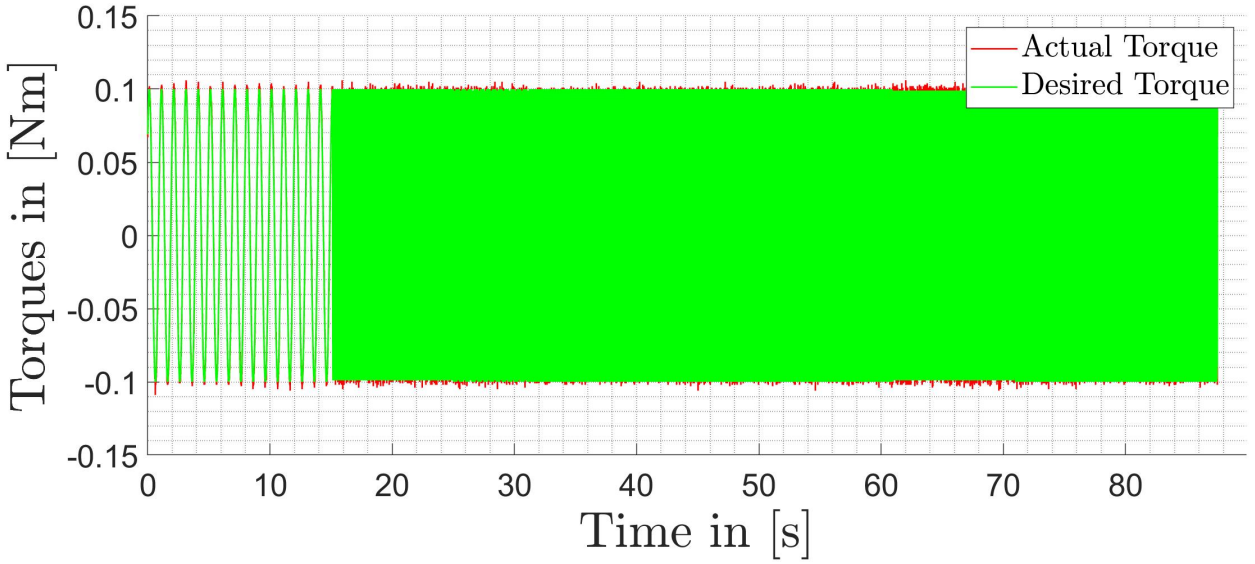

Figure 4.21: Tracking behaviour with direct torque control - Desired and actual torques. Red denotes the desired torque trajectory and blue denotes the actual torque provided by the motor.

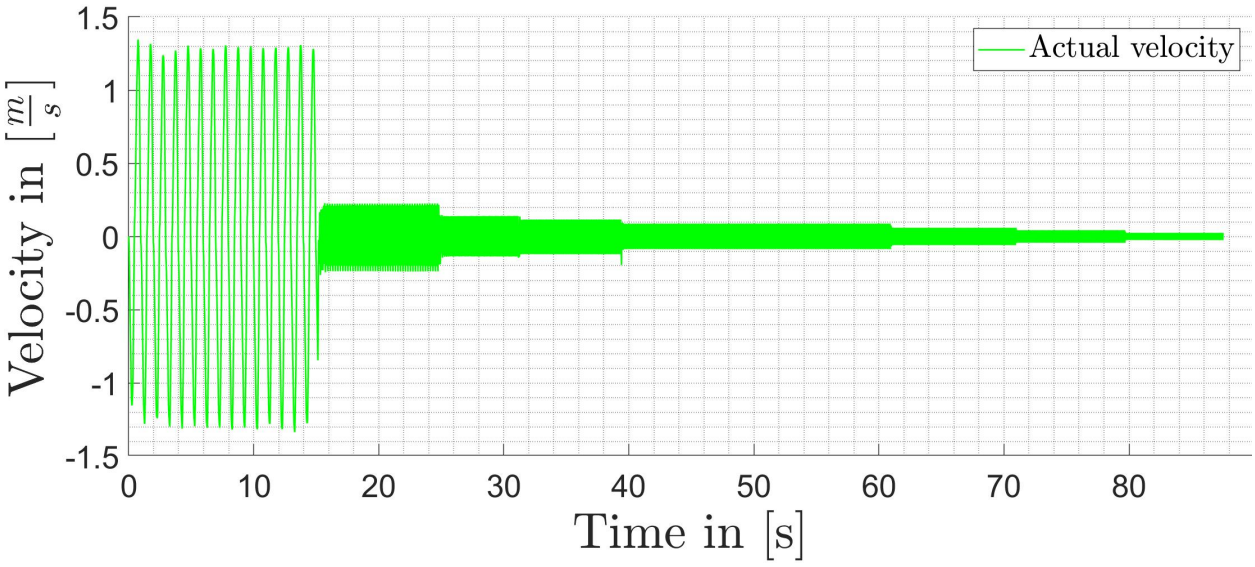

Figure 4.22: Tracking behaviour with direct torque control - Velocity decrease during torque control with increasing frequency

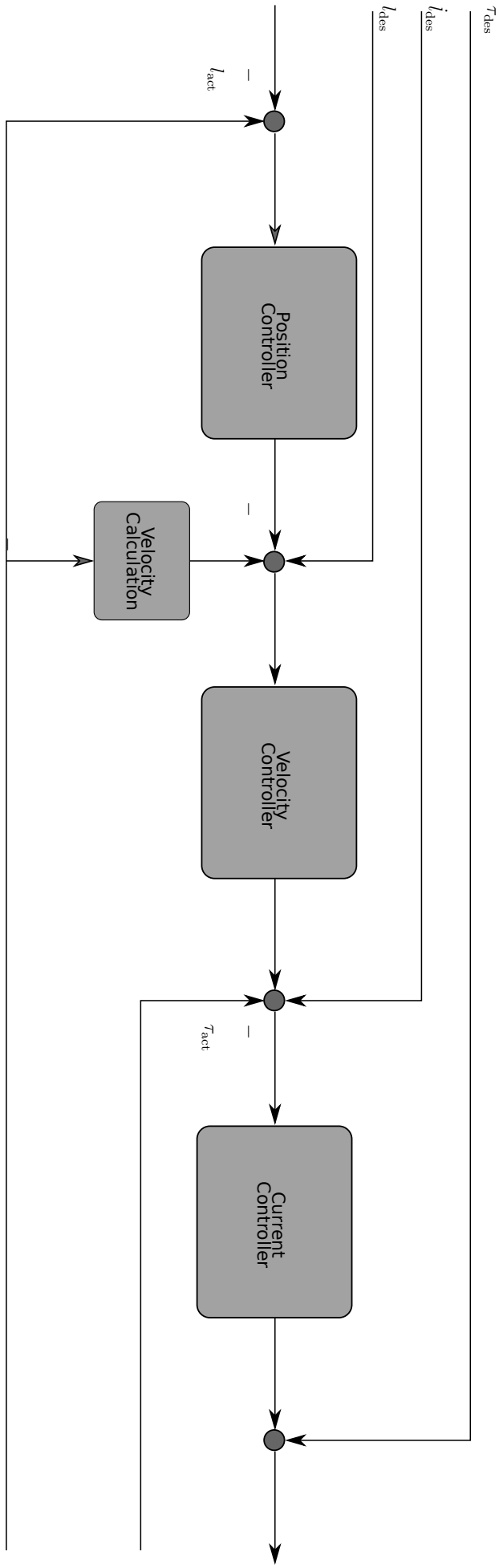

Figure 4.23: Low-Level Control schem of motors

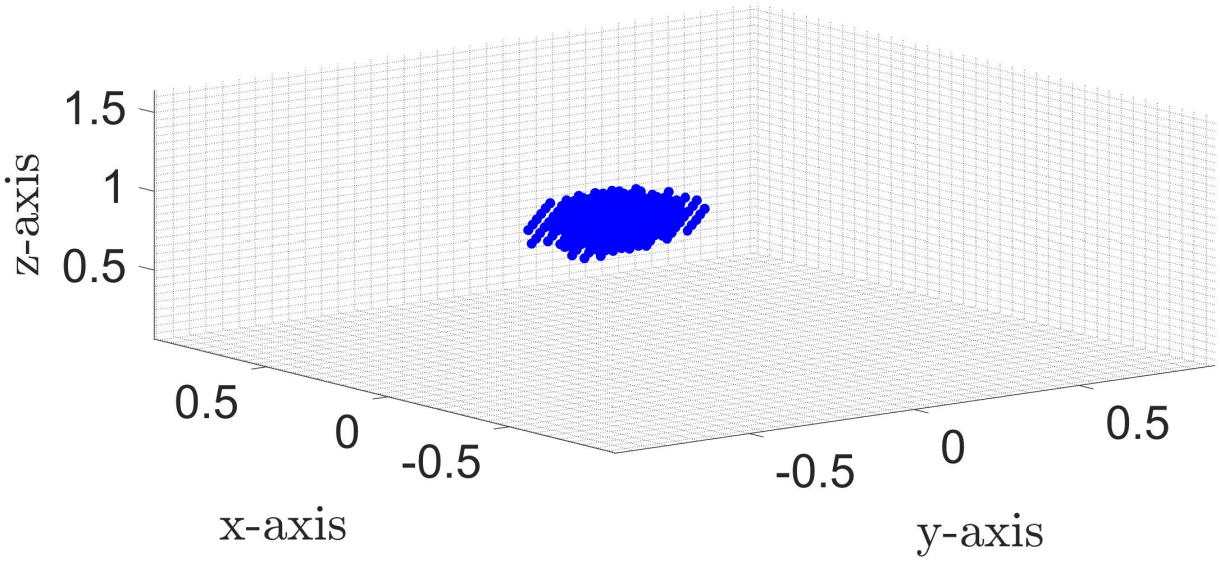

Figure 4.24: Compliance of simplified and extended kinematic model with $\boldsymbol{d}_{kin} \leq 1.287$mm

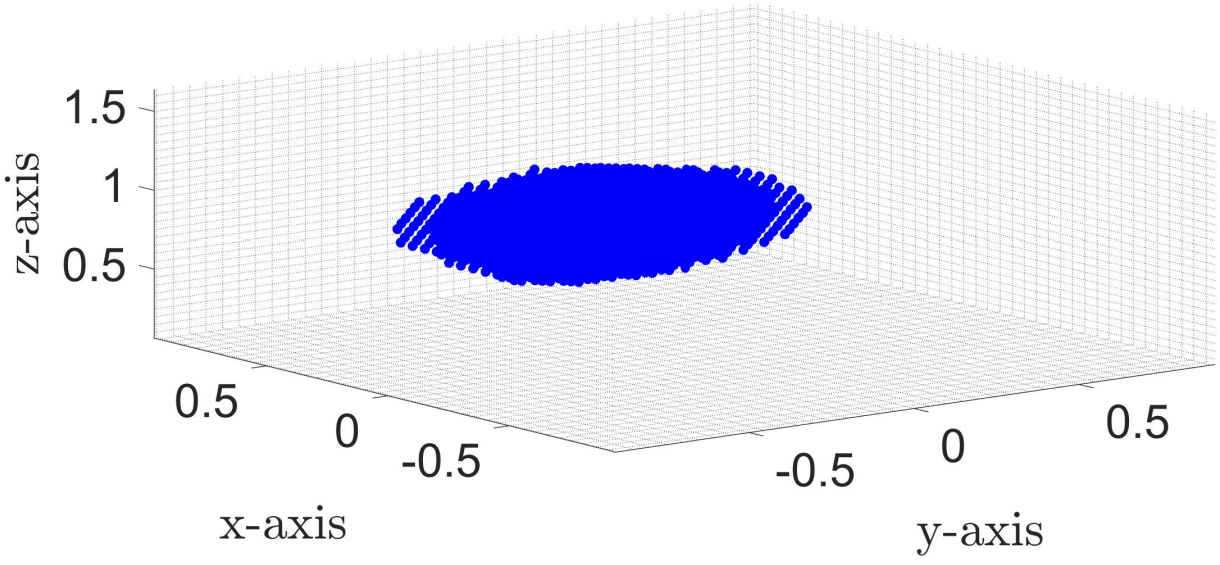

Figure 4.25: Compliance of simplified and extended kinematic model with $\boldsymbol{d}_{kin} \leq 1.346$mm

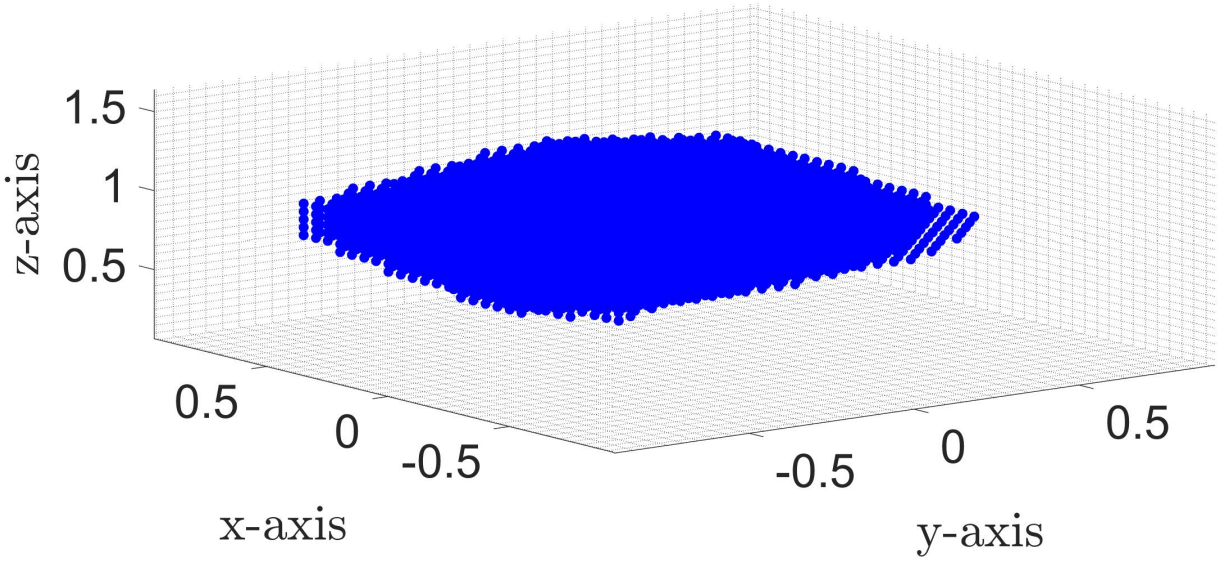

Figure 4.26: Compliance of simplified and extended kinematic model with $\boldsymbol{d}_{kin} \leq 1.404$mm

Table 4.2: Kinematic parameters of the Mini Cablerobot Simulator

Kinematic parameters								
	$\boldsymbol{a}_1$	$\boldsymbol{a}_2$	$\boldsymbol{a}_3$	$\boldsymbol{a}_4$	$\boldsymbol{a}_5$	$\boldsymbol{a}_6$	$\boldsymbol{a}_7$	$\boldsymbol{a}_8$
x $[m]$	-0.907	-0.853	0.911	0.871	0.907	0.860	-0.900	-0.870
y $[m]$	0.871	0.965	0.820	0.918	-0.845	-0.928	-0.829	-0.935
z $[m]$	1.640	0.068	1.590	0.079	1.610	0.079	1.600	0.063
	$\boldsymbol{b}_1$	$\boldsymbol{b}_2$	$\boldsymbol{b}_3$	$\boldsymbol{b}_4$	$\boldsymbol{b}_5$	$\boldsymbol{b}_6$	$\boldsymbol{b}_7$	$\boldsymbol{b}_8$
x $[m]$	-0.127	-0.206	0.014	0.134	0.135	0.008	-0.143	-0.220
y $[m]$	0.177	0.065	0.239	0.175	-0.186	-0.241	-0.206	-0.082
z $[m]$	0.115	-0.111	-0.102	0.122	-0.101	0.114	-0.092	0.107

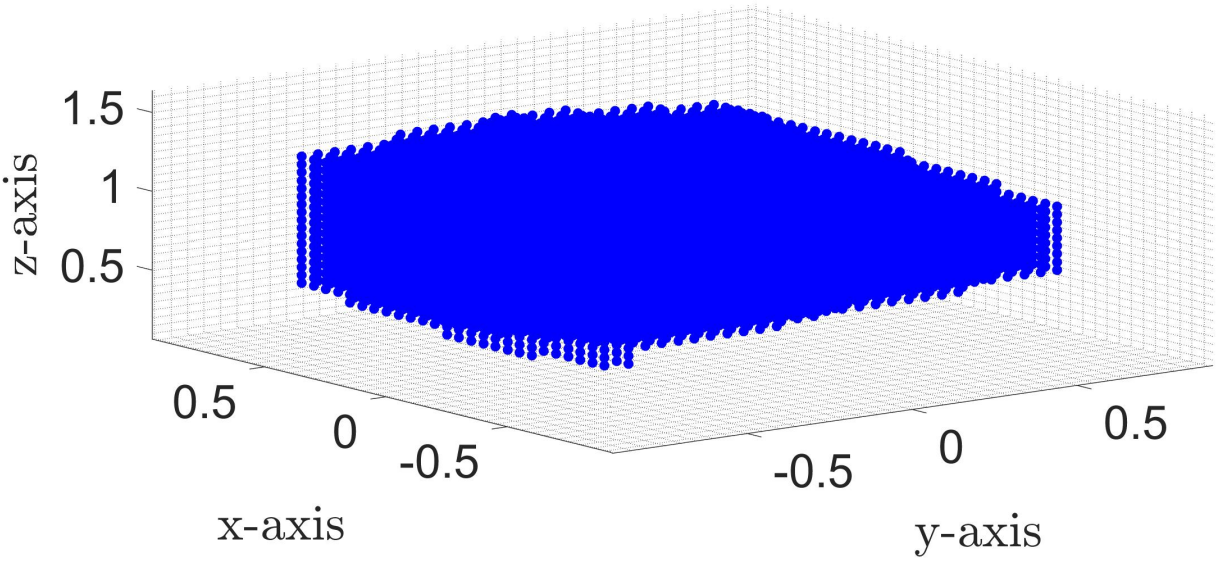

Figure 4.27: Compliance of simplified and extended kinematic model with $\boldsymbol{d}_{kin} \leq 1.463$mm

4.2.4 Investigations on modelling and drivetrain characteristics

Cable-Driven Parallel Robot are used in different fields with different system characteristics and requirements on robustness and accuracy. For instance, high precision tasks and precise acceleration tracking are demanding for the friction compensation and require a good understanding for the drivetrain characteristics, where friction occurs first and foremost. Thus, an accurate drivetrain analysis is fundamental for further modelling steps and controller design. The following experiments investigate damping, creeping, hysteresis and the drivetrain dynamics. Therefore one cable, attached at the motor, is connected with a force sensor at the frame (see Figure 4.29) Two experiments with the setup given in Figure (4.29) provide information about the damping characteristics of the drivetrain and their dynamics. The results of all drivetrains are similar to each other.

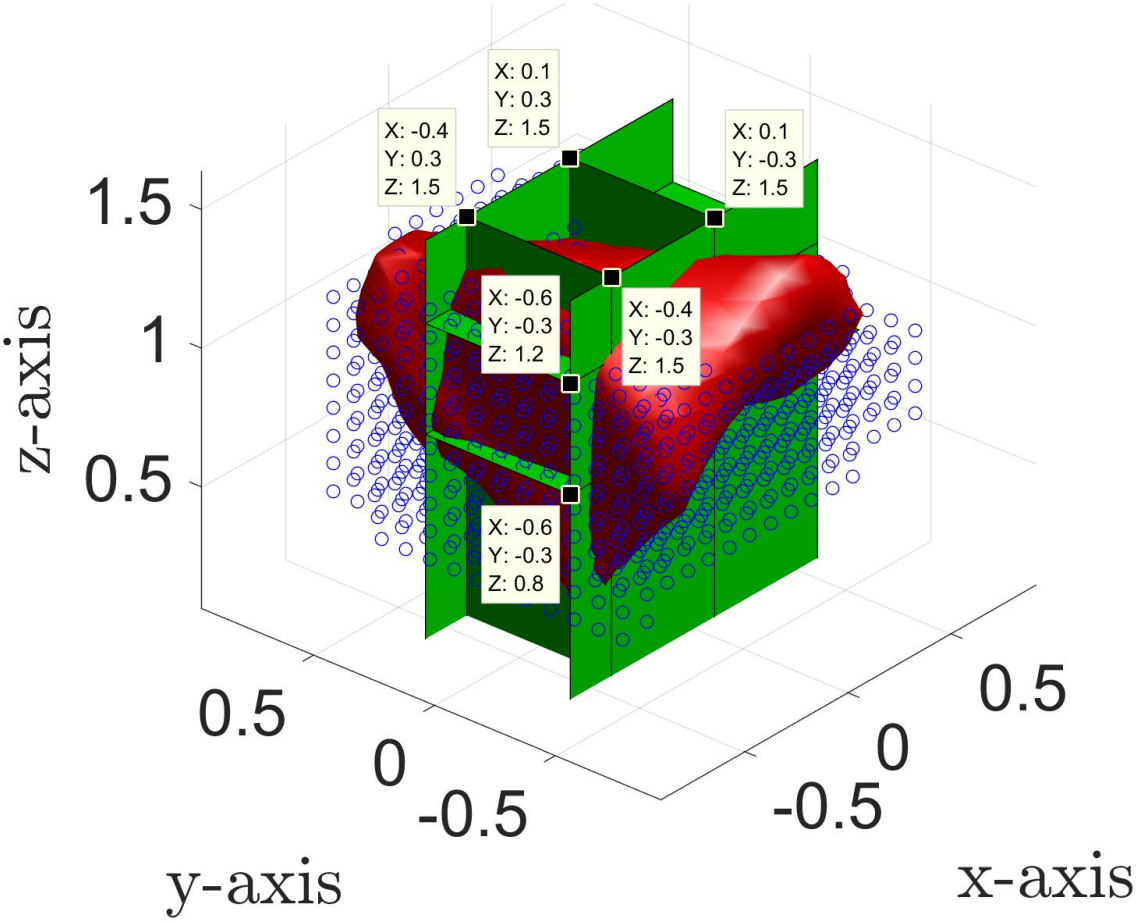

Figure 4.28: Set of points with difference in cable length less than 1.463mm and wrench-feasible workspace

Table 4.3: Kinematic parameters for comparison of extended and simplified kinematic model

Cable	$\boldsymbol{a}_i$ [m]			$\boldsymbol{b}_i$ [m]		
1	0.91	0.87	1.6	-0.13	0.18	0.12
2	-0.85	0.97	0.07	-0.21	0.07	-0.11
3	0.91	0.83	1.6	0.01	0.24	-0.1
4	0.87	0.92	0.08	0.13	0.18	0.12
5	0.91	-0.85	1.6	0.14	-0.19	-0.1
6	0.86	-0.93	0.08	0.01	-0.24	0.11
7	-0.9	-0.83	1.6	-0.14	-0.21	-0.09
8	-0.87	-0.94	0.06	-0.22	-0.08	0.11

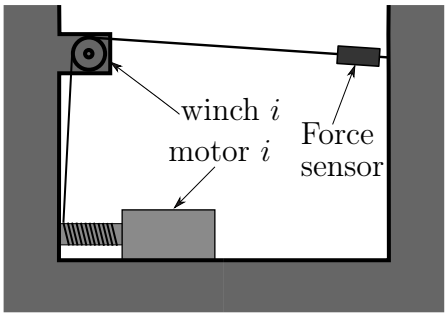

Figure 4.29: Experimental setup for drivetrain identification

Figure 4.30: Force sensor KM30z with forces up to 1kN

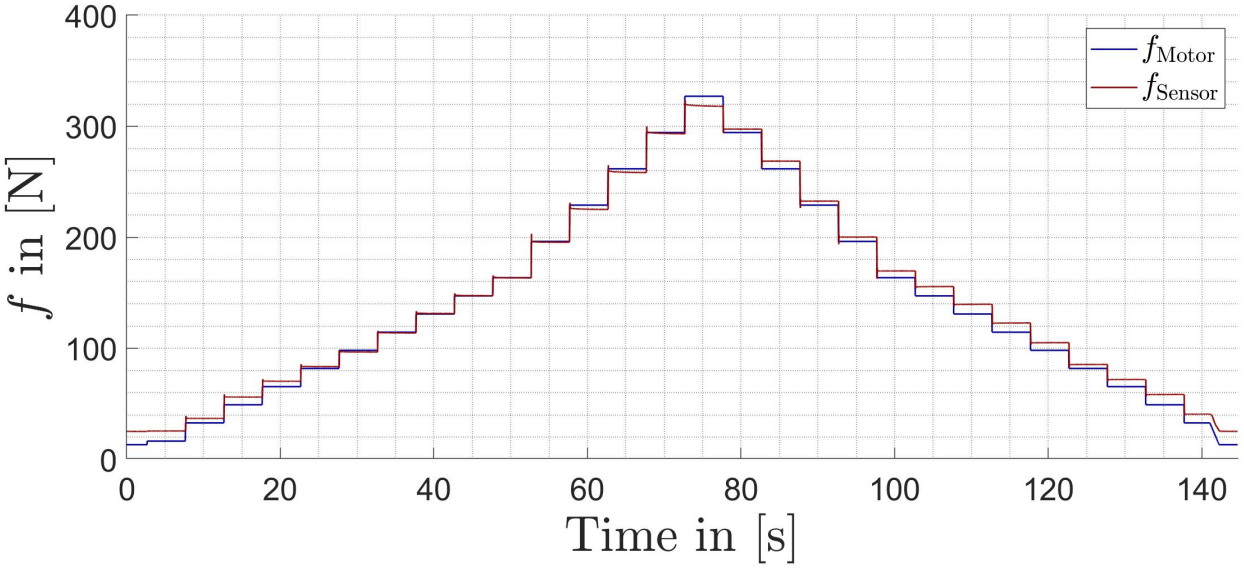

Figure 4.31: Applied and measured cable forces - entire experiment

Drivetrain characteristics - damping

Multiple step functions on different tension levels are applied. Based on the findings in previous sections, one presumes dependency of those characteristics on the cable tension level. Thus step function on different tension levels in ascending and descending direction are a reasonable choice. Ascending and descending tension levels account for presumed hysteresis effects. Figures 4.31-4.36 show in blue the applied forces at the motor and in magenta the measured forces provided by a force sensor of type KM30z from ME-Meßsystem GmbH (see Figure 4.30) for two desired tension levels in ascending and descending direction. The cable tensions increase from $70N$ to $300N$ and decrease back to $70N$ Figure 4.31 shows the applied and measured cable tensions over the entire experiment and Figure 4.32 plot the measured cable forces over the applied forces. Although the motor applies step functions with consistent step height, the step height measured by the force sensor is inconsistent. With increasing tension level, the force sensor falls behind the applied force, while for decreasing tension levels the force measurement of the sensor are higher than the applied force. Figure 4.32 depicts this hysteresis effect, that indicates energy loss due to friction. A closer look at 4 sections (two in ascending direction and two in descending direction) give the following insight

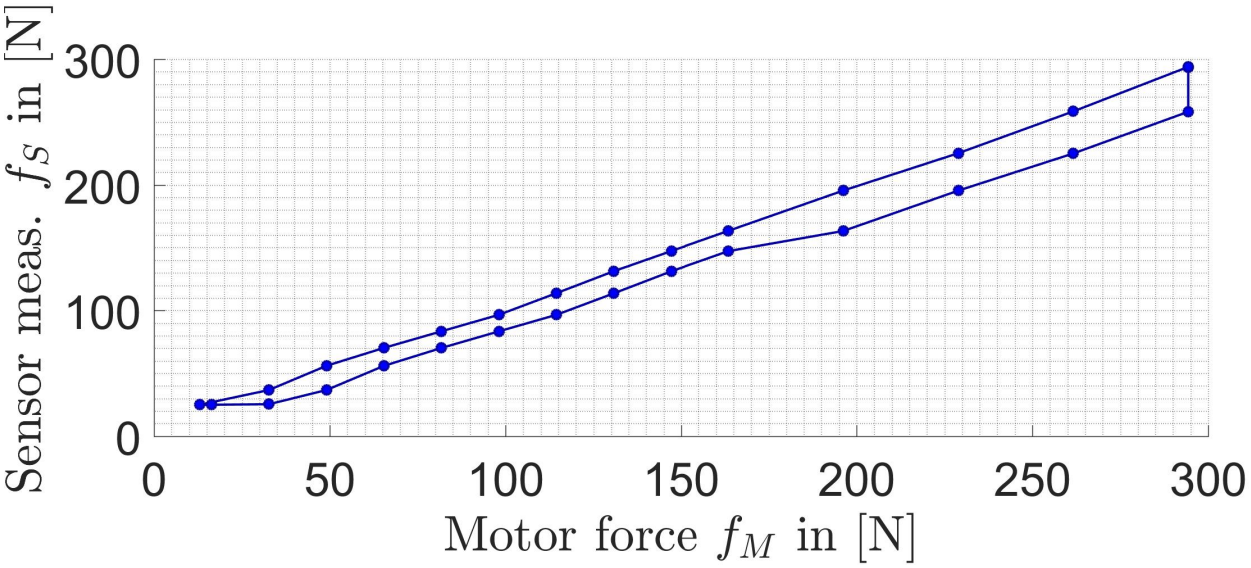

Figure 4.32: Applied and measured cable forces - Hysteresis

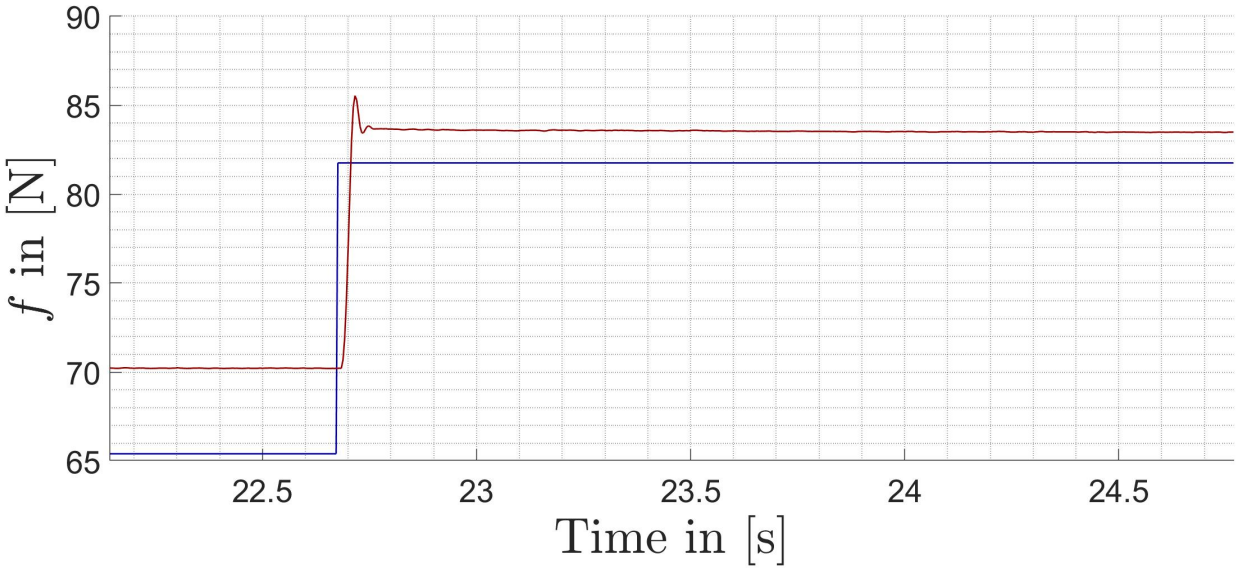

Figure 4.33: Increasing and Decreasing torques for torque step function - Low tension level and increasing tension levels

- **Figure 4.33 Low tension level with increasing tensions:** Already with low cable tensions the system is very stiff and under-damped The internal torque controller compensates for the first oscillations. This is why the overshoot at the beginning of each step decays after 0.2s. Afterwards oscillations are still present. The oscillations reduce and trend downwards.

- **Figure 4.34 High tension level with increasing tensions:** Here the downwards trend is distinct and could relate to creeping. Again the torque control reduces oscillation at the beginning.

- **Figure 4.35 and 4.36 Decreasing tensions:** These figures show the applied and measured cable forces for decreasing tension levels. In [47] the authors state that creeping is even more visible for unloading periods than for loading periods. This

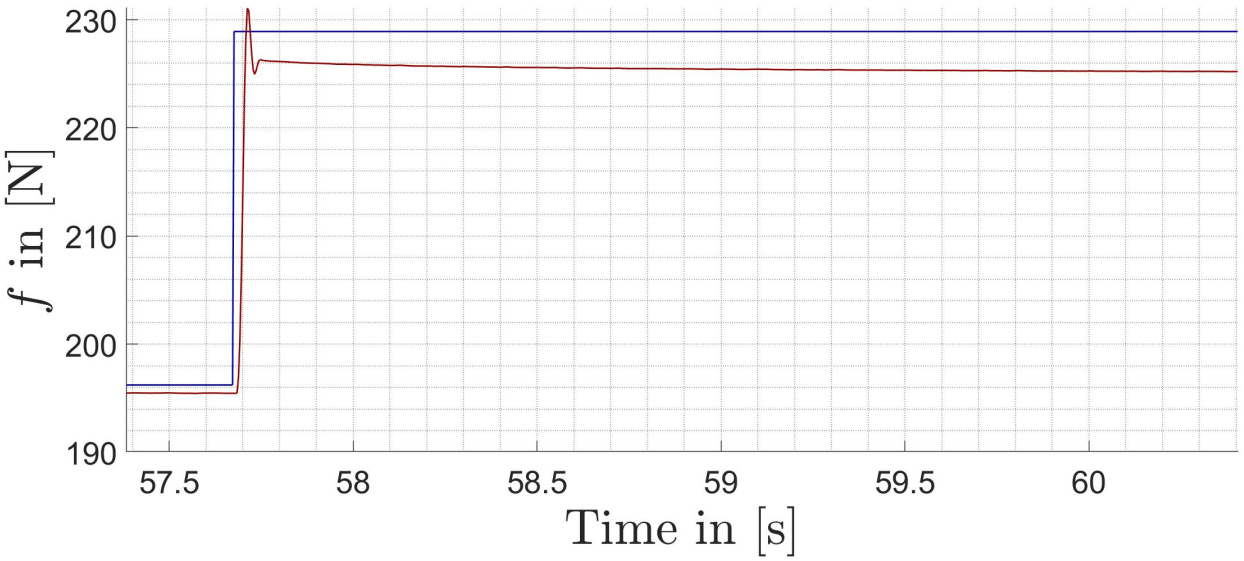

Figure 4.34: Increasing and Decreasing torques for torque step function - High tension level and increasing tension levels

is not the case in this experiment, which strengthen the assumption of mechanical settlement and excludes creeping.

In [69] the author showed the existence of non-linear drivetrain dynamics and identified parameters for the authors proposed model. This model composites the dynamics of a non-linear spring and a damper to incorporate hysteresis. Experimental evaluation of this model underlines the findings of this thesis. However, further investigations on hysteresis are out of the scope of this work and will not be pursuited. Instead, the following section will focus on friction compensation, since especially static friction in the drivetrain is of interest for vibration suppression. Since the development of a precise model for the MiCaRoSi is not a trivial task other more promising attempts are pursuited.

Drivetrain characteristics - dynamics

The second experiment investigates the open loop response of the system illustrated in Figure 4.29. For this purpose, the motor tracks a desired sinusoidal trajectory in position control[9]. Figure 4.37 shows the desired position $l_{3,des}$ and the actual position $l_{3,act}$ for drivetrain three. The amplitude of $l_{3,des}$ is set to 3mm. Higher amplitudes do not provide more accurate results and instead can cause instabilities. A Fast-Fourier transformation of the error $l_{3,des} - l_{3,act}$ reveals a minimum of tracking accuracy for 20 Hz. This minimum is characteristic for systems with two poles [92].However, the Matlab Identification Toolbox provides a transfer function with one pole and delay as a good fitting with the measurement

[9]Remember that direct torque control is not a suitable choice as control strategy because of poor performance in position tracking.

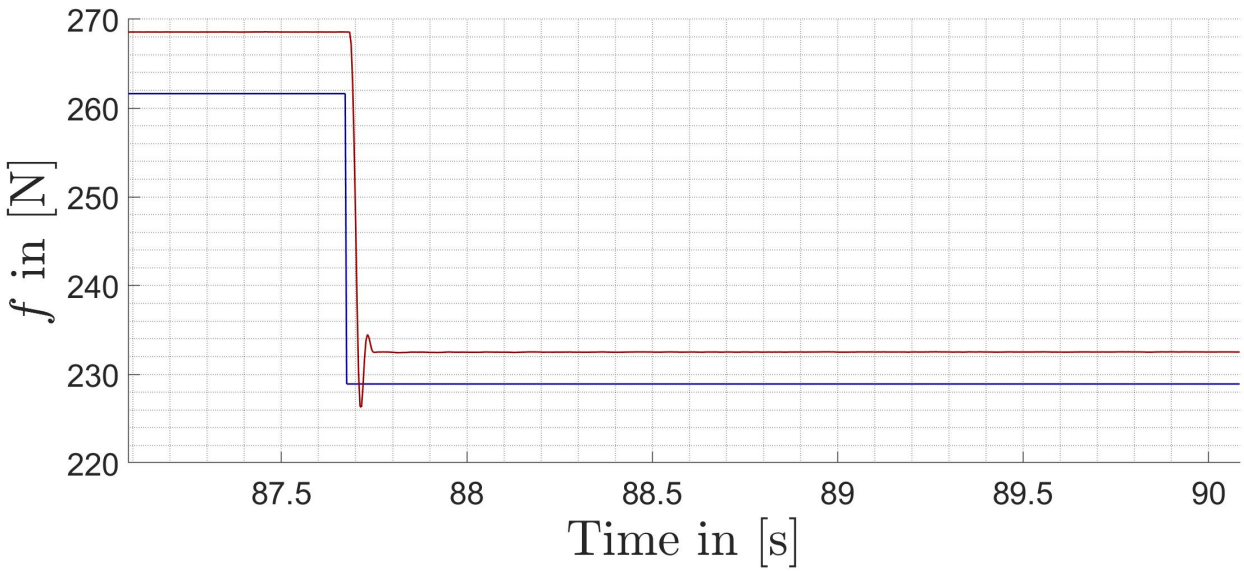

Figure 4.35: Increasing and Decreasing torques for torque step function - High tension level and decreasing tension levels

data. The identified transfer function reads:

$$G_{l_{des} \rightarrow l_{act}} = \frac{1}{1 + 0.00057665s} e^{0.006s} \tag{4.31}$$

and matches with the observations made in [92]. A second pole, that characterizes the minimum of tracking accuracy at $20Hz$, is probably close to one zero and thus cancels out. Indeed, a transfer function with two poles and one zero matches slightly better the experimental data.

Transfer functions are a linear representation for a mapping from one quantity to another one and are either valid for all possible values (linear systems) or only in the vicinity of a working point (non-linear systems). Here the complexity of the drivetrain (in particular the cables) is underestimated and internal cross-coupling and changing stiffness not considered. Thus, more investigations are necessary to pay consideration to the complexity of cable dynamics and to incorporate appropriate control techniques.

4.2.5 Evaluation of the Adaptive Friction compensation algorithm

Previous sections investigated experimentally cable dynamics and Low-Level Control structure. The findings of those experiments define the model and controller strategies to suppress efficiently vibrations induced by controllers, static friction and forwarded by the cable dynamics. In particular according to [52], control of flexible components (such as cables) in presence of stiction is even more difficult, than stiction itself. This section evaluates and verifies the two proposed control strategies for vibration suppression. The first experiment evaluates the proposed adaptive friction compensation in Section 4.2.5 experimentally for a similar sinusoidal trajectory. For this experiment the Low-Level-Controller operated in

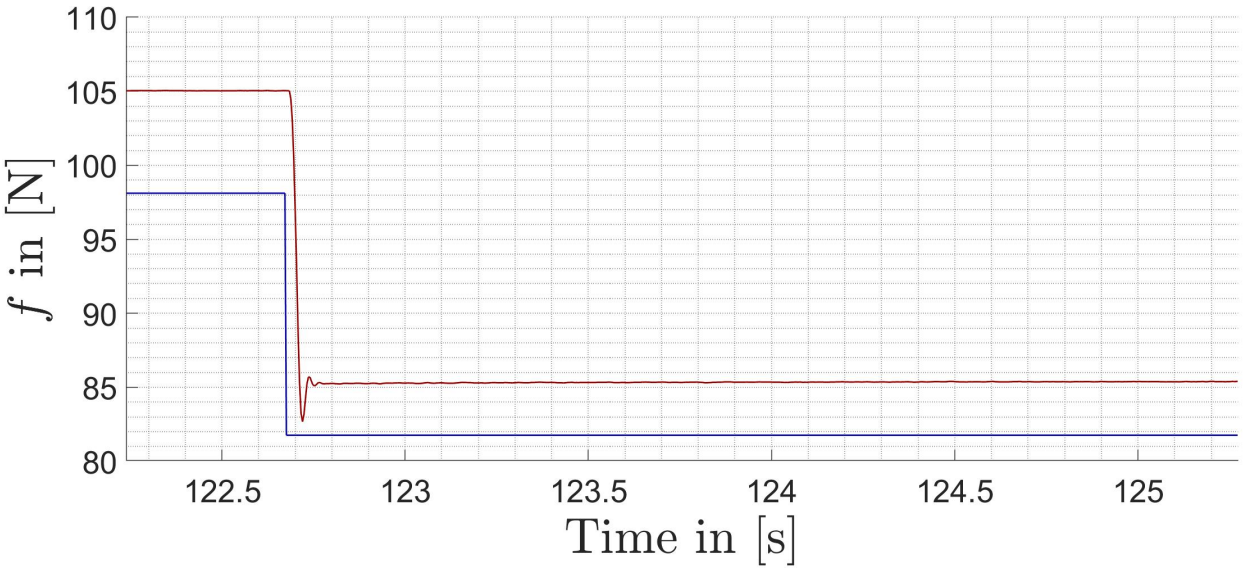

Figure 4.36: Increasing and Decreasing torques for torque step function - Low tension level and decreasing tension levels

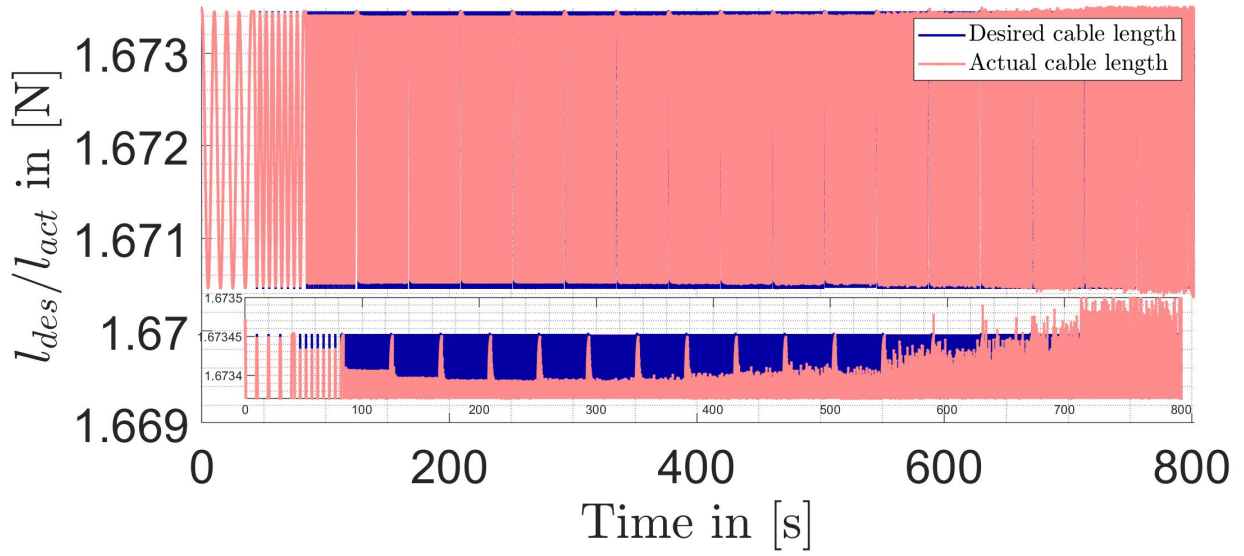

Figure 4.37: Desired and actual cable lengths for drivetrain identification process

position control. In the second experiment the system operates in torque control mode and evaluates the adaptive Super-Twisting Sliding-Mode Controller, proposed in Section 3.3.

Goal of the first experiment is to let motor three follow the desired length $l(t)_{3,des}$ in presence of friction. The desired length is a sinusoidal function with $1mm$ of amplitude and $0.2Hz$ of frequency. Because of small amplitudes stiction is more evident. At one end the motor pulls at the cable, while at the other end the cable is attached with a force sensor at the frame (see Figure 4.30 and Figure 4.29). Small amplitudes are necessary since the experimental setup does not allow big changes in cable lengths. Otherwise the motor torques exceed the feasible torque limits. The friction compensation is active during the first half, whereas it is inactive during the second half (see Figure 4.40a). Figure 4.39 plots the measured forces at the cable tip over the cable elongation and depicts hysteresis. The integral over the cable

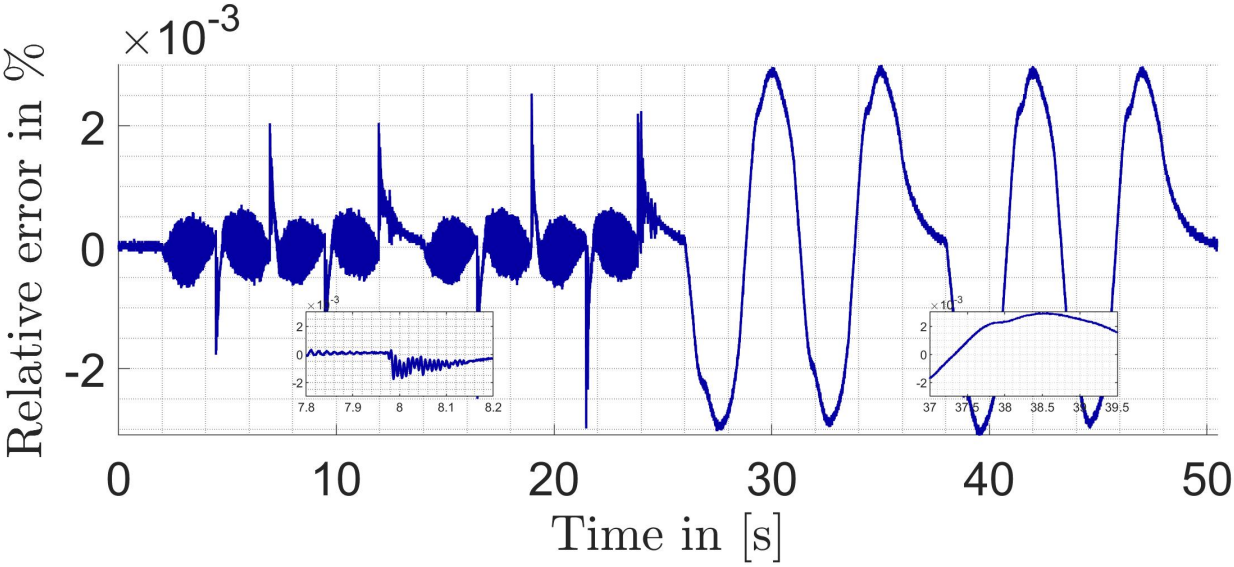

Figure 4.38: Experimental evaluation of the adaptive friction compensation algorithm - Error. The friction compensation is active during the first half of the experiment and inactive during the second half.

elongation reveals a loss of energy. More precisely, energy dissipates due to friction. To compensate for friction, the adaptive friction compensation algorithm adds the complement $\delta_{3,des}$ to the desired cable length. Based on this data the algorithm computes a virtual trajectory $l_{3,des,virt} = l_{3,des} + \delta_{3,des}$. Figure 4.40a shows the desired cable lengths in red, the commanded cable lengths in green and the actual cable lengths in blue. A significant improvement in tracking accuracy is visible, when the adaptive friction compensation is active (see Figure 4.40b). Furthermore, this experiment exhibits similar hysteresis effects as in [69]. During motion the friction compensation achieves almost perfect tracking of l_{des} The discontinuous signum function makes the actual cable length l oscillate around the desired cable length l_{des}. However, these oscillations carry no weight because of their small amplitudes. Only at the point of return the friction compensation does not match the expectations. In this particular moment δ_{des} equals l_{des} such that there is no visible improvement due to the friction compensation at the turn points. During the second half of the experiment the friction compensation is inactive (see Figure 4.40c). Then l_{des} equals $l_{3,\mathrm{des,virt}}$ and e increases. Figure 4.38 illustrates the improvement due to the proposed friction compensation algorithm. Figure 4.38 shows spikes in the first half every time a change in direction occurs. These spikes are in similar magnitude to the maximum error when the friction compensation is inactive. To draw a conclusion, the proposed friction compensation performed worse than expected when the velocity changed sign. However, during motion there is a significant improvement in accuracy thanks to the friction compensation.

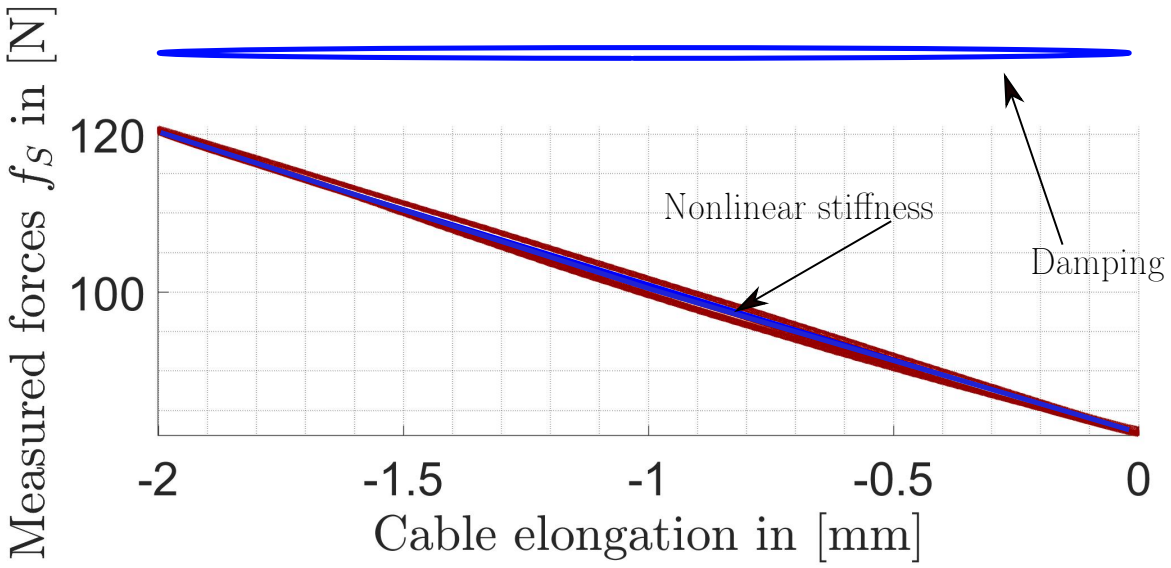

Figure 4.39: Experimental evaluation of the adaptive friction compensation algorithm - Measured cable forces over cable elongation in $[mm]$

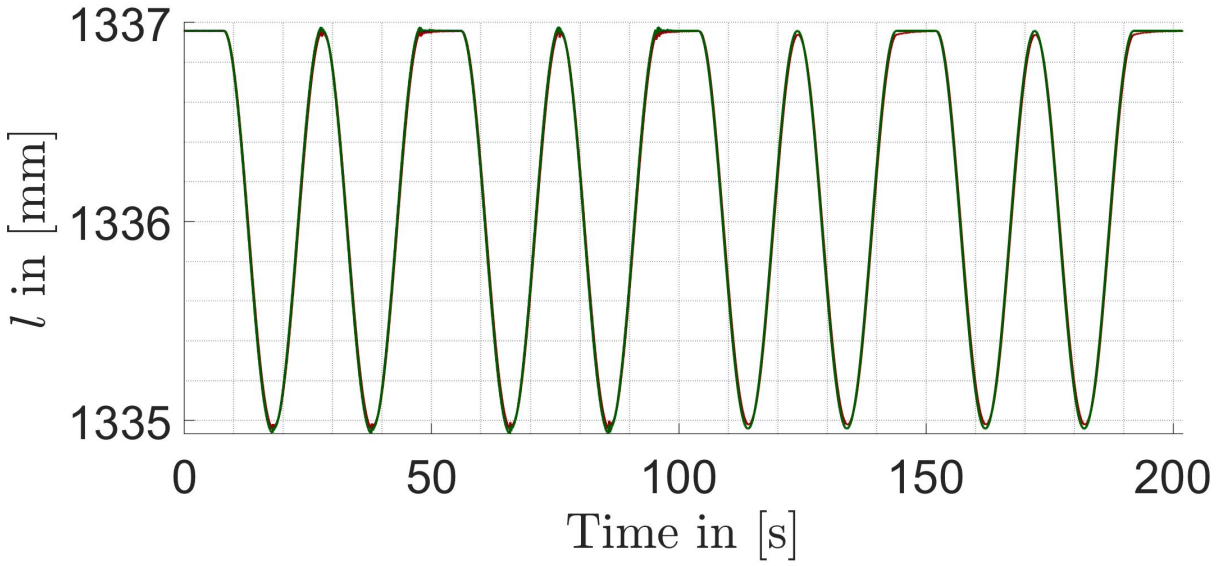

(a) Desired virtual and actual trajectory - friction compensation

4.2.6 Evaluation of the Adaptive Super-Twisting Sliding-Mode Controller

Goal in this section is to assess whether the Adaptive Super-Twisting Sliding-Mode Controller holds the promising features proposed in Chapter 3 or not. These features are finite-time convergence, robustness, stability and reduced chattering compared to classical Sliding-Mode Controller

The Adaptive Super-Twisting Sliding-Mode Controller has to stear the sliding variable $\boldsymbol{\sigma} = \dot{\boldsymbol{e}} + \boldsymbol{\Lambda}_{SMC}\boldsymbol{e}$ or $\boldsymbol{e} = \dot{\boldsymbol{e}} = \ddot{\boldsymbol{e}} = \mathbf{0}$ and its derivative $\dot{\boldsymbol{\sigma}} = \ddot{\boldsymbol{e}} + \boldsymbol{\Lambda}_{SMC}\dot{\boldsymbol{e}}$ to zero, i.e. $\boldsymbol{\sigma} = \dot{\boldsymbol{\sigma}} = \mathbf{0}$. Again $\boldsymbol{e} = \boldsymbol{z}_{1,des} - \boldsymbol{z}_1$ is the error in position and orientation, defined as the difference between the desired and the actual pose (see Equation (3.20)) and $\boldsymbol{\Lambda}_{SMC}$ is a positive definite

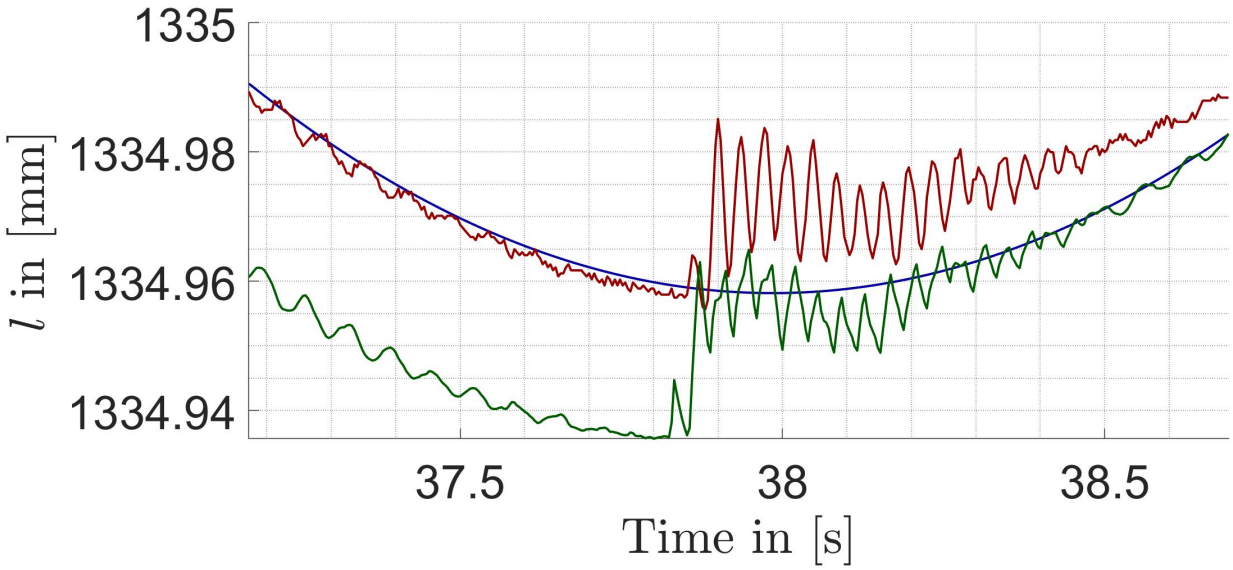

(b) Desired virtual and actual trajectory - friction compensation

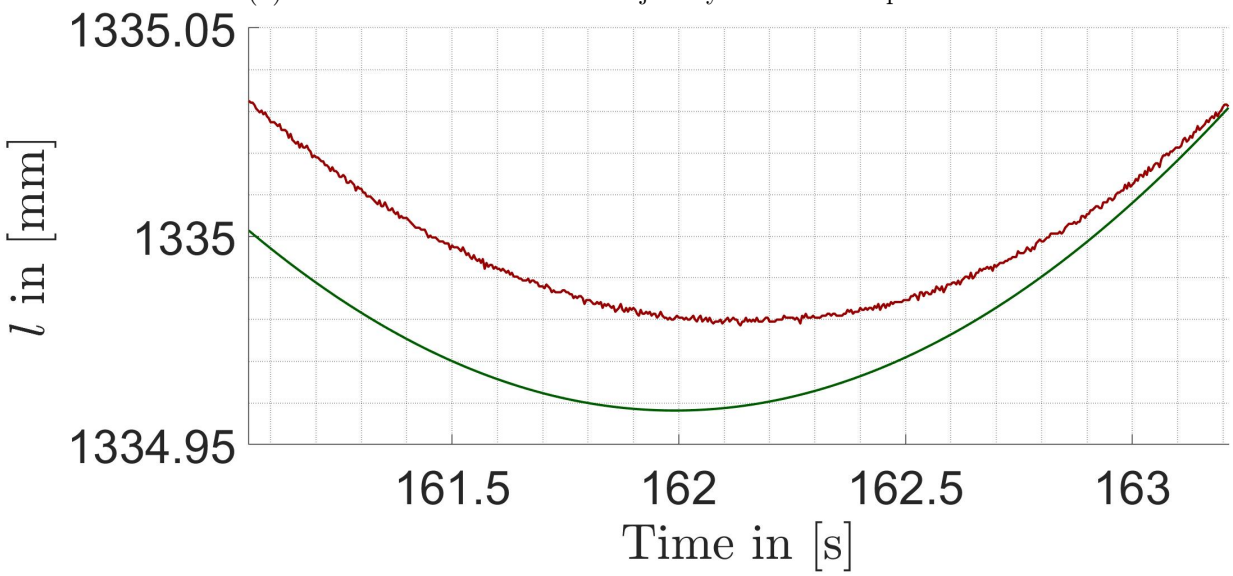

(c) Desired virtual and actual trajectory - friction compensation

Figure 4.40: Experimental evaluation of the adaptive friction compensation algorithm - Position tracking

matrix of proper size. Lumped perturbations $\boldsymbol{\xi}$ (external disturbances, uncertain parameters, unmodelled dynamics and measurement noise) perturb the system while the adaptive Super-Twisting Sliding-Mode Controller is performing this task. For the experiment the MiCaRoSi is working with the kinematic parameters of Table 4.3. The system runs in torque control and position and velocity control are suspended from the control loop.

Remark 4.3: Section 4.2 stated that direct torque control does not account for an accurate tracking of positions and velocities. However, Chapter 3 compared the adaptive Super-Twisting Sliding-Mode Controller with the Terminal Sliding-Mode Controller , with both systems in direct torque control. Hence, an experimental evaluation of the proposed adaptive Super-Twisting Sliding-Mode Controller should be done in direct-torque control, in-spite of the advantages of position control.

Figure 3.31 depicts the overall control structure, which composes of the following blocks:

- The Forward Kinematics (Section 2.1.2) reconstructs the platform pose $\boldsymbol{x}_P$ based on encoder measurements and the Inverse Kinematics subscribes the Jacobian matrix to the tension distribution algorithm.

- An arbitrary order Sliding-Mode Differentiator (Section 3.3.3) provides the platform velocities $\dot{\boldsymbol{x}}_P$ and accelerations $\ddot{\boldsymbol{x}}_P$ to compute $\boldsymbol{\sigma}$ and $\dot{\boldsymbol{\sigma}}$. Once the differentiator gains are set properly, the Sliding-Mode Differentiator achieves finite-time convergence, exact tracking in absence of measurement noise, exact stabilisation and provides robustness. The authors in [99] suggest to choose $\lambda_{SMD,0} = 1.1$,$\lambda_{SMD,0} = 1.5$ and $\lambda_{SMD,0} = 3$. Together with $L = 15$ the Sliding-Mode Differentiator estimates $\boldsymbol{x}_P$,$\dot{\boldsymbol{x}}_P$ and $\ddot{\boldsymbol{x}}_P$ accurately enough [20].

- Then the composite control input $\boldsymbol{u} = \boldsymbol{u}_{\mathrm{SM}} + \boldsymbol{u}_{FF}$ computes a wrench to achieve 2-sliding mode and to compensate for $\boldsymbol{\xi}$. Again, $\boldsymbol{u}_{FF}$ is the feed-forward control input, based on the inverse system dynamics of the nominal model (Section 2.2.1) and $\boldsymbol{u}_{SM}$ is the contribution of the adaptive Super-Twisting Sliding-Mode Controller (Section 3.3) with gain adaptation (Section 3.3.3).

- Finally, the closed-form force distribution algorithm [12] finds a map from $\boldsymbol{u}$ to a set of feasible cable tensions or torques respectively. The simple equation

$$\tau_i^\star = \frac{f_i r_D}{M_0} 1000\,, \tag{4.32}$$

  with the nominal standstill torque M_0 relates commanded torques $\tau_i^\star$ and cable forces f_i. The commanded torque $\tau_i^\star$ has no physical meaning.

This control structure fulfils the control objective based on encoder measurements only, that is the bare amount of measurement inputs Cable-Driven Parallel Robot can come up with.

In the evaluation experiment the platform has to follow the desired trajectory

$$\begin{aligned} \boldsymbol{r}_{des} &= \begin{bmatrix} 0.15 + 0.15\cos(\omega \cdot t - \frac{\pi}{2}) \\ -0.145 + 0.15 + 0.15\sin(\omega \cdot t - \frac{\pi}{2}) \\ 0.85 \end{bmatrix} m \\ \boldsymbol{\nu}_{des} &= \begin{bmatrix} 0 & 0 & 0 \end{bmatrix}^{\circ\, T}, \end{aligned} \tag{4.33}$$

with $\omega = 0.5$ (see Figure 4.41). Dashed vertical lines illustrate points in time at which external forces act on the platform. Between $55s$ and $61s$ the total mass of the platform increases due to an additional weight of $5kg$. This corresponds to $\approx 192\%$ of the original end-effector mass and an external disturbance $\boldsymbol{\zeta} = [0, 0, -50N, 0, 0, 0]^{\mathrm{T}}$. Then between $162s$ and $127s$ an external disturbance $\boldsymbol{\zeta} \approx [-100N, 0, 0, 0, 0, 0]^{\mathrm{T}}$ tries to distract the platform from the desired trajectory. This external disturbance is equivalent to $\approx 384\%$ of the platform mass. The

last two dashed lines between $143s$ and $155s$ depict the time when $\boldsymbol{\zeta} = [100N, 0, 0, 0, 0, 0]^{\mathrm{T}}$ pushes the platform in $\boldsymbol{x}_W$ direction. The controller parameters are $\epsilon_{STC} = 0.3$, $\gamma_{STC} = 1$, $\boldsymbol{\Omega_\Lambda} = 21.213$. Note, that the controller drives the platform to the desired trajectory in less than half a second. This provides a practical proof for the finite-time convergence. Figures 4.41-4.48 present the experimental results and reveal the following insights:

- **Figures 4.41-4.42** confirms the finite-time convergence of the Sliding-Mode Differentiator to the values computed by the forward kinematics. The Sliding-Mode Differentiator achieves convergence to $\boldsymbol{x}_{FK,P}$ in less than 10s.

- **Figures 4.43-4.44:** A platform velocity was not at hand, making numerical differentiation of $\boldsymbol{x}_{FK,P}$ the fastest way to obtain $\dot{\boldsymbol{x}}_P$. However, numerical differentiation, the Sliding-Mode Differentiator achieves smooth estimation of $\boldsymbol{x}_P$ due to its robustness against measurement noise and is preferred against numerical differentiation.

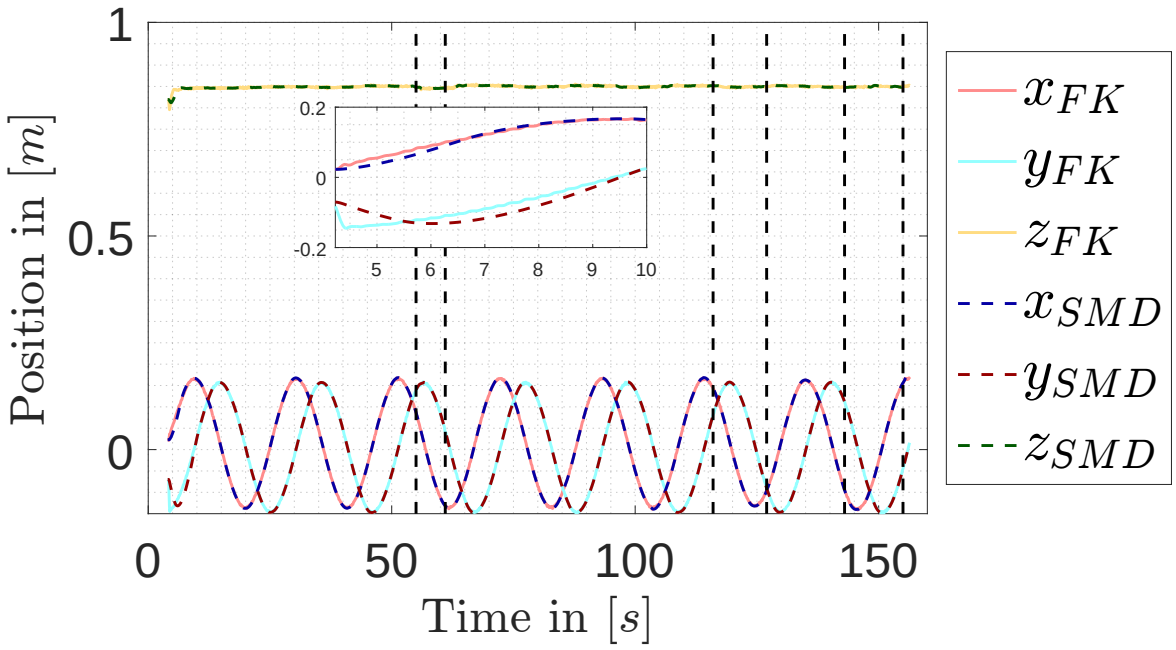

Figure 4.41: Experimental evaluation of the adaptive Sliding-Mode Differentiator - Position from forward kinematics and Sliding-Mode Differentiator

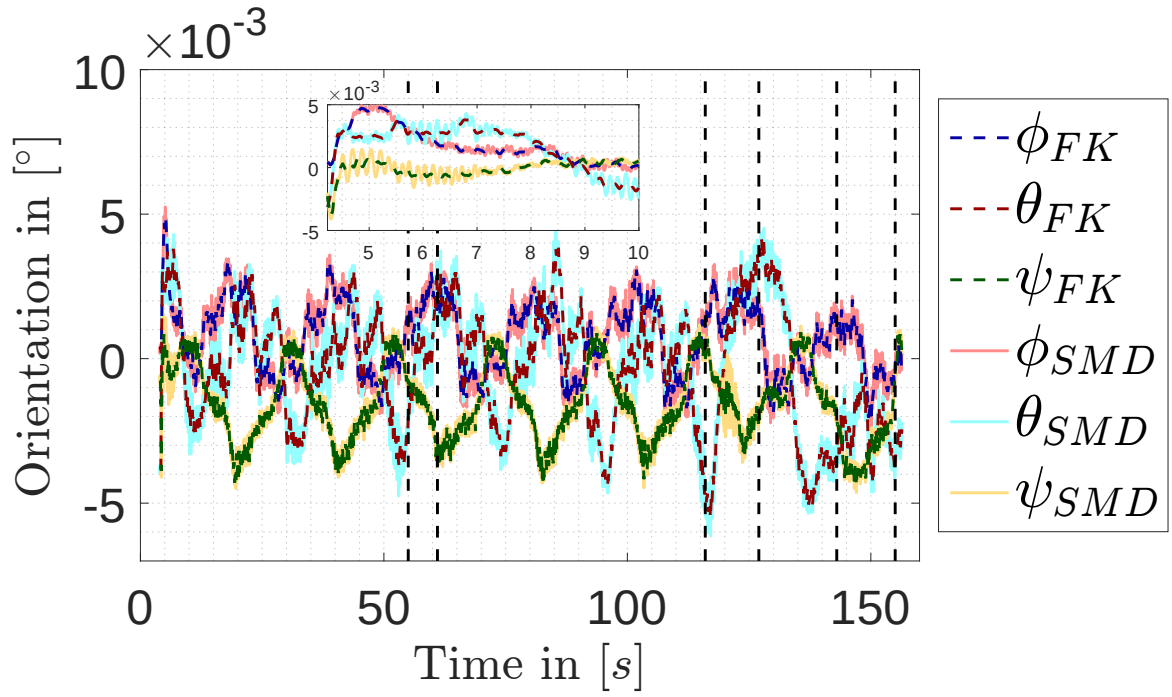

Figure 4.42: Experimental evaluation of the adaptive Sliding-Mode Differentiator - Orientation from forward kinematics and Sliding-Mode Differentiator

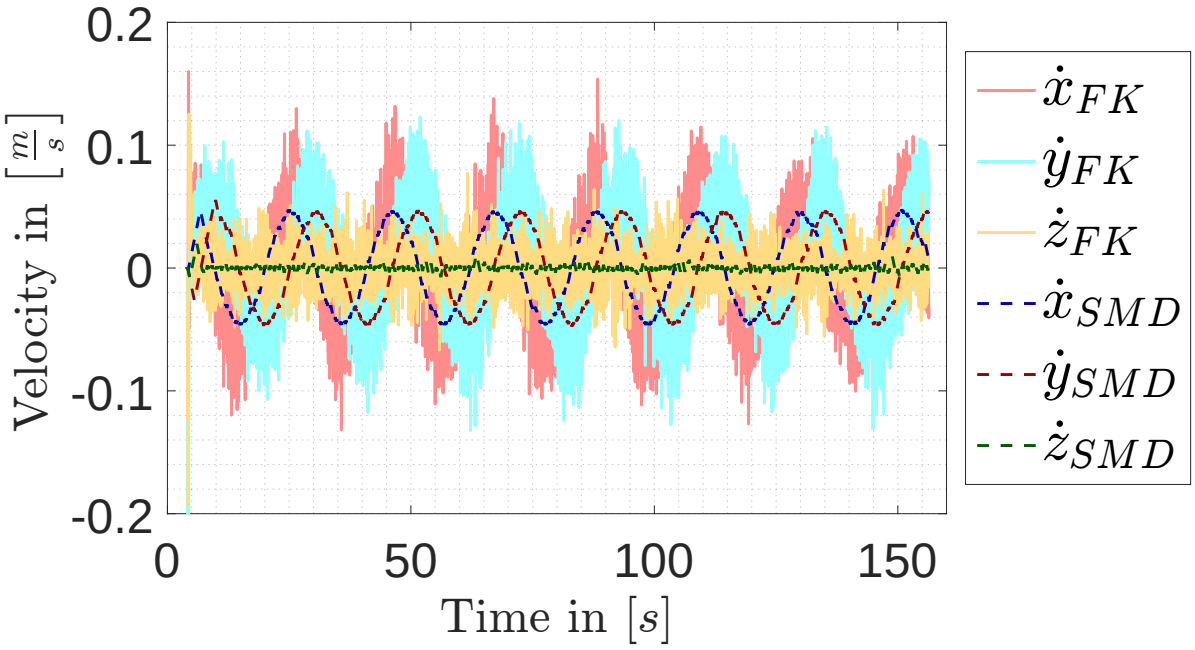

Figure 4.43: Experimental evaluation of the adaptive Sliding-Mode Differentiator - Translational velocity from forward kinematics and Sliding-Mode Differentiator

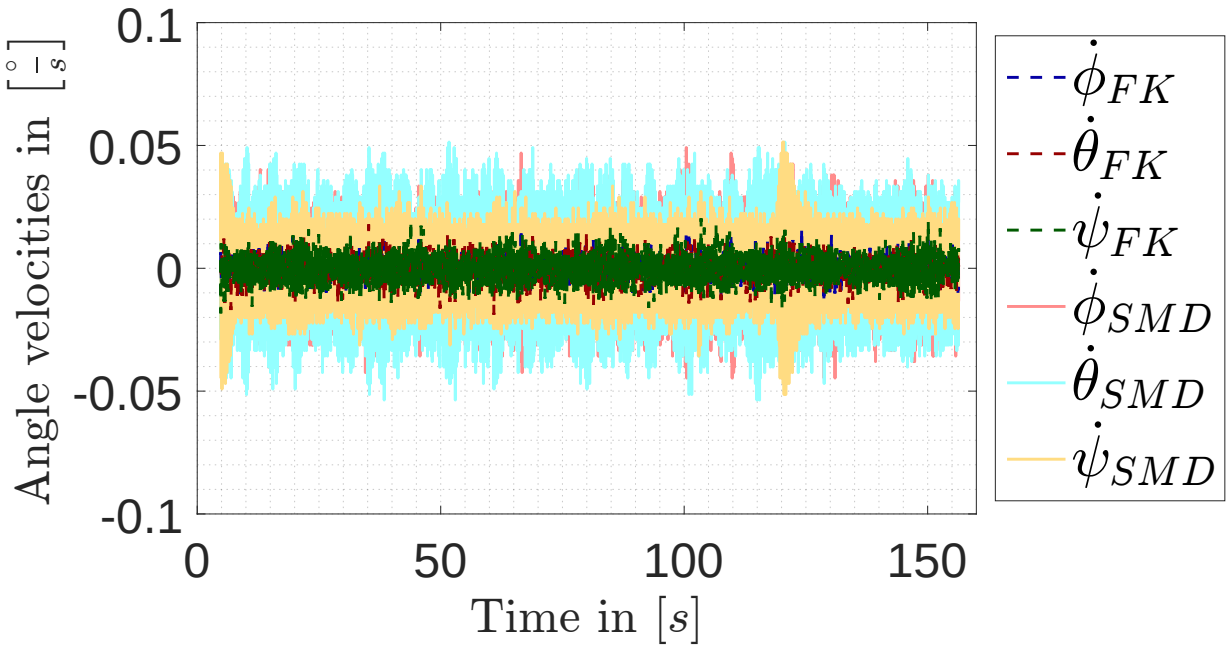

Figure 4.44: Experimental evaluation of the adaptive Sliding-Mode Differentiator - Euler rates from forward kinematics and Sliding-Mode Differentiator

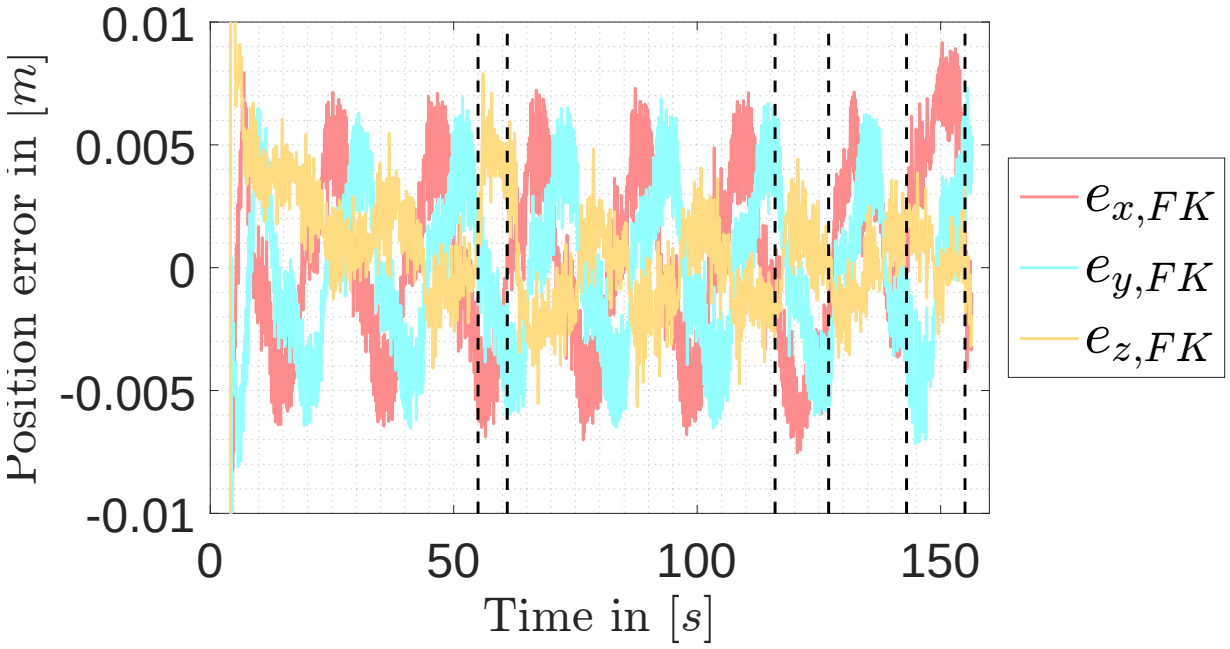

Figure 4.45: Experimental evaluation of the adaptive Sliding-Mode Differentiator - Position error

- **Figures 4.45, 4.46** and **4.48** confirms the robustness of the adaptive Super-Twisting Sliding-Mode Controller. Whenever external disturbances $\boldsymbol{\zeta}$ act on the platform, the error $\boldsymbol{e}$ and $\boldsymbol{\sigma} = \boldsymbol{e} + \boldsymbol{\Lambda}\dot{\boldsymbol{e}}$ increase but stay in a predefined range. The gain adaptation rule reacts according to exceeding of the threshold $\boldsymbol{\mu}$ in Equation (3.34). High values of $\boldsymbol{\mu}$ increase the tolerance for $|\boldsymbol{\sigma}|$ and vice versa. Thus as soon as $\boldsymbol{\sigma}$ exceeds narrow values of $\boldsymbol{\mu}$ the gain adaptation rule increases the controller gains $\boldsymbol{\Lambda}_1$ and $\boldsymbol{\Lambda}_2$ to limit $\boldsymbol{\sigma}$.

Due to this, $\boldsymbol{e}$ in Figure 4.45 and 4.46 never exceed $\pm 0.01m$ for position and $\pm 0.001°$ for orientation. Remember that one motivation for gain adaptation was the potential reduction of chattering. However, Figure 4.48 still depicts significant chattering effects. Uncompensated friction or instant configuration changes [51] might inject vibrations.

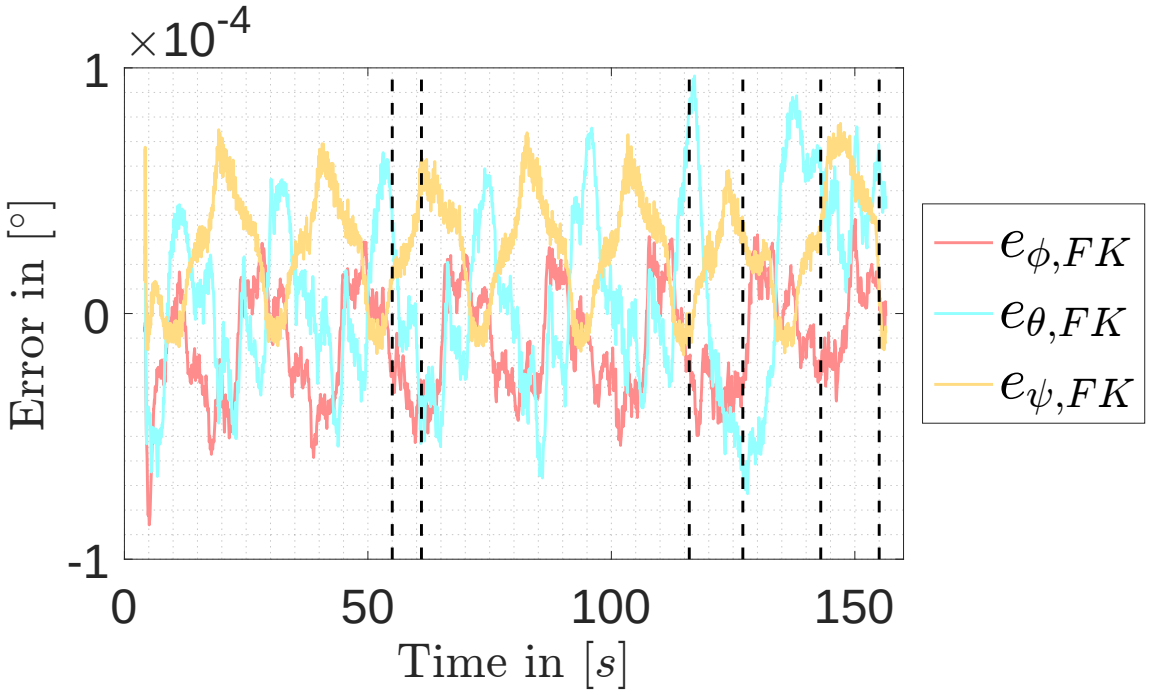

Figure 4.46: Experimental evaluation of the adaptive Sliding-Mode Differentiator - Orientation error

- **Figure 4.47** draw a similar picture. Everytime $\boldsymbol{\zeta}$ acts on the platform the corresponding gain $\boldsymbol{\Lambda}_1$ increases to limit efficiently $\boldsymbol{\sigma}$.

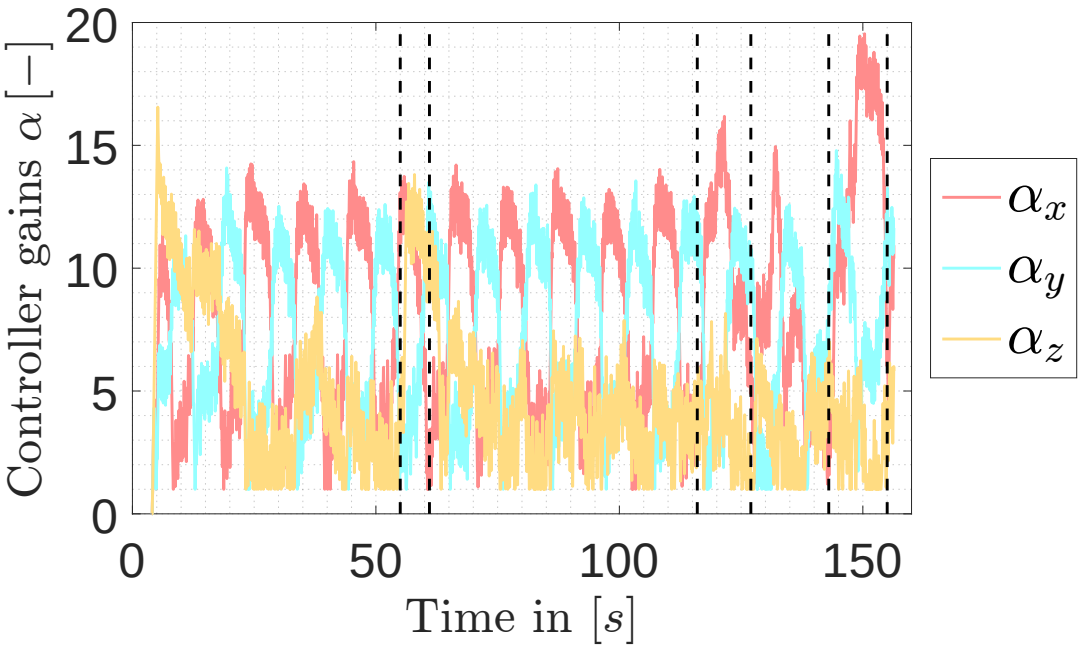

Figure 4.47: Experimental evaluation of the adaptive Sliding-Mode Differentiator - Control gain $\boldsymbol{\alpha}$

4.2.7 Summary of Chapter 4

Chapter 4 investigates cable dynamics, drivetrain characteristics and evaluates the proposed adaptive friction compensation and adaptive Super-Twisting Sliding-Mode Controller in Chapter 3. Two experiments, conducted at the Cablerobot Simulator, show that cables are highly non-linear coupled systems and damping is negligible for the Cablerobot Simulator. For both experiments, one cable is fixed on one end at the ground and connected at the other end with the motor. Four near-infrared cameras from VICON track eight markers, which are uniformly distributed along the cable. The first experiment shows, that damping is negligible for the cable of the Cablerobot Simulator. This finding simplifies modal analysis via a Finite-Element Method based model, since it spares imaginary eigenvalues of the stiffness matrix. The second experiment is dedicated to the analysis of cable vibrations. A sinusoidal torque function with stepwise increasing frequency excited the cable eigenmodes, everytime the frequency of the torque function equals an eigenfrequency of the cable. During the experiment the cable exhibited lateral oscillations. This distinctly shows the presence of coupled dynamics. These cross-coupling describe the ability to exert motions in directions, that differ from the direction of a driving force. The Finite-Element Method and a Dynamic Stiffness Matrix based model are linear models and can predict eigenfrequencies of a cable accurately as long as the cable is taut, since non-linearities are not so evident for taut cables. Furthermore, the second experiment revealed, that eigenfrequencies of the cable shift to higher values, when the cable tension increases. Both models can predict this shift.

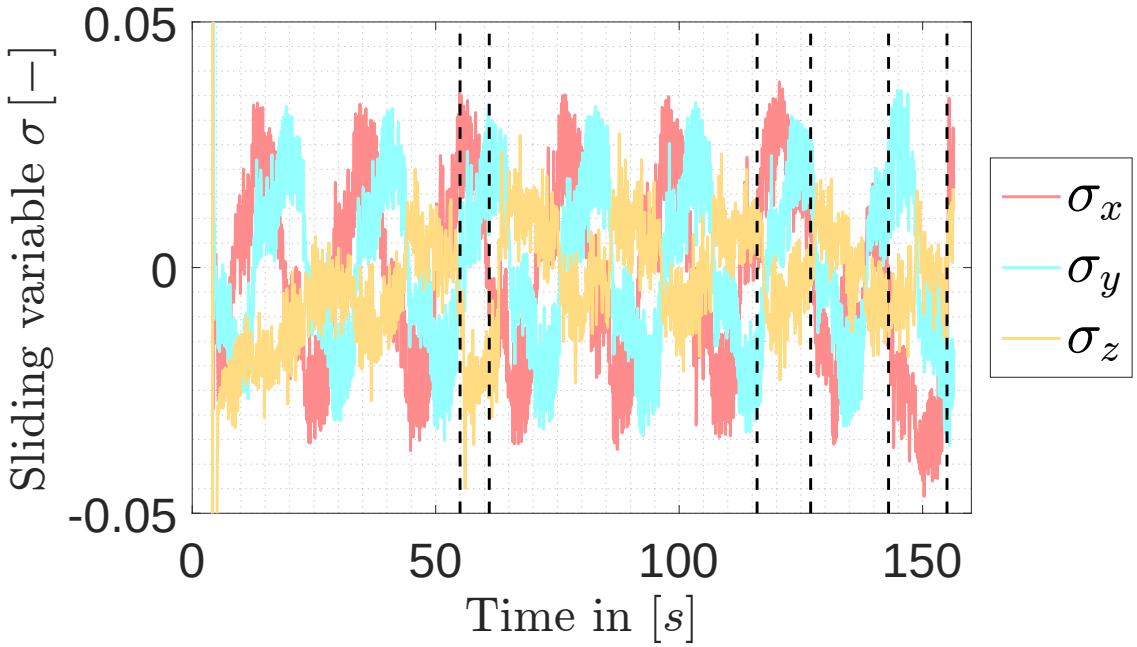

Figure 4.48: Experimental evaluation of the adaptive Sliding-Mode Differentiator - Sliding variable σ

Two experiments conducted at the Mini Cablerobot Simulator give insight to the accuracy

of direct torque control and drivetrain friction. Two more experiments evaluate the adaptive Super-Twisting Sliding-Mode Controller and the adaptive Friction Compensation, proposed in Chapter 3. For the first experiment, conducted at the Mini Cablerobot Simulator, one motor is detached from its cable and driven in direct torque control. It turned out, that an accurate tracking of torques does not imply an accurate tracking of positions and velocities, because of the motor inertia. This is a reason to incorporate also position and velocity control in the Low-Level Control scheme To investigate friction in bearings, that is one contributor to vibrations, one cable is attached at one end with the motor and at the other end with a fixed solid frame. The adaptive friction compensation proposed in Chapter 3 significantly improves trackings accuracy, i.e. position tracking, and almost perfectly compensates viscous friction. However, for static friction, the adaptive friction compensation could not completely fulfil all expectations. In an experiment with a desired sinusoidal trajectory, the adaptive friction compensation could reduce the tracking error from 3% to 2.5% during static friction and to 0.5% during viscous friction. Although the adaptive friction compensation could not fulfil all expectations, it excels classical compensation algorithms and is capable to handle different types of non-linear and time varying friction.

Finally, Chapter 4 evaluates the proposed adaptive Super-Twisting Sliding-Mode Controller of Chapter 3. The proposed controller strategy include the forward kinematics from Section 2.1.2, an arbitrary Sliding-Mode Differentiator (Section 3.3.2), the closed-form tension distribution (Section 3.2) and the adaptive Super-Twisting Sliding-Mode Controller (Section 3.3). With this setup, the adaptive Super-Twisting Sliding-Mode Controller has to stear the platform along a desired trajectory in presence of uncertain parameters, unmodelled dynamics (i.e. cable dynamics), measurement noise and external disturbances. Furthermore, the system only relies on encoder measurement, as the bare minimum of measurement inputs. The adaptive Super-Twisting Sliding-Mode Controller achieves finite-time convergence and is very robust. External disturbances with an amplitude of up to $\approx 384\%$ of the platforms weight are applied. In spite of these disturbances, the error stays in predefined narrow ranges, thanks to the proposed gain adaptation algorithm and the robustness of the Super-Twisting Sliding-Mode Controller. Although the gain adaptation algorithm reduces the controller gains, whenever it is possible, the cable forces exhibit still distinct vibrations. Since for this experiment, the adaptive friction compensation is inactive and the system is driven with direct torque control instead of position control, there is still space for improvements.

Chapter 5

Summary and Outlook

Due to their properties, Cable-Driven Parallel Robots are used in various fields among those as a simulators [2]. Simulators carry human beings, who are sensitive to vibrations and perceive them as disturbances. This motivates to identify sources of vibrations of CDPR and to investigate proper dynamic models and control strategies to suppress vibrations. It turned out, that friction in bearings, improper control inputs and cable properties, i.e. elasticity and internal cross-couplings contribute the most to vibrations.

5.1 Summary

Two experiments, conducted at the Cablerobot Simulator, gave insight to the characteristics of cable dynamics. Cables are non-linear coupled systems, which change their physical properties, depending on the cable length and cable tension. Internal cross-couplings describe the ability to exert eigenmodes, assigned to a direction, that differs from the direction of a driving force, exerted by the ground-placed actuators. Furthermore, eigenfrequencies increase with increasing tension level. These findings allow a definition of demands on cable models and rise up the question, if two commonly used models (Finite-Element Method based and Dynamic Stiffness Matrix based) can predict eigenfrequencies accurately. Both models are linear and thus lack of accuracy for low cable tensions since non-linearities are more evident for low cable tensions. However, both models can predict accurately eigenfrequencies for taut cables. Moreover, the Finite-Element Method based model is suitable for control design and therefore is preferred for further investigations.

So far the experiments limit to fixed end points. However, when the platform is in motion, the cable lengths changes and the motor wind/unwind the cables. During the winding process, cable stiffness, inertia and mass change. This complicates the modelling process, since mass transfers from cables to motors and vice versa and make those Finite-Element Method based models switching systems. Based on these findings the Finite-Element Method based model

is given in Port-Hamilton structure which allows passivity and stability proofs for switching systems.

This thesis presents the Port-Hamilton model of a Cable-Driven Parallel Robot in Port-Hamilton structure, that includes the platform dynamics, simple motor dynamics and the Finite-Element Method based cable dynamics. The latter one is proven to model accurately cable dynamics and is feasible for controller design. Simulations with a simple damping enhancing controller for a cable with fixed lengths showed, that lateral vibrations can not sufficiently be suppressed by one actuation unit alone. Moreover missing controllability and observability complicates immense reduction of cable vibrations. The Port-Hamilton based model paves the way for the design of sophisticated holistic control strategies. Those incorporate the cable dynamics and have the potential to actively suppress cable vibrations. Design of an Interconnection Damping-Assignment Passivity-Based Control is such a model-based approach, that allows to change the physical properties of a system, which makes it interesting for the control of simulator.

This work takes advantage of a Sliding-Mode Controller, which is robust and achieves finite-time convergence to 2-sliding mode. Robustness indicates effective disturbance rejection with unknown maximum, unmodelled dynamics and compensation for parameter uncertainties. In literature both is achieved by high controller gains. However, high gains amplify measurement noise and in combination with discontinuous control functions, cause chattering. The adaptive Super-Twisting Sliding-Mode Controller proposed in this thesis, proved in simulation to reduce significantly chattering. Based on predefined accuracy criteria, the adaptation algorithm keeps the controller gains as low as possible to reduce chattering and as high as necessary to allow an efficient perturbation compensation. Due to the discontinuous control function, the Adaptive Super-Twisting Sliding-Mode Controller is robust against perturbations. Simulations prove the efficiency of the proposed control strategy and compares the accuracy and robustness of the adaptive Super-Twisting Sliding-Mode controller with a Terminal Sliding-Mode Controller with fixed high gains. Experiments also prove the robustness of the adaptive Super-Twisting Sliding-Mode Controller. In spite of uncertain kinematic parameters, unmodelled cable dynamics and external disturbances, the controller drives accurately the platform along the desired trajectory. The error in position never exceeded a limit of $\pm 0.01m$ and $\pm 0.001°$. However, the controller did not suppress cable vibrations as efficient as expected. Uncompensated viscous friction is presumed to degrade the most vibration compensation strategies.

Another contributor for cable vibrations is static friction, also called stiction. Stiction is present during start-stop phases. Consider a driving force that acts on a system to initiate motion. As long the driving force does not excel the break-away force, no motion is induced. The break-away force denotes the maximum of the static friction force. This work adopts a modified signum function, that allows a more realistic friction model, in an adaptive friction compensation scheme. In simulation a composite controller with a model, based on

this modified signum function, achieves almost perfect tracking in start-stop and transient motion. The proposed adaptive friction compensation reacts immediately during abrupt direction changes. Besides the adaptive friction compensation accounts for changing friction parameters and does not need any a priori calibration. In an experiment, one cable is attached to the system frame at one end and connected with the motor drum at the other end. The corresponding motor pulls with a fixed frequency and amplitude at the cable. While the proposed adaptive friction compensation is active, the relative error in position reduces to 0.5% during motion and to 2.5% during start-stop phases. Deactivating the friction compensation increases the error to 3%.

Cable dynamics distinctly affect the platform pose and acceleration. In this light, platform state estimation based on encoder measurements only, might not be sufficient enough. Especially large scaled systems with high cable masses benefit from additional measurements, preferably at the platform. An Unscented Kalman-Filter fuses those measurements and has the potential to achieve more accurate state reconstruction than the forward kinematics alone. Furthermore, the Unscented Kalman-Filter, proposed in this work, comes with a bias estimation and accounts for the different sampling times of sensors and non-linear dynamics. Simulation results with the dynamic model of a redundant Cable-Driven Parallel Robot provide an accurate state reconstruction and IMU bias estimation.

5.2 Outlook

All results presented in this work, excess the state of the art. Until now, nobody tackled the challenges to fulfil the requirements on a Cable-Driven Parallel Robot as a simulator. However, perfect vibration compensation and tracking behaviour of such as system is challenging such that tasks in modelling, control and estimation stay open and shall motivate for future research projects.

Modelling:

The dynamic model of a cable via Finite-Element Method is simple and efficient for fixed cable lengths. However Finite-Element Method based cable models do not account for the winding process. This work introduces an activation matrix, that considers the winding process and the transfer of kinetic energy from the cables to the motor drums. Incorporated in the framework of a Port-Hamilton system, it is possible to prove passivity for such a switching system. Such a proof is out of the scope of this work and remains open for further investigations.

Control:

This work presents experimental results for suppression of controller induced and friction owed vibrations. An adaptive Super-Twisting Sliding-Mode Controller with Sliding-Mode Differentiator and an adaptive friction compensation significantly reduce cables vibrations and provide a robust framework. This control strategy achieves good tracking accuracy in presence of unmodelled dynamics, uncertain parameters, external disturbances and varying friction characteristics. A next step composites the adaptive Super-Twisting Sliding-Mode Controller, adaptive friction compensation with a adaptive Sliding-Mode Disturbance Observer for disturbance estimation. Figure 5.1 shows the entire control structure of this extended control scheme. An alternative to the already evaluated adaptive Super-Twisting Sliding-Mode Controller is an Interconnection Damping-Assignment Passivity-Based Controller, which accounts for platform and cable dynamics. Until now, the design of an Interconnection Damping-Assignment Passivity-Based Control for a Cable-Driven Parallel Robot is an open task, but is worth to be pursuited. Interconnection Damping-Assignment Passivity-Based Control is capable of changing the physical properties of a system and has the potential to efficiently suppress stiction induced vibrations and cable vibrations. Section 3.5.1 proposed a simple damping enhancing controller to suppress cable vibrations. However, control of one single cable is incapable of compensating lateral vibrations, because the actuation units can only apply forces in longitudinal direction. However, the task of controlling cable vibrations in lateral direction might be distributed over the entire system, such that lateral vibrations of one cable are compensated by the control of other cables. The problem of distributing control wrenches between cables is solved by the tension distribution, such that the only difficulty is, to distinguish between desired accelerations with low frequency and undesired cable vibrations with high frequencies.

Estimation:

The task to control cable vibrations requires further measurements, i.e. accelerations at the platform. One up to three Inertial Measurement Units can provide these measurements. Those devices should be incorporated in a holistic estimation scheme, such as the Unscented Kalman-Filter

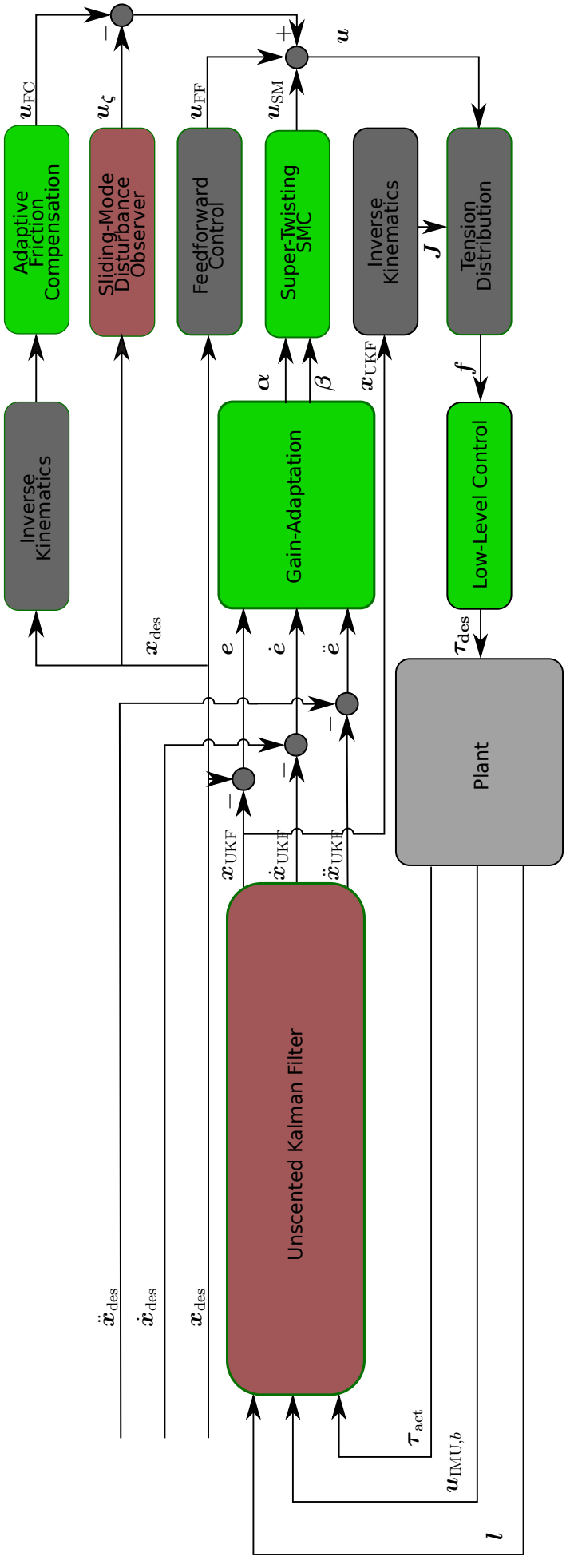

Figure 5.1: Proposed control structure for further investigations. Blocks in green depict all components which were already implemented in simulation and experimentally. Red blocks show components which were evaluated in simulation but not experimentally.

Bibliography

[1] Spydercam. `http://dev.spidercam.org/`, 2000.

[2] Cablerobot simulator. `https://www.mpg.de/9395107/seilroboter`, 2015. Accessed: 09.09.2015.

[3] Côté A., Cardou P., and Gosselin C. A tension distribution algorithm for cable-driven parallel robots operating beyond their wrench-feasible workspace. In *International Conference on Control, Automation and Systems*, pages 68–73. IEEE, 2016.

[4] Emmens A., Spanjer S., and Herder J. Modeling and control of a large-span redundant surface constrained cable robot with a vision sensor on the platform. In *Proceedings of the Second Conference on Cable-Driven Parallel Robots*, pages 249–260. Springer, 2015.

[5] Enmark A., Andersen T., Owner-Petersen M., Chakraborty R., and Labeyrie A. Integrated model of the carlina telescope. In *Integrated Modeling of Complex Optomechanical Systems*, volume 8336, page 83360J. International Society for Optics and Photonics, 2011.

[6] Kiani A. and Mashhadi S. Design sliding mode control method and a state observer for samen spacecam cable robot. *Majlesi Journal of Mechatronic Systems*, 3, 2014.

[7] Levant A. Sliding order and sliding accuracy in sliding mode control. *International journal of control*, 58(6):1247–1263, 1993.

[8] Pott A. An algorithm for real-time forward kinematics of cable-driven parallel robots. In *Advances in Robot Kinematics: Motion in Man and Machine*, pages 529–538. Springer, 2010.

[9] Pott A. Influence of pulley kinematics on cable-driven parallel robots. In *Latest Advances in Robot Kinematics*, pages 197–204. Springer, 2012.

[10] Pott A. *Cable-Driven Parallel Robots, Theory and Application*. Springer, 2018.

[11] Pott A., Mütherich H., Kraus W., Schmidt V., Miermeister P., and Verl A. Ipanema: a family of cable-driven parallel robots for industrial applications. In *Proceedings of the First Conference on Cable-Driven Parallel Robots*, pages 119–134. Springer, 2013.

[12] Pott A., Bruckmann T., and Mikelsons L. Closed-form force distribution for parallel wire robots. In *Computational Kinematics*, pages 25–34. Springer, 2009.

[13] van der Schaft A. and Jeltsema D. *Port-Hamiltonian systems theory: An introductory overview*. Now Publisher, Inc., 2014.

[14] Friedland B. and Park Y-J. On adaptive friction compensation. *Transactions on Automatic Control*, 37(10):1609–1612, 1992.

[15] Yüksel B., Secchi C., Bülthoff H., and Franchi A. Reshaping the physical properties of a quadrotor through ida-pbc and its application to aerial physical interaction. In *International Conference on Robotics and Automation*, pages 6258–6265. IEEE, 2014.

[16] Zitte B., Hamroun F., and Pitaul C. Representation of heat exchanger networks using graph formalism. In *Proceedings of the 6th IFAC Workshop on Lagrangian and Hamiltonian Methods for Nonlinear Control*, pages 44–49. IEEE, 2018.

[17] Masone C., Bülthoff H., and Stegagno P. Cooperative transportation of a payload using quadrotors: A reconfigurable cable-driven parallel robot. In *International Converence on Intelligent Robots and Systems*, pages 1623–1630. IEEE, 2016.

[18] Masone C., Giordano P., and Bülthoff H. Mechanical design and control of the new 7-dof cybermotion simulator. In *International Conference on Robotics and Automation*, pages 4935–4942. IEEE, 2011.

[19] Schenk C., Yüksel B., Secci C., and Bülthoff H. Port-hamiltonian modeling of a cable-driven robot. In *Proceedings of the 6th IFAC Workshop on Lagrangian and Hamiltonian Methods for Nonlinear Control*, pages 161–168, 2018.

[20] Schenk C., Masone C., Pott A., and Bülthoff H. Application of a differentiator-based adaptive super-twisting controller for a redundant cable-driven parallel robot. In *Proceedings of the Third Conference on Cable-Driven Parallel Robots*, pages 254–267. Springer, 2018.

[21] Schenk C., Masone C., Miermeister P., and Bülthoff H. Modeling and analysis of cable vibrations for a cable-driven parallel robot. In *International Conference on Information and Automation*, pages 454–461. IEEE, 2016.

[22] Schenk C., Bülthoff H., and Masone C. Robust adaptive sliding mode control of a redundant cable driven parallel robot. In *19th International Conference on System Theory, Control and Computing (ICSTCC)*, pages 427–434. IEEE, 2015.

[23] Secchi C., Stramigioli S., and Fantuzzi C. *Control of interactive robotic interfaces: A port-Hamiltonian approach*, volume 29. Springer Science & Business Media, 2007.

[24] Chen C-P. *Discrete-time signals and systems*. PhD thesis, 1983.

[25] Lau D., Eden J., Halgamuge S., and Oetomo D. Cable function analysis for the musculoskeletal static workspace of a human shoulder. In *Proceedings of the Second Conference on Cable-Driven Parallel Robots*, pages 263–274. Springer, 2015.

[26] Sbarbaro D. On the port-hamiltonian models of some electrochemical processes. In *Proceedings of the 6th IFAC Workshop on Lagrangian and Hamiltonian Methods for Nonlinear Control*, 2018.

[27] Surdilovic D., Radojicic J., and Bremer N. Efficient calibration of cable-driven parallel robots with variable structure. In *Cable-Driven Parallel Robots*, pages 113–128. Springer, 2015.

[28] Surdilovic D. and Bernhardt R. String-man: a new wire robot for gait rehabilitation. In *International Conference on Robotics and Automation*, pages 2031–2036, New Orleans, Louisiana, May 2004.

[29] Wan E. and Van Der Merwe r. The unscented kalman filter for nonlinear estimation. In *Adaptive Systems for Signal Processing, Communications, and Control Symposium 2000. AS-SPCC*, pages 153–158. Ieee, 2000.

[30] Wan E., Van Der Merwe R., and Nelson A. Dual estimation and the unscented transformation. In *Advances in neural information processing systems*, pages 666–672, 2000.

[31] G. El-Ghazaly, M. Gouttefarde, and V. Creuze. Adaptive terminal sliding mode control of a redundantly-actuated cable-driven parallel manipulator: CoGiRo. In A. Pott and T. Bruckmann, editors, *Cable-Driven Parallel Robots*, volume 32 of *Mechanisms and Machine Science*, pages 179–200. Springer Int. Publishing, 2015.

[32] Nieuwenhuizen F., Beykirch K., Mulder M., van Paassen M., Bonten J., and Bülthoff H. Performance measurements on the mpi stewart platform. In *AIAA Modeling and Simulation Technologies Conference and Exhibit*, page 6531, 2008.

[33] Plestan F., Shtessel Y., Bregeault V., and Poznyak A. New methodologies for adaptive sliding mode control. *International journal of control*, 83(9):1907–1919, 2010.

[34] Finn H. Discrete-time signals and systems, 2005.

[35] Godbole H., Caverly R., and Forbes J. Modelling of flexible cable-driven parallel robots using a rayleigh-ritz approach. In *Proceedings of the Third International Conference on Cable-Driven Parallel Robots*, pages 3–14. Springer, 2017.

[36] Goldstein H., Poole C., and Safko J. *Classical Mechanics, 3rd Edition*. Addison Wesley, 2000.

[37] Heerspink H., Berkouwer W., Stroosma O., van Paassen R., Mulder M., and Mulder B. Evaluation of vestibular thresholds for motion detection in the simona research simulator. In *AIAA Modeling and Simulation Technologies Conference and Exhibit*, page 6502, 2005.

[38] Irvine H. and Caughey T. The linear theory of free vibrations of a suspended cable. *Proc. R. Soc. Lond. A*, 341(1626):299–315, 1974.

[39] Olsson H., Aström K., De Wit C., Gäfvert M., and Lischinsky P. Friction models and friction compensation. *Eur. J. Control*, 4(3):176–195, 1998.

[40] Yuan H. *Static and dynamic stiffness analysis of cable-driven parallel robots, PhD thesis*. INSA de Rennes, 2015.

[41] Yuan H., Courteille E., and Deblaise D. Elastodynamic analysis of cable-driven parallel manipulators considering dynamic stiffness of sagging cables. In *International Conference on Robotics and Automation*, pages 4055–4060, May 2014.

[42] Jong IC. and Rogers BG. *Engineering mechanics: dynamics*, volume 2. Oxford University Press, 1990.

[43] A. Isidori. *Nonlinear Control Systems, 3rd edition*. Springer Verlag, 1995.

[44] Cuevas J., Laroche E., and Piccin O. Assumed-mode-based dynamic model for cable robots with non-straight cables. In *Proceedings of the Third Conference on Cable-Driven Parallel Robots*, pages 15–25. Springer, 2018.

[45] Du J., Ding W., and Bao H. Cable vibration analysis for large workspace cable-driven parallel manipulators. In *Proceedings of the First Conference on Cable-Driven Parallel Robots*, pages 437–449. Springer, 2013.

[46] Kim J. and Chang S. Dynamic stiffness matrix of an inclined cable. *Engineering structures*, 23(12):1614–1621, 2001.

[47] Piao J., Jin X., Choi E., Park J., Kim C., and Jung J. A polymer cable creep modeling for a cable-driven parallel robot in a heavy payload application. In *Proceedings of the Third Conference on Cable-Driven Parallel Robots*, pages 62–72. Springer, 2017.

[48] Zhao J. and Hill D. Dissipativity theory for switched systems. *Transactions on Automatic Control*, 53(4):941–953, 2008.

[49] Zhao J. and Hill D. Passivity and stability of switched systems: a multiple storage function method. *Systems & Control Letters*, 57(2):158–164, 2008.

[50] Merlet J-P. On the inverse kinematics of cable-driven parallel robots with up to 6 sagging cables. In *International Confererence on Intelligent Robots and Systems*, pages 4356–4361. IEEE, 2015.

[51] Merlet JP. Checking the cable configuration of cable-driven parallel robots on a trajectory. In *International Conference on Robotics and Automation*, pages 1586–1591. IEEE, 2014.

[52] Hekman K., Lawrence J., and Singhose W. Use of input shaping to decrease the effects of stiction. *IFAC Proceedings Volumes*, 34(6):289–294, 2001.

[53] Verbert KAJ., Toth R., and Babuvska R. Adaptive friction compensation: A globally stable approach. *ASME Transactions on Mechatronics*, 21(1):351–363, 2016.

[54] M. A. Khosravi and H. D. Taghirad. Experimental performance of robust pid controller on a planar cable robot. In T. Bruckmann and A. Pott, editors, *Cable-Driven Parallel Robots*, volume 12 of *Mechanisms and Machine Science*, pages 337–352. Springer Berlin Heidelberg, 2013.

[55] Gagliardini L, Caro S., Gouttefarde M., Wenger P., and Girin A. A reconfigurable cable-driven parallel robot for sandblasting and painting of large structures. In *Proceedings of the first Conference on Cable-Driven Parallel Robots*, pages 275–291. Springer, 2015.

[56] J. Lamaury, M. Gouttefarde, A. Chemori, and P.-E. Herve. Dual-space adaptive control of redundantly actuated cable-driven parallel robots. In *International Conference on Intelligent Robots and Systems*, pages 4879–4886, Nov 2013.

[57] Arsenault M. Stiffness analysis of a planar 2-dof cable-suspended mechanism while considering cable mass. In *Proceedings of the First Conference on Cable-Driven Parallel Robots*, pages 405–421. Springer, 2013.

[58] Gouttefarde M. and Gosselin C. Analysis of the wrench-closure workspace of planar parallel cable-driven mechanisms. *Transactions on Robotics*, 22(3):434–445, 2006.

[59] Gouttefarde M., Nguyen D., and Baradat C. Kinetostatic analysis of cable-driven parallel robots with consideration of sagging and pulleys. In *Advances in Robot Kinematics*, pages 213–221. Springer, 2014.

[60] Gouttefarde M. and Krut S. Characterization of parallel manipulator available wrench set facets. In *Advances in Robot Kinematics: Motion in Man and Machine*, pages 475–482. Springer, 2010.

[61] Hassan M. and Khajepour A. Optimization of actuator forces in cable-based parallel manipulators using convex analysis. *Transactions on Robotics*, 24(3):736–740, 2008.

[62] Hiller M., Fang S., Hass C., and Bruckmann T. Analysis, realization and application of the tendon-based parallel robot segesta. *Robotic Systems for Handling and Assembly*, 2:185–202, 2005.

[63] Khosravi M. and Taghirad H. Experimental performance of robust pid controller on a planar cable robot. In *Proceedings of the First Conference on Cable-Driven Parallel Robots*, pages 337–352. Springer, 2013.

[64] Khosravi M. and Taghirad H. Dynamic analysis and control of fully-constrained cable robots with elastic cables: variable stiffness formulation. In *Proceedings of the Second Conference on Cable-Driven Parallel Robots*, pages 161–177. Springer, 2015.

[65] Raghavan M. The stewart platform of general geometry has 40 configurations. *Journal of Mechanical Design*, 115(2):277–282, 1993.

[66] Van der Kooij MW. Model based friction compensation for an electromechanical stewart platform actuator, 2011.

[67] Bosscher P., Riechel A., and Ebert-Uphoff I. Wrench-feasible workspace generation for cable-driven robots. *Transactions on Robotics*, 22(5):890–902, 2006.

[68] Miermeister P., Masone C., Bülthoff H., and Tesch J. The cablerobot simulator - large scale motion platform based on cable robot technology. In *International Conference on Intelligent Robots and Systems*, October 2016.

[69] Miermeister P., Kraus W., Lan T., and Pott A. An elastic cable model for cable-driven parallel robots including hysteresis effects. In *Proceedings of the Second International Conference on Cable-Driven Parallel Robots*, pages 17–28. Springer, 2015.

[70] Tempel P., Schmidt A., Haasdonk B., and Pott A. Application of the rigid finite element method to the simulation of cable-driven parallel robots. In *Computational Kinematics*, pages 198–205. Springer, 2018.

[71] Tempel P., Lee D., and Pott A. Elastic-flexible cable models with time-varying length for cable-driven parallel robots - a rayleigh-ritz approch. In *International Conference on Intelligent Robots and Systems*, 2018.

[72] Babaghasabha R., Khosravi M., and Taghirad H. Adaptive control of kntu planar cable-driven parallel robot with uncertainties in dynamic and kinematic parameters. In *Cable-Driven Parallel Robots*, pages 145–159. Springer, 2015.

[73] Bostelman R., Albus J., Dagalakis N., Jacoff A., and Gross J. Applications of the nist robocrane. *Robotics and Manufacturing*, 5:403–407, 1994.

[74] Ortega R., Van Der Schaft A., Maschke B., and Escobar G. Interconnection and damping assignment passivity-based control of port-controlled hamiltonian systems. *Automatica*, 38(4):585–596, 2002.

[75] Verhoeven R. *Analysis of the workspace of tendon-based Stewart platforms*. Universität Duisburg-Essen, Fakultät für Ingenieurwissenschaften» Maschinenbau und Verfahrenstechnik, 2004.

[76] Yao R., Li H., and Zhang X. A modeling method of the cable driven parallel manipulator for fast. In *Proceedings of the First Conference on Cable-Driven Parallel Robots*, pages 423–436. Springer, 2013.

[77] Julier S. and Uhlmann J. New extension of the kalman filter to nonlinear systems. In *Signal processing, sensor fusion, and target recognition VI*, volume 3068, pages 182–194. International Society for Optics and Photonics, 1997.

[78] Julier S., Uhlmann J., and Durrant-Whyte H. A new method for the nonlinear transformation of means and covariances in filters and estimators. *Transactions on Automatic Control*, 45(3):477–482, 2000.

[79] Kawamura S. Development of an ultrahigh speed robot falcon using wire drive system^{o}. *International Conference on Robotics and Automation*, pages 215–220, 1995.

[80] Mondal S. and Mahanta C. Adaptive second order terminal sliding mode controller for robotic manipulators. *Journal of the Franklin Institute*, 351(4):2356–2377, 2014.

[81] Oh S. and Agrawal S. Nonlinear sliding mode control and feasible workspace analysis for a cable suspended robot with input constraints and disturbances. In *American Control Conference (ACC)*, volume 5, pages 4631–4636. IEEE, 2004.

[82] Peter S., Riethmüller R., and Leine R. Tracking of backbone curves of nonlinear systems using phase-locked-loops. In *Nonlinear Dynamics, Volume 1*, pages 107–120. Springer, 2016.

[83] L. Sciavicco and Siciliano B. *Modelling and control of robot manipulators*. Springer, 2000.

[84] L. Sciavicco and B. Siciliano. *Modelling and Control of Robot Manipulators*. Springer Verlag, 2005.

[85] Andersen T., Le Coroller H., Owner-Petersen M., and Dejonghe J. Linearized model of an actively controlled cable for a carlina diluted telescope. In *Improving the Performances of Current Optical Interferometers & Future Designs*, pages 153–173, 2014.

[86] Bruckmann T., Pott A., and Hiller M. Calculating force distributions for redundantly actuated tendon-based stewart platforms. In *Advances in Robot Kinematics*, pages 403–412. Springer, 2006.

[87] Singh T. and Singhose W. Input shaping/time delay control of maneuvering flexible structures. In *American Control Conference (ACC)*, volume 3, pages 1717–1731. IEEE, 2002.

[88] Starossek U. Dynamic stiffness matrix of sagging cable. *Journal of engineering mechanics*, 117(12):2815–2828, 1991.

[89] Schmidt V. *Modeling techniques and reliable real-time implementation of kinematics for cable-driven parallel robots using polymer fiber cables*. Stuttgart: Fraunhofer Verlag, 2017.

[90] Schmidt V. and Pott A. Implementing extended kinematics of a cable-driven parallel robot in real-time. In *Proceedings of the First Conference on Cable-driven parallel robots*, pages 287–298. Springer, 2013.

[91] Ho W., Kraus W., Mangold A., and Pott A. Haptic interaction with a cable-driven parallel robot using admittance control. In *Proceedings of the Second Conference on Cable-Driven Parallel Robots*, pages 201–212. Springer, 2015.

[92] Kraus W. *Force control of cable-driven parallel robots*. 2016.

[93] Kraus W., Kessler M., and Pott A. Pulley friction compensation for winch-integrated cable force measurement and verification on a cable-driven parallel robot. In *International Conference on Robotics and Automation*, pages 1627–1632. IEEE, 2015.

[94] O'Connor W. Wave-based control of flexible mechanical systems. In *Informatics in Control Automation and Robotics*, pages 25–34. Springer, 2008.

[95] Shiang W., Cannon D., and Gorman J. Optimal force distribution applied to a robotic crane with flexible cables. In *International Conference on Robotics and Automation*, volume 2, pages 1948–1954. IEEE, 2000.

[96] Greg Welch and Gary Bishop. An introduction to the kalman filter. department of computer science, university of north carolina. *ed: Chapel Hill, NC, unpublished manuscript*, 2006.

[97] Diao x. and Ma O. Vibration analysis of cable-driven parallel manipulators. In *Multibody system dynamics*, volume 21, pages 347–360. Springer, 2009.

[98] Weber X., Cuvillon L., and Gangloff J. Active vibration canceling of a cable-driven parallel robot in modal space. In *International Conference on Robotics and Automation*, pages 1599–1604. IEEE, 2015.

[99] Shtessel Y., Edwards C., Fridman L., and Levant A. *Sliding mode control and observation*, volume 10. Springer, 2014.

[100] Shtessel Y., Moreno J., Plestan F., Fridman L., and Poznyak A. Super-twisting adaptive sliding mode control: A lyapunov design. In *International Conference on Decision and Control (CDC)*, pages 5109–5113. IEEE, 2010.

[101] Shtessel Y., Taleb M., and Plestan F. A novel adaptive-gain supertwisting sliding mode controller: Methodology and application. *Automatica*, 48(5):759–769, 2012.